Exploring the F-Block through Non-Aqueous Coordination Chemistry

Bonnie E. Klamm

FLORIDA STATE UNIVERSITY

COLLEGE OF ARTS AND SCIENCES

EXPLORING THE F-BLOCK THROUGH NON-AQUEOUS COORDINATION CHEMISTRY

By

BONNIE E. KLAMM

A Dissertation submitted to the
Department of Chemistry and Biochemistry
in partial fulfillment of the
requirements for the degree of
Doctor of Philosophy

2020

Bonnie E. Klamm Defended this dissertation on March 30, 2020.
The members of the supervisory committee were:

Thomas E. Albrecht-Schmitt
Professor Directing Dissertation

Ingo Wiedenhöver
University Representative

Albert E. Stiegman
Committee Member

Kenneth A. Goldbsy
Committee Member

Michael Roper
Committee Member

The Graduate School has verified and approved the above-named committee members and certifies that the dissertation has been approved in accordance with university requirements.

ACKNOWLEDGMENTS

I would fist like to acknowledge Brenda Dingus at the Los Alamos National Laboratory, who encouraged me to apply to the Nuclear Forensics Summer School where I first fell in love with actinide chemistry. During the summer program I met Natalie and Donald Wall who further encouraged and supported me in the field. Shortly after, Ryan Hess at the Sandia National Labs hired me as an intern for nuclear materials related research. Thank you all for getting me started in the field of research, and more so, actinide research.

I also want to thank my advisor, Dr. Albrecht-Schmitt. You have supported my decision to pursue a doctorate in chemistry although I came from a geology background. I was drawn to the chemistry of actinides and have had your full support from the start. Additionally, I thank all the members of the Albrecht-Schmitt group (the Schminions!) I have had the pleasure of working with. Shane Galley, Frankie White, and Joe Sperling, you all helped me get started in the lab and continue to look after me. I especially thank Cory Windorff who has spent a lot of time teaching me how to write research papers and handle isotopes. We have worked on many projects together, and I hope to work with you in the future again. I also thank Cristan Celis-Barros who has spent many hours providing amazing computation results for my projects. You are a talented theorist and I've greatly enjoyed working with you. David Hobart has also been very supportive and has helped me make important connections at LANL. I'll never miss an opportunity to talk science and go rock hounding with you. I also thank Aaron Tondreau, Ben Stein, and the rest of my LANL family who has supported me through the Seaborg and Nuclear Energy University Program fellowships. I've been blessed with excellent and supportive mentors and co-workers.

Thanks to my committee members, Dr. Albert Stiegman, Dr. Michael Roper, and Dr. Ken Goldsby, and Dr. Ingo Wiedenhoever. Thank you for choosing to take place in my education over the last few years as a young scientist. I truly appreciate your time and attention.

Last, I would like to thank Florida State University for allowing me to thank the Chemical Sciences, Geosciences, and Biosciences Division, Office of Basic Energy Sciences, U.S. Department of Energy, for supporting the research as part of the Center for Actinide Science and Technology funded by the U.S. Department of Energy, Office of Science, Office of Basic Energy Sciences, under Award DE-SC0016568. Additionally, I gratefully acknowledge the support of the U.S. Department of Energy through the LANL/LDRD Program and the G. T. Seaborg Institute for this work.

TABLE OF CONTENTS

LIST OF TABLES

LIST OF FIGURES

ABSTRACT

The knowledge of actinide chemistry significantly lags behind the rest of the periodic table. Understanding the fundamental behavior of these elements is crucial for actinide separations and nuclear waste storage. Many separation strategies utilize various ligands to effectively coordinate specific actinides, however this remains an underdeveloped area of research.

It is generally accepted that actinides have slightly more diffuse *f*-orbitals which allow for more covalent character in the bonds they form with ligands, resulting in more stable complexes with softer donor ligands. This has resulted in the design of selective ligands to specifically bind actinides for effective separation. By carefully selecting solvents, a wide variety of ligands can be utilized in order to understand the relative participation of actinide frontier orbitals (6*p*, 6*d*, 5*f*, 7*s*, 7*p*) in bonding, and understanding these bonding differences is important for how they may be utilized for future designs of ligand systems for actinide separations.

The first part of this work focuses on *f*-element Schiff base coordination complexes in order to produce a clearer picture of the bonding between actinides and ligands. Schiff base ligands and their derivatives are of popular interest because of their ability to coordinate many different metal ions and stabilize them in a variety of oxidation states. First, a series of homoleptic tetravalent *f*-element and transition metal complexes have been synthesized, allowing for a comparison of coordination complexes containing metal cations in the formal 4+ oxidation state by structural, spectroscopic, and theoretical analysis. Utilizing the same ligand, this study was extended to the uranyl and neptunyl dications in the 6+ oxidation state. Furthermore, a series of heteronuclear complexes featuring a trivalent *f*-element and divalent transition metal were examined through crystallographic, spectroscopic, and magnetic analysis.

The second part of this work focuses on periodic trends in bonding and Lewis-acid catalysis of the lanthanides and mid actinides utilizing a neutral nitrogen donor cryptand ligand. An imine-cleavage methodology is used to generate bimetallic complexes from the ligand across the *f*-block. In this study, a divergence of coordination activity is observed between the early and late lanthanides in structure and bonding, and is extended to the actinides. Synthetic methods also show the importance of the starting material as well as the pH, in the generation of mono vs. bimetallic complexes. Lastly, a similar study was conducted utilizing different starting materials to focus on the monometallic cryptand complexes of Ce and Pu.

CHAPTER 1
INTRODUCTION

1.1 Applications and Issues with the *f*-elements

Understanding the complex chemistry of actinide elements has important applications in civilian nuclear fuel production, spent nuclear fuel processing, nuclear weapons production and dismantlement, treatment and storage of nuclear wastes, and environmental monitoring.[1–3] The management of spent fuel arising from nuclear power production and processing has long been considered an important issue due to political, economic, and societal implications associated with it. While the large amount of spent fuel is progressively being added to the cumulative inventory in the world, the significance of spent fuel products and other waste forms will continue to grow. At this time it is crucial to reduce the volume and long term radiotoxicity of high level waste (HLW) by partitioning and the transmutation of minor actinides.[2]

A total of 448 nuclear power reactors were in operation at the end of 2017, including four reactors that have been newly constructed.[4] According to the International Atomic Energy Association (IAEA), projections for global installed nuclear power capacity showed an increase of 42% by 2030, and 83% by 2040. The United States commercial power industry generates roughly 80% of the nation's total nuclear waste, with the U.S. government's nuclear weapons program and legacy waste accounting for most of the rest. This waste remains thermally hot, highly radioactive, and potentially harmful. The United States currently has no permanent disposal site for the approximate 90,000 metric tons of spent fuel that is stored across 35 states.[5] While storage or disposal facilities may take decades to develop, the amount of spent fuel stored off-site at commercial nuclear reactors will continue to accumulate, with an expected increase to about 140,000 metric tons over the next several decades.[5]

HLW is produced from the 'burning' of uranium fuel and contains the fission products and transuranic elements generated in the reactor core. While it only accounts for 3% of the volume, is contributes 95% of the total radioactivity of produced waste. The key risk posed by HLW is a release of radiation that could harm human health and the environment. Methods to significantly reduce the volume and radiotoxicity of waste for safe storage and handling is currently being investigated. Due to their high radiotoxicity, particular attention must be paid to

the transuranic actinides (Np, Pu, Am, and Cm) that contribute >99% the radiotoxicity even after several hundred years of storage. The approximate composition of spent nuclear fuel is shown in **Figure 1.1**. The majority of the waste is comprised of U, which is recovered in the PUREX (Plutonium and URanium EXtraction) process. Its removal reduces the long-lived radiotoxicity of the remaining waste from ~300,000 years to 9,000 years. However, if the minor actinides (Am, Cm) are subsequently removed, the radiotoxicity of the remaining waste takes only 300 years to reach the level of natural U. In partitioning and transmutation strategies, these long-lived radionuclides are recovered and converted into shorter-lived or stables ones through irradiation in dedicated reactors. The development of highly efficient methods to recover these elements from spent nuclear fuel is essential and requires further fundamental research to learn about the structure, bonding, and coordination behavior of the actinides.

While actinide chemistry has been increasing in interest, these elements are difficult to study because of their radioactivity and synthetic limitations that requires nuclear reactions and rapid separations. Some of the fundamental properties of the mid-late actinides remain to be calculated theoretically and measured experimentally. While new information and concepts have accumulated since the actinide concept was introduced by G.T. Seaborg, these elements remain poorly understood compared to the rest of the periodic table. For example, in comparison to the noble metals, the lanthanides and early actinides are at least an order in magnitude more abundant in the earth's crust. While these late transition metals may be rarer, there are significantly more structures in the Cambridge Crystallographic Data Center (CCDC) than the total number of actinide structures alone, **Table A.1**. This demonstrates that the knowledge and understanding of fundamental actinide bonding trends and coordination modes is significantly limited compared to other elemental series in the periodic table. The lack of actinide studies limits our grasp on the bonding and the electronic structure trends across the 5*f* series, and how the changes in ligand binding may impact speciation and separation selectivity to different metal ions. Furthermore, progress in transplutonium studies lag even further behind the contemporary knowledge of transition metal, lanthanide, and early actinide (Th and U) chemistry.

1.2 Chemistry of the *f*-elements

Actinides are the last elements on the periodic table where bulk chemical and physical properties can be measured without speculation. However, the ability to work with these

elements is challenging due to their radioactivity and availability. Elements beyond Am are made synthetically and rarely available in quantities larger than a few mg, which makes them scarce and costly. Additional safety procedures and tools are employed when handling these elements to practice ALARA (As Low As Reasonably Achievable), concerning worker safety. Common tools include lead bricks and aprons, Geiger, gamma, and alpha counters, and the use of yellow and magenta ropes or tape to designate radiation areas. Disposable sleeves along with double gloves taped to the lab coat are also donned when handling isotopes in the fume hood. Dust masks or respirators are also worn when solid-state actinide materials are brought out of the fume hood or glovebox. Personal dosimeters are worn to measure uptake of external dose, and hand and foot monitors and personal contamination monitors (PCMs) are commonly used to check for contamination prior to exiting the work area. Working in a radiation area at a national laboratory requires extra training and follows slightly different procedures than in a university setting. For the safety of the graduate students or other radiation workers, any work with actinides is typically limited to the hours of 8 am to 5 pm when the radiological control technicians (RCT) are available for help.

Due to the scarcity of these isotopes, most, if not all radiation laboratories reprocess their isotopes for further experiments. After several experimental campaigns, the isotope is purified from inorganic and organic contaminants using a series of precipitations and ion exchange chromatography steps.[6,7] For instance, after dissolving a $^{248}Cm^{3+}$ sample in HCl (6 M), initial purification begins by precipitating CmF_3 with HF. The resulting highly insoluble product is then dissolved in boric acid (H_3BO_3) and HCl. After an ammonium hydroxide (NH_4OH) precipitation, a more rigorous purification is achieved using a cation exchange resin. Due to the low concentrations (~5-10 mg) of Cm, small volumes (1 drop) of an eluted fraction must be dried and quantified by α-activity. For larger quantities, optical spectroscopy (absorption and fluorescence) is used for quantification. This reprocessing may require further purification steps or oxidation adjustments depending on the isotope and may take up to a week to complete.

In any radiation laboratory, work must be conducted in pairs when handling isotopes. One person will perform the chemistry or task while another assists. This minimizes error and risk of contamination and also helps the process along. For this reason, our lab works as a team when characterizing any actinide complex. This is especially important for characterizing isotopes with short half-lives (i.e. ^{249}Bk $t_{1/2}$ = 331 days), or isotopes that give off high energy

beta or gammas. For all of the above reasons, the use of non-radioactive analogs are extremely useful in order to practice and hone synthetic methods on a small scale before handling the isotopes. In this case, the best analogs for the actinides are the lanthanides.

Lanthanides play two roles in-terms of actinide chemistry. Because of their chemical similarity to actinides, they are difficult to separate from the minor actinides in HWL. Howbeit, due to the same similarities, the lanthanides are commonly used as structural and chemical models for the actinides. Both the lanthanide and actinide series possess similar outermost electronic configuration, through the filling of the *f*-subshell. There is a steady decrease in ionic radii of the lanthanides as the series is traversed from La to Lu, and a similar contraction is found for the actinide series. This contraction is explained as an electrostatic effect due to the poor screening by the *f*-electrons as the nuclear charge is increased. While the lanthanides are commonly accepted as reasonable analogs for actinides, the dissimilarity in chemistry between the lanthanides and actinides is partially caused by the differences in orbital behavior. The 4*f* shell remains nearly entirely shielded within the Xe core and plays essentially no part in the bonding in lanthanide complexes and crystal field effects. In comparison, the radial extension of the 5*f* subshell is more exposed than the 4*f* subshell, allowing them to be more chemically active.

The most stable oxidation state for all lanthanides is the 3+ oxidation state in aqueous solutions, however several lanthanides are capable of tetravalent and divalent chemistry. For Nd^{4+} and Dy^{4+}, this is confined to solid state fluoride complexes, while Pr^{4+} and Tb^{4+} can form the tetrafluoride and dioxide. Ce is the only lanthanide for which the 4+ oxidation state is stable in aqueous solution and the solid state. The lanthanides with the most extensive divalent chemistry are Eu^{2+}, Sm^{2+} and Yb^{2+}, and to a lesser extent Tm^{2+}. In contrast, the small energy difference between the 5*f*, 6*d*, and 7*s* electrons in the actinide series, especially for the early actinides, allows for more than one oxidation state. **Table A.2.** shows the oxidation states adopted by the actinides and lanthanides. Some of the lighter actinides resemble the transition metals in the range of possible oxidations states, while the later actinides behave more like lanthanides in favoring the 3+ oxidation state. This great range of oxidation states exhibited by the early actinides in comparison to lanthanides indicates that the valence electrons are less tightly bound and more available for bonding.

Moving along the 5*f* series, Th^{3+} is rapidly oxidized by water, and the aqueous chemistry of this ion is exclusively as Th^{4+}. U^{3+} is readily obtained by reduction of higher valent species

and can be stable for days in the absence of air. Aqueous solutions of Np^{3+} are stable in air and can be readily prepared by electrolytic reduction of acidic solutions of Np^{4+}. At Am, the trivalent ion is the preferred state. A similar trend is observed for the penta and hexavalent actinyl ions. Their stability falls across the series for U, where UO_2 predominates in the presence of air, to Cm for which the actinyls are still unknown. Pu is capable of attaining five oxidation states in water, from Pu^{3+} to Pu^{7+}. The redox potentials separating the most common states are roughly equal, and interconversion between oxidation states occurs through disproportionation and conproportionation reactions, **Figure 1.2**. Thus, it is commonly found that all Pu^{3+} to Pu^{6+} occur together in solution, and it can be difficult to prepare pure solutions of one ion. Most actinides with oxidation states higher than 4+ exist as actinyl cations AnO_2^{n+} (n = 1, 2), which contain essentially linear O–An–O units. In the case of U, both *d* and *f* orbitals play a role in bonding between U and O, and all 12 valence electrons participate for a U≡O bond order of three. AnO_2^{2+} (An = Np, Pu, Am) have 13, 14, and 15 electrons respectively, and have one, two, and three electrons in the non-bonding 5*f* orbitals. These ions are also linear, but the stability decreases from U > Np > Pu > Am.

Due to the large size of the lanthanides and actinides, high coordination numbers (up to 12) are often found depending on oxidation state. In aqueous solution, Ln^{3+} ions are surrounded by eight or nine water molecules, in contrast to smaller group three elements, such as Sc, which have six waters. The situation is further complicated for the actinides because of their redox chemistry, but U^{3+} for example is nine-coordinate.

The majority of the electronic transitions in Ln^{3+} ions involve only a redistribution of electrons within the 4*f* subshell. These *f*→*f* transitions are forbidden due to the electric dipole selection rules, and the resulting intensities are weak. The lack of 4*f* orbital/ligand interaction implies that the *f*→*f* transitions energies change little between compounds, often giving characteristic pale colors. Furthermore, the small interactions of the 4*f* atomic orbitals with the surrounding ligands is so that the transition energies are well defined, leading to sharper bands than would be observed for transition metal compounds. The electronic absorption spectra of actinide compounds are more difficult to interpret than the lanthanides. This is due to the increase in spin-orbit coupling and the greater interaction of the 5*f* atomic orbitals with the surrounding ligands that result in *J* no longer being a good quantum number. Although vibronic coupling is greater in actinide compounds than in those of lanthanides, *f*→*f* transitions are still

weak, but less so than for the lanthanides. The increased 5*f* orbital interactions also result in actinide *f*→*f* bands being slightly broader.

While these elements are similar, their chemical and electronic differences are important to understand for ligand design and separation schemes. Due to the limitations present with actinides, current laboratory-based instrumentation allows for a detailed analysis of small samples (<1 mg). Single crystal X-ray analysis allows for structure determination from microcrystals, and microspectrophotometers allow for detailed spectroscopic measurements on micrometer-sized materials. Other techniques including cyclic voltammetry and NMR are also explored in this work, using samples on the scale of several mg. In addition, coupling experimental and computation efforts has allowed for in depth understanding and has recently changed our view in the chemistry of the actinides.

1.3 Thesis Objectives

It is generally accepted that actinides have slightly more diffuse *f*-orbitals which allow for more covalent character in the bonds they form with ligands, resulting in more stable complexes with softer ligands. This has resulted in the design of selective ligands to specifically bind actinides for effective separation. By carefully selecting solvents, a wide variety of ligands can be utilized in order to understand the relative participation of actinide frontier orbitals (6*p*, 6*d*, 5*f*, 7*s*, 7*p*) in bonding, and understanding these bonding differences is important for how they may be utilized for future designs of ligand systems for actinide separations.

The first part of this work focuses on using several methods to characterize Schiff base coordination complexes involving the *f*-elements to produce a clearer picture of the bonding between actinides and ligands. Specifically examining periodic bonding trends and coordination modes of the early to mid-actinides in various oxidation states.

The second part of this work focuses on periodic bonding and Lewis-acid catalysis of the lanthanides and mid actinides utilizing a neutral nitrogen donor cryptand ligand. An imine-cleavage methodology is used to generate bimetallic complexes from the ligand across the *f*-block. In this study a divergence of coordination activity is observed between the early and late lanthanides. These synthetic studies show the importance of the starting material as well as the pH, in the generation of bi- vs. monometallic complexes, which are also explored. This work can provide the basis for new ligands for selective separations, new complexes with specific

spectroscopic or electrochemical properties, and/or other various properties we can take advantage of to improve the applications of actinides.

1.4 Figures

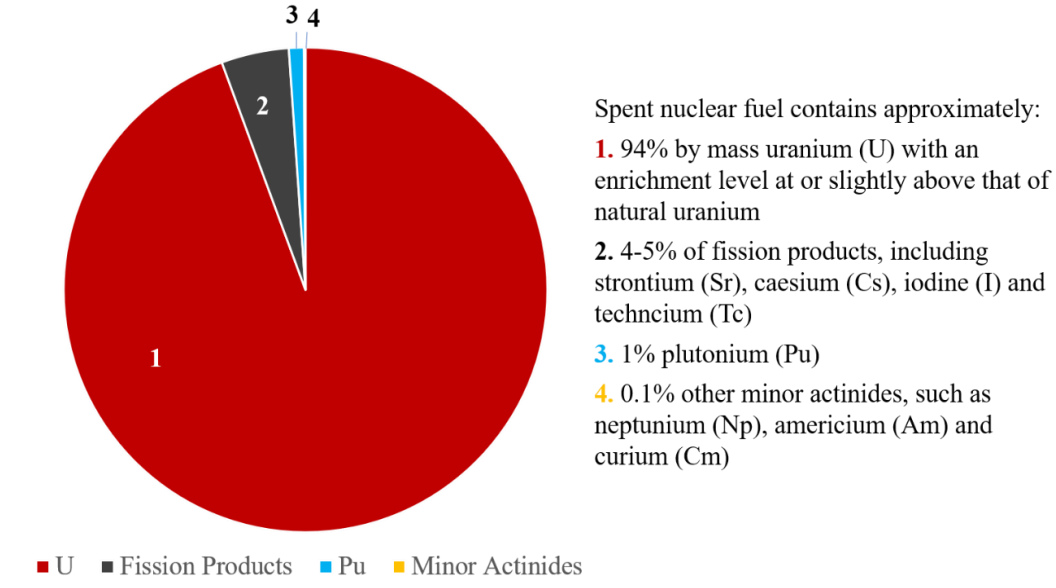

Figure 1.1. Approximate composition of spent nuclear fuel.

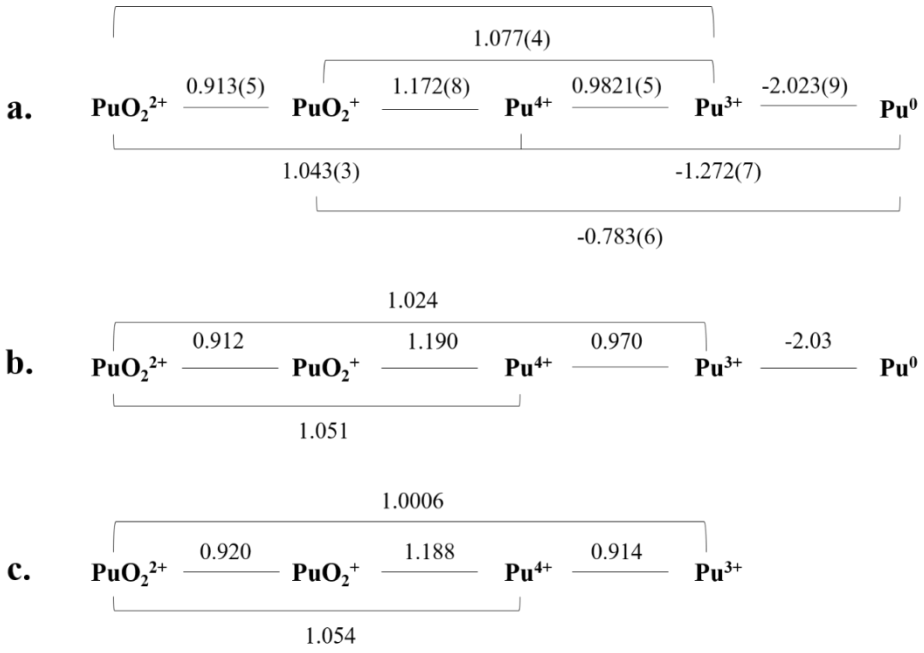

Figure 1.2. Formal redox potentials for selected Pu couples at 25 °C in V vs SHE(a) in 1 M $HClO_4$, (b) in 1 M HCl, and (c) 1 M HNO_3.

CHAPTER 2

SYNTHESIS AND CHARACTERIZATION OF SCHIFF BASE TETRAVALENT COORDINATION COMPLEXES

Adapted with permission from Bonnie E. Klamm, Cory J. Windorff, Cristian Celis-Barros, Matthew L. Marsh, Daivid S. Meeker, and Thomas E. Albrecht-Schmitt. *Inorg. Chem.* 2018, 57, 24, 15389-15398, and Bonnie E. Klamm, Cory J. Windorff, Matthew L. Marsh, David S. Meeker, and Thomas E. Albrecht-Schmitt. *Chem. Commun*. 2018, 54,62, 8634-8636.

2.1 Introduction

The knowledge and understanding of fundamental actinide bonding trends and coordination modes is significantly limited compared to other elemental series in the periodic table. The lack of actinide studies limits our grasp on the bonding and the electronic structure trends across the 5*f* series, and how the changes in ligand binding may impact speciation and separation selectivity to different metal ions. There are few comparisons of isostructural molecular complexes in the tetravalent oxidation state. The few studies presented to date are largely limited to comparisons of U^{4+} to Th^{4+} and comparisons to Pu^{4+} are rare.[8–11] Our interest in the chemistry of the early tetravalent actinides is based on the periodic trends through the series. Moving from Th to Pu in: ionic radius, electron configuration, ion acidity, and trends in coordination chemistry and reactivity have been established.[12–18] These elements and their trends provide a way to understand the structural, electronic, and chemical properties of the early actinide elements. In this study, the focus has been placed on the effect of neutral nitrogen donors in the backbone of the ligand as a soft donor. Understanding these bonding differences is important for how they may be utilized for future designs of ligand systems for actinide separations. Of greater interest are the relationships between the actinides, and to the remainder of the periodic table, importantly their tetravalent homologues Zr, Hf, and Ce.

Schiff base ligands have been heavily utilized for their ability to stabilize metals in various oxidation states and control the behavior of metals during catalysis.[19] In addition, their steric and electronic properties are highly modular.[20] Salen ligands and their derivatives have been crystallized and characterized with transition metals,[19,21–23] lanthanides,[19,24–28] early actinides (Th and U),[28–33] and very few studies with transuranium elements.[34–37] By utilizing a

phenyl-based rigid backbone N,N′-bis[(4,4′-diethylamino)salicylidene]-1,2-phenylenediamine (**H_2L**), isolable, crystalline homoleptic compounds of **ML_2** (M = Zr, Hf, Ce, Th, U, Pu).

In this study, we sought to compare the differences between different *f*-elements and group IV transition-metal complexes by combining synthetic, multinuclear NMR, UV/vis/NIR spectroscopy, and electrochemical and computational work to offer an electronic structure basis to explain bonding differences.

2.2 Experimental

2.2.1 General considerations and instrumentation

Caution! ^{232}Th and ^{238}U isotopes are long-lived, low specific activity α-particle emitting radionuclides and their use presents hazards to human health. ^{239}Pu [$t_{1/2}$ = 24,110(30) y] is a serious health threat, due to its radioactive decay, as well as that of its daughters. Hence, all studies with actinides were conducted with appropriate controls for the safe handling and manipulation of radioactive materials, i.e. in a radiation laboratory equipped with a HEPA filtered hood. All free-flowing solids that contained plutonium were handled in negative-pressure gloveboxes or were covered in oil.

Where noted, manipulations were performed with the rigorous exclusion of air and water using glovebox techniques under an argon atmosphere. All air sensitive manipulations were conducted in a negative pressure glovebox dedicated to actinide (^{232}Th–^{249}Cf) chemistry. All manipulations of actinides not inside a glovebox were conducted in a well-ventilated fume hood. THF used for air-sensitive manipulations was purchased anhydrous and stored successively over activated 4 Å molecular sieves two times, and then stored over the sodium metal. Pentane used for air-sensitive manipulations was purchased anhydrous and stored over activated 4 Å molecular sieves. Transition-metal chemistry took place in a routine positive pressure glovebox. THF (Sigma) was sparged with argon, passed through towers containing Q-5 and molecular sieves, and stored over activated 4 Å molecular sieves. $ZrCl_4$ (Sigma) and $HfCl_4$ (Sigma) were used as received and stored in the glovebox. $KN(SiMe_3)_2$ (Sigma) was crystallized from toluene at −35 °C before use and stored in the glovebox. Other solvents used for manipulations in air including MeOH (Sigma), dichloromethane (DCM; Sigma), and pentane (Sigma) were used as received. The following compounds were purchased of reagent grade from commercial sources and were

used as received: $CeCl_3$•$7H_2O$ (Sigma-Aldrich), $Th(NO_3)_4 \cdot xH_2O$ (Fluka), NEt_3 (Sigma), toluene (VWR), and $CDCl_3$ (Sigma). UCl_4[38] and N,N′-bis[(4,4′-diethylamino)salicylidene]-1,2-phenylenediamine (**H_2L**)[39] were prepared according to the literature. ^{239}Pu was obtained from Los Alamos National Laboratory as PuO_2 and converted to $PuCl_3$•xH_2O by repeated dissolution in concentrated HCl.

Solid-state UV/vis/NIR spectroscopic data were obtained from single crystals using a CRAIC Technologies UV/vis/NIR microspectrophotometer. Crystals were placed on glass slides in immersion oil and data were collected from 300 to 1100 nm. Solution phase UV/vis/NIR data were obtained from 0.08 mM solutions using an Agilent Technologies Cary Series UV/vis/NIR spectrophotometer 6000i. Samples were dissolved in toluene and placed into 1 mm quartz cells. Data were collected from 300 to 1100 nm. ^{1}H and ^{13}C{1H} NMR spectra were recorded on a Bruker 600 MHz spectrometer operating at 600.1 and 150.9 MHz, respectively, at 298 K unless otherwise stated. ^{1}H and ^{13}C{1H} NMR spectra were referenced internally to solvent resonances. NMR samples were removed from the glovebox, dissolved in $CDCl_3$, and placed in an NMR tube with no attempt to exclude air or water. Electrochemical data was recorded on a CH Instruments model 600E Series potentiostat. A three-electrode configuration comprising a platinum disk working electrode (2 mm diameter), a platinum wire counter electrode, and a silver wire pseudoreference electrode were used in all experiments. Cyclic voltammetric scans were conducted in DCM with 0.1 M [N^nBu_4][PF_6] electrolyte for characterization of the ligand species, and **ML_2** (M = Zr, Hf, Ce, Th, U, Pu). C/H/N elemental analysis were carried out by Midwest Microlab, Indianapolis, IN, for Zr, Hf, and Ce samples, and Berkeley Microlab for Th and U samples. Single crystals selected for data collection were mounted on a MITOGEN mount cryoloop and optically aligned on a Bruker D8 Quest X-ray diffractometer. Crystallographic data were collected under a low-temperature nitrogen gas flow using a Mo Kα (λ = 0.71069 Å) X-ray microsource and a CMOS detector. The unit cell determination and subsequent data collection were performed using the APEX III software.[40] Raw data frames were processed using SAINT[41] and SADABS.[42] Subsequent calculations were carried out using the OLEX 2 program.[43] Structures were solved by olex2.solve and refined by full-matrix least-squares on F2 techniques. Crystallographic information is included in **Tables B.1**.

The electronic structure and bonding interactions were analyzed using Density Functional Theory (DFT) and Time-Dependent DFT (TD-DFT). All calculations were carried out using the

ORCA 4.0.1.2 package.[44] No geometry optimizations were carried out since the geometries are well predicted by DFT using GGA and hybrid functions, and the crystallographic molecular structures were used as the starting geometries used to calculate the wavefunctions. Absorption spectra and excited states were calculated by TD-DFT using the GGA functional BP86. Other well-known functionals such as CAM-B3LYP and PBE0 were tested, however yielded poor experimental resemblance. The SARC-TZVP basis set was used for all metal centers except Hf^{4+} due to structural disorder. The def2-TZVP basis set was used for **HfL$_2$**. Bonding parameters based on the Bader's theory of Quantum Theory of Atoms in Molecules (QTAIM)[45] were calculated and analyzed using the MultiWFN software,[46] and based on wave functions calculated at PBE0//SARC-TZVP/def2-TZVP level of theory. The electron densities, ρ(r); localization λ(A) and delocalization δ(A-B) indexes; Lagrangian kinetic energies, G(r); potential energy densities, V(r); and total energy densities, H(r); are reported.

2.2.2 Synthesis

H$_2$L. **H$_2$L** was synthesized in a manner similar to procedures utilized with other Schiff base salen ligands molecules previously reported.[28,47,48] To a stirred solution of 1,2-phenylenediamine, *o*-$C_6H_4(NH_2)_2$ (0.500 g, 4.62 mmol) in methanol (10 mL), 4-diethylamino-salicylaldehyde HC(O)C_6H_3,2-OH,4-NEt_2 (1.79 g, 9.25 mmol) in methanol (15 mL), was added and refluxed for 8 h. The mixture was cooled to room temperature and concentrated under vacuum. The crude product was washed with methanol and dried under vacuum, giving **H$_2$L** as a fine yellow powder (1.17 g, 55%). ^{1}H NMR ($CDCl_3$): δ 13.69 (s, 2H, O-*H*), 8.45 (s, 2H, *H*-C(Ar)=N), 7.22 (s, 4H, Ar-*H*), 7.15 (s, 2H, Ar-*H*), 6.26 (s, 2H, Ar-*H*), 6.24 (s, 2H, Ar-*H*), 3.40 (s, 8H, NCH_2CH$_3$), 1.21 (s, 12H, CH_2CH_3); ^{13}C{^{1}H} NMR ($CDCl_3$): δ 164.61 (Ar-*C*), 160.90 (Ar-*C*), 151.91 (Ar-*C*), 142.58 (Ar-*C*), 133.81 (Ar-*C*), 126.17 (Ar-*C*), 119.32 (Ar-*C*), 109.61 (Ar-*C*), 103. 71 (Ar-*C*), 98.23 (Ar-*C*), 44.65 (*C*H_2), 12.88 (*C*H_3).

ZrL$_2$. Inside the glovebox, $KN(SiMe_3)_2$ (34 mg, 0.17 mmol) was combined with **H$_2$L** (39 mg, 0.086 mmol) and added to a solution of $ZrCl_4$ (10 mg, 0.043 mmol), in THF (1 mL) causing an immediate color change to dark orange, identified as **ZrL$_2$** (9.1 mg, 52% crystalline yield). Orange X-ray quality crystals were grown from THF layered with pentane. ^{1}H NMR ($CDCl_3$): δ 8.55 (s, 2H, *H*–C(Ar)═N), 8.05 (s, 2H, Ar-*H*), 7.82 (d, $^3J_{HH}$ = 7.82 Hz, 2H, Ar-*H*), 7.14 (s, 2H, Ar-*H*), 7.08 (d, $^3J_{HH}$ = 7.07 Hz, 2H, Ar-*H*), 6.95 (d, $^3J_{HH}$ = 6.93 Hz, 2H, Ar-*H*), 6.79 (m, 4H, Ar-

H), 6.04 (d, $^{3}J_{HH}$ = 6.03 Hz, 2H, Ar-*H*), 5.96 (d, $^{3}J_{HH}$ = 5.96 Hz, 2H, Ar-*H*), 5.56 (s, 2H, Ar-*H*), 5.11 (s, 2H, Ar-*H*), 3.27 (m, 4H, C*H*$_2$), 3.17 (d, $^{2}J_{HH}$ = 3.18 Hz, 8H, C*H*$_2$), 3.11 (m, 4H, C*H*$_2$), 1.09 (t, $^{2}J_{HH}$ = 1.08 Hz, 24H, C*H*$_3$); ^{13}C{^{1}H} NMR ($CDCl_3$): δ 169.00 (Ar-*C*), 167.11 (Ar-*C*), 166.72 (Ar-*C*), 158.44 (Ar-*C*), 157.41 (Ar-*C*), 153.00 (Ar-*C*), 147.92 (Ar-*C*), 146.93 (Ar-*C*), 134.84 (Ar-*C*), 134.32 (Ar-*C*), 125.45 (Ar-*C*), 124.99 (Ar-*C*), 124.13 (Ar-*C*), 117.96 (Ar-*C*), 116.87 (Ar-*C*), 116.28 (Ar-*C*), 114.57 (Ar-*C*), 114.32 (Ar-*C*), 113.36 (Ar-*C*), 103.09 (Ar-*C*), 102.35 (Ar-*C*), 100.95 (Ar-*C*), 43.94 (*C*H$_2$), 13.31 (*C*H$_3$). Anal. Calcd for $C_{56}H_{64}N_8O_4Zr \cdot 0.5OC_4H_8$: C, 66.89; H, 6.59; N, 10.77. Found: C, 62.63; H, 6.29; N, 10.66. Despite repeated attempts, low carbon content was observed.

HfL$_2$. Inside the glovebox, $KN(SiMe_3)_2$ (25 mg, 0.13 mmol) was combined with **H$_2$L** (29 mg, 0.062 mmol) and added to a solution of $HfCl_4$ (10 mg, 0.031 mmol) in THF (1 mL) causing an immediate color change to orange, identified as **HfL$_2$**. (15 mg, 22% crystalline yield) Yellow X-ray quality crystals were grown from THF layered with pentane. ^{1}H NMR ($CDCl_3$): δ 8.55 (s, 2H, *H*–C(Ar)═N), 8.07 (s, 2H, Ar-*H*), 7.81 (d, $^{3}J_{HH}$ = 7.81 Hz, 2H, Ar-*H*), 7.15 (s, 2H, Ar-*H*), 7.05 (d, $^{3}J_{HH}$ = 7.05 Hz, 2H, Ar-*H*), 6.93 (d, $^{3}J_{HH}$ = 6.93 Hz, 2H, Ar-*H*), 6.78 (t, $^{3}J_{HH}$ = 6.78 Hz, 4H, Ar-*H*), 6.02 (d, $^{3}J_{HH}$ = 6.02 Hz, 2H, Ar-*H*), 5.94 (d, $^{3}J_{HH}$ = 5.94 Hz, 2H, Ar-*H*), 5.57 (s, 2H, Ar-*H*), 5.12 (s, 2H, Ar–*H*), 3.26 (m, 4H, C*H*$_2$), 3.16 (d, $^{2}J_{HH}$ = 3.18 Hz, 8H, C*H*$_2$), 3.12 (m, 4H, C*H*$_2$), 1.09 (t, $^{2}J_{HH}$ = 1.09 Hz, 24H, C*H*$_3$); ^{13}C{^{1}H} NMR ($CDCl_3$): δ 169.19 (Ar-*C*), 167.53 (Ar-*C*), 166.89 (Ar-*C*), 158.84 (Ar-*C*), 157.75 (Ar-*C*), 153.10 (Ar-*C*), 147.93(Ar-*C*), 146.79 (Ar-*C*), 134.81 (Ar-*C*), 134.23 (Ar-*C*), 125.48 (Ar-*C*), 125.08 (Ar-*C*), 124.19 (Ar-*C*), 118.12 (Ar-*C*), 116.88 (Ar-*C*), 116.37 (Ar-*C*), 114.75 (Ar-*C*), 113.61 (Ar-*C*), 103.12 (Ar-*C*), 102.61 (Ar-*C*), 102.14 (Ar-*C*), 101.37 (Ar-*C*), 44.44 (*C*H$_2$), 13.140 (*C*H$_3$). We were unable to obtain satisfactory elemental analysis, ^{1}H and ^{13}C{^{1}H} NMR spectra of the isolated product.

CeL$_2$. In the open atmosphere, **H$_2$L** (25 mg, 0.050 mmol) and NEt_3 (200 µL, 1.43 mmol) in DCM (1 mL) were added to a solution of $CeCl_3 \bullet 7H_2O$ (10 mg, 0.025 mmol) in methanol (1 mL). The color of the solution immediately changed from orange to black. Pentane (5 mL) was carefully layered on top of the solution and after 1 d at room temperature, X-ray quality crystals of **CeL$_2$** were isolated as black block-like crystals, washed with pentane and dried in air (14 mg, 60%). ^{1}H NMR ($CDCl_3$): δ 8.34 (s, 4H, *H*-C(Ar)=N), 7.04 (s, 12H, Ar-*H*), 5.99 (s, 4H, Ar-*H*), 5.40 (s, 4H, Ar-*H*), 3.26 (s, 16H, C*H*$_2$CH$_3$), 2.93 (s, 16H, C*H*$_2$CH$_3$), 1.24 (s, 24H, CH$_2$C*H*$_3$), 1.09 (s, 24*H*, C*H*$_2$), ; ^{13}C{^{1}H} NMR ($CDCl_3$): δ 169.48 (Ar-*C*), 158.19 (Ar-*C*), 152.86 (Ar-*C*), 146.33

(Ar-*C*), 135.21 (Ar-*C*), 125.2 (Ar-*C*), 116.96 (Ar-*C*), 114.70 (Ar-*C*), 103.37 (Ar-*C*), 99.11 (Ar-*C*), 45.89 (*C*H_2), 44.21 (*C*H_2), 13.05 (*C*H_3), 8.65 (*C*H_3). Anal. Cal'd For $C_{56}H_{64}CeN_8O_4 \cdot 2CH_2Cl_2$; C, 56.95; H, 5.60; N, 9.16. Found, C, 57.22; H, 5.78; N, 9.25.

ThL$_2$. In the open atmosphere, **H$_2$L** (17 mg, 0.036 mmol) and NEt_3 (200 μL, 1.43 mmol) in DCM (1 mL) were added to a solution of $Th(NO_3)_4 \cdot xH_2O$ (10 mg, 0.018 mmol, using the assumption x = 4) in methanol (1 mL). The solution quickly changed from colorless to yellow. Pentane (5 mL) was carefully layered on top of the solution and after 1 d at room temperature, X-ray quality crystals were isolated as yellow columnar crystals, washed with pentane, and dried in air (17 mg, 71% crystalline yield). ^{1}H NMR ($CDCl_3$): δ 8.06 (s, 4H, *H*–C(Ar)═N), 7.04 (m, 4H, Ar-*H*), 6.98 (m, 4H, Ar-*H*), 6.95 (d, $^3J_{HH}$ = 6.95 Hz, 4H, Ar-*H*), 6.02 (dd, $^3J_{HH}$ = 6.02 Hz, 4H, Ar-*H*), 5.73 (s, 4H, Ar-*H*), 3.27 (m, $^2J_{HH}$ = 3.27 Hz, 16H, C*H*$_2$), 1.11 (t, $^2J_{HH}$ = 1.11 Hz, 24H, C*H*$_3$); ^{13}C{^{1}H} NMR ($CDCl_3$): *δ* 167.94 (Ar-*C*), 160.32 (Ar-*C*), 153.53 (Ar-*C*), 145.56 (Ar-*C*), 136.00 (Ar-*C*), 125.33 (Ar-*C*), 117.84 (Ar-*C*), 114.54 (Ar-*C*), 102.51 (Ar-*C*), 101.60 (Ar-*C*), 44.38 (*C*H_2), 13.13 (*C*H_3). Anal. Calcd for $C_{56}H_{64}N_8O_4Th \cdot 2CH_2Cl_2$: C, 52.92; H, 5.21; N, 8.52. Found: C, 52.63; H, 5.20; N, 8.52.

UL$_2$. **Method A**- Inside the glovebox, a vial was charged with UCl_4 (10 mg, 0.026 mmol), capped and removed from the glovebox. In a separate vial, **H$_2$L** (24 mg, 0.053 mmol) and NEt_3 (200 μL, 1.43 mmol) were combined in DCM (1 mL). In a well-ventilated fume hood with no attempt to exclude air or water, the ligand solution was quickly added to UCl_4 in MeOH (1 mL) causing an immediate change from light green to dark red, and then black. Pentane (5 mL) was carefully layered on top of the solution and after 1 d at room temperature, X-ray quality crystals of **UL$_2$** were isolated as red columnar crystals. The crystals were washed with pentane and dried in air (24.0 mg, 69% crystalline yield). Because of the paramagnetism of the U^{4+} ion, only unambiguously identifiable resonances are reported; ^{1}H NMR ($CDCl_3$): δ 10.15 (br, s, $\nu_{1/2}$ = 380 Hz, 2H, Ar-*H*), 7.74 (br, s, $\nu_{1/2}$ = 260 Hz, 4H, Ar-*H*), 3.46 (br, s, $\nu_{1/2}$ = 170 Hz, 8H, Ar-*H*), 2.92 (br, s, $\nu_{1/2}$ = 153 Hz, 8H, Ar-*H*), 1.76 (s, 4H, Ar-*H*), 1.35 (br, m, $\nu_{1/2}$ = 95 Hz, 24H, C*H*$_3$), −5.33 (br, s, $\nu_{1/2}$ = 80 Hz, 4H, Ar-*H*); Anal. Calcd for $C_{56}H_{64}N_8O_4U \cdot 2CH_2Cl_2$: C, 52.69; H, 5.19; N, 8.48. Found: C, 48.32; H, 5.36; N, 8.45. Despite repeated attempts, low carbon content was observed.

Method B- Inside the glovebox, $KN(SiMe_3)_2$ (21 mg, 0.11 mmol) was added to **H$_2$L** (24 mg, 0.053 mmol) in THF (2 mL) quickly causing a change from yellow to red. After 5 min, the

ligand solution was added to a pale green solution of UCl_4 (10 mg, 0.026 mmol) in THF (1 mL). The solution quickly changed to dark red with the generation of a gray precipitate (presumably KCl). The mixture was filtered on a glass fiber circle inside a pipette and layered with pentane. After 1 day at ambient glovebox temperature (ca. 23 °C), dark red solids identified as **UL_2** (21.5 mg, 60% crystalline yield), as confirmed by ^{1}H NMR spectroscopy, were collected, washed with pentane, and dried under reduced pressure.

PuL_2. In the open atmosphere, **H_2L** (25 mg, 0.050 mmol) and NEt_3 (200 µL, 1.43 mmol) in DCM (1 mL) were added to a solution of $PuCl_3$•xH_2O (10 mg, 0.029 mmol, based on elemental Pu content) in methanol (1 mL). The color of the solution immediately changed from light violet to black. Pentane (5 mL) was carefully layered on top of the solution and after 1 d at room temperature, X-ray quality crystals of **PuL_2** were isolated as black block-like crystals, washed with pentane and dried in air.

2.3 Results and Discussion

2.3.1 Direct comparison between Ce^{4+} and Pu^{4+} coordination complexes

The protio ligand, **H_2L** was synthesized in a modified manner to that of the literature. Condensation of 1,2-phenylenediamine, *o*-$C_6H_4(NH_2)_2$, and two equivalents of 4-diethylaminosalicylaldehyde, HC(O)C_6H_3,2-OH,4-NEt_2 in refluxing methanol to form **H_2L** in high yield[39] and characterized by ^{1}H and ^{13}C. Then, in air, MCl_3•xH_2O (M = Pu, Ce) was reacted with two equivalents of **H_2L** in methanol and in the presence of excess NEt_3 and layered with pentane. This method produced X-ray quality crystals overnight, **Figure 2.1**. Single crystal X-ray diffraction studies reveal that **CeL_2** and **PuL_2** are isomorphous, and crystallize in the monoclinic space group, *C*2/*c*. The metal is 8-coordinate forming a distorted square antiprism. The two ligands are skewed from one another and stack on top of each other (i.e. a sandwich-type structure), rather than a perpendicular geometry as exhibited by other **Ce(Salen)$_2$** complexes.[19,24,27,39] The sandwich structure is due to the rigidity of the phenelene moiety in the backbone of the ligand.[19] The average M–O and M–N bond distances for Pu and Ce, respectively, are 2.225(1), 2.24(2) Å, and 2.55(2), 2.59(1) Å, with an O(1)–M–O(2) and N(1)–M–N(2) angles for Pu and Ce, respectively, of 84.9(1)˚, 85.82(6)° and 61.6(1)°, 61.09(6)°.

The solid-state UV/vis/NIR spectra for both compounds reveal a broadband feature that begins in the high-energy region of the visible spectrum and extends into the UV. The λ_{max} for **PuL$_2$** occurs at 529 nm, and at 411 nm for **CeL$_2$**. This feature is consistent with a Laporte-allowed charge-transfer band and the intense dark-red/black coloring. In **PuL$_2$**, the band is followed by much weaker peaks that have been assigned to 5*f*→5*f* transitions. Although weak, these absorption peaks are indicative of Pu^{4+}.

To further investigate the redox potentials of **PuL$_2$** and **CeL$_2$**, both complexes and of the ligand were measured via cyclic voltammetry in non-aqueous solution as shown in **Figure 2.2**. While the ligand is redox active, **Figure 2.3**, its non-innocent behavior is altered by the onset of complexation by both Ce^{4+} and Pu^{4+} (0.45 V vs. Fc/Fc^+) for causing dearomatization.[39,49] This oxidation was best observed at a slow (10 mV/sec) scan rate, but becomes significantly elongated at faster rates, while for the reduction (–1.29 V vs. Fc/Fc^+), rearomatization is only observed at faster rates (>100 mV/sec). A full series of scan dependence and baseline corrections reveals that I_{pc}/I_{pa} ratios increase substantially beyond 50 mV/sec, and this suggests that reoxidation is quick. Both hydroxylated positions on the ligand can be oxidized, but are unresolved in ligand exclusive experiments. When Ce^{4+} is bound, however, both sites become nonequivalent. Site 1 becomes easier to oxidize; while the second site becomes much more difficult to oxidize (Site 1 = 0.27 V and Site 2 = 0.80 V vs. Fc/Fc^+). Ce^{4+} is stabilized by complexation, yet shows irreversible behavior (E_{anode} = 0.52 V and $E_{cathode}$ = −1.75 V vs. Fc/Fc^+). In contrast, Pu^{4+} appears to be stabilized by the ligand to a greater extent ($E_{1/2}$ = −1.75 V vs. the Fc/Fc^+ couple) and displays quasi-reversible electrochemical behavior with a peak-to-peak separation value of 266 mV. Additionally, the greater itinerancy of the 6*d* and 5*f* shells likely serve to stabilize the redox transitions of the ligand, as all sites become more reversible overall (Site 1 = 0.23 V, Site 2 = 0.36 V, and $E_{cathode}$ = 0.028 V vs. Fc/Fc^+).

2.3.2 Further analysis of the tetravalent series

The analogous tetravalent *f*-element complexes were prepared in a manner similar to **CeL$_2$** and **PuL$_2$**. Briefly, in air, addition of 2 equivalents of **H$_2$L** in DCM with an excess of triethylamine to a solution of UCl_4 in MeOH results in the formation of an intense dark red/black solution, characteristic of complexation. Layering with pentane yielded X-ray quality crystals overnight. **ThL$_2$** was prepared in the same manner starting from the tetravalent starting material,

$Th(NO_3)_4 \cdot xH_2O$ (assuming $x = 4$) resulting in an intense yellow solution. Layering with pentane yielded X-ray quality crystals overnight. Single-crystal X-ray diffraction studies reveal the structure complexes to be isomorphous with the Ce and Pu analogs and crystallize in the *C*2/*c* space group. As was observed with the Pu and Ce analogs, the complex forms a distorted square antiprismatic geometry with the ligands forming a facial "sandwich" type structure. The ligands bend at a slight 17° from the equatorial plane, typical of these phenyl-substituted backbone Schiff base complexes.[23,39]

The average Th–O bond length in **ThL_2** is 2.306(1) Å, which is comparable to other 8-coordinate Th Schiff base complexes, **$Th(L^1)_2$**[50] and **$Th(L^4)_2$**,[28] with average Th–O distances of 2.3(4) and 2.29(3), Å, respectively, and is significantly longer than the mono/bis Th(salophen) complexes: **$Th(L^5)_2$**[31] and **$Th(L^3)Cl_2(py)_2$**[32] with average Th–O distances of 2.270(1) and 2.21(1), Å, respectively, **Table B.2**, whereas the average Th–N bond length of 2.639(1) Å in ThL_2 compares well with the 2.61(1)–2.658(2) Å average Th–N lengths. The O(1)–Th–O(2) and N(1)–Th–N(2) angles are 87.40(4) and 60.43(4)°, respectively. Although the O(1)–Th–O(2) angle agrees with the range 83.9(3)–93.69°, the monosalen complex **$Th(L^3)Cl_2(Py)_2$**[32] is significantly different, 154.1(6)°, and the N(1)–Th–N(2) angle compares well with the range 60.01–64.3(6)° reported for other Th(salen) complexes.

The average U–O and U–N bond lengths of **UL_2** are 2.250(1) and 2.588(2) Å, respectively, and in comparison to other U^{4+} Schiff base complexes, the U–O bond lengths are significantly longer than the unsubstituted bis salophen complex **$U(L^1)_2$**[30] and the monosalen complex **$U(L^3)Cl_2(Py)_2$**;[32] 2.220(1) and 2.190(4) Å, respectively. The U–N bond lengths are similar to the 2.59(2)–2.63(1) Å range reported for other **UL_n^x** (n = 1, 2) complexes, **Table B.3**. The O(1)–U–O(2) and N(1)–U–N(2) angles for **UL_2** are 86.23(5) and 61.09(5)°, respectively. The N(1)–U–N(2) compare well with the 61.11–65.7(2)° range reported for the mono Schiff base complexes **$U(L^2)_2$** and **$U(L^3)Cl_2(Py)_2$** and the unsubstituted bis salophen complex **$U(L^1)_2$**; 62.65(15), 65.7(2), 61.11°, respectively, whereas the O(1)–U–O(2) angle is only comparable with **$U(L^1)_2$** complex and significantly smaller than the angles reported for **$U(L^2)_2$** and **$U(L^3)Cl_2(Py)_2$**; 154.56(15), 152.2(2)°, respectively.

Because of the sensitivity of $HfCl_4$ and $ZrCl_4$ to moisture, **HfL_2** and **ZrL_2** were synthesized inside a glovebox. Additionally, the uranium analog was synthesized in a glovebox for comparison with its synthesis in air to confirm that no oxidation was taking place. Briefly, in

situ deprotonation of **H₂L** with $KN(SiMe_3)_2$ in THF quickly caused a color change from yellow to red-orange, addition of this solution to MCl_4 in THF caused a color change to orange for Zr, yellow for Hf, and dark red for U. Filtration followed by layering with pentane at ambient glovebox temperature (ca. 23 °C) gave X-ray quality crystals after one day for **ZrL₂** and **HfL₂**, **UL₂** was confirmed by ^{1}H NMR analysis.

ZrL₂ and **HfL₂** are isomorphous with one another and crystallize with two independent units in the $P2_1/c$ space group, **Figure 2.4**. The average Zr–O and Zr–N bond lengths of **ZrL₂** are 2.113(2) and 2.375(2) Å, respectively, and in comparison to other Zr^{4+} Schiff base complexes. The Zr–O bond lengths are slightly longer than the bis salophen complexes **Zr(L⁶)₂**[23] and **Zr(L⁷)₂**;[51] 2.109(5) and 2.085(5) Å respectively, **Table B.4**. The Zr–N bond lengths are slightly shorter than the 2.40(2)–2.42(1) Å range reported for other **Zr(L^x)₂** complexes. The average O–Zr–O and N–Zr–N angles for **ZrL₂** are 74.73(7) and 66.21(8)°, respectively. The N–Zr–N angles compare well with both of the salophen complexes **Zr(L⁶)₂** and **Zr(L⁷)₂**; 66.21 and 67.2(4)°, respectively, whereas O–Zr–O is only comparable with the **Zr(L⁶)₂** complex and significantly smaller than the angle reported for **Zr(L⁷)₂**; 74.25(7) and 96.5(2)°, respectively.

The Hf–O and H–N average bond lengths in **HfL₂** are 2.108(2) and 2.358(3) Å, respectively. For Hf, there are only two other 7-coordinate crystallographically characterized complexes with salen-like Schiff base ligands, both complexes feature a saturated cyclohexyl backbone rather than a rigid phenyl ring, namely, **Hf₂O₂(L⁸)₂(OBu^t)₂** [**L⁸** = *N*,*N*′-bis(3,5-di-*t*-butylsalicylidene)-1,2-cyclohexanediamine][52] and **Hf(L⁹)(OPh)₂(H₂O)** {**L⁹** = [1,1′-binaphthalen]-2-ol, 3,3″-[(1*R*,2*R*)-1,2-cyclohexanediylbis[(*E*)-nitrilomethylidyne]]bis-(1*R*,1″*R*), R = napthalene}[53] which have relevant Hf–O and Hf–N average bond distances of 2.099(4), 2.35(3) and 2.06(1), 2.35(1) Å, respectively. Although Hf–O bond lengths are similar to the Zr analog, the Hf–N bonds are significantly smaller. The average O–Hf–O and N–Hf–N bond angles are 74.2(6) and 66.5(5)°, respectively. The two ligands coordinating to Hf and Zr are rotated 143.2° and 143.8° from each other, respectively, and are significantly bent from the central plane by a difference of 20°. The ligands on Hf and Zr exhibit a bend of ∼10° on one side and ∼30° on the other. These parameters are significantly different from Ce, Th, U, and Pu structures.

The homoleptic nature of the reported **ML$_2$** (M = Zr, Hf, Ce, Th, U, Pu) complexes allow for a rare direct comparison of solid-state metrical parameters between Ce, Th, U, and Pu. The average M–O and M–N bond distances, and the O(1)–M–O(2) and N(1)–M–N(2) angles are listed in **Table B.4**. The O–M–O angles are periodic with the largest for **ThL$_2$**, 87.40(4)° and smallest for **PuL$_2$**, 84.9(1)°, whereas the N(1)–M–N(2) bond angle follows the opposite trend with **PuL$_2$** having the greatest angle 61.6(2)° and **ThL$_2$** with the smallest angle 60.43(4)°. The rotation of the two overlapping salophen ligands for complexes **AnL$_2$** [calculated from the average value of torsion angles between O(1)···O(2)^O(1′)···O(2′) and N(1)···N(2)^N(1′)···N(2′)] is largest for **ThL$_2$** 50.4° and smallest for **PuL$_2$** 49.5°.

A crystallographic comparison across several **ML$_2$** complexes shows that the transition metal compounds **ZrL$_2$** and **HfL$_2$** have similar bond and angle metrics and are significantly shorter than their *f*-element analogs. However, amongst the *f*-element complexes, only **ThL$_2$** features bond distances that are significantly longer than another *f*-element complexes, likely due to the larger ionic radius of the Th^{4+} ion (1.05 Å, 8-coordinate). All of the O–M–O and N–M–N for the *f*-elements are distinct from one another and from the transition-metal complexes.

The complexes reported **ZrL$_2$**, **HfL$_2$**, and **ThL$_2$** are all diamagnetic and give typical ^{1}H and $^{13}C\{^1H\}$ NMR shifts in $CDCl_3$, with the notable exceptions that because of the small ionic radii of Zr and Hf, the aromatic protons become unique between the two ligands rather than symmetric as is observed in the **ThL$_2$** and **CeL$_2$** complexes. Additionally in all diamagnetic complexes, some stereochemical uniqueness is observed in the methylene unit of the $-N(CH_2CH_3)_2$ substituent giving rise to multiple resonances such as **ZrL$_2$**, where there are three resonances in 4:8:4 integration, or in **ThL$_2$**, where a multiplet of 10 is observed with the expected integration of 16. The paramagnetic U^{4+} ion in **UL$_2$** gave a typical paramagnetic spectrum with several broad signals in the range of +11 to −6 ppm, with only unambiguously identifiable peaks being assigned.

Solution UV/vis/NIR spectroscopy of **ML$_2$** (M = Zr, Hf, Ce, Th, U) in toluene reveals an intense broad band with λ_{max} in the range of 367–384 nm, with ε values in the range of 190 000–240 000 (L mol^{-1} cm^{-1}). Despite attempts to measure more concentrated solutions, no $5f \rightarrow 5f$ peaks were observed for **UL$_2$**. Solid-state UV/vis/NIR spectra of **ML$_2$** (M = Zr, Hf, Ce, Th, U, Pu), **Figure 2.5**, reveal an intense broad band with λ_{max} at 491, 483, 411, 462, 546, and 529 nm,

respectively. These intense, broad features are characteristic of **ML$_2$** complexes, accounting for the intense coloring of each crystal. The weak absorptions between 700 and 1100 nm for An^{4+} are assigned to Laporte-forbidden $5f \rightarrow 5f$ transitions, characteristic of the tetravalent state.

To further investigate the tetravalent series, the redox potentials of **ML$_2$** were measured via cyclic voltammetry in nonaqueous solution to compare with **CeL$_2$** and **PuL$_2$**, **Figure 2.6**. The reductive capacity of the plain salophen ligand has been explored in the **UL$^1_2$**[30] complex, which showed that chemical addition of $2e^-$ caused ligand reduction and coupling displaying the reduction potential of the unsubstituted salophen ligand ($E_{1/2} = -1.14$ V vs Fc^+/Fc)[30,33] to be less than the generic $U^{4+/3+}$ potential of −0.12 V versus Fc^+/Fc.[54] However, in this study, it has been observed that the first major anodic peak gives the best comparisons between the different **ML$_2$** complexes. The oxidation peaks, which occur between 0.08 and 0.486 V potentials, can be plotted against the 8-coordinate ionic radii. As the ionic radius increases, the oxidation potential decreases, that is, becomes less positive and gives a good linear fit across all **ML$_2$** complexes (M = Zr, Hf, Ce, Th, U, Pu). The calculated potential stabilization because of reduction in ionic radii from this plot is derived to be 140 mV/Å.

2.3.3 Theoretical analysis

Time-Dependent DFT. The excited states of **ML$_2$** (M = Zr, Hf, Ce, Th, U, Pu) complexes were calculated by time dependent density functional theory (TD-DFT) to understand similarities and differences between their electronic structures. Although DFT fails to describe static correlation properly because the theory is based on the total density rather than individual electrons,[55] it remains the best option for closed shell systems due to its computational costs and accuracy. Open-shell systems are more difficult to treat due to their sensitivity to electron correlation, and multiconfigurational methods are highly recommended. In this study, **UL$_2$** and **PuL$_2$** were analyzed together as open-shell sets, where Complete Active Space Self Consistent Field (CASSCF) was unsuccessfully applied. When calculations were performed on the full molecule in CASSCF, the calculations failed to converge. Thus, DFT is a good alternative for insight on the nature of the electronic structure of **UL$_2$** and **PuL$_2$**.

The calculated absorption spectra of **UL$_2$** and **PuL$_2$** are characterized by low-intensity bands at low-energies that correspond to predominantly $f \rightarrow f$ transitions, **Figure 2.7**. These transitions are not well reproduced (peak 3a) due to the inability of DFT to include spin-orbit

coupling. Additionally, the strong mixing between the actinide 5*f* and ligand 2*p* orbitals produce variation in the nature of these transitions between **UL$_2$** and **PuL$_2$** (**Table B.5**). This mixing is also responsible for the broad band feature observed at around 450 nm, which is assigned as a ligand-to-metal charge transfer (LMCT) for both U^{4+} and Pu^{4+}, with some additional metal-to-ligand charge transfer (MLCT) transitions in the U^{4+} the broad band.

In comparison, the closed-shell **ML$_2$** (M = Zr, Hf, Ce, Th) systems are characterized mainly by $\pi \rightarrow \pi^*$ and LMCT transitions that are responsible for the high intensity of the transitions in the TD-DFT spectra, **Figure 2.8**. The band intensity for **CeL$_2$** is significantly decreased in both the experiment and theory that could be attributed to the dominating $\pi \rightarrow f$ and $\pi \rightarrow f\pi$ transitions, **Table B.6**. The $4f-\pi^*$ orbital mixing is an important factor in terms of the electronic structure of the closed-shell complexes. This can also be seen in the excited states of **CeL$_2$**, **Table B.6** band c, where virtual bonding molecular orbitals that are formed by the mixture of unoccupied ligand orbitals and 4*f* Ce orbitals, are populated. These transitions are not seen in the isoelectronic actinide analog, **ThL$_2$**.

Quantum Theory of Atoms in Molecules. Bader's theory[45] has been a useful tool to analyze the nature of bonding in molecules by not only analyzing its electron density (ρ) but also relating it with its radial extent, ρ(r). This specific term, called the energy density (H) is referred to as the sum of potential energy [5+] and Lagrangian kinetic energy (G).[56] Due to crystallographic symmetry, the **ML$_2$** (M = Ce, Th, U, Pu) asymmetric unit contains only one ligand. The M−O(1) and M−O(2) bonds are significantly different for **UL$_2$** [2.258(1), 2.241(1) Å] and the M−N(1), and M−N(2) bonds are significantly different for **ML$_2$** (M = Ce, Th, U, Pu) by 0.024, 0.017, 0.020, and 0.028 Å respectively, and can be compared in terms of the electron and total energy density, **Figure 2.9**. The M−O bond critical points (BCPs) have an increased accumulation of electron density over the M−N bonds. In addition, the increased electron density at the M−O bond critical point is accompanied by more negative values of the total energy density, related to the increased covalency character of the M−O over the M−N bonds.

Hf^{4+} differs from the *f*-block metals by the differential bonding parameters, in that it is able to bind more covalently to nitrogen atoms. The decrease in energy density in the Hf−O bonds could also be understood as a less pronounced preference for hard-donor ligands. Ce^{4+} and Th^{4+} present subtle differences which are seen in the decreased electron density in Th–O bond critical points, and less negative energy densities that argue in favor of increased covalent

character of Ce^{4+}. U^{4+} and Pu^{4+} also present similar bonding parameters, however differ from the other metals by the increased electron density and enhanced energy densities that agree with the well-known covalent character of these metals. While the Pu^{4+} seems to be more covalent by the increased overlap in the molecular orbitals, this is recognized as the overestimation of correlation in DFT.

The V(r)/G(r) ratio is useful to see the degree of predominance of the potential energy over the kinetic energy, i.e. for |V(r)|/G(r) > 1, the interaction is stabilized by a local concentration of the charge.[57] This also can be understood as the stabilization of the electron density at the BCP produced by an increased potential energy and/or a reduction of the kinetic energy of these electrons. According to **Table B.7**, the energy of the M–O bonds are in the range of 17-18% of potential energy predominance except for Hf–O that is reduced to 14%. However, the Hf–N bonds presents 18% of predominance being the highest percentage with respect to the M–N bonds. This explains why Hf bonds are similar in terms of covalent character as previously mentioned. Additionally, Ce/Th differences can be seen more clearly in M–N bonds, where Th^{4+} shows around 6% of increased predominance of the potential energy with respect to the isoelectronic Ce^{4+}. Thus, Ce differs from Th in how they bind to softer-donor ligands rather than hard-donor ligands.

Due to the scarcity of reported bonding parameters for these tetravalent metals, it is difficult to compare with other complexes. There are few studies that report the electron densities, Laplacian of the electron density and integrated parameters for tetravalent lanthanide/actinide systems.[58–60] Although the best way to compare bonding parameters between complexes is to compare their normalized energy densities (H/ρ), none have been reported. Electron densities have been reported for other coordination complexes, however these are not directly comparable as the electron density localized in the BCP decreases with increasing coordination number. In another study where the 5-coordinate **M(BIPM^{TMS})(ODipp)$_2$**, [M = Ce, Th, U; BIPM^{TMS} = C(PPh$_2$NSiMe$_3$)$_2$; Dipp = C$_6$H$_3$-2,6-^{i}Pr$_2$] complexes were examined, the total electron densities of Ce^{4+}, Th^{4+}, and U^{4+} were reported to be 0.4008, 0.3989 and 0.4568 a.u. respectively.[60] However, the study on **M(BIPM^{TMS})(ODipp)$_2$** examined metals in a lower coordination environment that feature an unusual M=C bonding interaction, and used a higher level of theory in terms of electron correlation. Therefore, these reported values are not completely comparable and should be considered carefully. In the 8 coordinate **ML$_2$** complexes

reported here the calculated electron densities of Ce^{4+}, Th^{4+}, and U^{4+} are 0.5294, 0.5125 and 0.5631 a.u., respectively. While the values reported here suggest a higher degree of covalency for **ML_2** over the previously reported **$M(BIPM^{TMS})(ODipp)_2$** complexes, they need to be confirmed using a more correlated wave function.

2.4 Conclusion

Herein we have structurally characterized a series of tetravalent transition (Zr, Hf), lanthanide (Ce), and actinide (Th, U, Pu) metal complexes with the Schiff-base ligand, **H_2L** {**L** = *N*,*N*′-bis[(4, 4'-diethylamino)salicylidene]-1,2-phenylenediamine} in the form of **ML_2**. The **ML_2** family of complexes allow for a comparison across a series of elements by various spectroscopic and theoretical techniques. Crystallographic analysis finds that the bonding trends follow the ionic radii of the elements with **ThL_2** showing the longest bond lengths while **HfL_2** shows the shortest bond lengths. The absorbance spectra of all **ML_2** complexes show intense, broad MLCT bands with several $f \rightarrow f$ peaks in the **UL_2** and **PuL_2** spectra, in the solid state, which were successfully modelled by TD-DFT. Comparison of **UL_2** and **PuL_2** reveal similar bonding parameters, while the **CeL_2** shows increased covalent behavior compared to **ThL_2**. The ligand-metal overlap is also clearly enhanced in **UL_2** and **PuL_2**.

2.5 Figures

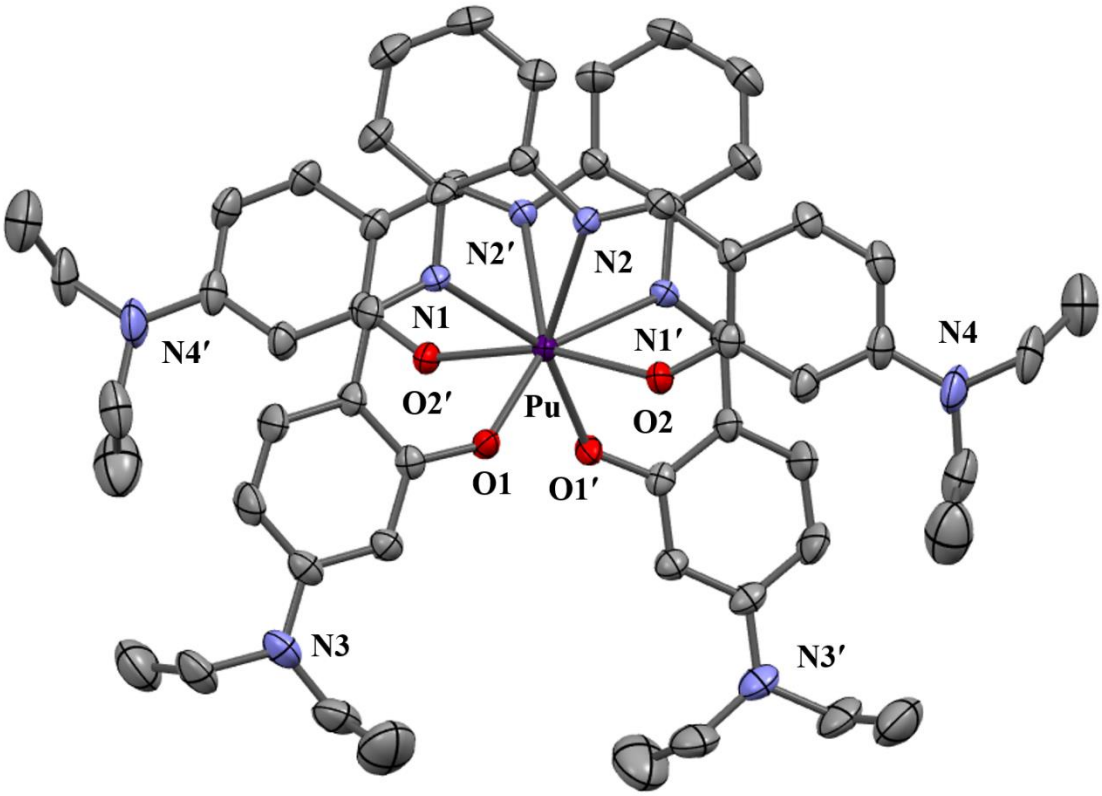

Figure 2.1. Molecular structure of **PuL**$_2$ (L = *N*,*N*′–bis[(4,4'-diethylamino)salicylidene]-1,2-phenylenediamine) drawn at the 50% probability level with hydrogen atoms and lattice solvent omitted for clarity. The Ce, Th, and U analogs are isomorphous.

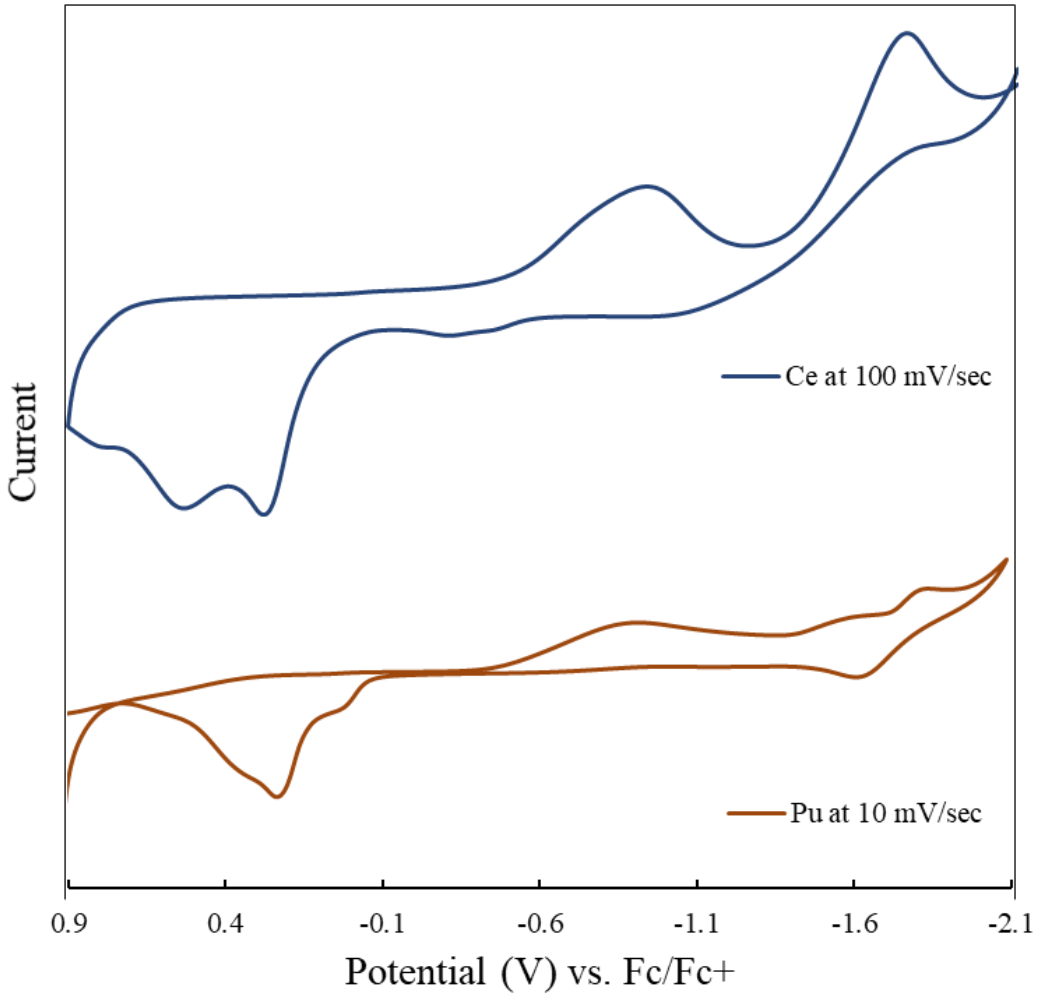

Figure 2.2. Cyclic voltammogram showing both **CeL$_2$** at a concentration of 5x10^{-3} M and ν = 100 mV/sec (above) and **PuL$_2$** at ν = 10 mV/sec (below). Both scans are taken at 25 °C and with 0.1 M [N^{n}Bu$_4$][PF$_6$] in DCM.

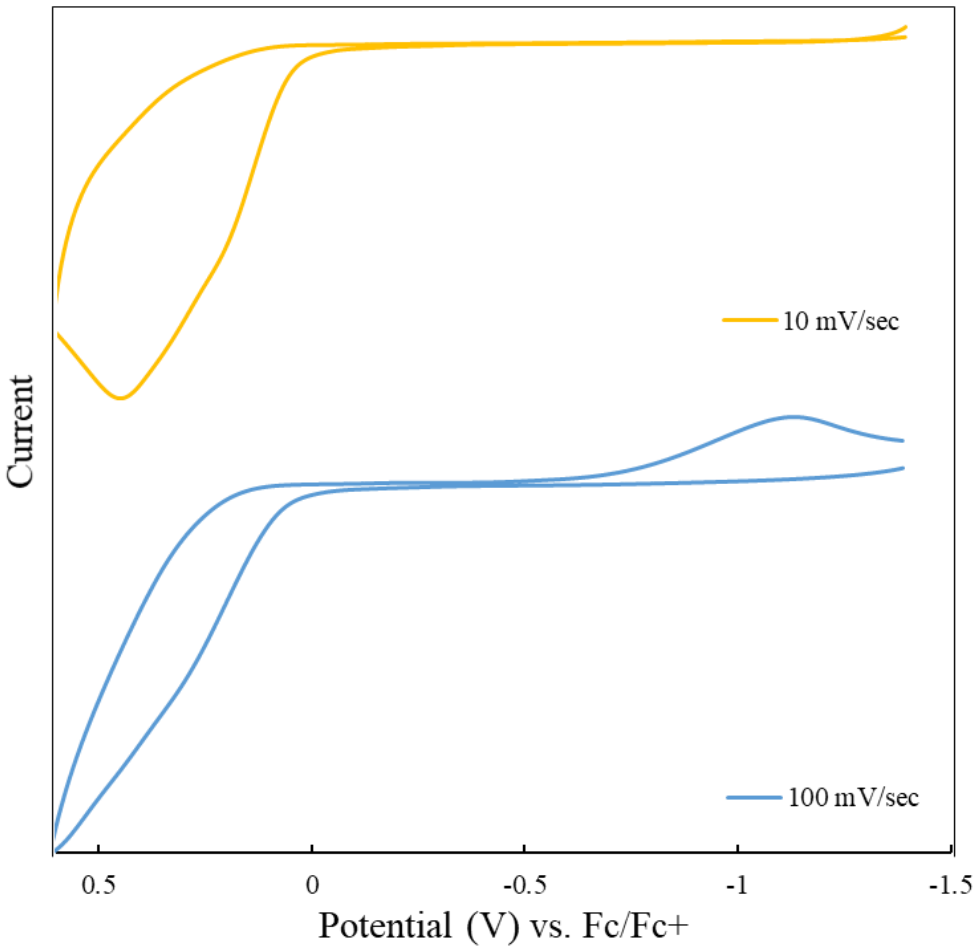

Figure 2.3. Cyclic voltammograms showing **H_2L** at a concentration of $5x10^{-3}$ M and ν = 10 mV/sec and ν = 100 mV/sec. Both scans are taken at 298 K with 0.1 M $[N^nBu_4][PF_6]$ in DCM.

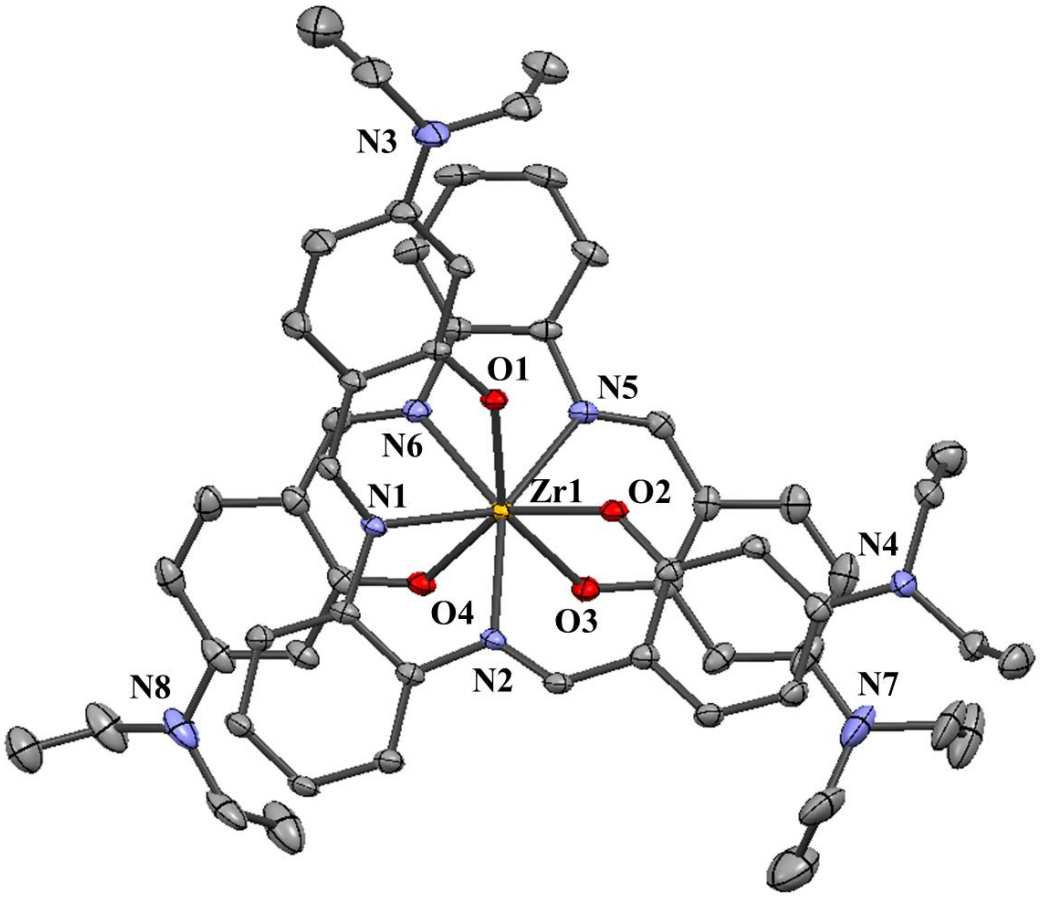

Figure 2.4. Thermal ellipsoid plot of one of the two crystallographic independent units of $\mathbf{ZrL_2}$ drawn at the 50% probability level with hydrogen atoms, disorder, and lattice solvent omitted for clarity. The $\mathbf{HfL_2}$ compound is isomorphous.

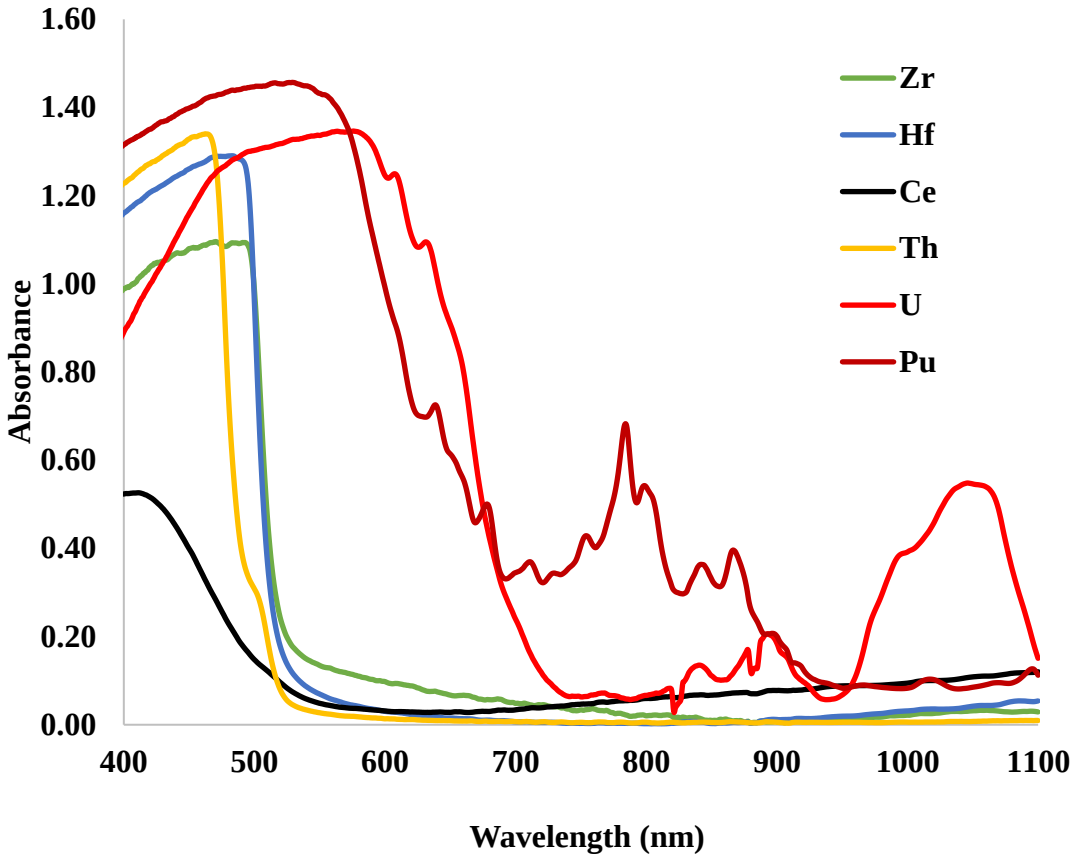

Figure 2.5. Solid-state UV/vis/NIR absorbance spectra of **ML**$_2$ (M = Zr, Hf, Ce, Th, U, Pu).

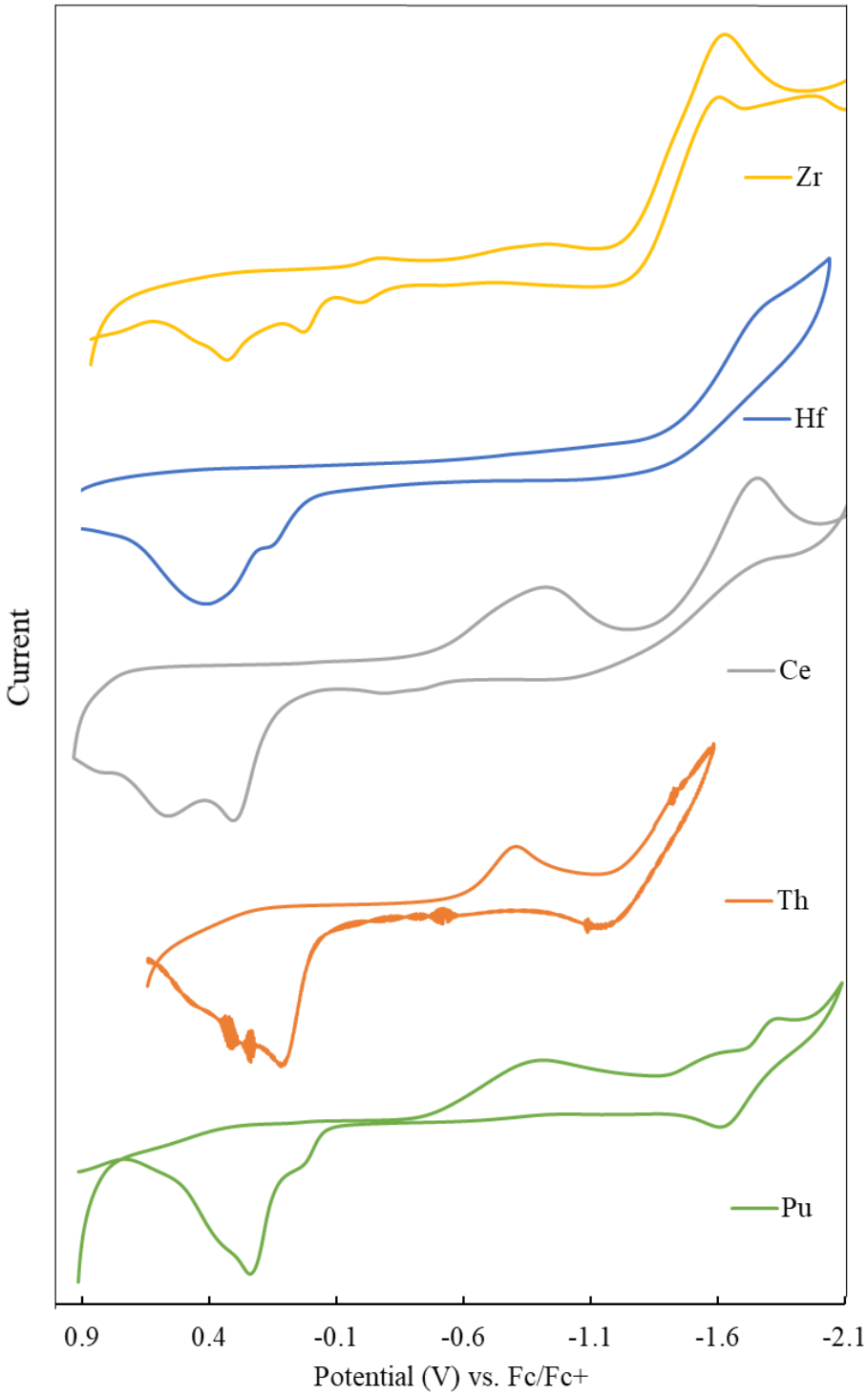

Figure 2.6. Cyclic voltammograms of **ML$_2$** for M = Zr (25 mV/sec), Hf (25 mV/sec), Ce (100 mV/sec), Th (25 mV/sec), and Pu (10 mV/sec) in DCM with 0.1 M [N^{n}Bu$_4$][PF$_6$] supporting electrolyte.

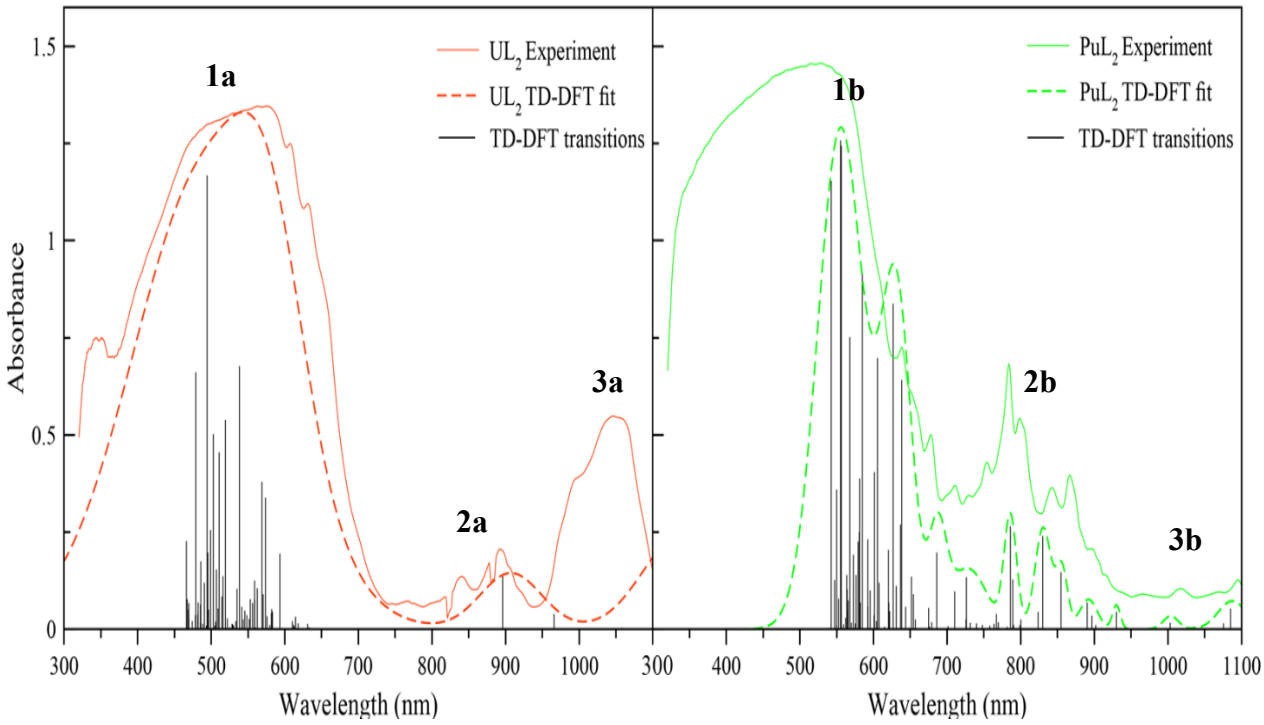

Figure 2.7. Calculated TD-DFT UV/vis/NIR absorption spectra of **UL2** (left) and **PuL2** (right). Solid and dashed lines correspond to the experimental and gaussian fit of the calculated transitions, respectively. The oscillator strength for **UL2** and **PuL2** was scaled up to 20 and 35%, respectively.

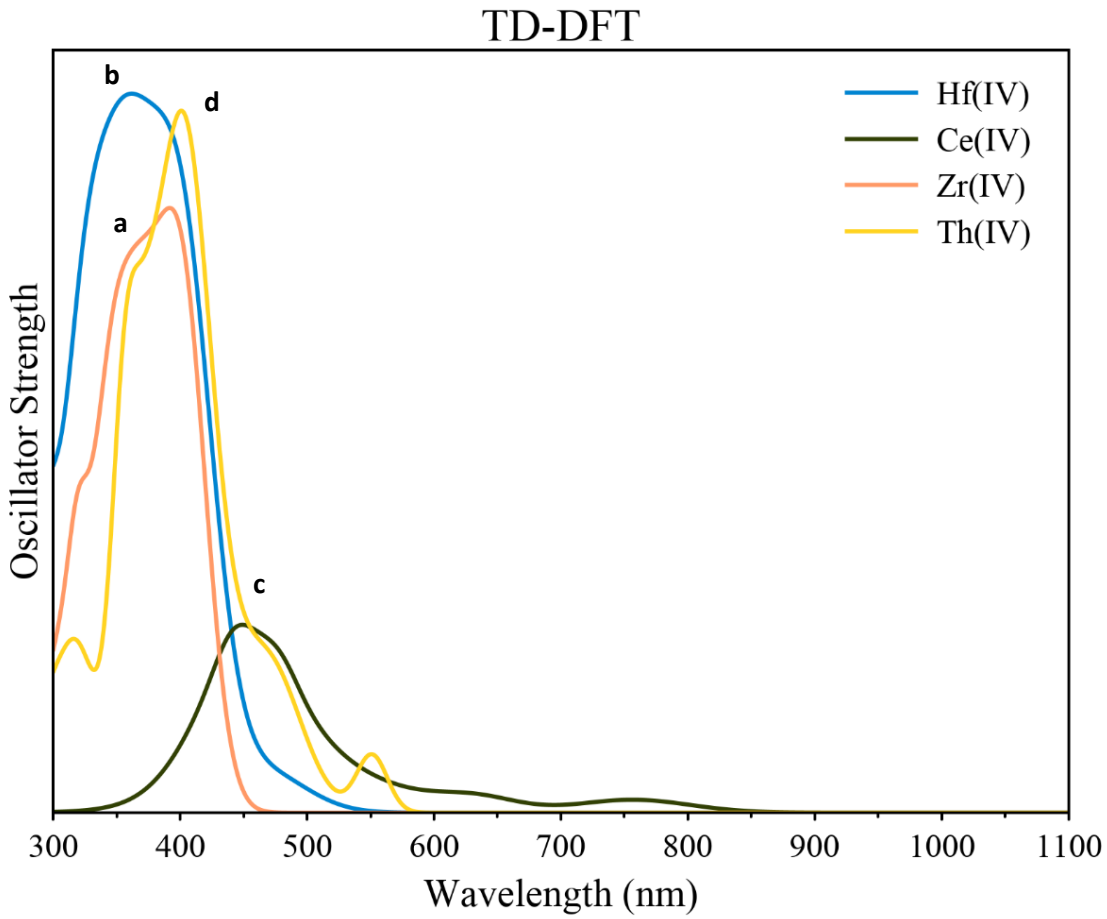

Figure 2.8. Calculated TD-DFT absorbance spectra of **ZrL_2**, **HfL_2**, **CeL_2**, and **ThL_2**. Solid lines correspond to the gaussian fit of the calculated transition. Labeled peaks correspond to transition assignments described in **Table B.7**.

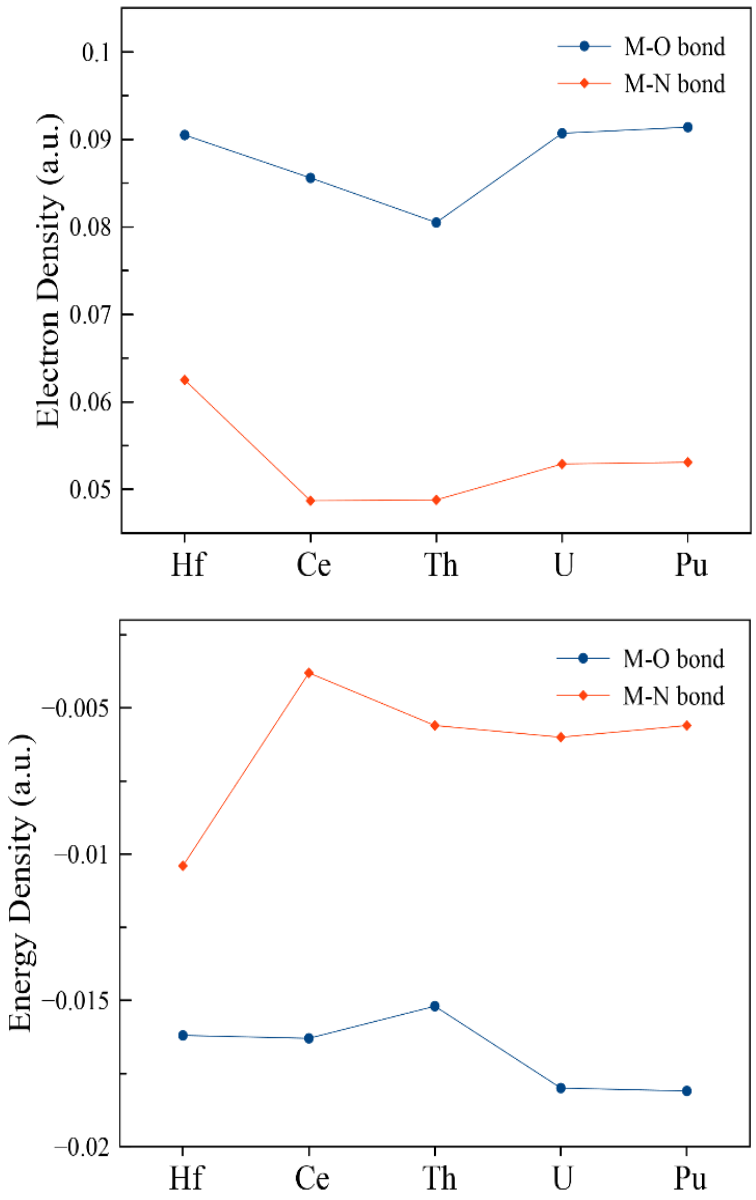

Figure 2.9. Electron (top) and total energy (bottom) density parameters in the M−O and M−N bond critical points in **ML**$_2$ (M = Hf, Ce, Th, U, Pu). All parameters were calculated from their corresponding DFT wavefunctions.

CHAPTER 3

SYNTHESIS AND SPECTROSCOPY OF URANYL SCHIFF BASE COMPLEXES

Adapted with permission from Bonnie E. Klamm, Cory J. Windorff, Cristian Celis-Barros, Matthew L. Marsh, and Thomas Albrecht-Schmitt. *Inorg. Chem.* 2020, 59, 1, 23-31

3.1 Introduction

The coordination chemistry of uranyl cations with Schiff base ligands has been probed for their potential applications in the remediation of nuclear waste from reactor fuels as well as the extraction of uranium from seawater, groundwater, and soil.[61–65] Additionally, uranyl ions have been studied for decades because of their rich coordination behavior, reactivity, and unusual interactions with a wide variety of ligands[16,66–71] as well as their potential optical, magnetic, catalytic, and ion-exchange applications.[72,73] Generally, U^{6+} prefers to bind to axial O atoms to form the linear UO_2^{2+} species and forms stable complexes with various O-, N-, and S-donor ligands.[68,74–76] These uranyl complexes are able to adopt a variety of coordination environments and have been observed in structures with coordination numbers ranging from 6 to 8.[75,77,78]

To date, many uranyl complexes with Schiff base ligands and related analogs have been reported.[30,72,73,79–81] The tetradentate Schiff base ligand has an N_2O_2 set of donor atoms well suited to coordinate the uranyl ion in a pentagonal-bipyramidal geometry, where the equatorial plane of the uranyl cation is coordinated to the Schiff base and typically a solvent molecule.[79,82–84] The high modularity of the salen ligands has allowed the exploration and targeting of different properties via control of the coordination sphere using the ligand.[19] In recent work, we have shown that the ligand *N*,*N*′-bis[(4,4′-diethylamino)salicylidene]-1,2-phenylenediamine (**H_2L**) forms highly stable tetravalent compounds with extremely intense charge-transfer bands using the group IV metals Zr, Hf, and Ce and the actinides Th, U, and Pu. Here we extend our studies to the uranyl dication utilizing single-crystal X-ray crystallography, multinuclear NMR, UV/vis/near-IR (NIR) spectroscopy, and electrochemistry and coupled with computational studies to offer an electronic structure basis to explain bonding parameters and stability.

3.2 Experimental

3.2.1 General considerations and instrumentation

Caution! ^{238}U is a low-specific-activity α particle emitting radionuclide and its use presents hazards to human health. All manipulations were conducted in a well-ventilated fume hood with no attempt to exclude air or water. The solvents methanol (MeOH; Sigma-Aldrich), dichloromethane (DCM; Sigma-Aldrich), pentane (Sigma-Aldrich), dimethyl sulfoxide (DMSO; Sigma-Aldrich), and deuterated DMSO (Cambridge Laboratories Inc.) were used as received. The following compounds were purchased as reagent grade from commercial sources and used as received: KOH (Sigma-Aldrich), [TBA][PF_6] (Sigma-Aldrich), $UO_2(NO_3)_2 \cdot 6H_2O$ (Sigma-Aldrich), and NaCl (Sigma-Aldrich). A saturated saline solution of MeOH was prepared by dissolving NaCl in a solution of MeOH. $UO_2Cl_2 \cdot 3H_2O$ was prepared by dissolution of $UO_3 \cdot 2H_2O$ (Strem) in concentrated HCl, evaporated to dryness, redissolved in deionized water, and dried. N,N′-Bis[(4,4′-diethylamino)salicylidene]-1,2-phenylenediamine (**H_2L**) was made according to the literature.

Solid-state UV/vis/NIR spectroscopic data were obtained from single crystals using a CRAIC Technologies UV/vis/NIR microspectrophotometer. Crystals were placed on glass slides in immersion oil, and data were collected from 300 to 1100 nm. Solution-phase UV/vis/NIR spectroscopic data were obtained from 0.08 mM solutions using an Agilent Technologies Cary series 6000i UV/vis/NIR spectrophotometer. **$UO_2Cl_2(H_2L)$** was separated a la Pasteur for spectroscopy. Samples were dissolved in DMSO and placed in 1 mm quartz cells. Data were collected from 300 to 1100 nm. ^1H and $^{13}C\{1H\}$ NMR spectra were recorded on a Bruker 600 MHz spectrometer operating at 600.1 and 150.9 MHz, respectively, at 298 K unless otherwise stated. ^1H and $^{13}C\{1H\}$ NMR spectra were referenced internally to solvent resonances. Attenuated total reflectance infrared (ATR-IR) spectra were recorded using a Bruker Alpha Fourier transform infrared (FTIR) spectrometer (SiC Glowbar source and DTGS detector) with a Platinum ATR QuickSnap sampling module (single-reflection diamond crystal). Spectra were obtained by placing powder on the diamond face, and data were acquired from 400 to 4000 cm^{-1} at a resolution of 4 cm^{-1}. All ATR-IR spectra are reported in absorbance with a blank versus atmosphere. Electrochemical data were recorded on a CH Instruments model 600E series potentiostat. A three-electrode configuration comprising a platinum disk working electrode (2

mm diameter), a platinum wire counter electrode, and a silver wire pseudoreference electrode was used in all experiments. Cyclic voltammetry scans were conducted in DMSO with 0.1 M [TBA][PF_6] electrolyte. C/H/N elemental analyzes were carried out by Midwest Microlab, Indianapolis, IN. Single crystals selected for data collection were mounted on a MITOGEN mount cryoloop and optically aligned on a Bruker D8 Quest X-ray diffractometer. Crystallographic data were collected under a low-temperature nitrogen gas flow, 150 K, using a Mo Kα (λ = 0.71069 Å) X-ray microsource and a CMOS detector. The unit cell determination and subsequent data collection were performed using the APEX III software. Raw data frames were processed using SAINT and SADABS. Subsequent calculations were carried out using the OLEX 2 program. Structures were solved by olex2.solve and refined by full-matrix least squares on F2 techniques. Crystallographic information is included in **Table C.1**.

UO_2^{2+}, **UO_2L(MeOH)**, and **$UO_2Cl_2(H_2L)$** were examined by Density Functional Theory (DFT) and Complete Active Space Self Consistent Field (CASSCF). DFT was utilized to obtain Natural Bond Orbitals (NBOs) and quantum theory of atoms in molecules (QTAIM) information, while CASSCF was used to analyze the multiconfiguration character of the ground state including the case of the isolated uranyl ion. The interacting quantum atom (IQA) energy decomposition analysis was carried out at HF/TZVP level of theory to assess the role of covalent interactions in these complexes. All corresponding calculations were carried out using the ORCA 4.0.1.2 package in combination with NBO6.0 and AIMAll packages.

DFT wave functions were obtained using the PBE0 functional in combination with the def2-TZVP basis set for all atoms except U, which was modeled using the SARC-TZVP basis set. The geometries were obtained directly from the experimental crystal structures for **UO_2L(MeOH)** and **$UO_2Cl_2(H_2L)$**, and a bond length of 1.732 Å was assumed for UO_2^{2+}. The resulting wave functions were used as input for DFT and multiconfigurational CASSCF calculations. The active space included the σ_u, and π_u orbitals ($D_{\infty h}$ symmetry notation) to represent the interaction between U^{6+} and the axial O^{2-} ions in a CAS(6,10). Due to the large size of **UO_2L(MeOH)** and **$UO_2Cl_2(H_2L)$**, an active space including the role of 6*d* orbitals was not possible. The scalar relativistic effects were considered using the relativistic DKH Hamiltonian to obtain the state-average CASSCF wave function that recovers static correlation, and spin-orbit coupling was taken into account using the Quasi-Degenerate Perturbation Theory (QDTP). Dynamical correlation was also included to correct the energies under the NEVPT2 formalism.

The resulting wave function including spin-orbit coupling and dynamical correlation are referred as SO-PT2 in the main manuscript. While multiconfigurational calculations provide a more accurate description of actinide systems, these wave functions are not always the best choice for obtaining integrated parameters under the QTAIM or IQA methodologies, therefore the NBO and QTAIM were obtained from DFT wavefunctions.

3.2.2 Synthesis

$UO_2L(MeOH)$. From $UO_2(NO_3)_2{\cdot}6H_2O$: An excess of a 5 M solution of KOH in MeOH (50 μL, 0.25 mmol) was added to a solution of **H_2L** (9 mg, 0.020 mmol) in DCM (1 mL), causing an instant color change from yellow to red. Then added to a solution of $UO_2(NO_3)_2{\cdot}6H_2O$ (10 mg, 0.020 mmol) in MeOH (1 mL). The solution quickly changed from pale yellow to dark red/black. Pentane (5 mL) was carefully layered on top of the solution, and after 1 day at room temperature, X-ray-quality crystals of **$UO_2L(MeOH)$** (13 mg, 85%) were isolated as red blocks, washed with pentane, and dried in air. ^{1}H NMR (DMSO-d_6): δ 9.23 (s, 1H, Ar–*H*), 8.89 (s, 1H, Ar–*H*), 7.64 (s, 1H, Ar–*H*), 7.59 (d, 1H, Ar–*H*), 7.51 (d, 2H, Ar–*H*), 7.37 (s, 2H, Ar–*H*), 6.52 (d, 1H, Ar–*H*), 6.24 (s, 1H, Ar–*H*), 6.20 (d, 1H, Ar–*H*), 6.12 (s, 1H, Ar–*H*), 3.47 (s, 8H, C*H*$_2$), 1.17 (t, 12H, C*H*$_3$). ^{13}C{^{1}H} NMR (DMSO-d_6): δ 171.80 (Ar–*C*), 163.12 (Ar–*C*), 147.56 (Ar–*C*), 137.63 (Ar–*C*), 126.97 (Ar–*C*), 114.96 (Ar–*C*), 103.39 (Ar–*C*), 96.65 (Ar–*C*), 44.62 (*C*H$_2$), 12.63 (*C*H$_3$). UV/vis/NIR [DMSO; λ_{max}, nm (ε, M^{-1} cm^{-1})]: 382 (88000). UV/vis/NIR (solid crystal; λ_{max}, nm): 536. FTIR (ν, cm^{-1}): 3616vw, 3445vw, 3372vw, 2979w, 2941vw, 2900vw, 2869w, 2772br, 1651w, 1600s, 1590s, 1558s, 1494s, 1473s, 1420s, 1405s, 1372sh, 1341s, 1298s, 1282s, 1259m, 1232s, 1202s, 1174s, 1139s, 1096m, 1072m, 1037w, 1000w, 967m, 898s, 860sh, 822m, 781m, 746s, 700s, 661w, 603m, 570w, 559w, 520w, 474w, 463w, 447sh, 425w, 402w. Anal. Calcd for $C_{29}H_{36}N_4O_5U$: C, 45.91; H, 4.78; N, 7.39. Found: C, 42.95; H, 4.67; N, 7.33. A low C content was observed repeatedly.

$UO_2L(MeOH)$ and $UO_2Cl_2(H_2L)$. From $UO_2Cl_2{\cdot}3H_2O$: In a manner similar to that described above, an excess of a 5 M solution of KOH in MeOH (50 μL, 0.25 mmol) was added to a solution of **H_2L** (12 mg, 0.025 mmol) in DCM (1 mL), causing an instant color change from yellow to red, and to a solution of $UO_2Cl_2{\cdot}3H_2O$ (10 mg, 0.025 mmol) in MeOH (1 mL). The solution quickly changed from pale yellow to dark red/black. Pentane (5 mL) was carefully layered on top of the solution, and after 1 day at room temperature, red blocks

of **$UO_2L(MeOH)$** and orange block crystals of **$UO_2Cl_2(H_2L)$** were washed with pentane and dried in air.

3.3 Results and Discussion

3.3.1 Crystallography

$UO_2L(MeOH)$ was prepared from two different starting materials. Briefly, deprotonation of **H_2L** with KOH in MeOH/DCM quickly caused a color change from yellow to red-orange; this solution was added to a MeOH solution of $UO_2(NO_3)_2 \cdot 6H_2O$ or $UO_2Cl_2 \cdot 3H_2O$ and further caused a color change to red/black for both solutions. Layering with pentane at ambient temperature (ca. 23 °C) gave red and orange X-ray-quality crystals after 1 day. The crystals were analyzed by X-ray crystallography and determined to be the expected MeOH solvate of the dianionic ligand complex [**$UO_2L(MeOH)$**, red crystal], as well as the unexpected, neutral ligand complex [**$UO_2Cl_2(H_2L)$**, orange crystal], **Figure 3.1**.

$UO_2L(MeOH)$ crystallizes in the $P2_1/c$ space group, forming a 7-coordinate pentagonal bipyramid, typical of UO_2(salophen) complexes, **Figure 3.2**. The average U–O_L and U–N bond lengths in **$UO_2L(MeOH)$** are 2.285(2) and 2.543(2) Å, respectively, which are comparable to other 7-coordinate uranyl Schiff base complexes, **Table C.2**. The average U≡O_{yl} bond distance is 1.783(2) Å with an angle of 178.92(7)°, significantly more linear than other reported uranyl salophen complexes, indicating that the uranyl moiety is slightly bent in the direction of the coordinating MeOH. Like typical salen complexes, the U^{6+} ion is coordinated to the tetradentate N_2O_2 cavity of the ligand. The ligand bends from the equatorial plane by 53° into the shape of a soft taco, comparable to other reported UO_2(salophen) complexes. While the salophen ligand is known to be planar in its metal complexes because of its conjugated π-electron system, the observed "soft taco conformation" is unique to uranyl Schiff base complexes and is considered to be caused by the small size of UO_2^{2+} (0.73 Å ionic radii for 6-coordinate and 0.81 Å ionic radii for 7-coordinate).

When $UO_2(NO_3)_2 \cdot 6H_2O$ was used as the starting material, **$UO_2L(MeOH)$** was isolated as the only product; however, when $UO_2Cl_2 \cdot 3H_2O$ was used as the starting material, a second product, characterized as the neutral ligand compound **$UO_2Cl_2(H_2L)$**, cocrystallizes

with **$UO_2L(MeOH)$** in basic conditions. Because of the similar solubilities of the two complexes, we have not been able to chemically separate them. However, the differing color (and morphology) of the two complexes allows the selection of small amounts of material for X-ray analysis and some spectroscopy. Attempts to synthesize **$UO_2Cl_2(H_2L)$** by mixing $UO_2Cl_2 \cdot 3H_2O$ with **H_2L** in the absence of a base gave a mixture of the two products. However, in saline conditions, **$UO_2Cl_2(H_2L)$** forms within seconds in high yield as pure crystalline material but not X-ray-quality.

Single-crystal X-ray diffraction studies reveal the structure of **$UO_2Cl_2(H_2L)$** to be a 6-coordinate octahedral compound crystallizing in the *P*1 space group, **Figure 3.3**. This unusual structure displays an empty N_2O_2 pocket, with $(UO_2)^{2+}$ coordinating only to the phenolic O atoms with two Cl^- anions. The average U–O_L and U–Cl bond lengths are 2.294(2) and 2.6779(7) Å, respectively. The average U≡O_{yl} bond distance is 1.769(2) Å, 0.014(2) Å shorter than that for **$UO_2L(MeOH)$**, with an angle of 178.70(8)°, comparable to **$UO_2L(MeOH)$**. The O_L–U–O_L bond angle indicates that the uranyl moiety is bent slightly away from the coordinating Cl atoms. Because the N_2O_2 pocket is empty, the ligand bends only 34° from the equatorial plane. The N atoms of the imine groups carry protons transferred from the phenolic groups upon coordination, providing a nonionic Schiff base ligand. The protons were located as Q peaks with an average O···H distance of 1.96 Å, consistent with an internal hydrogen bond between the two atoms, as evidence of a neutral ligand. While there have been many reports of U^{4+} and 6+ complexes with nonionized Schiff bases, there are few that have been crystallographically characterized. In addition, there are no other 6-coordinate crystallographically characterized Schiff base complexes with the uranyl ion.

3.3.2 Spectroscopy

Solution-phase UV/vis/NIR spectra of **$UO_2L(MeOH)$** and **$UO_2Cl_2(H_2L)$**, **Figure 3.4**, reveal an intense broad band featuring a shoulder with λ_{max} of 382 and 385 nm and ε values of 88000 and 118000 L mol^{-1} cm^{-1}, respectively. Solid-state UV/vis/NIR spectra of **$UO_2L(MeOH)$** and **$UO_2Cl_2(H_2L)$**, **Figure 3.5**, reveal an intense broad band with λ_{max} at 536 and 513 nm, respectively. The unusually high ε values of these compounds are dominated by the electron-donating $-NEt_2$ substituent, giving rise to strong $\pi \rightarrow \pi^*$ transitions, typical of these salophen complexes. The difference in λ_{max} between the solution-phase and solid-state spectra is

attributed to dynamic fluxion processes. No fluorescence was observed for either complex. The compounds were analyzed by ^{1}H and $^{13}C\{^{1}H\}$ NMR spectroscopies and gave typical diamagnetic spectra.

3.3.3 Electrochemistry

Previously, the electrochemistry of the tetravalent **ML₂** complexes (M = Zr, Ce, Hf, Th, U, Pu) was performed in DCM; however, the uranyl analogs reported here were only soluble in DMSO. This limited solubility is consistent with other reports of UO_2(salophen) complexes. Studies investigating the redox potentials of uranyl Schiff base complexes found that the U^{6+} complexes required large negative potentials between −1.5 and −1.7 V (vs Fc/Fc^{+}) in DMSO beyond the ligand-based reduction peak(s) to achieve metal-based reductions to U^{5+} species.

The cyclic voltammogram (CV) of **UO_2L(MeOH)** highlights the ligand-based reduction peak at $E = -1.35$ V (vs Fc/Fc^{+}) and the metal-based $(UO_2)^{2+}/(UO_2)^{+}$ quasi-reversible couple at $E_{1/2} = -1.78$ V (vs Fc/Fc^{+}), **Figure 3.6**. A small half-peak at $E = \sim -1$ V was observed in the CV and is attributed to an unknown impurity. The redox couple also was found to tolerate both a large number of n scans and a wide scan rate range (0.01–10 V s^{-1}; **Figure 3.7**). Discontinuities in the faradaic quality of the peaks due to charging currents were only found at above 6 V s^{-1}.

The study of the rates of electron-transfer reactions at the electrode/electrolyte solution interface is a fundamental issue in electrochemistry. Information on the kinetics of the reaction at the surface of the electrode is of great importance for a basic understanding of the kinetics of heterogeneous electron-transfer reactions. The standard rate constant (k_0) for **UO_2L(MeOH)** was estimated by Nicholson's equation **Eq. 3.1**,[85] on the basis of the assumption that the diffusion coefficient (D) of the reduced and oxidized species were equal:

$$\Psi = \frac{k_0}{\sqrt{D\pi(\frac{nF}{RT})\upsilon}} \quad \textbf{(Eq. 3.1)}$$

where ψ is the kinetic parameter defined by Nicholson. The D value was estimated by **Eq. 3.2**.,[86]

$$i_{pc} = 2.985 \times 10^{2} n A C_o^0 \sqrt{(\alpha n_B)} \sqrt{v} \sqrt{D} \quad \textbf{(Eq. 3.2)}$$

where A, C_o^0, α, and n_B are the surface area of the working electrode, concentration of the oxidant, transfer coefficient, and electron stoichiometry in the rate-determining process, respectively. The αn_B value was calculated as 0.65 from **Eq. 3.3**.,[87]

$$\alpha_{nB} = \frac{0.4768}{\Delta E_p} \textbf{(Eq. 3.3)}$$

where ΔE_p is the change in the variation of reversibility. Because of the charging currents exhibited, a baseline correction was made in order to calculate the diffusion constant and heterogeneous electron-transfer rate constant (k_0) for the system. It was noted that the ratio of the peak current constants (I_{pc}/I_{pa}) only remains near 1 for up to 500 mV s^{-1}; subsequently, some deviations can be found in the anodic current. For this limited scan rate range, consistent results between the cathodic and anodic peak currents versus (scan rate)$^{1/2}$ can be used to calculate D = 2.56 ± 0.21 × 10^{-7} cm^2 s^{-1}. In general, this value is small compared to other UO_2(salophen) complexes,[88] but it is unclear why. The resulting k_0 is estimated to be k_0 = 8.55 ± 0.84 × 10^{-4} cm s^{-1}. This supports the electrochemical reaction as being quasi-reversible under the present experimental conditions because the estimated k_0 value (8.55 ± 0.84 × 10^{-4} cm s^{-1}) is compatible with the range (3.0–5.3) × 10^{-2} > k_0 > (0.73–1.3) × 10^{-6} and comparable to those of other quasi-reversible uranyl complexes in DMSO.[88,89]

A similar CV is obtained for **$UO_2Cl_2(H_2L)$**, with a metal-based $(UO_2)^{2+}/(UO_2)^{+}$ quasi-reversible couple at $E_{1/2}$= −1.66 V (vs Fc/Fc^+), **Figure 3.8**. The slightly more positive shift for the metal-based reduction could be due to the ligand coordination environment. However, there are a few key differences for interpretation. The altered ligand environment appears to alter the metal-based redox; therefore, accurate diffusion and rate constants were not obtained. For the ligand-based redox chemistry, two peaks were observed at E = −1.34 V and E = −1.0 V (vs Fc/Fc^+). The more negative peak is attributed to reduction of the aryl ring, whereas the larger, less negative peak is due to reduction of the imines, **Figure 3.9**.

3.3.4 Theoretical analysis

To obtain a better understanding of the role of $\mathbf{L^{2-}}$ and $\mathbf{H_2L}$ in the bonding structure of the UO_2^{2+} unit, KS-DFT and CASSCF were used to analyze their bonding properties. These wave functions were analyzed by Natural Bonding Orbitals (NBO), Quantum Theory of Atoms In Molecules (QTAIM), and Interacting Quantum Atom (IQA) calculations to provide insight into the role of covalent interactions (see below). Briefly, NBO provides the more classical picture of the Lewis structure, while QTAIM provides a deeper insight into the topology of the electron density. IQA offers an alternative perspective to the bonding situation by decomposing

the energy into the classical and exchange portions which is a manifestation of covalent interactions.

The bonding structure of the uranyl unit is well established and has also been considered as a reference point for calculations. For completeness, the bonding in UO_2^{2+}, **$UO_2L(MeOH)$** and **$UO_2Cl_2(H_2L)$** are compared. To understand potential deviations and the role of the 5*f* shell in coordination of the **L^{2-}** and **H_2L** ligands, the active space selected for CASSCF calculations included three ligand O_{yl} 2*p* orbitals ($1\sigma_u$ and $2\pi_u$) and the seven U 5*f* orbitals in a CAS(6,10) calculation. Axial symmetry was used for comparison, where the ground state corresponds to the Σ_g, **Table C.2**. According to the SO-PT2 wave functions, the ground state for the three complexes is multiconfigurational in nature where the Hartree-Fock (HF) wave function represents 79%, 76%, and 73%, of the metal based wave function for UO_2^{2+}, **$UO_2Cl_2(H_2L)$**, and **$UO_2L(MeOH)$**, respectively. This reflects the increase of static electron correlation in the salophen complexes, implying ligation in the equatorial plane favors correlation in the axial plane. However, it is important to note that an increase in the correlation does not necessarily imply an increase in covalency.

In general terms, the molecular orbital structure of the complexes resembles that of the uranyl ion, with slight deviations observed in the non-bonding $5f_{\pm3}$ (φ) and $5f_{\pm2}$ (δ) orbitals, **Figure 3.10**. These deviations are expected due to the coordination environment produced in the equatorial plane. In **$UO_2L(MeOH)$** there is inversion of the φ and δ symmetry metal-based orbitals from the free UO_2^{2+} ion, while in **$UO_2Cl_2(H_2L)$**, these four orbitals are quasi-degenerated.

To understand NBOs it is important to point out that the wave function is described by maximum-occupancy localized orbitals in 1– and 2–center regions of the molecule with orbital occupancies close to 2.00. The total electron density of the molecule is typically recovered in the "natural Lewis structure." This refers to the typical 2-center bonding (BD) and antibonding (BD*) orbitals, the 1–center core (CR), and lone-pair (LP) orbitals. Other non-Lewis orbitals generated are assigned as lone-vacancies (LV) and Rydberg (Ry) orbitals. The construction of NBOs is based on the mixing of natural hybrid orbitals (NHO) h_A and h_B, that are built from natural atomic orbitals (NAOs), according to the following expressions, **Eq. 3.4** and **3.5**,

$$BD_{AB} = c_A h_A + c_B h_B \quad \textbf{(Eq. 3.4)}$$

$$BD^*_{AB} = c_A h_A - c_B h_B \quad \textbf{(Eq. 3.5)}$$

The mixing coefficients c_A and c_B provide information regarding the polarization of covalent bonds, where ionic bonds correspond to the limit case ($c_A >> c_B$).

In the study herein, six bonding and six antibonding NBO's are predicted for the three structures, confirming three formal U≡O_{yl} covalent bonds. However, they are predicted to be highly polarized according to their corresponding compositions, with the σ bonding interaction being less polarized than the π bonding interaction. The free uranyl ion presents the least polarized bonds, while both **$UO_2Cl_2(H_2L)$** and **$UO_2L(MeOH)$** show an increase of ~3% and 9% in the polarization of the π and σ bonds, respectively. In addition to the formal Lewis orbitals, a group of lone-vacancies (LV) corresponding to non-bonding orbitals are predicted for all the structures. While the free uranyl ion clearly shows the four remaining 5*f* orbitals not involved in bonding, **$UO_2L(MeOH)$** and **$UO_2Cl_2(H_2L)$** form hybrid orbitals (5*f*-6*d* mixtures) responsible of the occupation numbers observed, **Table C.3**.

Bader's QTAIM theory has been widely used to understand chemical bonds based on the topological atom concept. The electron density (ρ), as an experimental observable, provides a natural partition of the molecular space into basins. Within the QTAIM framework this partition is represented by a zero-flux surface between two bonded atoms where bonds are found to be lines of local maximum density. Along the bond path, the value of the density reaches its minimum when intersecting the zero-flux surface partitioning the two bonded atoms. This is the bond critical point (BCP) where chemical interactions are analyzed and collected as bond properties. Parameters including the Laplacian of the electron density ($\nabla^2\rho$), Lagrangian kinetic (G), potential (V), and total energy densities (H), and integrated parameters such as localization (λ) and delocalization (δ) indices can be obtained.

The useful concept of natural partition of the molecule into topological atoms has brought into light the development of a new method to decompose the energy of a molecule into atomic and interatomic contributions, the Interacting Quantum Atom (IQA). Within IQA, an insightful picture of covalency can be obtained by integrating the electron density through the 1-electron and 2-electron density matrices to assess the energy within a basin or two-interacting basins. For two interacting atoms, the total energy can be decomposed into classical and quantum mechanical contributions.

The QTAIM parameters at the bond critical point (BCP) that are commonly used to understand the nature of the chemical bond are: the electron density ρ(r), the Laplacian of the

electron density ($\nabla^2\rho$), localization (λ), and delocalization (δ) indices. Since the Laplacian does not properly describe heavy elements, energy density parameters avoid this issue and provide valuable information between Lagrangian kinetic energy (G), and potential energy (V). Because energy densities can be compared with pressures, V(r) represents the pressure exerted around the BCP, whereas G(r) accounts for the pressure exerted back by the electrons at the BCP. In this context, any predominance of V(r) over G(r), i.e. $|V|/G > 1$, implies local concentration of the electron density at the BCP. In terms of total energy density, if $H(r) < 0$ implies that a certain covalent character is found in the bond.

In the present study examining **$UO_2L(MeOH)$**, **$UO_2Cl_2(H_2L)$** and UO_2^{2+} as a reference, all atoms coordinated to UO_2^{2+} present covalent interactions. As expected, the axial bonds $U{\equiv}O_{yl}$ have the strongest covalent interactions and the largest values of electron density at the BCP compared to the atoms bound to the equatorial plane.

It is observed that the covalent character of the $U{\equiv}O_{yl}$ bond is decreased upon ligation. The covalent character of the $U{\equiv}O_{yl}$ bond is consistent with changes in length, whereas UO_2^{2+} has the most covalent character and shortest bonds (1.732 Å), **$UO_2L(MeOH)$** has the least covalent character and longest bond lengths [1.783(2) Å]. In **$UO_2Cl_2(H_2L)$** the $U–O_L$ bonds show as much covalent character as the U–Cl bonds, **Table C.4.** This can be attributed to the involvement of the O_L atoms in an internal hydrogen bonding network with the imino nitrogens. This allows a comparison of the calculated covalency for a $U–O_L$ bond which is participating in a hydrogen bond versus a dedicated U–O bond, the later of which shows decreased covalency.

Another proposed parameter within the QTAIM context is the covalency degree. Mathematically, it is the division of the total energy density by the electron density at that region (H/ρ) interpreted as the total pressure experienced by an electron in the BCP. The concept of covalency degree allows the covalent character of a bonding interaction to be described as a single electronic property. Or, restated, the total covalency degree can be viewed as a global property of the atom independently of the number of coordinated atoms. The total covalency degree in the U^{6+} ion in the compounds examined here, UO_2^{2+}, **$UO_2L(MeOH)$** and **$UO_2Cl_2(H_2L)$**, reveals the perturbation of covalency upon ligation of the free uranyl ion, **Table C.5**. The axial contribution to covalency is decreased by equatorial coordination, however, the global degree of covalency is increased in both salophen complexes, where **$UO_2Cl_2(H_2L)$** is the most globally covalent molecule examined in this study.

Unlike energy densities, IQA is capable of quantifying the role of shared electrons in the total energy of interaction between two atoms. In **Table C.6**, exchange interactions represent 44.2% of the total energy of interaction in the isolated uranyl ion, significantly larger than both salophen complexes. Of the two salophen complexes, the **$UO_2Cl_2(H_2L)$** uranyl moiety is only 0.5% more covalent. The U–Cl bonds present similar energies to the U–O_L bonds of **$UO_2Cl_2(H_2L)$**, however the electrostatic contribution of the U–O_L bonds is nearly twice the value of the U–Cl bonds, resulting in a significant difference in the covalent contribution to the bond. Although this may be unexpected, the ability of oxygen to donate charge to the metal is stronger than the chlorine. In the overall energy of interaction (E_{AB}), the U–O_L bond is significantly stronger than the U–Cl bonds. The low covalent contributions observed in the equatorial plane for **$UO_2L(MeOH)$** have values below 10%, that indicates these bonds are mainly stabilized by charge-transfer/electrostatic interactions. In comparison to the global total energy densities, the total exchange interactions involving U follow the same pattern; –2862.6, –3075.5, and –3051.9 kJ/mol for UO_2^{2+}, **$UO_2Cl_2(H_2L)$**, and **$UO_2L(MeOH)$**, respectively. The similarities between the total exchange interactions for these Schiff base complexes may explain their comparable stabilities.

3.4 Conclusion

Herein, we report two new uranyl coordination complexes with the Schiff base ligand **H_2L** in the form of **$UO_2L(MeOH)$** and **$UO_2Cl_2(H_2L)$**, which have been structurally and spectroscopically characterized. Synthetic studies show the importance of the starting material as well as the pH and salinity. Crystallographic analysis finds that **$UO_2L(MeOH)$** adopts the typical 7-coordinate uranyl Schiff base "soft taco confirmation". The rate constants were calculated from electrochemical experiments, confirming a quasi-reversible UO_2^{2+}/UO_2^{+} couple. In contrast, the 6-coordinate **$UO_2Cl_2(H_2L)$** complex features a neutral ligand with an unusual coordination mode outside the N_2O_2 binding site. Theoretical analysis shows that **$UO_2Cl_2(H_2L)$** exhibits slightly more covalent character in the equatorial plane than **$UO_2L(MeOH)$** because of the covalent contributions from the U–Cl bonds. This may also explain the cocrystallization of these two complexes despite basic conditions.

3.5 Figures

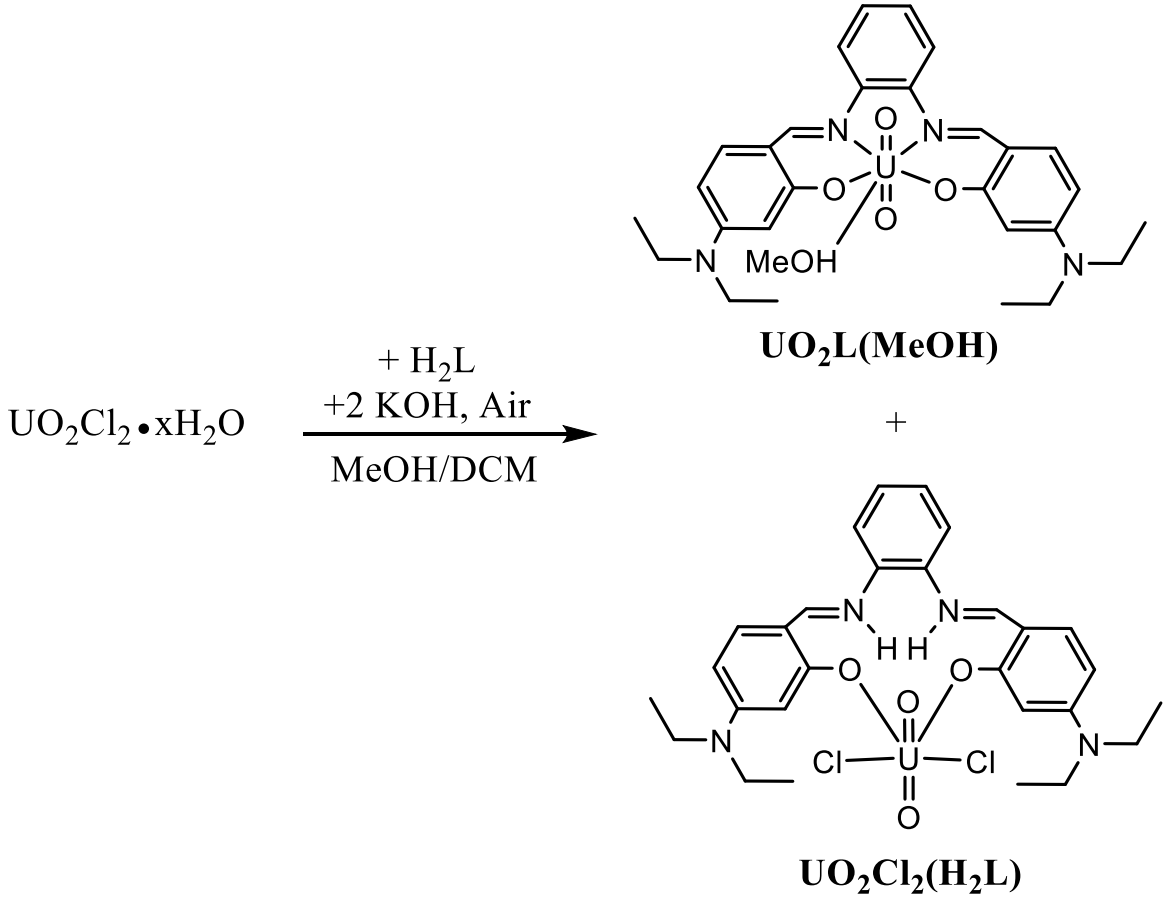

Figure 3.1. Synthesis of **$UO_2L(MeOH)$** and **$UO_2Cl_2(H_2L)$**.

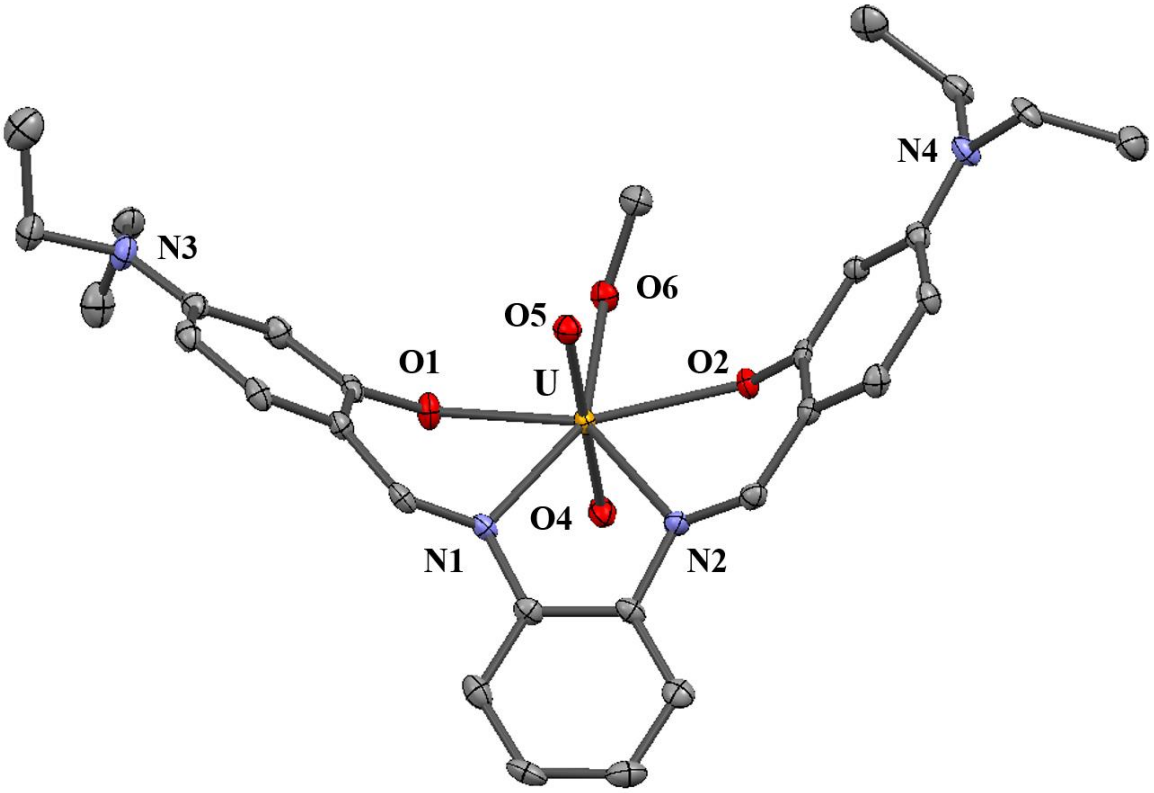

Figure 3.2. Molecular structure of **$UO_2L(MeOH)$** drawn at the 50% probability level with H atoms omitted for clarity.

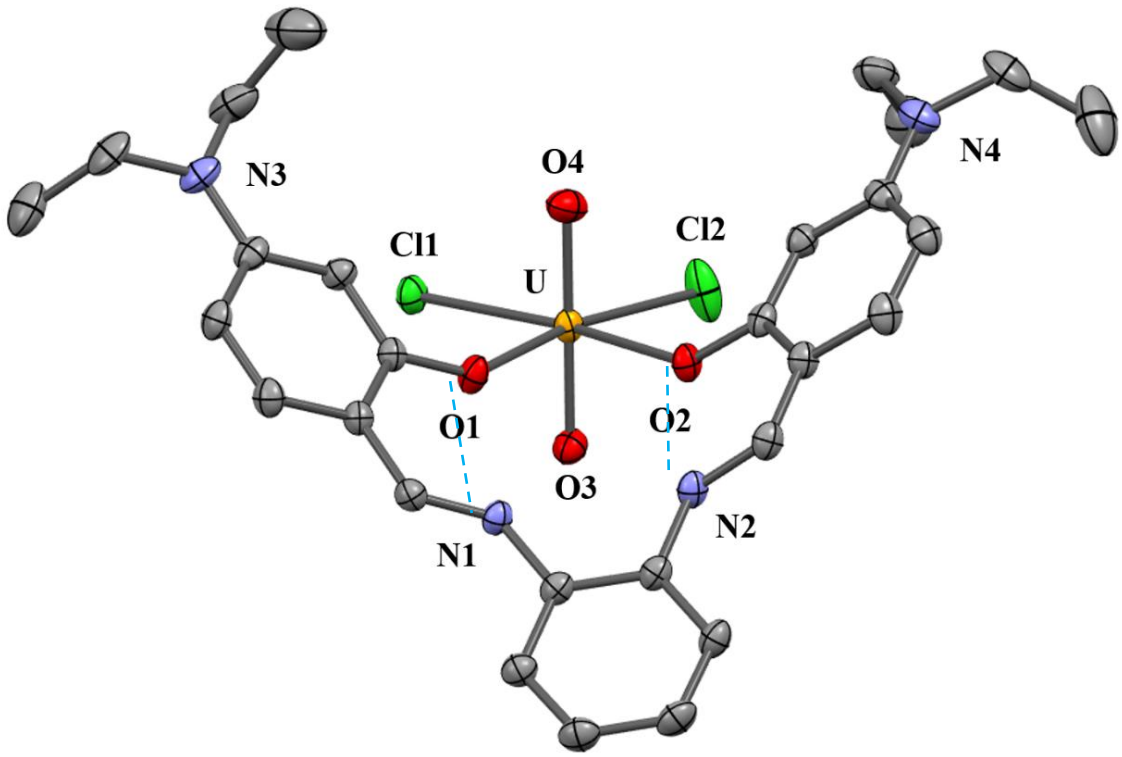

Figure 3.3. Molecular structure of **$UO_2Cl_2(H_2L)$** drawn at the 50% probability level with H atoms omitted for clarity, except H1 and H2, which participate in a hydrogen bond between N1–H1–O1 and N2–H2–O2, indicated by a dashed blue line.

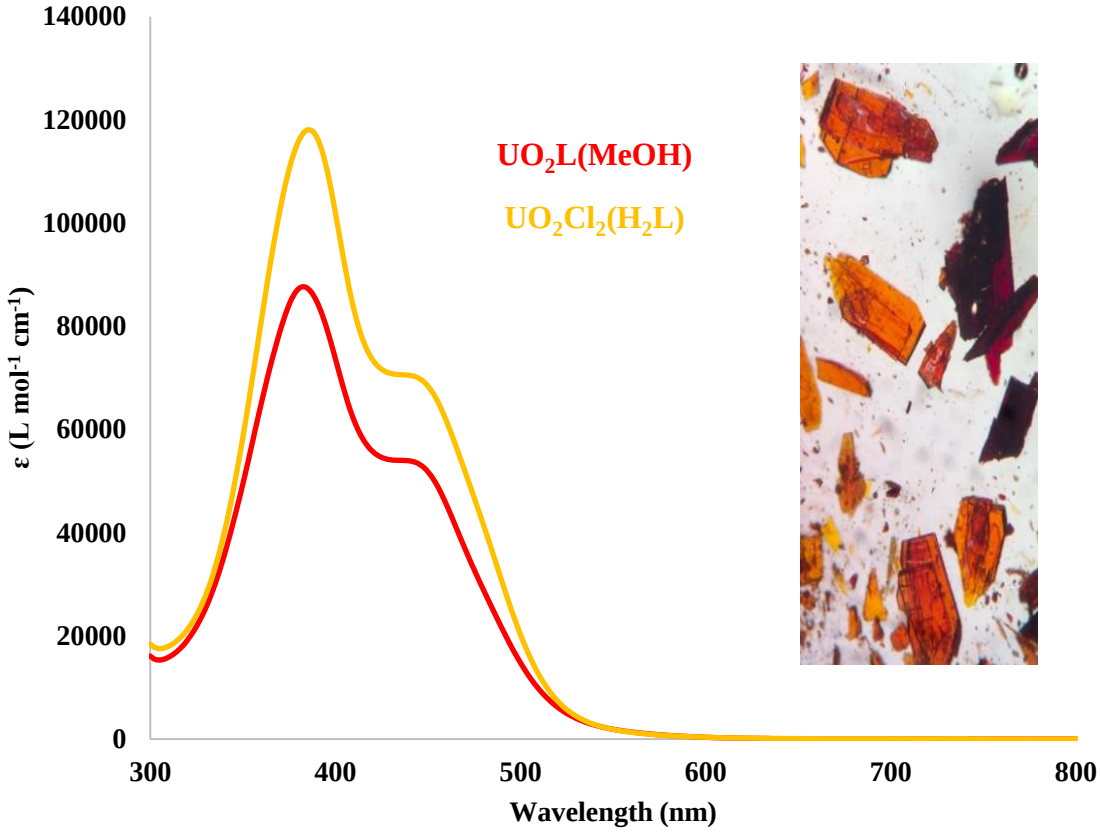

Figure 3.4. Solution phase UV/vis/NIR absorption spectra of **$UO_2L(MeOH)$** and **$UO_2Cl_2(H_2L)$** in DMSO at 298 K and photograph of complexes.

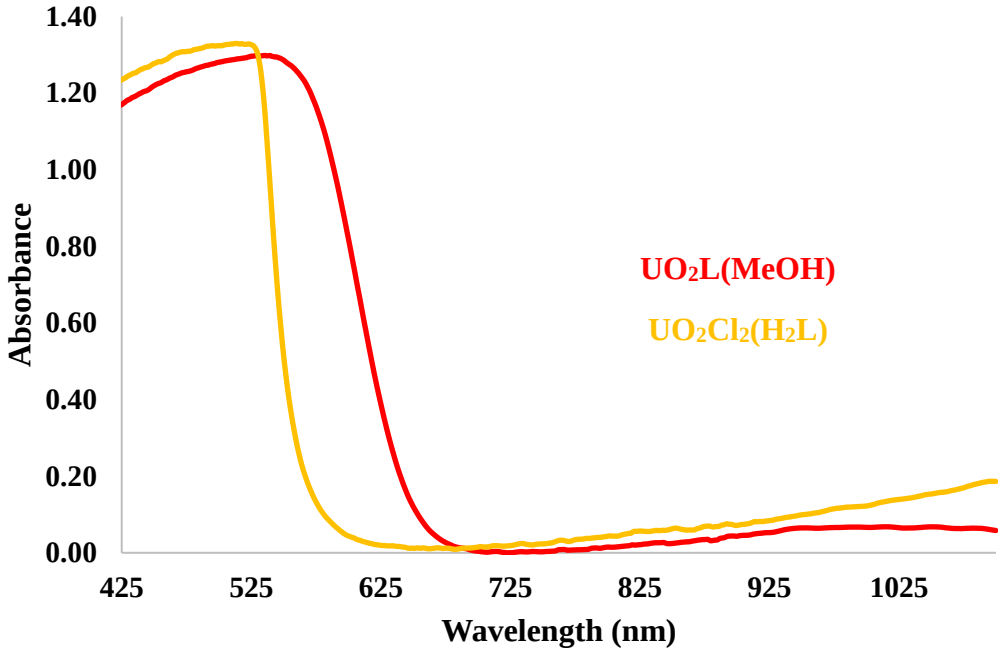

Figure 3.5. Solid state UV/vis/NIR absorption spectra of **$UO_2L(MeOH)$**, and **$UO_2Cl_2(H_2L)$**.

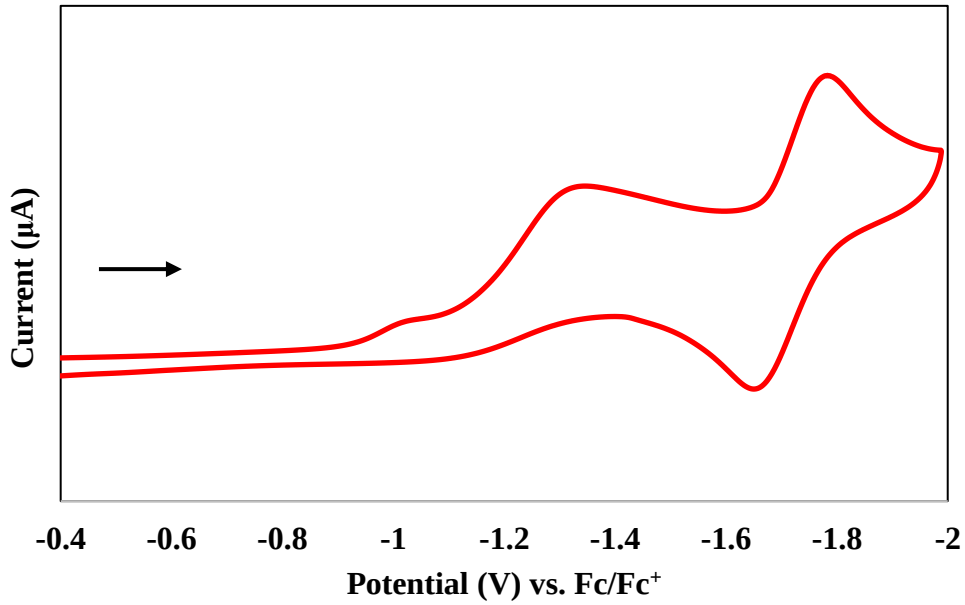

Figure 3.6. Cyclic voltammogram of 5 mM **$UO_2L(MeOH)$** at a scan rate of 100 mV/s in DMSO with 0.1 M [TBA][PF_6] supporting electrolyte.

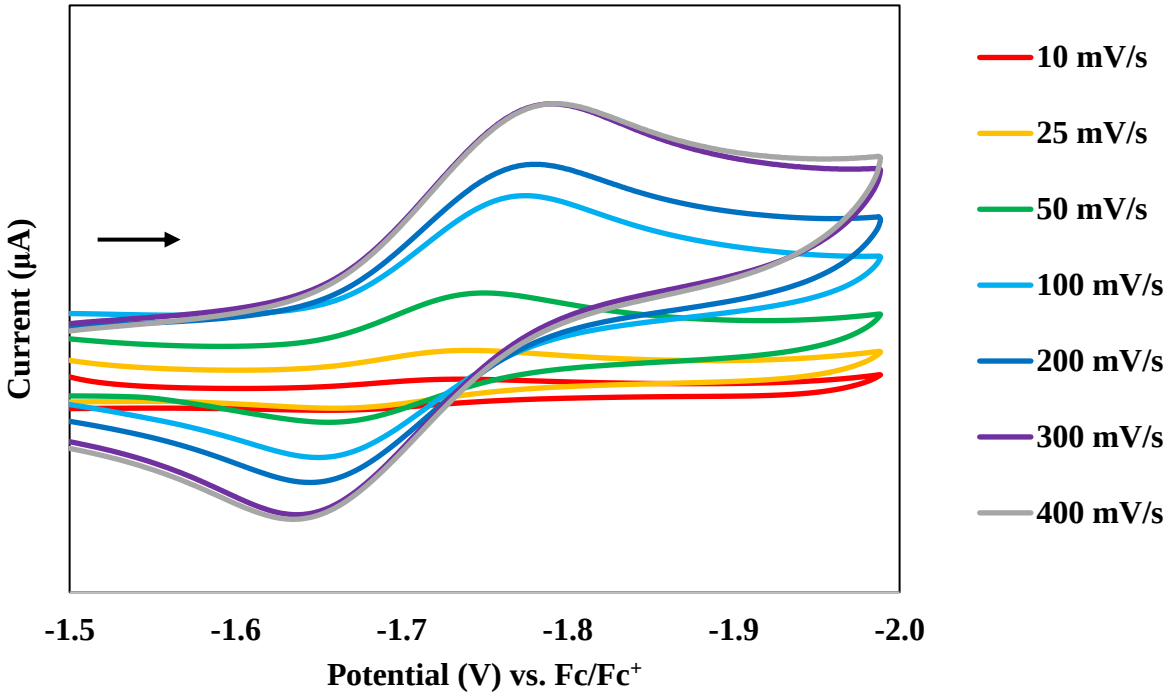

Figure 3.7. Cyclic voltammograms of 5 mM **$UO_2L(MeOH)$** in 0.1 M [TBA][PF_6] and DMSO at various scan rates (0.01 – 0.4 V/s) showing the stability and relative peak separations.

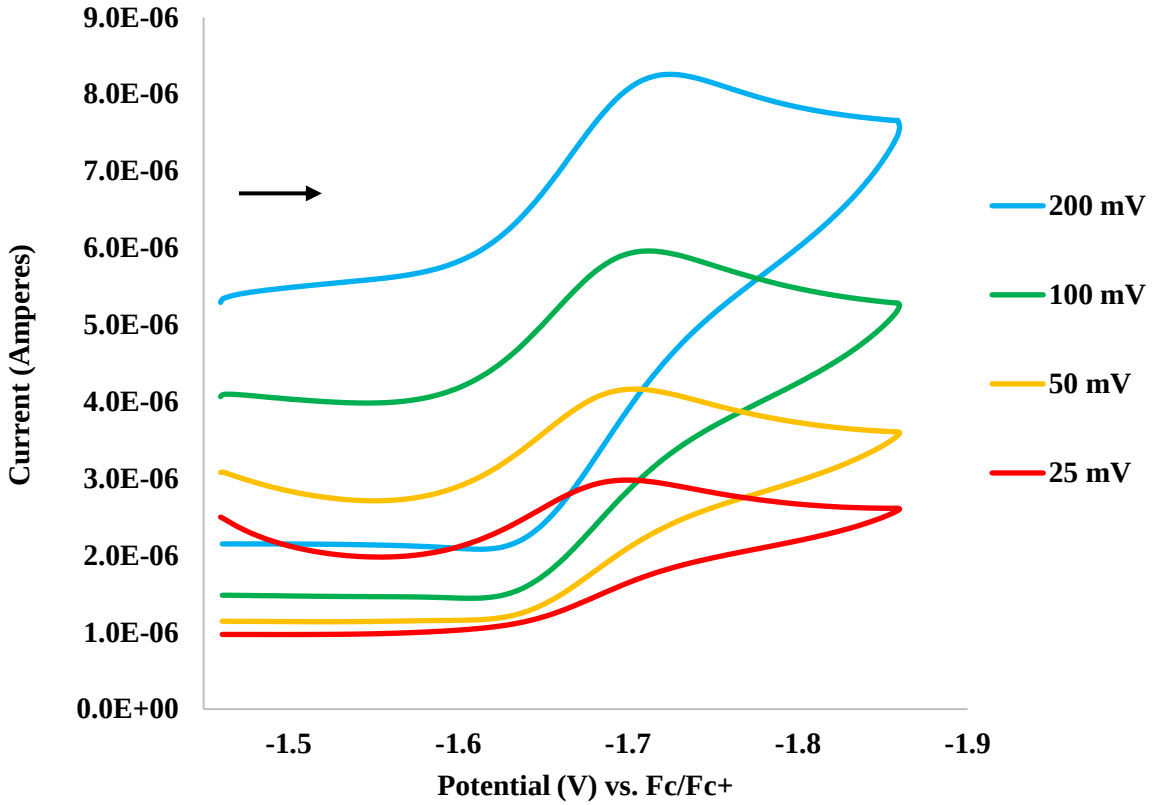

Figure 3.8. Cyclic voltammogram of 4 mM **$UO_2Cl_2(H_2L)$** at a scan rate of v = 25, 50, 100, and 200 mV/sec in DMSO with 0.1 M [TBA][PF_6] supporting electrolyte.

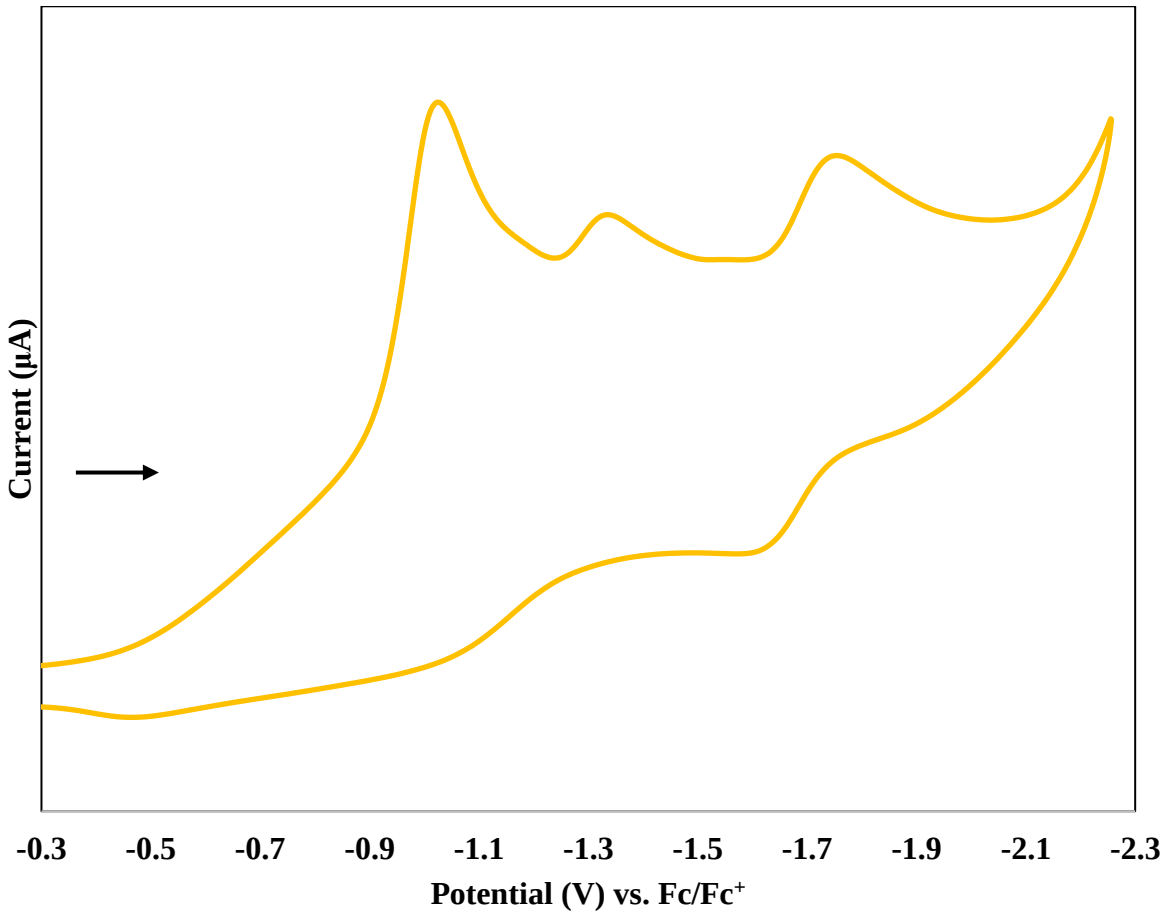

Figure 3.9. Cyclic voltammogram of 5 mM **$UO_2Cl_2(H_2L)$** at a scan rate of 25 mV/s in DMSO with 0.1 M [TBA][PF_6] supporting electrolyte.

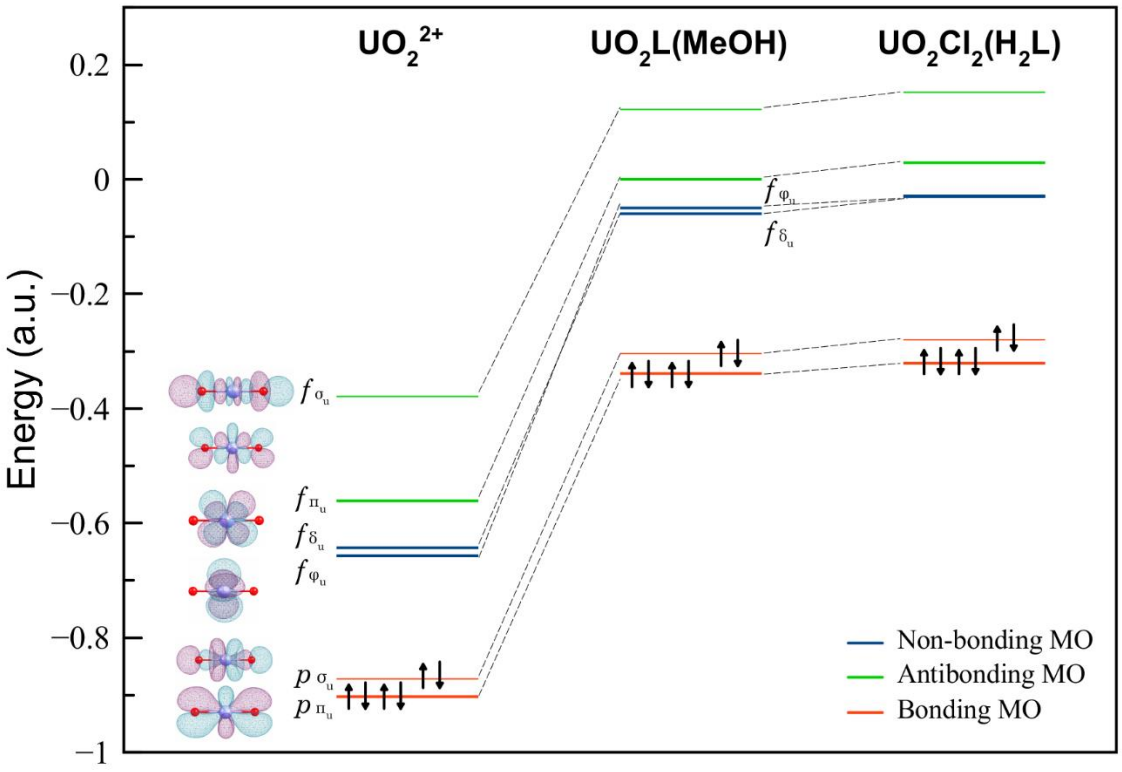

Figure 3.10. Molecular orbital diagram computed from DFT wave functions, where p_σ and p_π refer to the 2*p* oxygen orbitals that mix with the 5*f* orbitals. Energy values are expressed in atomic units.

CHAPTER 4

EXPLORING THE OXIDATION STATES OF NEPTUNIUM SCHIFF BASE COORDINATION COMPLEXES

4.1 Introduction

The radionuclide ^{237}Np [$t_{1/2}$ = 2.144(7)×10^6 y] is routinely produced in nuclear reactors as a result of the neutron irradiation of ^{235}U and ^{238}U, the two most common constituents of nuclear fuel.[90] While there is no known commercial use for Np, it largely resides in spent nuclear fuel, high-level waste (HLW), and other various solutions stored at various reprocessing facilities.[91] The need for ^{238}Pu as a heat source for radioisotope thermoelectric generators (RTGs) and radioisotope heater units is the main reason to separate and purify ^{237}Np, which is used to generate ^{238}Pu, ^{237}Np(n,γ)^{238}Np $\xrightarrow{\beta-}$^{238}Pu. Future needs to separate Np and the other actinides from spent fuel and HLW may be required by the proposed transmutation of actinides. Constraints on the final waste repository ultimately derive from the radiotoxicity and heat load of long-lived actinides.[92] Removal of these transuranics, especially ^{237}Np, has the advantage of eliminating these concerns for the long-term storage of radioactive waste. Therefore, enhanced exploitation of actinide-ligand interactions under non-aqueous conditions is crucial for the development of actinide separation systems.[93]

Np coordination compounds have been prepared and characterized, but not nearly to the extent of U.[1,93–96] Interest in coordination chemistry of Np compounds is brought by the unique properties of the six solution phase oxidation states of Np and changes in coordination chemistry caused by the decreasing ionic size across the actinide series.[1] The prevalence of the +5 oxidation state provides easier access to the +4 and +6 states for comparison to Pu and U, where spectroscopic properties can change across the series. These oxidations states are liable to change through redox reactions and disproportionation of Np^{5+}. The stability of the oxidation state is strongly affected by factors including oxidants/reductants, acidity, complexing ligand, and the concentration of Np in the solution.

In recent work, complexation of the Schiff base ligand, *N,N′*–bis[(4,4'-diethylamino)salicylidene]-1,2-phenylenediamine (**H_2L**) has been studied with a number of metal ions, including tetravalent Pu, Ce, U, Th, Hf, Zr, **Figure 4.1**.[97,98] In these complexes, two

H_2L ligands coordinate to the metal center via the N_2O_2 pocket in a tetradentate fashion, forming an 8-coordinate distorted square-antiprismatic geometry, which differs from the dinuclear,[19,24,99] polymeric,[19,24,100] or meridinal[19,48,101,102] geometries typically observed with other salen complexes because of the small charge to radius of the ion. These tetradentate Schiff base ligands are also highly π-delocalized and can provide a way to store electrons. As observed with U^{6+}, the salophen ligand is also capable of stabilizing reduced tetravalent complexes, as observed with **U(salophen)$_2$**,[30] by storing electrons in C–C bonds formed by reductive coupling of the imino groups. To date, the only missing *f*-block tetravalent ions are Np^{4+}, Bk_{4+} and Tb^{4+},[103,104] and the addition of **NpL_2** in this series allows for a direct comparison of the bonding parameters between the tetravalent early actinides.

Recently, the chemistry of **L^{2-}** was extended to UO_2^{2+}, forming a soft-taco geometry with **L** in the forms **UO_2L(MeOH)** and **$UO2Cl_2(H_2L)$**. We found that when $UO_2(NO_3)_2{\cdot}6H_2O$ was used as the starting material, **UO_2L(MeOH)** was isolated as the only product; however, when $UO_2Cl_2{\cdot}3H_2O$ was used as the starting material, a second product, characterized as the neutral ligand compound **$UO_2Cl_2(H_2L)$**, cocrystallized with **UO_2L(MeOH)** in basic conditions.

Currently, only a handful of NpO_2^+ and NpO_2^{2+} Schiff base complexes have been synthesized and characterized for their structural, and selective extraction properties.[36,37,105] Here we report Np^{4+} and Np^{6+} Schiff base coordination complexes with **L^{2-}** for a structural and spectroscopic comparison with its previously reported tetravalent and hexavalent analogs and the in situ observation/preparation of proposed $(NpO_2)^+$ and $(PuO_2)^{2+}$ complexes.

4.2 Experimental

4.2.1 General considerations and instrumentation

Caution! Hydrofluoric acid is an acutely toxic and corrosive chemical. All manipulations were performed with appropriate precautions and safety apparel, in a well ventilated fume hood with a tube of calcium gluconate within arm's reach.

Caution! ^{237}Np represents a serious health risk owing due to its α and γ emission, and its decay to the short-lived isotope ^{233}Pa ($t_{1/2}$ = 27.0 days), which is a strong β and γ emitter. All studies with neptunium were conducted in a laboratory dedicated to studies on transuranic elements.

Where noted, manipulations were performed with the exclusion of air and water using negative pressure glovebox techniques under an argon atmosphere. All manipulations not inside a glovebox were conducted in a well ventilated fume hood. Solvents used for manipulations in air including HF (48% wt, Sigma) HNO_3 (Sigma), HCl (Sigma) MeOH (Sigma), DCM (Sigma), pentane (Sigma) benzene (Sigma), toluene (Sigma) CCl_4 (Sigma), 1,4-Dioxane (Sigma), THF (stabilized, VWR) pyridine (Sigma) $CDCl_3$, DMSO-*d*$_6$ (Cambridge), were used as received. The following reagents and compounds were purchased reagent grade from commercial sources and used as received KOH (Sigma), NaOH (Sigma), NEt_3 (Sigma), $NaNO_2$ (Sigma), NH_2OH•HCl (Sigma) PPh_4Cl (Sigma), 15-crown-5 (Sigma) and $^{237}NpO_2$ (Oak Ridge National Laboratory). *N,N′*–bis[(4,4'-diethylamino)salicylidene]-1,2-phenylenediamine (**H_2L**) was prepared according to literature,[106,107] we found it is important to recrystallize both *o*-$C_6H_4(NH_2)_2$ from hot EtOH:$CHCl_3$ (~4:1) cooled to −5 °C overnight and diethylaminosalicaldehyde from hot EtOH cooled to −5 °C overnight as extended standing on the benchtop causes oxidation of both reagents. **H_2L** was also recrystallized after synthesis from hot (~60 °C) EtOH:DCM (~2:1) cooled to −5 °C overnight. Na_2NpCl_6 was prepared by dissolution of $^{237}NpO_2$ in HNO_3 (2 M, ~ 5 mL) with HF (single drop, concentrated), placed under a heat lamp, if the solution went to dryness more HNO_3 was added (2 M, ~5 mL), followed by precipitation of the hydroxide using $NaOH_{(aq)}$ (10 M, ~10 mL, excess) and dissolved in HCl (2 M, ~5 mL). UV/vis/NIR spectroscopy in $HClO_{4(aq)}$ (1 M) was utilized to determine the ratios of Np^{4+}:Np^{5+}, (comparison of 960 nm and 980 nm peaks for Np^{4+} and Np^{5+}, respectively) NH_2OH•$HCl_{(aq)}$ (10 M) was added to reduction to Np^{4+} and dried down to a green residue. NpO_2Cl_2•nH_2O was prepared by dissolving NpO_2 in HCl (2 M, 5 mL) and HF (concentrated, single drop) and placed under a heat lamp, if the solution went to dryness more HCl (2 M, ~5 mL) was added, once dissolved $O_{3(g)}$ was bubbled though the Np solution in HCl (2 M) overnight. Full oxidation Np^{6+} was confirmed by UV/vis/NIR spectroscopy in 1M $HClO_4$.[1,108]

Solid-state UV/vis/NIR spectroscopic data were obtained from single crystals using a CRAIC Technologies UV/vis/NIR microspectrophotometer. Crystals were placed on glass slides in immersion oil and data were collected from 300 nm to 1700 nm. Room temperature fluorescence spectroscopy was performed on a CRAIC Technologies UV/vis/NIR microspectrophotometer using an excitation wavelength of 365 and 420 nm and an integration time of 1000 s. Solution-phase UV/vis/NIR spectroscopic data were obtained using an Agilent

Technologies Cary series 6000i UV/vis/NIR spectrophotometer. Samples were dissolved in toluene (**NpL_2**) and DMSO-d_6 [**$NpO_2L(MeOH)$**] and placed in a 1 cm small volume quartz cell. ^1H and NMR spectra was recorded on a Bruker 400 MHz spectrometer operating at 400.1 MHz at 298 K and referenced internally to solvent resonances. NMR sample was dissolved in DMSO-d_6 with a drop of $CHCl_3$ and placed in an NMR tube with no attempt to exclude air or water. Electrochemical data was recorded on a CH Instruments Model 600E Series potentiostat in a negative pressure glovebox under an argon atmosphere. A three-electrode configuration comprising a platinum disk working electrode (2 mm diameter), a platinum wire counter electrode, and silver wire pseudo-reference electrode were used in all experiments. Cyclic voltammetric scans were conducted in DMSO with 0.2 M [TBA][PF_6] electrolyte for characterization of the ligand species, **NpL_2** and **$NpO_2L(MeOH)$**. Ozone was generated using pure oxygen with an Ozonology ozone generator at 100% voltage using an initial flow rate of 8 SCFH which was decreased to a flow rate of 4 SCFH for standing overnight. Ozone test strips were used to confirm the initial presence of O_3 bubbled into water. Elemental analysis was performed on samples using a FEI NOVA 400 scanning electron microscope coupled with energy-dispersive X-ray spectroscopy (SEM-EDS). A small powdered sample of Na_2NpCl_6 was affixed to an aluminum SEM-EDS puck using double-sided carbon tape, Analysis used 30 kV accelerating voltage and an accumulation time of 60s. Single crystals selected for data collection were mounted on a MITOGEN mount™ cryoloop and optically aligned on a Bruker D8 Quest X-ray diffractometer. Crystallographic data was collected at room temperature using a Mo-Kα (λ = 0.71069 Å) X-ray micro source and a CMOS detector. The unit cell determination and subsequent data collection was performed using the APEX III software.[40] Raw data frames were processed using SAINT[41] and SADABS.[42] Subsequent calculations were carried out using the OLEX 2 program.[43] Structures were solved by ShelXL and refined by least squares on F^2 techniques. Crystallographic information is included in **Table D.1**.

4.2.2 Synthesis

NpL_2. An excess of KOH in MeOH (50 μL, 5 M, 0.25 mmol) was added to a solution of **H_2L** (17 mg, 0.036 mmol) in DCM (0.25 mL) and added to a solution of Na_2NpCl_6 (7 mg, 0.018 mmol) in MeOH (0.50 mL). The solution quickly changed from green to dark red/black. Pentane (5 mL) was carefully layered on top of the solution and after 1 d at room temperature, X-ray

quality crystals of **NpL_2** were isolated as orange columnar crystals, washed with pentane and dried in air.

$NpO_2L(MeOH)$. NpO_2 (12 mg, 0.045 mmol) was suspended in 5 mL $HCl_{(aq)}$ (c.a. 3 mL, concentrated) and $HF_{(aq)}$ (single drop, concentrated) was added and left under a heat lamp overnight during which time it slowly dissolved to give a green solution which was dried to a soft green/brown residue. The residue was dissolved in dilute HCl (2 M, 5 mL) and slowly dried under a heat lamp overnight. A slow stream of ozone was bubbled through the green/brown Np solution in HCl (2 M) overnight and a color change to pink occurred and the oxidation state was confirmed to be pure Np^{6+} via solution UV/vis/NIR spectroscopy, formulated as $NpO_2Cl_2 \bullet nH_2O$. NEt_3 (50 μL, 0.25 mmol) was combined with a yellow solution of **H_2L** (20 mg, 0.045 mmol) in DCM (0.25 mL) and added to an emerald green solution of $NpO_2Cl_2 \bullet nH_2O$ in MeOH (0.625 mL). The solution quickly changed from emerald green to dark brown/black. Pentane (5 mL) was carefully layered on top of the solution and after 1 d at room temperature, X-ray quality crystals of **$NpO_2L(MeOH)$** were isolated as irregular black blocks, The mother liquor was decanted, the solids were washed with pentane and dried in air. After standing for 1 day X-ray quality crystals of **NpL_2** were isolated, as determined by unit cell analysis and solid state UV/vis/NIR spectroscopy, from the mother liquor as orange columnar crystals.

In situ reduction of $NpO_2L(MeOH)$. Excess $NaNO_2$ (20 μL, 10 M, DMSO-d_6) and $NH_2OH \bullet HCl$ (20 μL, 10 M, DMSO-d_6) were added to a solution of **$NpO_2L(MeOH)$** (0.5 mM, DMSO-d_6) in a 1 cm small volume quartz UV/vis/NIR cell and monitored by UV/vis/NIR spectroscopy. Within 1 hr the characteristic 980 nm peak for $(NpO_2)^+$ grew substantially coupled with the loss of the 1223 nm peak for $(NpO_2)^{2+}$, along with a decrease in the intensity of the charge transfer feature, **Figure 4.2**, **4.3**

Direct Synthesis of $(NpO_2L)^-$. Method A. NpO_2 (12 mg, 0.045 mmol) was suspended in HNO_3 (c.a. 5 mL, concentrated), $HF_{(aq)}$ (single drop, concentrated) was added and left under a heat lamp overnight during which time it slowly dissolved to give a green solution which was dried to a soft residue. The residue was dissolved in HNO_3 (2 mL, 1 M) $NaNO_{2(aq)}$ (5 μL, 10 M) was added, and the mixture was slowly dried overnight under a heat lamp giving a green residue formulated as $NpO_2(NO_3) \bullet nH_2O$. The Np^{5+} oxidation state was confirmed via UV/vis/NIR in $HClO_{4(aq)}$ (1 M). The Np solution was combined with a yellow solution of **H_2L** (20 mg, 0.045 mmol) in DCM (0.25 mL), causing a change to orange, and added to a solution of

$NpO_2(NO_3)$•nH_2O in MeOH (0.625 mL). The solution quickly changed from green to dark brown/black. Pentane (5 mL) was carefully layered on top of the solution and after 1 d at room temperature a brown precipitate formed. Neat 15-crown-5 (9 μL, 0.045 mmol) was added to the solution to aid in crystallization; however no single crystals were obtained from this solvent mixture. Slow evaporation of the solvent produced a dark black residue which was analyzed by ^{1}H NMR spectroscopy and solution phase UV/vis/NIR showed the presence of a single Np^{5+} complex tentatively formulated as "$(NpO_2L)_x^{n-}$". Attempted crystallization from pyridine yielded yellow X-ray quality crystals of Na(15-crown-5)NO_3 as determined by X-ray crystallography. The solution was evaporated, washed with water (3 × 0.5 mL) to remove any remaining Na(15-crown-5)NO_3. Further crystallization attempts from THF or pyridine, neat or layered with pentane or ether, slow evaporation also did not produce X-ray quality crystals. A dilute solution in DMSO-d_6 layered with CCl_4, Benzene, or Dioxane did not produce X-ray quality crystals.

Method B. $NpCl_4$•nH_2O (8 mg, 0.021 mmol) in HCl (2 M) was dried to a soft residue under a slow stream of air. The residue was dissolved in HNO_3 (3 mL, concentrated) to which $NaNO_2$ (30 μL, 10 M) was added. The Np^{5+} oxidation state was confirmed via UV/vis/NIR, and formulated as $NpO_2(NO_3)$•nH_2O. The solution was dried to a soft residue under a stream of air and dissolved in MeOH (1 mL) giving a pale green/blue solution. The Np^{5+} oxidation state was reconfirmed in MeOH via UV/vis/NIR. NEt_3 (50 μL, 0.25 mmol) was combined with a solution of **H_2L** (10 mg, 0.021 mmol) in DCM (0.25 mL) and added to solution of $NpO_2(NO_3)$•nH_2O in MeOH (1 mL). The Np^{5+} solution quickly changed from green/blue to dark brown/black. PPh_4Cl (10 M, 0.026 mmol) in MeOH (0.25 mL) was added to the solution and filtered. Pentane (5 mL) was carefully layered on top of the solution and after 1 d at room temperature a brown precipitate formed.

$(PuO_2)^{2+}$ analog. A slow stream of ozone was bubbled through $PuCl_3$ (15 mg) dissolved in 2 M HCl (3 mL) until the oxidation state was confirmed to be pure Pu^{6+} via solution UV/vis spectroscopy as PuO_2Cl_2. NEt_3 (50 µL, 0.25 mmol) was combined with a solution of **H_2L** (20.5 mg, 0.045 mmol) in DCM (0.25 mL) and added to solution of PuO_2Cl_2•nH_2O in MeOH (0.625 mL). The Pu^{6+} solution quickly changed from pink to dark brown/black. Pentane (5 mL) was carefully layered on top of the solution. After one day a black/brown precipitate formed, no single crystals were obtained for X-ray analysis.

4.3 Results and Discussion

4.3.1 Crystallography of NpL_2

The tetravalent **NpL_2** complex was prepared in a manner similar to **ML_2** (M = U, Th). Briefly, in air, addition of two equivalents of **H_2L** in DCM with an excess of KOH, was added to a solution of Na_2NpCl_6 in MeOH resulting in the formation of an intense dark red/black solution, characteristic of complexation. Layering with pentane yielded X-ray quality crystals of **NpL_2** overnight, **Figure 4.4**. Single-crystal X-ray diffraction studies reveal the structure to be isomorphous with the Pu, Ce, U, and Th analogs,[97,98] crystallizing in the *C*2/*c* space group. As was observed with the other complexes, **NpL_2** forms a distorted square antiprismatic geometry where the ligands form a facial "sandwich" type structure. The ligands bend at a slight 17˚ angle from the equatorial plane, typical of these phenyl substituted backbone Schiff base complexes.[23,39,109]

While there have been reports of Np^{5+} and Np^{6+} Schiff base coordination complexes, there are no Np^{4+} structures for a direct comparison of Np. However the isomorphous nature of **NpL_2** with **ML_2** (M = Pu, Ce, U, Th) complexes allow for a rare direct comparison of solid-state metrical parameters, **Table D.1.** The average Np−O and Np−N bond lengths of **NpL_2** are 2.231(2) and 2.562(2) Å, respectively, completing a linear trend with the other reported tetravalent *f*-element Schiff base complexes which range from 2.306(1) to 2.225(3) and 2.639(1) to 2.55(1) Å for Th and Pu, respectively, **Figure 4.5**. The O(1)−Np−O(2) and N(1)−Np−N(2) intraligand angles are 85.37(7) and 61.38(7)° and compare well with the 84.9(1) – 87.40(4)° range for the O(1)−M−O(2) angle and the 60.43(4) to 61.6(2) ° range for the N(1)−M−N(2) angle reported for **ML_2**.

4.3.2 Crystallography of $NpO_2L(MeOH)$

The actinyl **$NpO_2L(MeOH)$** complex was prepared in a manner similar to **$UO_2L(MeOH)$**.[110] Briefly, a solution of $NpCl_4$ in 2 M HCl was bubbled with O_3 overnight to yield $NpO_2Cl_2{\bullet}nH_2O$ with a color change from green to pink. The oxidation state of pure Np^{6+} was confirmed via solution UV/vis. $NpO_2Cl_2{\bullet}nH_2O$ was dried to a residue and dissolved in MeOH, affording a dark green solution. In air, one equivalent of **H_2L** in DCM with an excess of NEt_3 was added to the solution of $NpO_2Cl_2{\bullet}nH_2O$, resulting in the formation of an intense dark

brown/black solution, characteristic of complexation. Layering with pentane yielded black X-ray quality crystals overnight of **$NpO_2L(MeOH)$**. Single-crystal X-ray diffraction studies reveal the structure to be isomorphous with the U analog, **$UO_2L(MeOH)$**. However unlike the U analog, a second product was not observed, e.g. the protonated ligand forming **$NpO_2Cl_2(H_2L)$**. **$NpO_2L(MeOH)$** crystallizes in the $P2_1/c$ space group, forming a 7-coordinate pentagonal bipyramid geometry, **Figure 4.6**. The average Np−O_L and Np−N bond lengths are 2.266(2) and 2.530(3) Å, respectively, which are comparable to **NpO_2(salen)(MeOH), Table D.2**.[36] The average Np≡O_{yl} bond distance is 1.762(2) Å, with an angle of 179.2(1)°. The Np^{6+} ion is coordinated to the tetradentate N_2O_2 cavity of the ligand, where the ligands bend from the equatorial plane by 53° into the shape of a soft taco, similar to the **$UO_2L(MeOH)$** analog. This is unlike the other NpO_2 salen complexes due to the rigid backbone of the salophen ligand.

Attempted synthesis of $(NpO_2L)_x^{n-}$ complex. The $(NpO_2)^+$ analog was synthesized by the reduction of **$NpO_2L(MeOH)$** in DMSO, producing a yellow solution. Attempts to crystallized by vapor diffusion with benzene followed by further additions of 15-crown-5 were unsuccessful and resulted in brown powder. An attempt was made to prepare a $(NpO_2)^+$ complex. It is difficult to model Np^{5+} chemistry as well as Np^{6+} and Np^{4+} where U, Pu, and in the case of M^{4+}, Ce, Th can be utilized to understand the synthesis and crystallization of a complex. Np^{5+} shows significantly more stability than its $(AnO_2)^+$ analogs Pu, U. However, it is difficult to predict the properties a Np^{5+} complex will exhibit while carefully planning out use of these precious elements. Preparation of $NpO_2(NO_3)\bullet nH_2O$ through oxidation of Np as a mixture of oxidation states with $NaNO_{2(aq)}$ in dilute HNO_3 cleanly provided a source of $(NpO_2)^+$, as confirmed by UV/vis/NIR spectroscopy. Here it is important to note the use of $Np(NO_3)_4$ in dilute HNO_3 rather than $NpCl_4$ in dilute HCl to avoid the reaction of $NaNO_2$ with HCl. $NpO_2(NO_3)\bullet nH_2O$ was dried to a residue and dissolved in MeOH, affording a pale blue/green solution. In air, one equivalent of **H_2L** in DCM with an excess of NaOH was added to the solution, resulting in the formation of an intense dark brown/black solution. 15-crown-5 was added to encapsulate the Na+ ion(s), or an attempted cation exchange with PPh_4Cl to add crystallinity. These methods did not yield X-ray quality crystals, nor did slow evaporation, however analysis by ^1H NMR spectroscopy and solution phase UV/vis/NIR suggested the presence of a single $(NpO_2)^+$ complex. Several attempts were made to grow single crystals for X-ray diffraction, including standing in THF or pyridine, as well as layering with pentane or ether

did not yield single crystals that contained Np, a small amount of crystals were isolated from neat pyridine and were analyzed to be Na(15-crown-5)NO_3 by X-ray crystallography. Additionally, attempted crystallization of spectroscopy samples in DMSO-d_6 layered with benzene, 1,4-Dioxane or CCl_4 did not yield solids.

The $(PuO_2)^{2+}$ analog was also attempted using a similar synthesis for **NpO_2L(MeOH)**. Briefly, a solution of $PuCl_3$ in 2 M HCl was bubbled with O_3 overnight to yield PuO_2Cl_2•nH_2O with a color change from blue to pink. The oxidation state of pure Pu^{6+} was confirmed via solution UV/vis. PuO_2Cl_2•nH_2O was dried to a residue and dissolved in MeOH, affording a dark green solution. In air, one equivalent of **H_2L** in DCM with an excess of NEt_3 was added to the solution of PuO_2Cl_2•nH_2O, resulting in the formation of an intense dark brown/black solution, characteristic of complexation. Layering with pentane produced a brown/black precipitation overnight.

4.3.3 Spectroscopy and electrochemistry

Solid-state UV/vis/NIR spectrum of **NpL_2** reveals an intense broad band with λ_{max} 493 accounting for the orange coloration of the crystals, **Figure 4.7**. The weaker absorptions between 500 and 1300 nm are assigned to Laporte-forbidden 5*f*→5*f* transitions, characteristic of the tetravalent state.[1] Solution-phase UV/vis/NIR in toluene reveals an intense broad band similar to the other reported **ML_2** (M = U, Th, Ce, Hf, Zr,) complexes, however despite attempts to measure more concentrated solutions, no 5*f*→5*f* peaks were observed. A similar event was observed with **UL_2**, likely due to the intense absorption of the charge transfer band.[98]

Solid-state and solution-phase UV/vis/NIR spectra of **NpO_2L(MeOH)** also reveal an intense broad band with λ_{max} 473 nm that continues into the NIR region accounting for its intense dark color. The characteristic $(NpO_2)^{2+}$ peak at 1223 nm remains absent in both spectra, yet remains unknown why. Previous studies have found that the behavior of Np^{6+} in organic solvents changes its dissolution, producing various amounts of Np^{5+} that contribute to the presence of the Np^{5+} peak at 980 nm (reported ε = 395 $Lmol^{-1}cm^{-1}$).[1,111] However this peak remains absent as well.

As observed in the previous study, the ligand is redox active and exhibits quasi-reversible behavior with several oxidation and reduction peaks. The cyclic voltammogram (CV) of **NpL_2** highlights the ligand-based reduction peak at E = −2.21 V (vs. Fc/Fc^+) and the metal-based

Np^{4+}/Np^{3+} reduction peak at $E = -2.91$ V (vs. Fc/Fc^{+}), **Figure 4.8**. Np^{4+} is stabilized by complexation, yet shows irreversible behavior, similar to the previously reported **CeL$_2$** complex.[97] A small half peak at $E = \sim -2.49$ V was observed in the CV and is attributed to an unknown impurity. No features were observed when scanned cathodically within the solvent window.

The redox couple of **NpO$_2$L(MeOH)** was found to tolerate a large number of sans and a wide scan rate range (0.025–5 V/s), with an $E_{1/2}$ of −0.612 V (vs. Fc/Fc^{+}), **Figure 4.9**.
The diffusion coefficient (D) for **NpO$_2$L(MeOH)** was calculated using the Randles-Sevcik equation,[112,113] by plotting the peak current (i_p) vs. the square root of the scan rate ($v^{1/2}$), **Figure 4.10**:

$$i_p = 0.4463nFAC^0\left(\frac{nF\nu D}{RT}\right)^{1/2} \qquad \textbf{Eq. 4.1}$$

where n, A, and C^0, are the electron stoichiometry in the rate determining process, surface area of the working electrode, and concentration of the oxidant, respectively. Rearranging,

$$D = \left(\frac{slope}{0.4463nFAC}\right)^2 \left(\frac{RT}{nF}\right)$$

Estimating the heterogeneous electron transfer constant, k^0 is of primary interest when the performance of electrode materials are examined. This allows for an indication of the speed of electron transfer between an electroactive species and an electrode surface. The Nicholson method used here has been simplified by Lavagnini et al.,[114,115] and utilizes the link between the Nicholson parameter and k^0 by investigating the peak to peak separation (ΔE_p), **Table D.4**:

$$\Psi = \frac{-0.6288 + 0.0021(\Delta E_p)}{1 - 0.017(\Delta E_p)} \qquad \textbf{(Eq. 4.2)}$$

which allows for the estimation of the heterogeneous electron transfer rate constant (k^0):

$$\Psi = k^0\left(\frac{\pi DnF\nu}{RT}\right)^{-1/2} \qquad \textbf{(Eq. 4.3)}$$

Through mathematical manipulation, k^0 is taken directly from the slope of the graph of Ψ vs. $\left(\frac{\pi DnF\nu}{RT}\right)^{-1/2}$. This method only works for quasi reversible systems, since it relies upon the fact that as the ΔE_p increases, the scan rate increases because the rate of mass transport becomes quicker or equal in rate as the electron transfer.

For a scan range up to 400 mV/s, D is estimated 2.18×10^{-8} cm^2/s, smaller compared to other UO_2(salophen) complexes including **UO$_2$L(MeOH)**. The resulting k^0 is estimated to be

2.14×10^{-4} cm/s, compatible with the range $(3.0–5.3) \times 10^{-2} > k^0 > (0.73–1.3) \times 10^{-6}$ and also comparable to other quasi-reversible uranyl complexes in DMSO.[79,88,89]

4.4 Conclusion

Two new Np Schiff base complexes have been synthesized in the forms **NpL_2** and **$NpO_2L(MeOH)$**. **NpL_2** is isomorphous to the tetravalent **ML_2** (M = Ce, Pu, Th, U) series, forming an 8-coordinate distorted anti-square prism. Cyclic voltammetry reveals an irreversible metal-based reduction peak at –2.9 V (vs. Fc/Fc^+), similar to **CeL_2**. **$NpO_2L(MeOH)$** is isomorphous to the uranyl analog, however does not form the expected neutral ligand adduct "**$NpO_2Cl(H_2L)$**." Electrochemical experiments directly compare to the uranyl complex, showing the greater stabilization of UO_2^{2+} compared to NpO_2^{2+}.

4.5 Figures

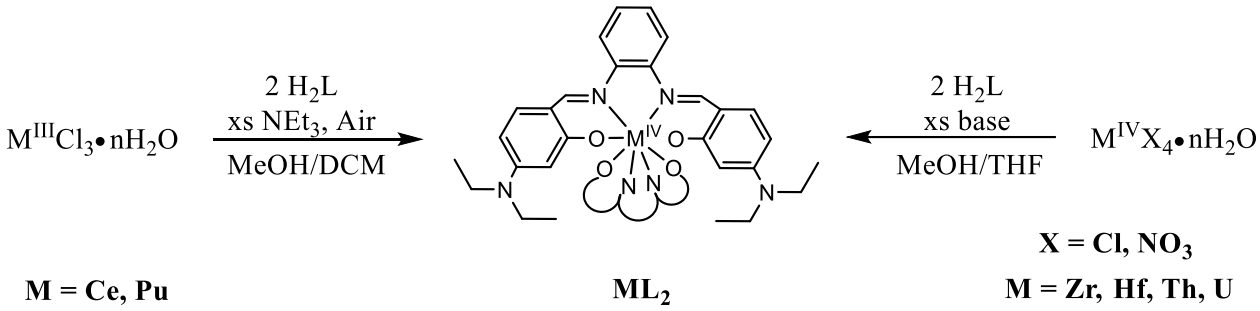

Figure 4.1. Synthesis of **ML_2** (M = Pu, U, Th, Ce, Hf, Zr).

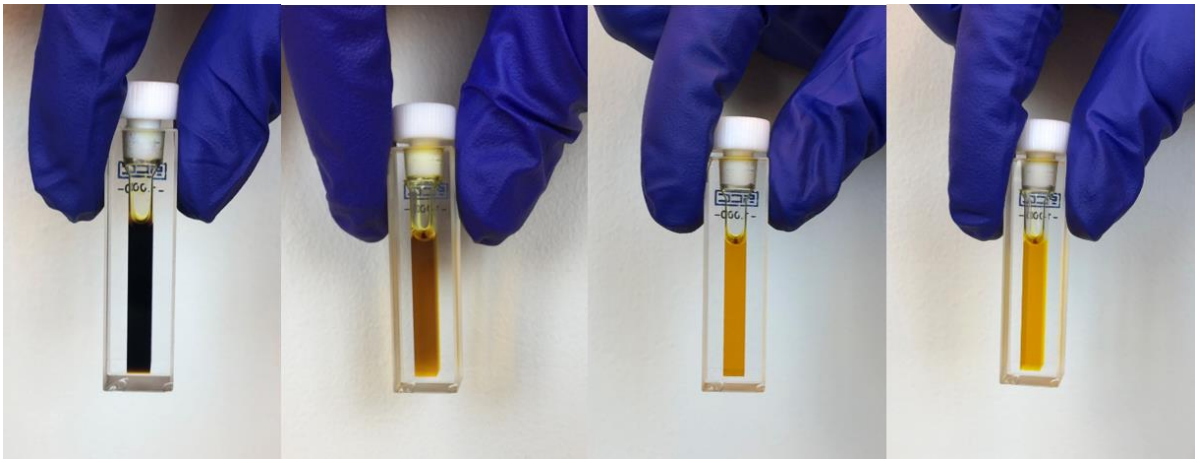

Figure 4.2. Photographs of 4.75 mM **$NpO_2L(MeOH)$** in DMSO-*d6* (left) with excess additions of $NaNO_2$ and NH_2OH, showing the reduction of $(NpO_2)^{2+}$ to $(NpO_2)^{+}$ in solution over time (progressing right).

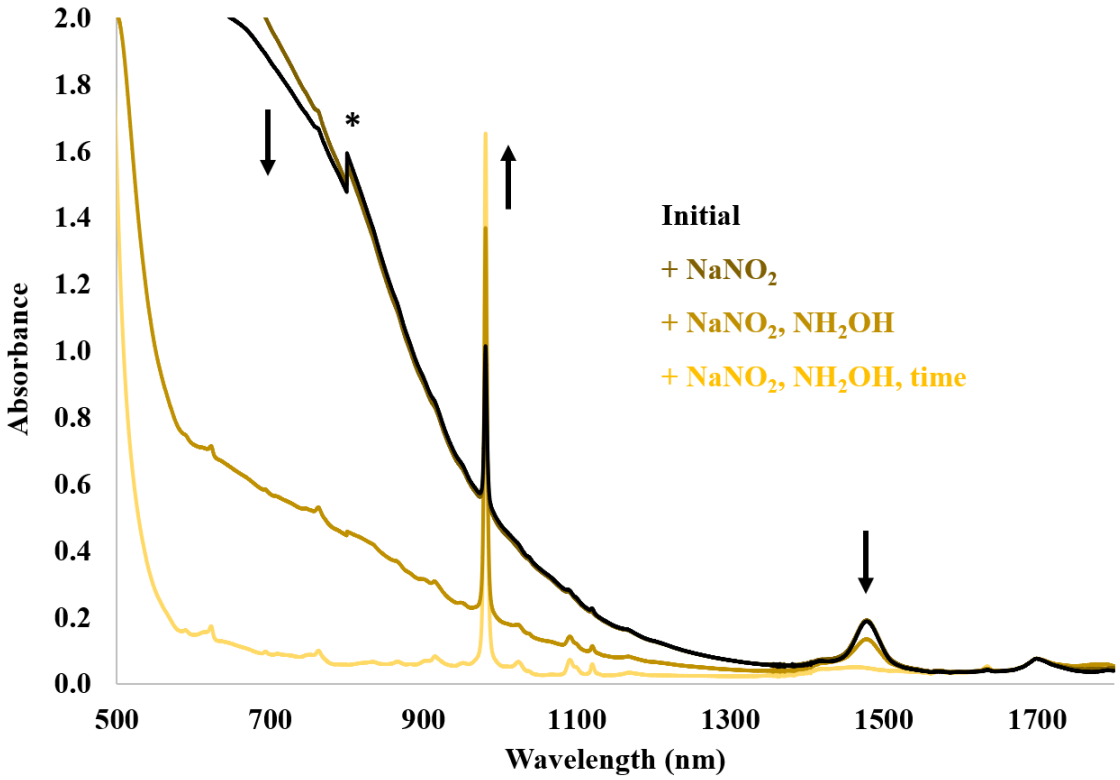

Figure 4.3. Solution-phase UV/vis/NIR of 4.75 mM **$NpO_2L(MeOH)$** in DMSO-d_6, with additions of $NaNO_2$ and NH_2OH for reduction to $(NpO_2)^+$. *denotes detector change, arrows indicating growth and decrease in absorbance.

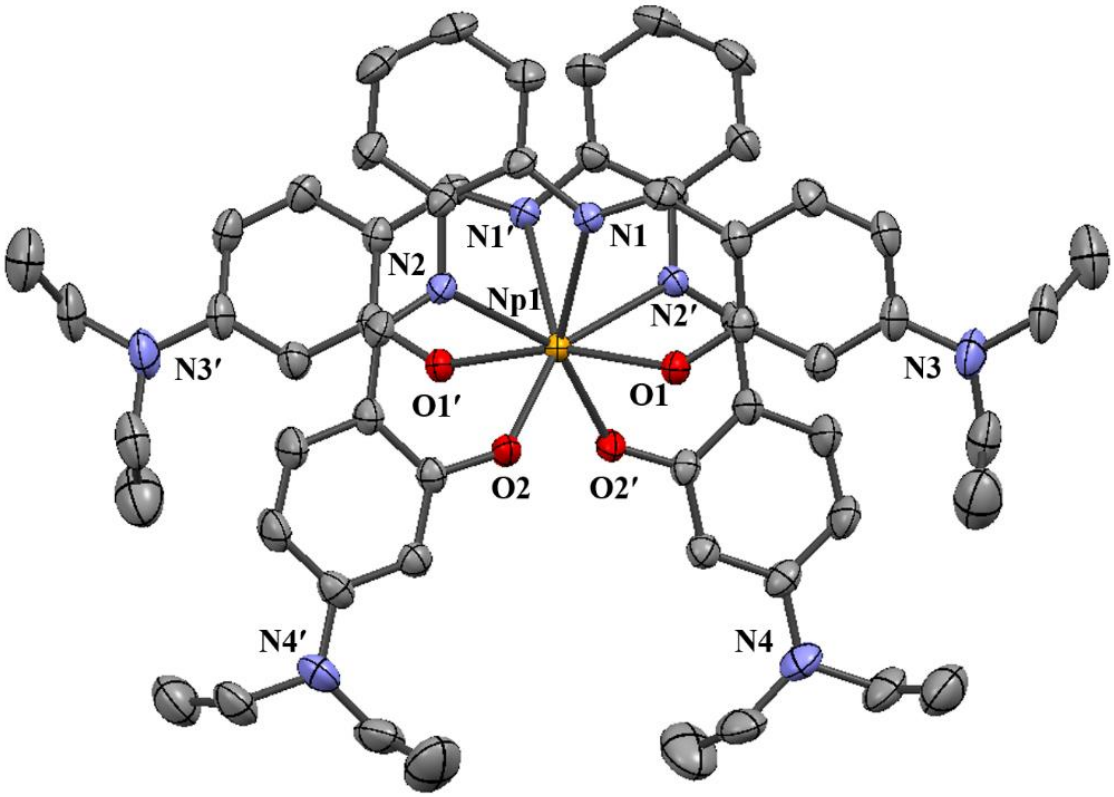

Figure 4.4. Molecular structure of **NpL$_2$** drawn at the 50% probability level with hydrogen atoms and lattice solvent omitted for clarity.

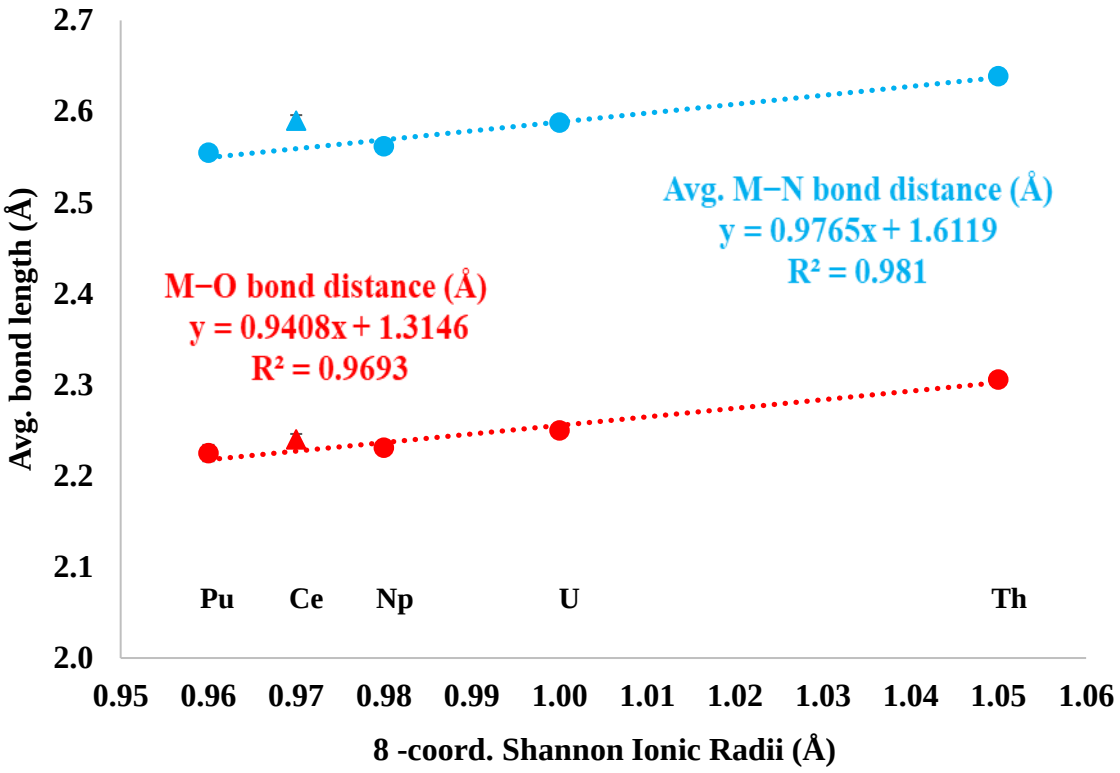

Figure 4.5. Plot of the mean M−N (blue) and M−O (red) bond distances (Å) in **ML$_2$** (M = Pu, Ce, Np, U, Th) relative to the 8-coordinate Shannon ionic radius. Error bars calculated from the 3 σ standard deviation in the mean distance of M−N and M−O bonds. Trendlines calculated from actinide data.

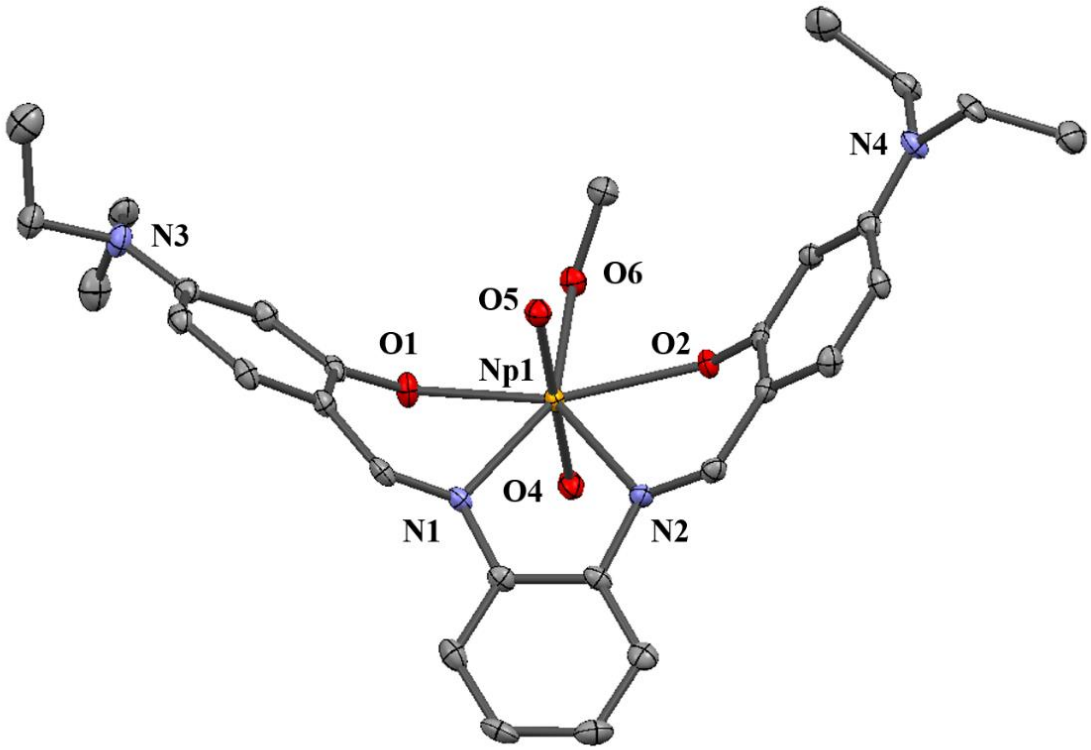

Figure 4.6. Molecular structure of **$NpO_2L(MeOH)$** drawn at the 50% probability level with hydrogen atoms and lattice solvent omitted for clarity.

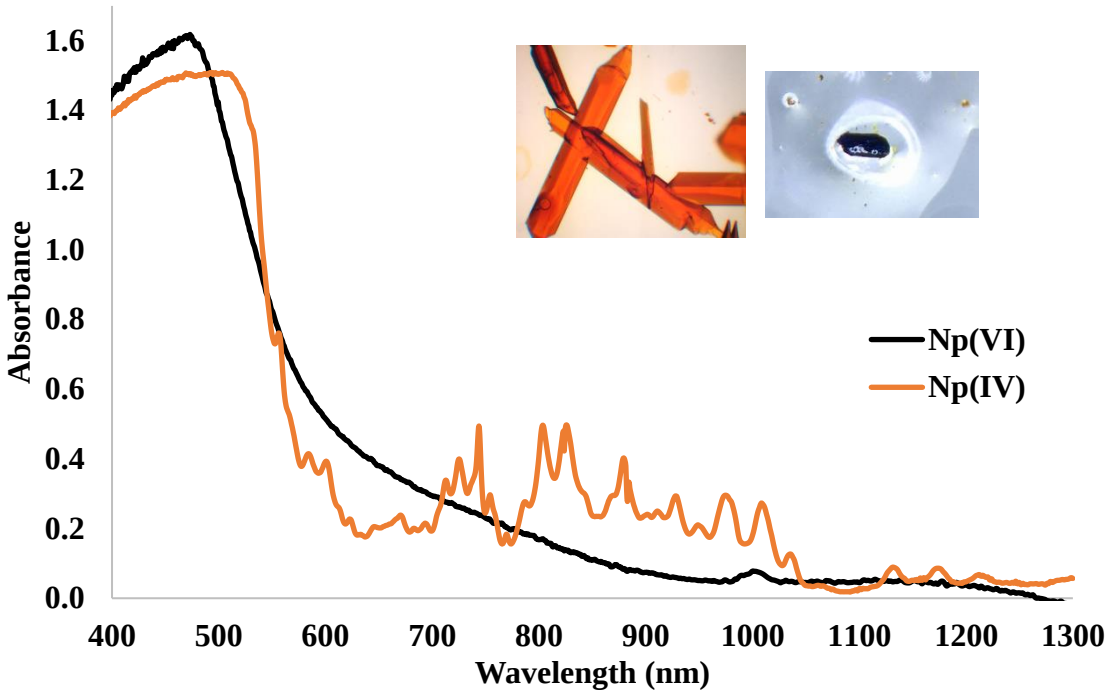

Figure 4.7. Solid state UV/vis/NIR absorbance spectra and images of NpL_2 (orange) and **$NpO_2L(MeOH)$** (black).

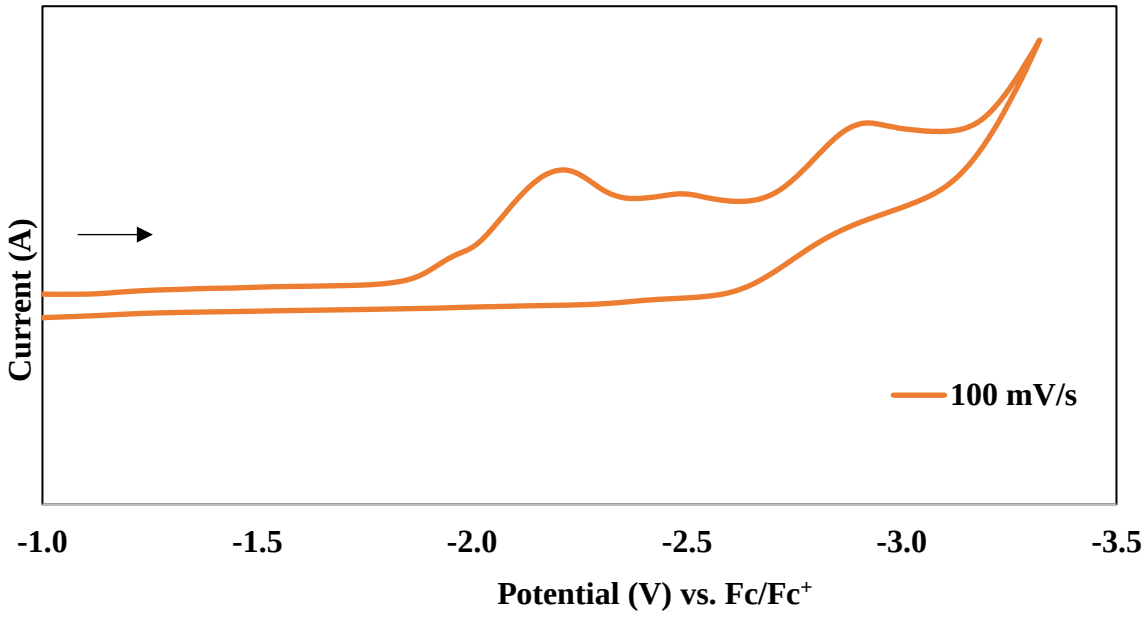

Figure 4.8. CV of 5 mM **NpL_2** at a scan rate of 100 mV/s in DMSO with a 0.2 M [TBA][PF_6] supporting electrolyte.

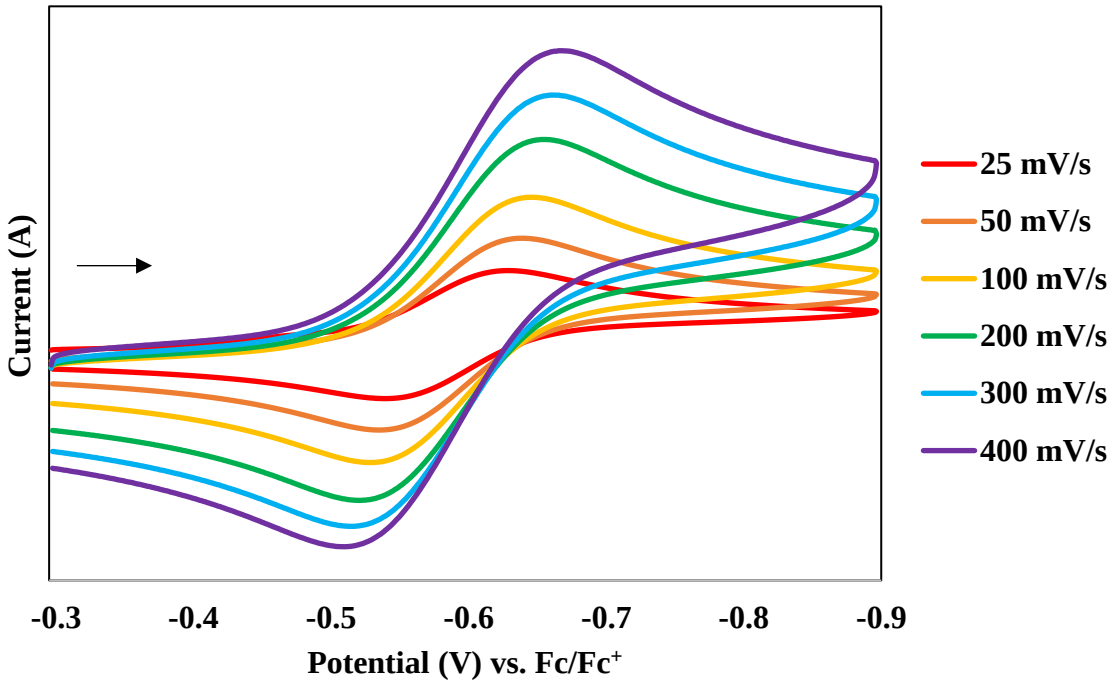

Figure 4.9. CVs of 5 mM **$NpO_2L(MeOH)$** in DMSO with 0.2 M [TBA][PF_6] at various scan rates (0.025–0.4 V/s) showing the stability and relative peak separations.

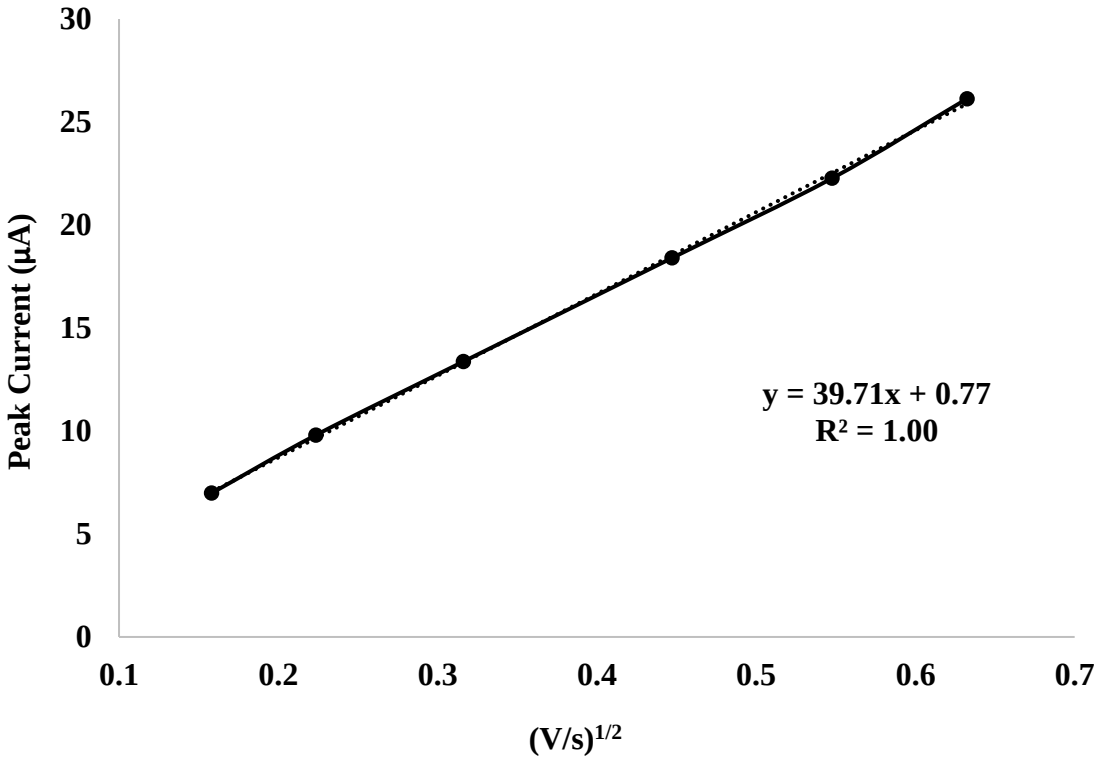

Figure 4.10. A plot of the (scan rate)$^{1/2}$ and value of cathodic peak currents show a linear relationship, allowing a calculation of D = 2.18 × 10^{-8} cm^2/s for **$NpO_2L(MeOH)$**.

CHAPTER 5
BIMETALLIC SCHIFF BASE COORDINATION COMPLEXES

5.1 Introduction

Understanding the complexation chemistry of americium and other actinide elements has important implications in nuclear energy and related processes. In the development of nuclear energy, spent nuclear fuel in storage is accumulating at a rate of 7,000 t/year, with long-term potential radioactivity threats to the environment. Although the PUREX (**P**lutonium **U**ranium **Re**dox **E**xtraction) process recovers 99.5% of uranium and plutonium from the spent nuclear fuel is well established, the remaining high-level radioactive liquid waste (HLLW) contains most of the fission products and minor actinides (americium, curium) that are the main contributors of radiotoxicity. Partitioning these minor actinides from HLLW and transmuting them into short-lived stable nuclides can reduce the time isolated from the environment from more than 20,000 years to ~400. Approximately 1/3 of the fission products include lanthanides, some of which with large neutron absorption cross sections, act as neutron poisons, and should be separated prior to the transmutation step.

The minor actinides and lanthanides exist primarily as trivalent cations in solution with comparable radii and coordination numbers, providing separation to be difficult and requires high selectivity for the separation materials or ligands. Current studies on americium coordination behavior lags far behind that of transition metal, lanthanide, and the early actinides. This provides us the opportunity to better understand the structural preferences, reactivity, and photophysical properties of americium coordination complexes.

Metal-salen Schiff base complexes have been widely used across the periodic table with a wide range of applications for their ability to stabilize unusual oxidation states of metal ions. These metal complexes are of particular interest for their antibacterial, magnetic, photophysical and chromophoric properties. Recently, salen-type ligands have been utilized to stabilize heteronuclear 3*d*-4*f* complexes. While many studies have focuses on their magnetic behavior, relatively few have described the photophysical properties of the compounds. For lanthanide and actinide ions, *f*→*f* transitions are parity forbidden causing the absorption coefficients to be very low with slow emissive rates compared to transition metals. Previous studies have shown that by

incorporating Zn, the complex will act as a sensitizer to excite lanthanide ions, amplifying their luminescent behavior.

The Schiff base ligand *N,N′*–bis[(4,4'-diethylamino)salicylidene]-1,2-phenylenediamine (**H_2L**) has previously been reported with several tetravalent metals as the homoleptic **ML_2** (M = Pu, Ce, Np, U, Th, Zr, Hf) and hexavalent actinyl complexes **$MO_2L(MeOH)$** (M = Np, U) complexes. To better understand the coordination behavior and photophysical properties of americium and its lanthanide analogs, we have investigated and reported a series of heterobimetallic Schiff base complexes by crystallographic and spectroscopic methods.

5.2 Experimental

5.2.1 General considerations and instrumentation

Caution! ^{243}Am ($t_{1/2}$ = 7,370 years, specific activity = 0.2 Ci g^{-1}) represents a serious health risk due to its strong α (5.27 MeV), and γ (74 keV) emissions, as well as its daughters. All studies with ^{243}Am were conducted in a laboratory dedicated to studies on transuranium elements.

All manipulations were conducted in a well ventilated fume hood. Solvents used for manipulations in air including MeOH (Sigma), DCM (Sigma), pentane (Sigma), trimethylamine (Sigma) were used as received. The following compounds were purchased reagent grade from commercial sources and used as received $Zn(NO_3)_2•6H_2O$ (Sigma) and $CDCl_3$ (Sigma). $LnBr_3•xH_2O$ (Ln = Ce, Nd, Sm, Eu, Gd, Dy, Er) was prepared by reactions of Ln_2O_3 (Sigma) with HBr (Sigma). *N,N′*–bis[(4,4'-diethylamino)salicylidene]-1,2-phenylenediamine (**H_2L**) were prepared according to literature. ^{243}Am was recovered from residues that had been used in previous experiments. A chemically pure ^{243}Am stock solution was prepared using well-established dissolution/separation procedures previously reported.[6] The resulting $AmCl_3$ hydratewas dried to a residue and dissolved in concentrated HBr to yield $AmBr_3$ hydrate.

UV/vis/NIR spectroscopic data were obtained from single crystals using a CRAIC Technologies UV/vis/NIR microspectrophotometer. Crystals were placed on glass slides in immersion oil and data were collected from 350 nm to 1300 nm. Single crystals selected for data collection were mounted on a MITOGEN mount™ cryoloop and optically aligned on a Bruker D8 Quest X-ray diffractometer. Crystallographic data was collected at room temperature using a

Mo-Kα (λ = 0.71069 Å) X-ray micro source and a CMOS detector. The unit cell determination and subsequent data collection was performed using the APEX III software.[40] Raw data frames were processed using SAINT[41] and SADABS.[42] Subsequent calculations were carried out using the OLEX 2 program.[43] Structures were solved by ShelXL and refined by least squares on F^2 techniques.

5.2.2 Synthesis

$Am(ZnL)_2(NO_3)_2Br(H_2O)$, (1-Am). In the open atmosphere H_2L (10 mg, 0.022 mmol) and NEt_3 (0.10 mL) in DCM (0.25 mL) were added to a solution of $Zn(NO_3)_2$•$6H_2O$ (6.6 mg, 0.022 mmol) in methanol (0.25 mL). A solution of $^{243}AmBr_3$•nH_2O (5.2 mg, 0.012 mmol ^{243}Am metal content) in methanol (0.25 mL) was added affording a color change to dark orange. After 2 hrs at room temperature, X-ray quality orange plate crystals were isolated, washed with methanol and dried in air. UV/vis/NIR (solid state): λ_{max} = 510 nm.

General Synthesis of **$Ln(ZnL)_2(NO_3)_2Br(H_2O)$, (1-Ln)**. In the open atmosphere H_2L (10 mg, 0.022 mmol) and NEt_3 (0.10 mL) in DCM (0.25 mL) were added to a solution of $Zn(NO_3)_2$•$6H_2O$ (6.6 mg, 0.022 mmol) in methanol (0.25 mL). A solution of $LnBr_3$•xH_2O (0.011 mmol) in methanol (0.25 mL) was added affording a color change to dark orange. After 2 hrs at room temperature, X-ray quality crystals were isolated as orange plates, washed with methanol and dried in air.

1-Ce. UV/vis/NIR (solid state): λ_{max} = 492 nm.

1-Nd. UV/vis/NIR (solid state): λ_{max} = 497 nm. Anal. Calc'd for $C_{56}H_{74}N_{10}O_{15}BrZn_2Nd$: C, 45.38; H, 5.03; N, 9.45. Found: C, 45.88; H, 4.96; N, 8.99.

1-Sm. UV/vis/NIR (solid state): λ_{max} = 515 nm.

1-Eu. UV/vis/NIR (solid state): λ_{max} = 523 nm. Anal. Calc'd for $C_{56}H_{74}N_{10}O_{15}BrZn_2Eu$: C, 45.14; H, 5.01; N, 9.40. Found: C, 45.18; H, 4.89; N, 8.96.

1-Gd. UV/vis/NIR (solid state): λ_{max} = 504 nm.

1-Dy. UV/vis/NIR (solid state): λ_{max} = 511 nm

1-Er. UV/vis/NIR (solid state): λ_{max} = 514 nm

5.3 Results and Discussion

5.3.1 Crystallography

Briefly, in air, addition of one equivalents of **H_2L** in DCM with an excess of triethylamine, to a solution of $Zn(NO_3)_2$•$6H_2O$ in MeOH results in the formation of orange solution. Half an equivalent of $AmBr_3$•xH_2O in MeOH was added with a slight color change to dark orange. Vapor diffusion with pentane at ambient temperature (ca. 23 °C) gave orange X-ray quality crystals of **1-Am** overnight, **Figure 5.4**. Single crystal X-ray diffraction studies reveal the structure crystallizes in the monoclinic *C*2/*c* space group. The Zn cations are bound to the inner N_2O_2 pocket of the ligand, forming two ZnL units with a fifth ligand that is either a Br^- atom or a H_2O molecule forming a square pyramidal geometry. The ZnL units are approximately parallel to each other, with Am^{3+} bound to the phenolic oxygens of the ligand, with two κ2 NO3's forming an eight-coordinate distorted square anti-prism. This geometry is an unusual crystallographic example of an eight-coordinate americium complex. **Figures 5.5, 5.6.**

To prepare for the synthesis of **1-Am**, the synthesis of several lanthanides was performed to help understand the synthetic scope of the experiment and test the generality of the experiment across several different sized lanthanides. Therefore the synthesis of **1-Ln, (Ln = Ce, Nd, Sm, Eu, Gd, Dy, Er)** was performed in a similar manner to **1-Am**. All of the 1-Ln complexes are the same bright orange color, except **1-Ce**, which formed a dark brown/orange solution similar to **1-Am**. Vapor diffusion with pentane yielded orange plate-like crystals overnight. Single crystal X-ray analysis determined **1-Ln** (Ln = Ce, Nd, Sm, Eu, Gd, Dy, Er) to be isomorphous across the series and with **1-Am**

The average M–O_L, M···Zn, Zn(1)–Zn(2) (M = Am, Ln) distances and Zn(1)–M–Zn(2) angles are listed in **Table E.1**. The Zn(1)–M–Zn(2) angles follow a periodic trend with the largest being **1-Ce** , 3.4800(6)°, and smallest for **1-Er**, 3.3530(1)°, **Figure 5.7**. The rotation of the two overlapping salophen ligands for complexes **1-M** [calculated from the average value of torsion angles between O(1)···O(2)^O(4)···O(3) and N(1)···N(2)^N(4)···N(3)] is largest for 1-Ce**,** 36.5°, and smallest for **1-Er,** 36.0°, following the same trend as **ML_2** (M = Pu, Ce, Np, U, Th). The eight-coordinate Am^{3+} and Nd^{3+} have the same Shannon ionic radii (1.09 Å), allowing for a direct comparison between their structures. The M–O_L bond distance is significantly shorter for **1-Nd**, 2.356(1) Å, compared to **1-Am**, 2.384(1) Å. This is also observed in the larger Zn(1)–M–Zn(2)

angle for **1-Nd**, 83.49(2)°, vs **1-Am**, 83.14(8)°, where the neodymium atom sits closer between the zinc atoms

Further attempts to crystallize other transition metal-lanthanide analogs, e.g. **Ln(TML)$_2$(NO$_3$)$_2$Br(H$_2$O)** (TM^{2+} = V, Cr, Mn, Fe, Co, Ni, Cu) were unsuccessful. Many of these trials yielded poor quality crystals to perform single crystal X-ray diffraction experiments. On occasion when X-ray quality crystals were isolated they were devoid of lanthanide and were determined to be the known TM(L) structure (TM = Ni, Cu).

5.3.2 Spectroscopy

The solid state UV/vis/NIR spectrum of **1-Am** reveals an intense broad charge transfer band with λ_{max} at 510 nm accounting for the intense orange coloring of the crystal, **Figure 5.8**. Typically, these Schiff base complexes provide large charge transfer bands. Previously, solution UV/vis/NIR spectroscopy of **ML$_2$** (M = Zr, Hf, Ce, Th, U) in toluene revealed an intense broad band with with ε values in the range of 190 000–240 000 (L mol^{-1} cm^{-1}).[98] The uranyl analogs have shown similarly large ε values in the range 88 000–118 000 (L mol^{-1} cm^{-1}).[110] While **1-Am** also exhibits weaker 5*f*→5*f* transitions of the trivalent state, the characteristic $^7F_0 \rightarrow {}^5L_6$ transition for Am^{3+} is hidden beneath the large charge transfer band. This feature is also observed in the lanthanide analogs, **1-Ln** (Ln = Ce, Nd, Sm, Eu, Gd, Dy, Er), **Figure 5.9**, with λ_{max} ranging 492–523 nm.

Previous studies have shown that salophen ligands can support strong solid state and solution phase fluorescence.[116,117] With this in mind, all of the complexes were checked for solid state fluorescence at room temperature and cooled to –180°C for **1-Am**. Unfortunately, none of the complexes examined here exhibited emissive properties. However, in the solution phase, **1-Eu** shows weak fluorescence at λ_{max} 536 when excited with 325 nm in DCM, **Figure 5.10**. The Eu^{3+} fluorescence at 613 nm is also present.

5.4 Conclusion

The bimetallic complexes 1-**M** (M = Ce, Nd, Am, Sm, Eu, Gd, Dy, Er) are isomorphous across the series, allowing for a direct comparison between americium and several lanthanides in an eight-coordinate environment. Zinc was the only transition metal that allowed the crystallographic characterization of the heterometallic complexes. The Zn–M–Zn angle and

Z···M distance is periodic, adjusting to the size of the cation and bond strength between M and O_L atoms. While americium and neodymium have the same eight-coordinate ionic radius, **1-Nd** has significantly shorter M–O bond lengths and larger Zn–M–Zn angle than **1-Am**. While none of the complexes exhibited emissive properties in the solid state, **1-Eu** showed weak fluorescence in the solution phase.

5.5 Figures

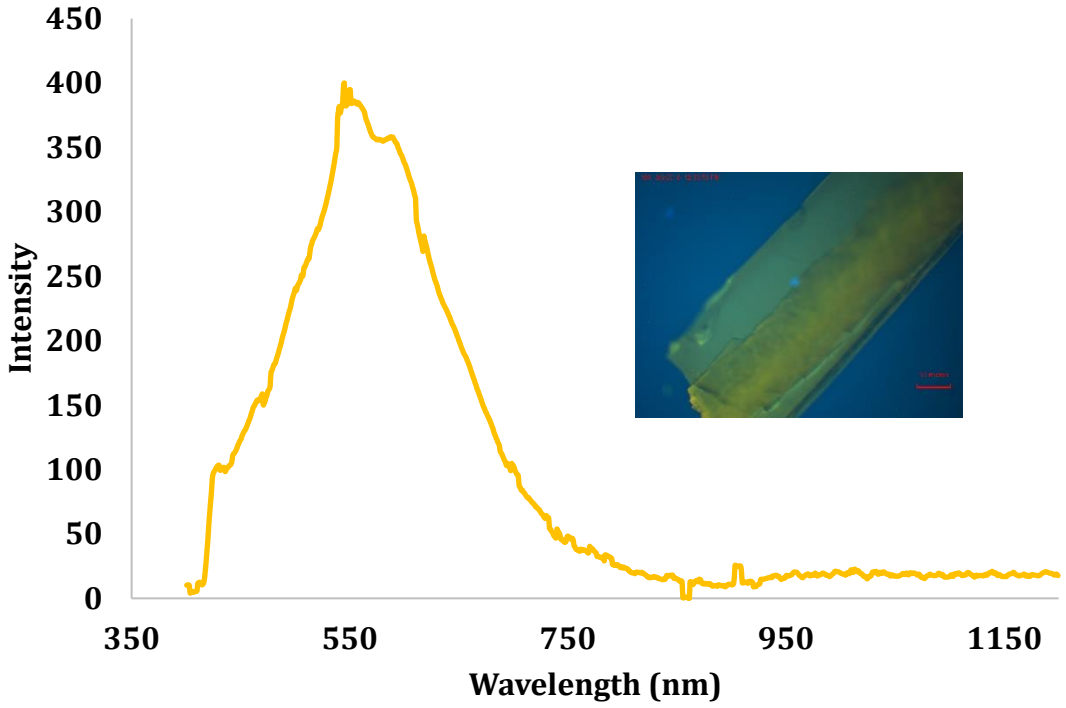

Figure 5.1. Solid-state luminescence of **H_2L** at room temperature, excited with 365 nm.

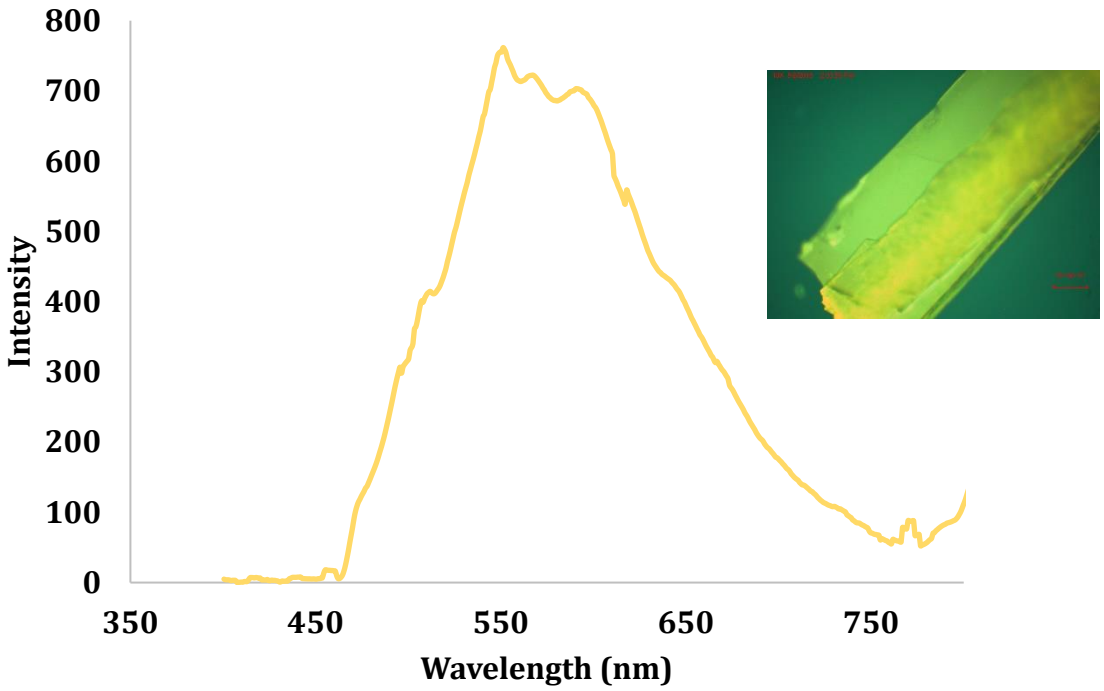

Figure 5.2. Solid-state luminescence of **H_2L** at room temperature, excited with 420 nm.

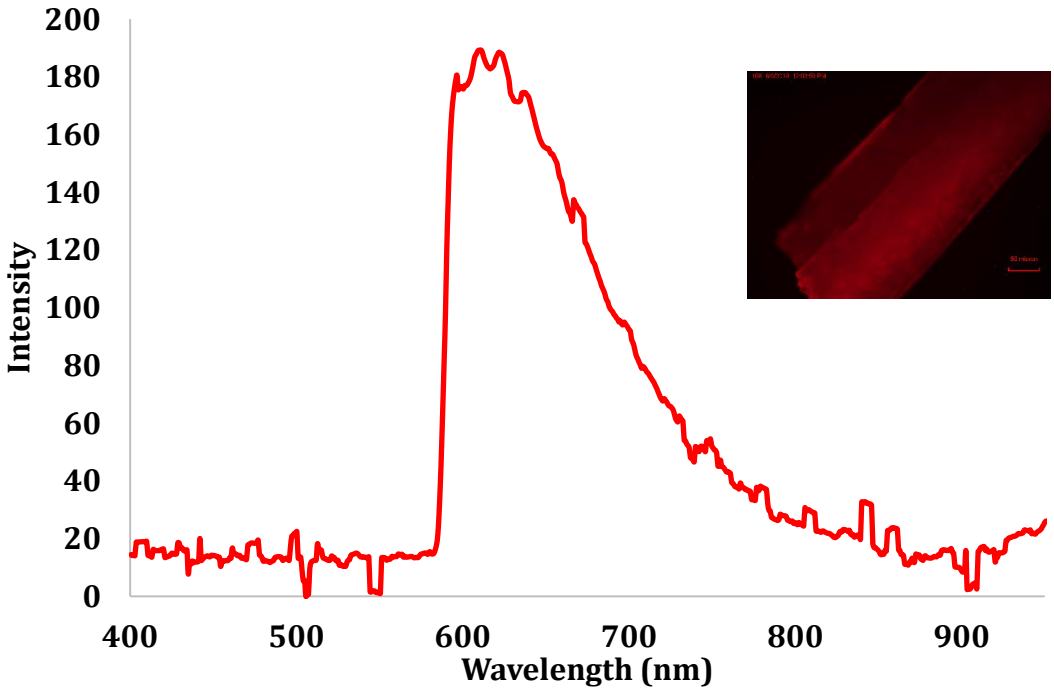

Figure 5.3. Solid-state luminescence of **H_2L** at room temperature, excited with 546 nm.

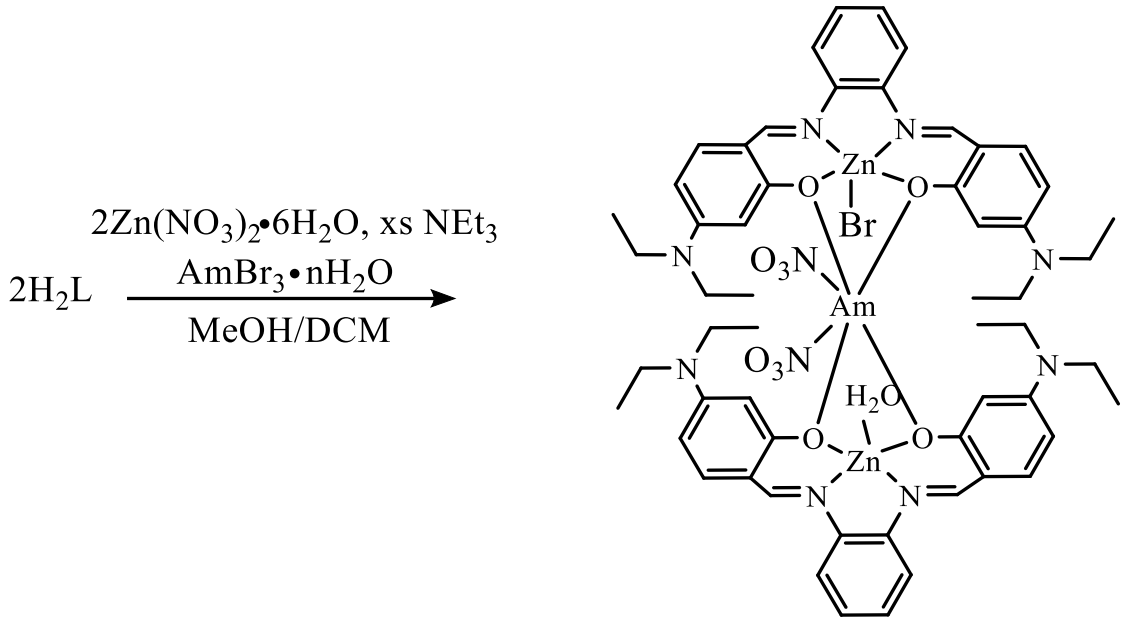

Figure 5.4. Synthesis of **1-Am**.

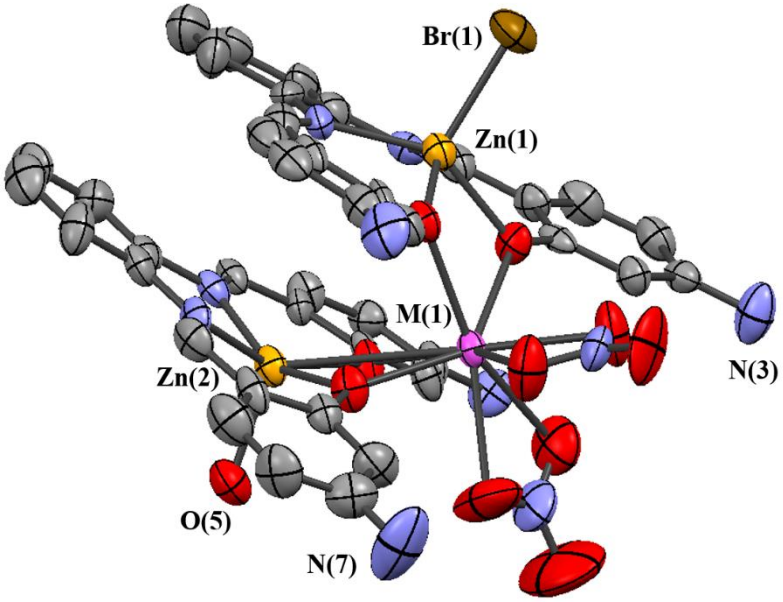

Figure 5.5. Molecular structure of **1-M** drawn at the 50% probability level with hydrogen atoms, ethyl groups, and lattice solvent omitted for clarity.

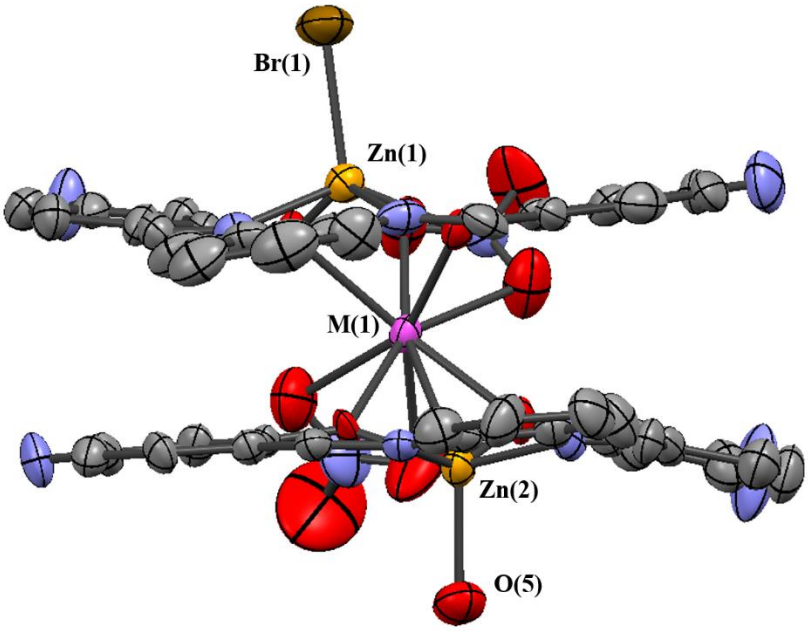

Figure 5.6. Molecular structure of **1-M** drawn at the 50% probability level with hydrogen atoms, ethyl groups, and lattice solvent omitted for clarity, displaying the sandwich geometry.

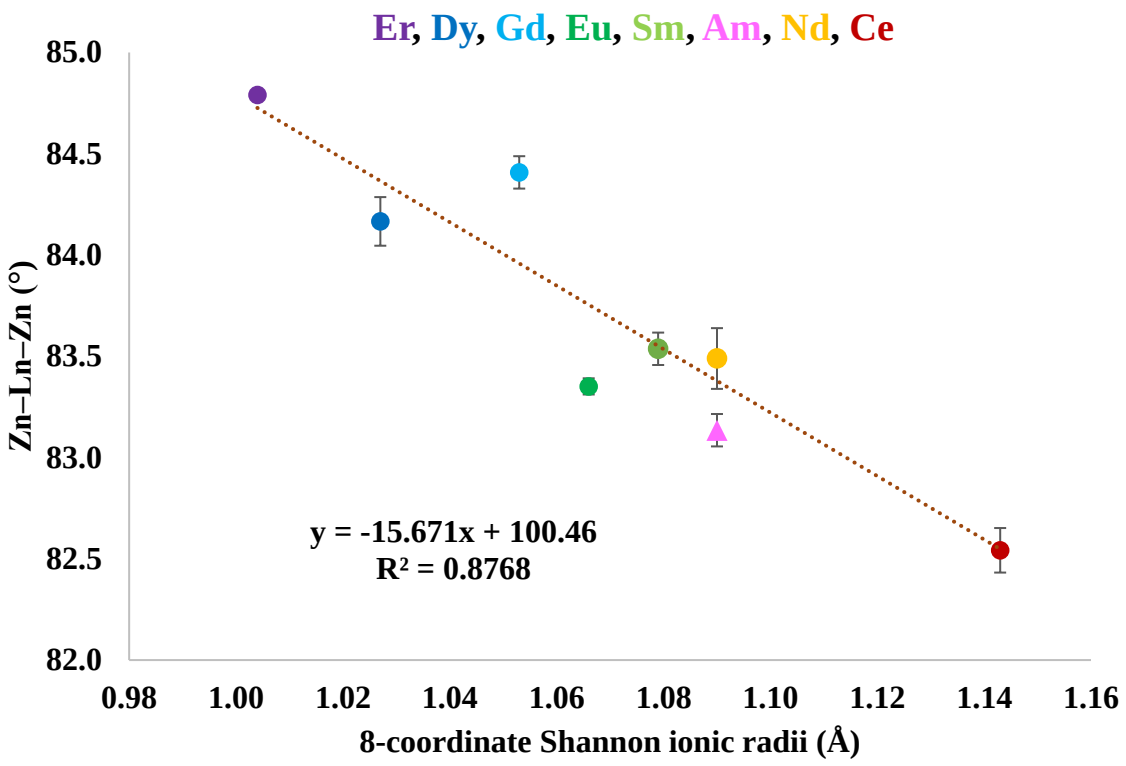

Figure 5.7. Zn–M–Zn angle vs. 8-coordinate Shannon ionic radii for **1-M (M = Ce, Nd, Am, Sm, Eu, Gd, Dy, Er)**. Error bars calculated from the 3σ standard deviation. Best fit line calculated from Ln data.

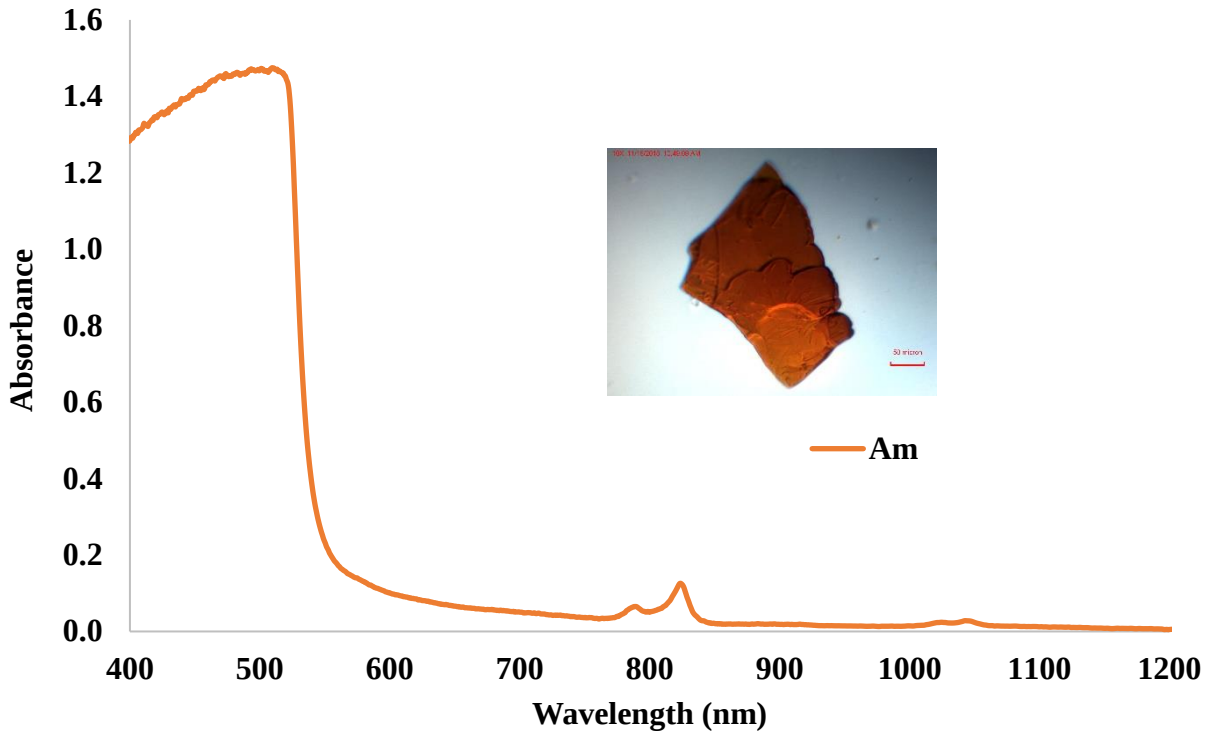

Figure 5.8. Solid-state UV/vis/NIR absorption spectrum at room temperature and photograph of **1-Am**.

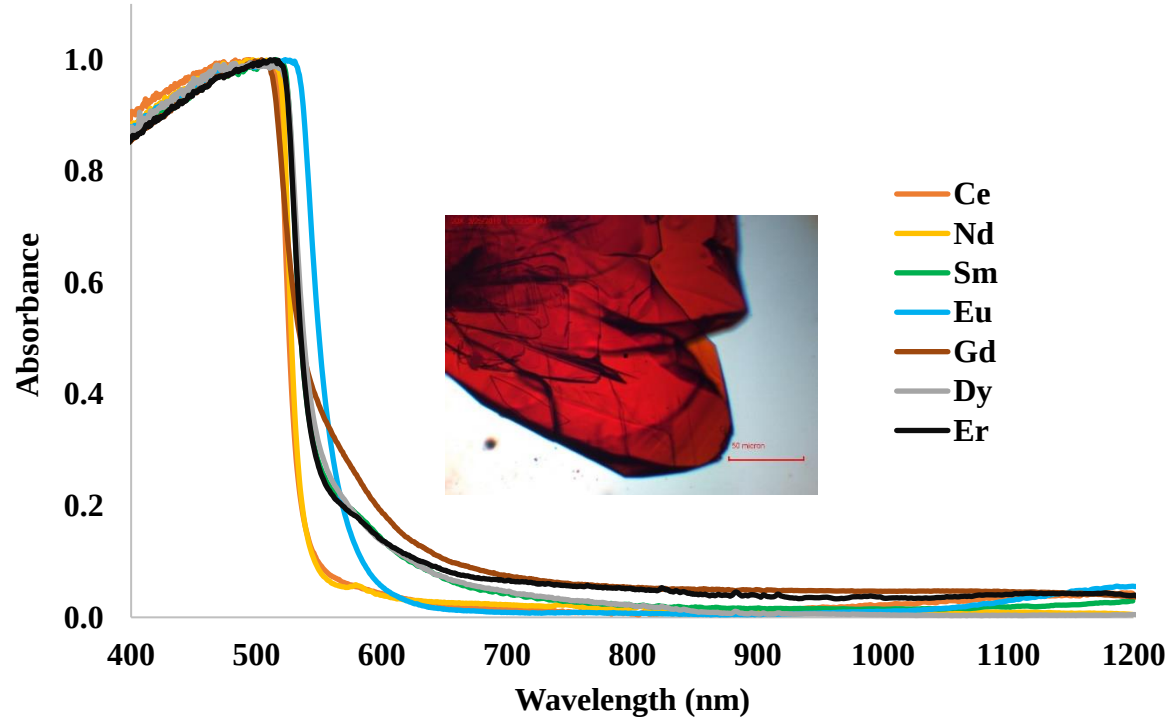

Figure 5.9. Solid-state UV/vis/NIR absorption spectra of **1-Ln** and photograph of **1-Dy** at room temperature, with absorbance normalized to 1.

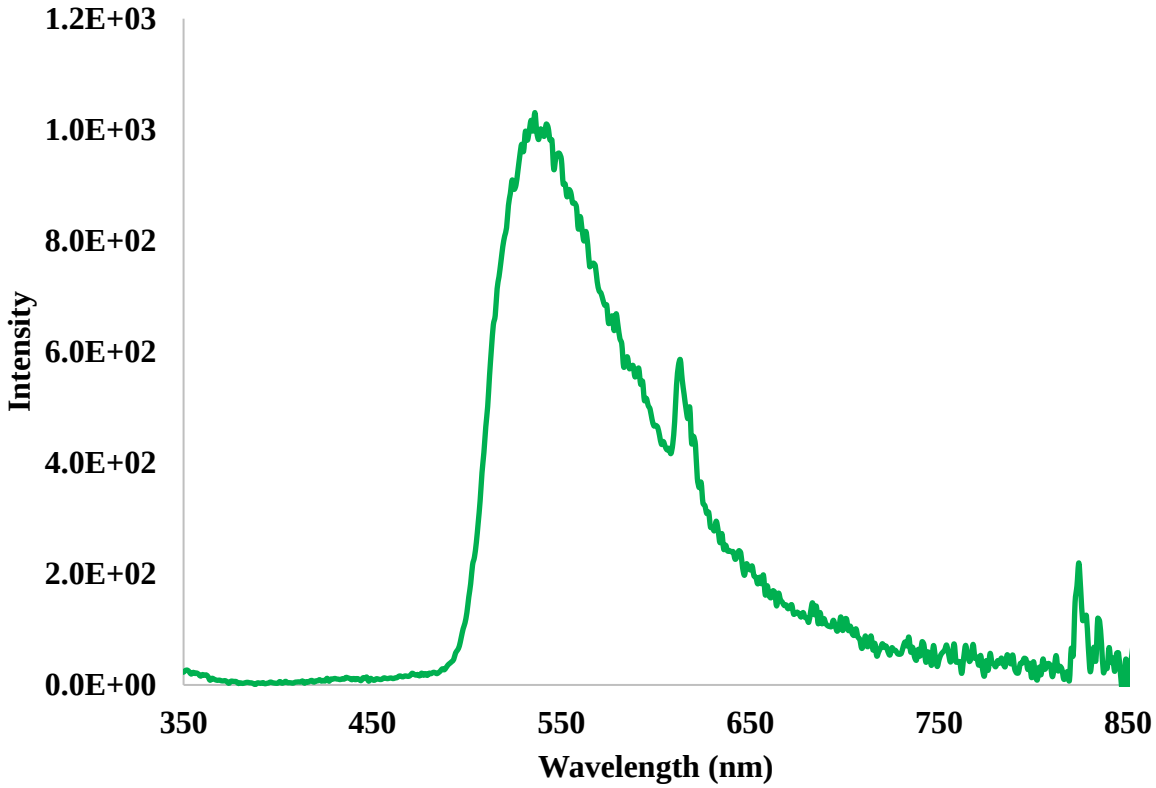

Figure 5.10. Room temperature solution phase emission spectrum of **1-Eu** in DCM with 325 nm excitation.

CHAPTER 6

CONTROLLING LANTHANIDES AS LEWIS ACID CATALYSTS TO GENERATE BIMETALLIC COMPLEXES

Adapted with permission by Bonnie E. Klamm, Thomas Albrecht-Schmitt, Ryan E. Baumbach, Brennan S. Billow, Frankie D. White, Stosh A. Kozimor, Brian L. Scott, and Aaron M. Tondreau. *Submitted to Inorg. Chem.*

6.1 Introduction

The selective complexation of lanthanide ions in coordination chemistry is important for many different areas including the design of metal complexes for diagnostic and imaging[118,119] applications, therapeutic agents,[120,121] and preparation of selective metal extractants for hydrometallurgy[122] and nuclear waste management.[50,91,123,124] However, the selective complexation of trivalent lanthanides is challenging due to their similar physical and chemical properties. According to the classification by Pearson,[125] they behave as Lewis acids of similar radii with a contraction of the ionic radius from La^{3+} to Lu^{3+} by only 16%. This size contraction, however, has been reported to affect their respective Lewis acidity, with prior reports delineating the reactivity of the early lanthanides and the late lanthanides around the Gd boundary.[126–128]

Developing chelating ligands for selective lanthanide coordination is a continuous area of research. Cryptand ligands with appropriate binding sites have been designed to form a variety of lanthanide cryptates, and have received substantial interest as multidentate ligands with unique topological properties and as chelates for bimetallic systems.[129] Cryptands have previously been generated *via* template synthesis using Ln metals as catalysts to assist with the formation of imine bonds, using the inherent Lewis acidity of lanthanide metals to catalyze the formation of cryptands and macrocycles *in-situ*.[130,131,132] Here, we invert this paradigm and use known Lewis-acid catalysis to develop an imine-*cleavage* methodology to generate bimetallic complexes from imine-based cryptands. The cleaved cage ligand retains an imino pyridine coordination site in the pocket of the ligand, and a hemiacetalate functionality bridging the terminal Ln metal with the pocketed metal. Hemiacetalate coordination remains rare in lanthanide chemistry, with only a handful of previous reports.[133–135]

The synthesis of cryptand **TPT** (**TPT =** Tris(Pyridinediimine)bis[Tren]) was previously described by the condensation of 2,6-diformylpyridine with tris-(2-aminoethyl)amine (Tren).[136]

This prior art describes the use of both aprotic acetonitrile as a solvent, as well as protic methanol, or a mix of both, at reflux temperatures to yield identical lanthanide cage complexes. Several **TPT** lanthanide cryptates were synthesized by directly reacting the free ligand with the lanthanide nitrate, forming the reported encapsulated metal complexes [**LnTPT][3X]** (Ln = Nd, Eu – Tb; X = Cl, Br, NO_3), as red, block-like crystals which are poorly characterized due to poor solubility properties.[137–140] In this study, the Lewis-acidity of the lanthanides was employed to generate bimetallic complexes within an imine/hemiacetalate framework to provide the series **Ln_2TPT^{OMe}** [**TPT^{OMe}** = Tris(Pyridineimine)(Tren)tris(methoxyhemiacetalate)]. These products are generated from hydrolysis and methanolysis of the cage ligand **TPT**, **Figure 6.1**.

6.2 Experimental

6.2.1 Materials and instrumentation

Solvents used for manipulations including MeOH (VWR), MeCN (Sigma), Hexane (Alfa Aesar), Diethyl Ether (Sigma), and δ-DMSO (Sigma) were used as received. The following compounds were purchased reagent grade from commercial sources and used as received $Ln(NO_3)_3•xH_2O$ [Ln = La, Pr, Gd, Tb, Dy, Ho (Alfa Aesar)] [Ln = Nd, Sm, Tm, Yb, Lu (Strem)], [Ln = Ce, Eu (Sigma)], tris(2-aminoethyl)amine (Acros). 2,6-diformylpyridine (Asta Tech) was recrystallized from fluorobenzene. Cryptand **TPT** was prepared by the condensation of tris(2-aminoethyl)amine and 2,6-diformyl-pyridine as described in literature.

Solid State UV/vis/NIR spectroscopic data were obtained from single crystals using a CRAIC Technologies UV/vis/NIR microspectrophotometer ^1H NMR and ^{13}C NMR spectra were recorded on a Bruker Avance 400 MHz operating at 400.1 MHz and 100.6 MHz, respectively. All ^1H and $^{13}C\{1H\}$ NMR chemical shifts are reported relative to $SiMe_4$ using the ^1H (residual in the deuterated solvents) and ^{13}C chemical shifts of the solvent as a secondary standard. Crystals were placed on glass slides in immersion oil and data were collected from 320 nm to 1200 nm. The photoluminescence and excitation spectra were obtained on an Edinburgh FLS980 fluorescence spectrometer with a housed 450 W Xe lamp/single grating (1800 λ/mm, 250 nm blaze). Attenuated total reflectance infrared (ATR-IR) spectra were recorded using a Bruker Alpha Fourier transform infrared (FTIR) spectrometer (SiC Glowbar source and DTGS detector) with a Platinum ATR QuickSnap sampling module (single-reflection diamond crystal). Spectra were obtained by placing

powder on the diamond face, and data were acquired from 400 to 4000 cm^{-1} at a resolution of 4 cm^{-1}. All ATR-IR spectra are reported in absorbance with a blank versus atmosphere. DC magnetic susceptibility $c = M/H$ measurements were carried out at temperatures T = 1.8 - 300 K under an applied magnetic field of H = 1 kOe using a Quantum Design VSM Magnetic Property Measurement System. Collections of small single crystalline samples were enclosed in a gel-cap that was suspended in a straw for the measurement. C/H/N elemental analyzes were carried out by Midwest Microlab, Indianapolis, IN. Single crystals selected for data collection were mounted on a nylon loop using N-paratone oil and optically aligned on a Bruker D8 Quest X-ray diffractometer. Crystallographic data were collected under a low-temperature nitrogen gas flow, 100 K, using a Mo Kα (λ = 0.71069 Å) X-ray microsource and a CMOS detector. The unit cell determination and subsequent data collection were performed using the APEX III software.[40] Raw data frames were processed using SAINT[41] and SADABS.[42] Subsequent calculations were carried out using the OLEX 2[43] program. Structures were solved by olex2.solve and refined by full-matrix least squares on F2 techniques. Crystallographic information is included in **Table F.1**.

6.2.2 Synthesis

Ce_2TPT^{OMe}(MeOH). In an open atmosphere, **TPT** (9 mg, 0.018 mmol) and $Ce(NO_3)_3$•$6H_2O$ (15 mg, 0.036 mmol) in MeOH (1 mL) were stirred for 5 min. The reaction solution changed quickly from colorless to orange. The solution was filtered, and the reaction mixture was allowed to sit for 1 d at room temperature. After this time, orange block-like X-ray quality crystals were isolated, washed with hexane/ether and dried in air (6 mg, 30 % yield). Anal. Calc'd for $C_{30}H_{36}N_{10}O_{15}Ce_2$: C, 34.09 ; H, 3.43 ; N, 13.25. Found: C, 31.30 ; H, 3.30 ; N, 18.09. Despite multiple EA attempts the % found consistently reported low C and H, and high N. The experimental for Ln = Pr–Lu, except Pm, follows the same procedure.

Synthesis of **Lu_2TPT^{MeOEt}** and **Lu_2TPT^{OBz}** follow the same experimental with 2-methoxyethanol and benzyl alcohol respectively.

Pr_2TPT^{OMe}(MeOH). Yellow needles (8 mg, 40 % yield). Anal. Calc'd for $C_{30}H_{36}N_{10}O_{15}Pr_2$: C, 34.04 ; H, 3.43 ; N, 13.23. Found: C, 31.02 ; H, 3.25 ; N, 16.81. Despite multiple EA attempts the % found consistently reported low C and H, and high N.

Nd_2TPT^{OMe}(MeOH). Yellow needles cocrystallized with orange blocks assumed **NdTPT[$(NO_3)_3$]**, and we were unable to perform elemental analysis.

Sm_2TPT^{OMe}(MeOH). Yellow needles cocrystallized with orange blocks assumed **SmTPT[$(NO_3)_3$]**, and we were unable to perform elemental analysis.

Eu_2TPT^{OMe}. Yellow needles (17 mg, 85% yield). Anal. Calc'd for $C_{30}H_{36}N_{10}O_{15}Eu_2$: C, 33.34 ; H, 3.36 ; N, 12.96. Found: C, 33.16 ; H, 3.23 ; N, 13.03.

Gd_2TPT^{OMe}. Yellow needles (14 mg, 74% yield). Anal. Calc'd for $C_{30}H_{36}N_{10}O_{15}Gd_2$: C, 33.02 ; H, 3.33 ; N, 12.84. Found: C, 32.39 ; H, 3.27 ; N, 12.75. Anal. Calc'd for $C_{31}H_{40}N_{10}O_{16}Gd_2$: C, 33.15 ; H, 3.59 ; N, 12.47. Calculated as **Gd_2TPT^{OMe}•MeOH**.

Tb_2TPT^{OMe}. Yellow needles (16 mg, 83 % yield). Anal. Calc'd for $C_{30}H_{36}N_{10}O_{15}Tb_2$: C, 32.92 ; H, 3.32 ; N, 12.80. Found: C, 32.83 ; H, 3.33 ; N, 12.65. Anal. Calc'd for $C_{31}H_{40}N_{10}O_{16}Tb_2$: C, 33.05 ; H, 3.58 ; N, 12.43. Calculated as **Tb_2TPT^{OMe}•MeOH**.

Dy_2TPT^{OMe}. Yellow needles (18 mg, 95% yield). Anal. Calc'd for $C_{30}H_{36}N_{10}O_{15}Dy_2$: C, 32.71 ; H, 3.29 ; N, 12.71. Found: C, 32.60 ; H, 3.26 ; N, 12.62.

Ho_2TPT^{OMe}. Yellow needles (14 mg, 73 % yield). Anal. Calc'd for $C_{30}H_{36}N_{10}O_{15}Ho_2$: C, 32.56 ; H, 3.28 ; N, 12.66. Found: C, 32.41 ; H, 3.20 ; N, 12.61.

Er_2TPT^{OMe}. Yellow needles (6 mg, 32 % yield). Anal. Calc'd for $C_{30}H_{36}N_{10}O_{15}Er_2$: C, 32.43 ; H, 3.27 ; N, 12.61. Found: C, 32.20 ; H, 3.05 ; N, 12.29.

Tm_2TPT^{OMe}. Yellow needles (10 mg, 53 % yield). Anal. Calc'd for $C_{30}H_{36}N_{10}O_{15}Tm_2$: C, 32.33 ; H, 3.26 ; N, 12.57. Found: C, 32.10 ; H, 3.22 ; N, 12.20.

Yb_2TPT^{OMe}. Yellow needles (8 mg, 42 % yield). Anal. Calc'd for $C_{30}H_{36}N_{10}O_{15}Yb_2$: C, 32.09 ; H, 3.23 ; N, 12.48. Found: C, 32.14 ; H, 3.36 ; N, 12.13. Anal. Calc'd for $C_{31}H_{40}N_{10}O_{16}Yb_2$: C, 32.24 ; H, 3.49 ; N, 12.13.Calculated as **Yb_2TPT^{OMe}•MeOH**.

Lu_2TPT^{OMe}. Yellow needles (9 mg, 47 % yield). Note: Repeated synthesis, purification and analysis by ^{1}H NMR yielded similar results of unexpected peaks in the spectrum. The following spectral data are reported to the best of our abilities. ^{1}H NMR (DMSO-*d6*): δ 8.81 (s, 3H, CH), 8.19 (t, 3H, Ar-H), 7.92 (d, 3H, Ar-H), 7.68 (d, 3H, Ar-H), 5.71 (s, 3H, N=CH), 3.37 (s, 3H), 3.24-2.93 (m, 12H), 2.80-2.65 (m, 3H), 2.42 (d, 3H). ^{13}C NMR (DMSO-d6): δ 169.35, 162.68, 149.51, 149.25, 140.56, 125.85, 125.50, 124.43, 101.39, 64.94, 58.24, 56.43, 53.55, 53.29, 48.63. Anal. Calc'd for $C_{30}H_{36}N_{10}O_{15}Lu_2$: C, 31.98 ; H, 3.22 ; N, 12.43. Found: C, 31.80 ; H, 3.22 ; N, 12.13.

Lu_2TPT^{MeOEt}. Yellow needles (14 mg, 67 % yield). Note: Due to splitting in the aliphatic region, accurate integrals were not attainable, the approximate values have been reported here.^{1}H

NMR (DMSO-*d6*): δ 8.81 (s, 3H, CH), 8.20 (t, 3H, Ar-H), 7.90(d, 3H, Ar-H), 7.69 (d, 3H, Ar-H), 5.85 (s, 3H, N=CH), 3.48 (t, 2H), 3.33 (t, 2H), 3.24 (s, 2H), 3.20 (s, 9H, OMe), 3.19-3.12 (m, ~6H), 3.09-2.93 (m, ~6H), 2.77-2.64 (m, ~3H), 2.58-2.51 (m, ~3H). ^{13}C NMR (DMSO-*d6*): δ 170.03, 162.83, 150.00, 140.95, 125.99, 124.91, 101.08, 74.36, 71.65, 65.43, 61.88, 60.49, 58.60. Anal. Calc'd for $C_{36}H_{48}N_{10}O_{18}Lu_2$: C, 34.35 ; H, 3.84 ; N, 11.13. Found: C, 34.30 ; H, 4.03 ; N, 10.88.

Observation of Lu_2TPT^{OBz}. Pale Yellow needles (trace yield). Anal. Calc'd for $C_{48}H_{48}N_{10}O_{15}Lu_2$: C, 42.55 ; H, 3.57 ; N, 10.34. Found: C, 31.80 ; H, 3.22 ; N, 12.13. Anal. Calc'd for $C_{55}H_{56}N_{10}O_{16}Lu_2$: C, 45.15 ; H, 3.86 ; N, 9.57. Calculated as **Lu_2TPT^{OBz}•BzOH.**

6.3 Results and Discussion

6.3.1 Crystallography

In this study, a divergence of coordination activity of the lanthanides is shown, where both the metal cryptand as well as bimetallic complexes, **Ln_2TPT^{OMe}** (Ln = Ce–Lu), that arise from cleavage of the ligand, are generated. These compounds were prepared by the addition of **TPT** to $Ln(NO_3)_3$ in MeOH at room temperature, generating orange or yellow color from the colorless starting compounds. Crystals formed overnight from methanol and the solid-state structures were investigated through the use of single-crystal X-ray crystallography. The Tren moiety that is cleaved off in the reaction can be isolated from the mother-liquor of the reaction as the trinitrate $[H_3Tren][NO_3]_3$. **Ce_2TPT^{OMe}** and **Pr_2TPT^{OMe}** formed orange blocks and yellow needles, respectively, and both crystals solved in monoclinic *P*2/*n* space group in low yield. Ln(1) coordinates inside the **TPT** pocket to the pyridyl and imine-nitrogen atoms, forming a 9-coordinate tricapped trigonal prism. Ln(2) forms a 10-coordinate distorted bicapped square antiprism coordinated to the hemiacetalate and nitrate groups, and also a coordinating MeOH, **Figure 6.2**. Yellow plates of **Nd_2TPT^{OMe}** co-crystallized with orange block crystals that were cursorily identified as the previously reported monometallic cage complex.[139] The yellow plates were identified as **Nd_2TPT^{OMe}**, which crystallized in the orthorhombic *P*222 space group, with the same structural formula as the Ce and Pr complexes. Yellow needles of **Sm_2TPT^{OMe}** also co-crystallized with a small percentage of the orange monometallic cage complex that solved in the

*P*222 space group. Coordination of Sm in the yellow needles is consistent with the earlier lanthanides, save for one fewer MeOH molecules present in the unit cell.

Progressing along the lanthanide series of **Ln_2TPT^{OMe}** (Ln = Eu – Lu), the products crystallize exclusively as yellow needles in high yield in the *P*222 space group, where the terminal metal, Ln(2) is nine-coordinate due to the absence of a coordinated MeOH. For the whole series, the Ln(1)–Ln(2) distance decreases linearly proportional to ionic radius across the series, with the largest separation of 3.689(1) Å observed with Ce and smallest of 3.347(1) Å in Lu, **Table F.1**. Several other metrical parameters of the cage change proportionally to the ionic radius of the metal. The pocket size of the ligand adjusts to the size of the lanthanide, where both the Ln(1)–N(1) distance [N(1) = tertiary nitrogen of Tren] and C–N(1)–C angle increase with decreasing ionic radius **Figures 6.3, 6.4**. The smaller the cation, the more the closer to the metal center the pyridine coordinates, causing an increase to the pyrimidalization angle of the nitrogen atom. The twist angles of the ligand are also affected by the size of the metal ion. Comparing the planes formed from the atoms of the imine nitrogen atoms, the pyridyl nitrogen atom, and the acetalate bridging oxygen atoms, a linear trend in the twist angle is observed as the ionic radius of the metal changes, **Figure 6.5**.

6.3.2 NMR and UV/vis/NIR spectroscopy

The ^{1}H and ^{13}C NMR spectra of **Lu_2TPT^{OMe}** in DMSO-d_6 show unexpected but reproducible minor peaks, suggesting the formation of isomeric complexes, coordination of DMSO, or, potentially, decomposition. Importantly, CHN analysis confirms purity of the bulk sample. In order to interrogate this further, we attempted crystallization of the complex from DMSO. The resulting structure matched that crystallized from MeOH, indicating DMSO coordination was unlikely. However, when we analyzed the ^{1}H NMR spectrum in D_2O to check stability of the complex the resulting spectrum that suggested total decomposition. This led us to suspect the water content of the DMSO was contributing to the extra peaks in the ^{1}H spectrum.

In order to further probe the unexpected resonances, we performed synthesis of the complex in deuterated solvent. Performing the synthesis of **Lu_2TPT^{OMe}** in methanol-d_4 was implemented for two reasons: to incorporate the label into the hemiacetal group and also to try and get NMR data in this solvent to forego the possibility of decomposition in DMSO. Unfortunately, the poor solubility of the complex in methanol inhibited an improved ^{1}H NMR

analysis relative to DMSO; the complex almost quantitatively precipitated from the methanol and analysis of the mother liquor revealed only peaks for the byproduct of the reaction, $[H_3Tren][NO_3]_3$. We were still able to confirm the origin of the methoxy groups of the ligand. Analysis of the precipitated product in DMSO-d_6 showed the expected septet centered at 126.30 ppm for the CD_3 groups in the ^{13}C NMR spectrum, as well as a small resonance in the ^{1}H spectrum centered at 3.09 ppm.

In order to determine the generality of the alcoholytic cleavage, methanol was replaced by other primary alcohols and the products were determined by X-ray crystallography. 2-methoxyethanol and benzyl alcohol were used as solvents in reaction conditions otherwise identical to those using methanol. These experiments were conducted with Lu in order to probe the products using NMR spectroscopy. This resulted in the formation of the hemiacetal bridged species similar to **Ln$_2$TPT^{OMe}**, but with 2-methoxyethyl or benzyl groups in place of the methyl group of the hemiacetalate fragment. **Lu$_2$TPT^{MeOEt}** and **Lu$_2$TPT^{OBz}** were obtained from these solvents for comparison. Both complexes crystallized in the monoclinic space group, $P2_1/n$. **Lu$_2$TPT^{OBz}** crystallized in low yield as pale yellow-colorless needles and was obtained as an impure mixture with unidentified side-products. Comparison of the solid-state metrics shows that **Lu$_2$TPT^{OBz}** has significantly shorter Lu(1)–Ln(2) and Lu(1)–N_{Tren} bond distances, than what is observed for **Lu$_2$TPT^{OMe}** , **Table F.2**. In terms of size correlation, the steric demands of the benzyl group distort the complex metrics to a greater degree than MeOEt as compared to **Lu$_2$TPT^{OMe}**. Other alcohols such as phenol, isopropanol, and *tert*-butanol were unsuccessfully attempted.

Surprisingly, NMR analysis of **Lu$_2$TPT^{MeOEt}** reveals a much cleaner spectrum than **Lu$_2$TPT^{OMe}**, suggesting either a lower ratio of isomer formation or enhanced stability of the complex. All expected resonances for the complex were observed, with minor signals observed in the baseline indicating minor isomer formation or degradation, but to a lesser extent than what was observed with **Lu$_2$TPT^{OMe}**. It is possible that decomposition occurs at the hemiacetal moiety, and enhanced steric protection of this position lends stability to the ligand.

Solid-state UV/vis/NIR spectra of the series of **Ln$_2$TPT^{OMe}** complexes reveal an intense, broad band with λ_{max} near 400 nm. The weaker absorptions between 450 and 1100 nm for Ln^{3+} are assigned to Laporte-forbidden $4f \rightarrow 4f$ transitions. These are most prominent for Ln = Nd, Dy, and Ho. Excitation at 420 nm shows several intense peaks for **Eu$_2$TPT^{OMe}**, fluorescing at 593,

617, and 698 nm. Solid-state IR remains similar for all complexes, with bands at 1600 and 1590 cm^{-1} acting as a fingerprint for the molecules that is attributed to the imine stretches of the dilanthanide complexes. SQUID data was obtained for **Gd_2TPT^{OMe}** and **Dy_2TPT^{OMe}** to probe variable temperature magnetic behaviour, **Fig. 6.6**. While similar helicate complexes have shown unusual magnetic characteristics at lower temperatures, these complexes display expected magnetic behavior for lanthanide ions.[141] In both cases, the metals magnetic behavior consistent with discrete metal ions, with average moments of 8.3 μ_B and 11.08 μ_B (Gd and Dy, respectively), that are only slightly higher than the accepted moments for the free metal ions of 8.0 μ_B and 10.6 μ_B (Gd and Dy, respectively).[142–144]

6.4 Conclusion

The work presented here is remarkably different from the prior reports of **TPT** reactivity with Ln starting materials. The synthesis of the half-cage complexes, **Ln_2TPT^{OMe}**, is an example of harnessing the inherent properties of the *f*-block metals to generate new species to study. This reaction also represents a pointed example of metals' ability to self-assemble into different molecular motifs, and in this case they do so by generating a hemiacetalate moiety to bridge two lanthanide centers. This reactivity is an avenue into further studies of actinide metals, magnetism, separations, and further synthetic fine-tuning to assist with solubility and tailored coordination spheres.

6.5 Figures

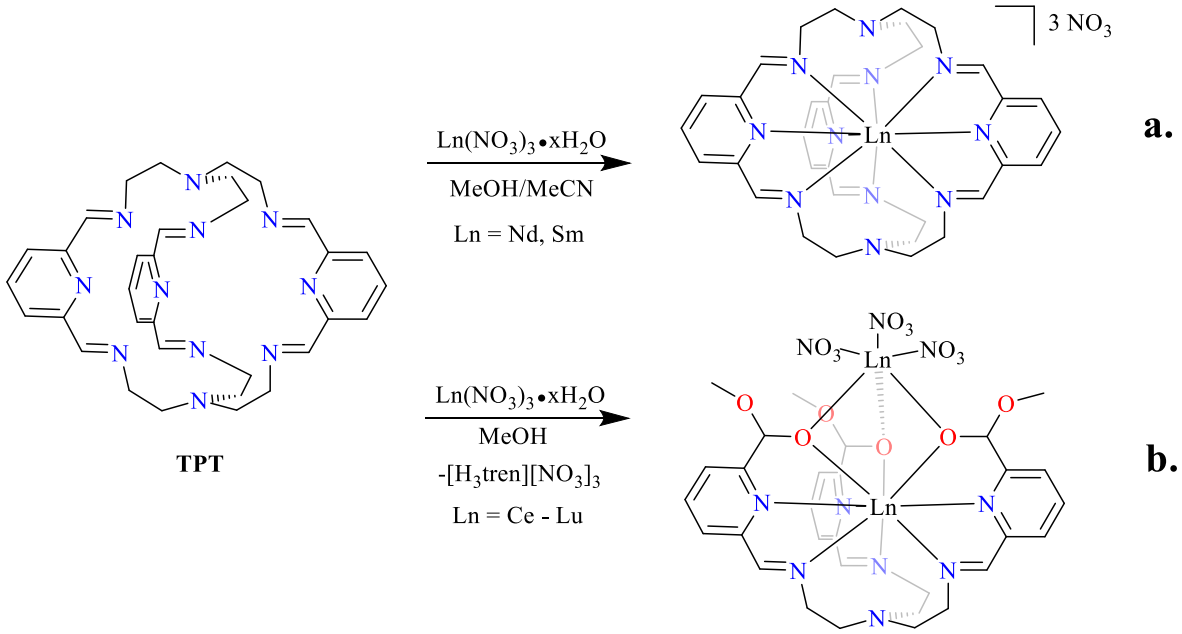

Figure 6.1. Synthesis of **[LnTPT][3(NO$_3$)]** **(a)** and **LnTPT^{OMe}** **(b)**.

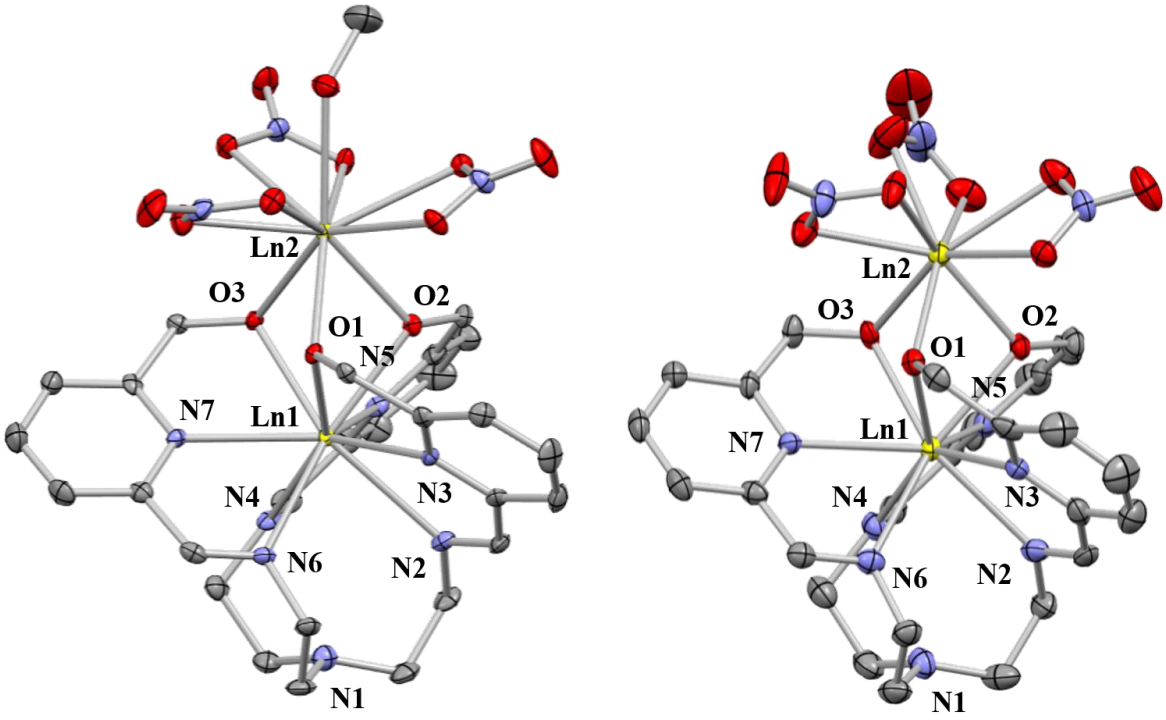

Figure 6.2. Molecular structure of **Ln_2TPT^{OMe}(MeOH)** (Ln = Ce–Sm) and **Ln_2TPT^{OMe}** (Ln = Eu–Lu) drawn at the 50% probability level with H atoms and solvent omitted for clarity.

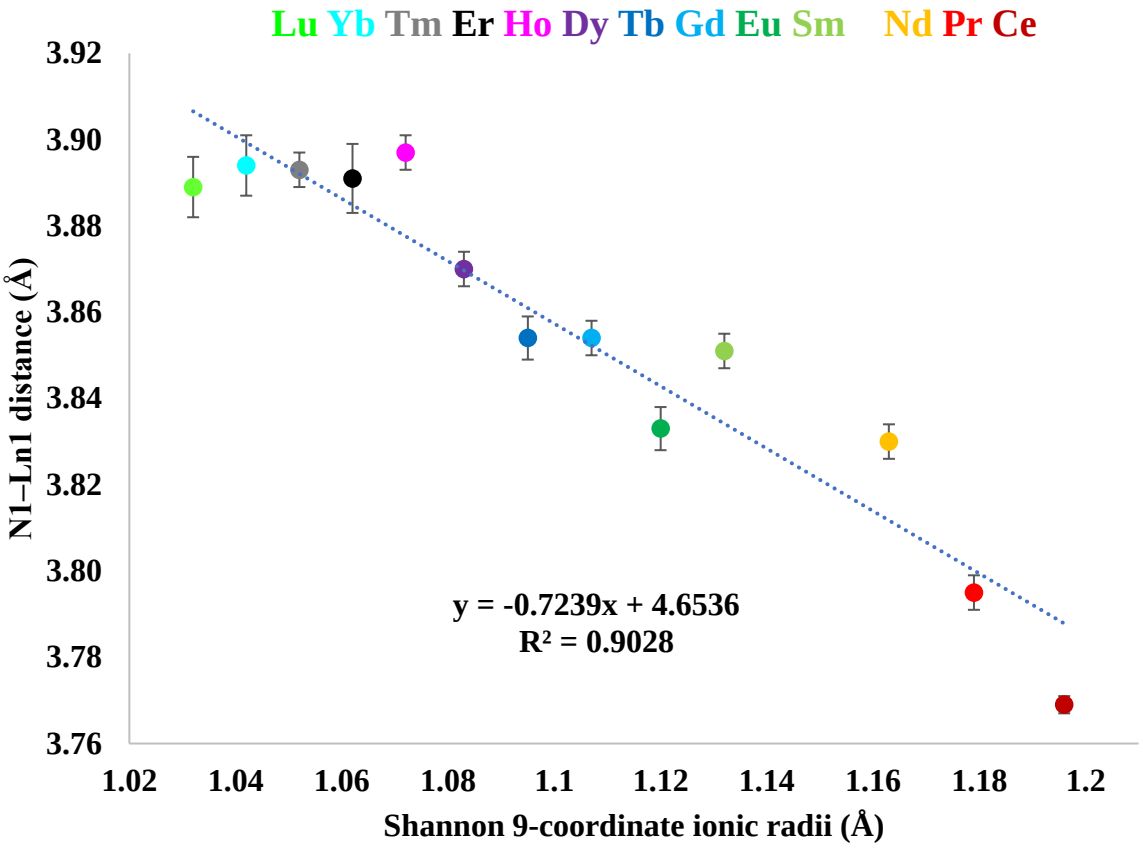

Figure 6.3. Plot of the N1–Ln1 distance (Å) for **Ln_2TPT^{OMe}(MeOH)** (Ln = Ce–Sm) and **Ln_2TPT^{OMe}** (Ln = Eu–Lu).

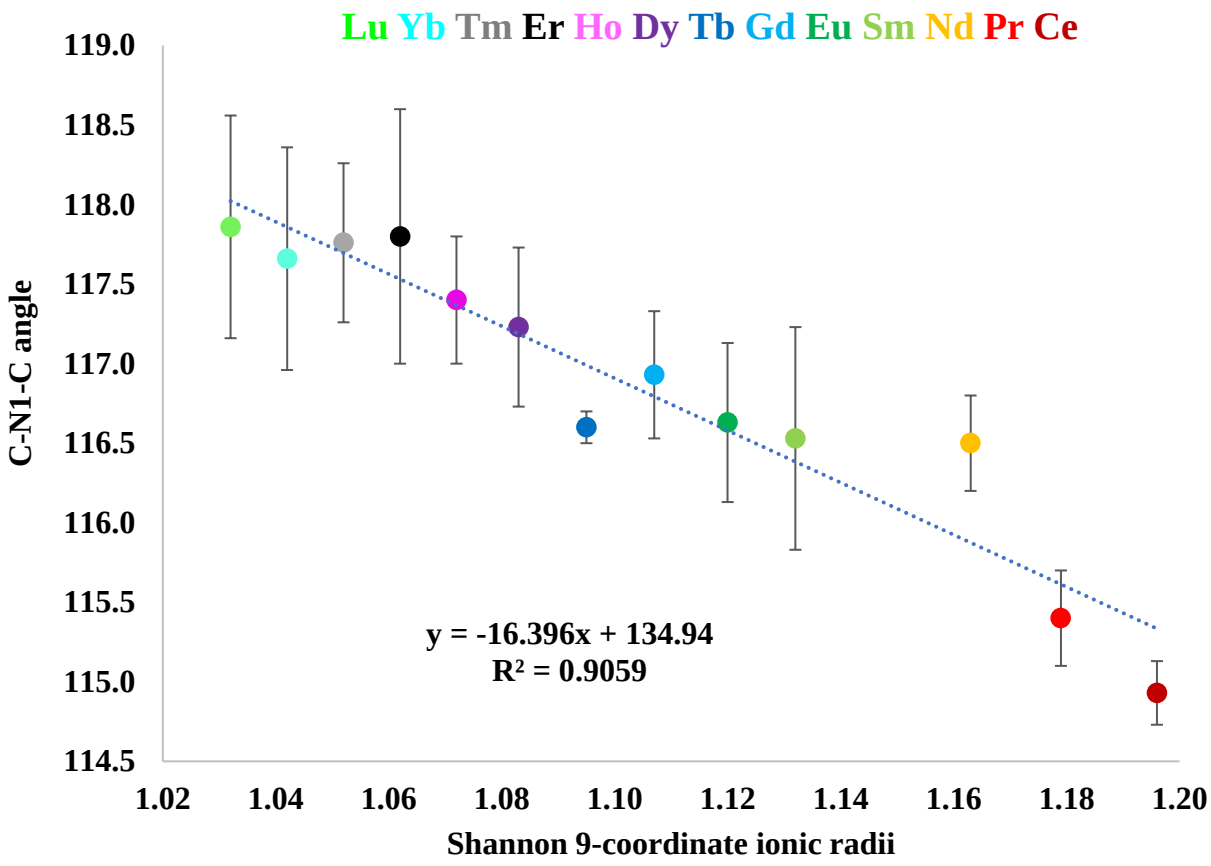

Figure 6.4. Plot of the average C–N1–C angle (nitrogen pyramidalization) for **Ln_2TPT^{OMe}(MeOH)** (Ln = Ce–Sm) and **Ln_2TPT^{OMe}** (Ln = Eu–Lu).

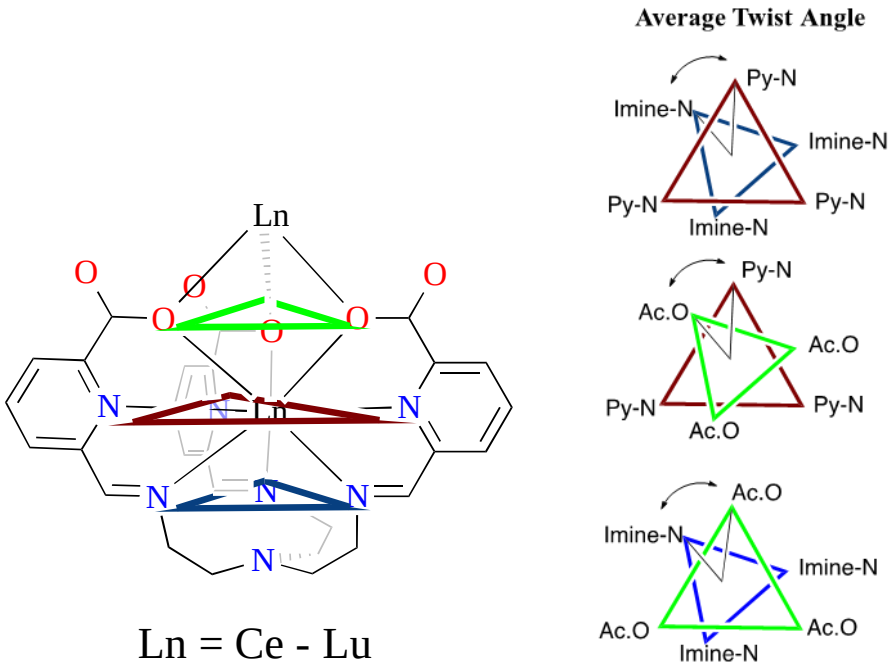

Figure 6.5. Cartoon representation of planes and twists angles of **Ln_2TPT^{OMe}**.

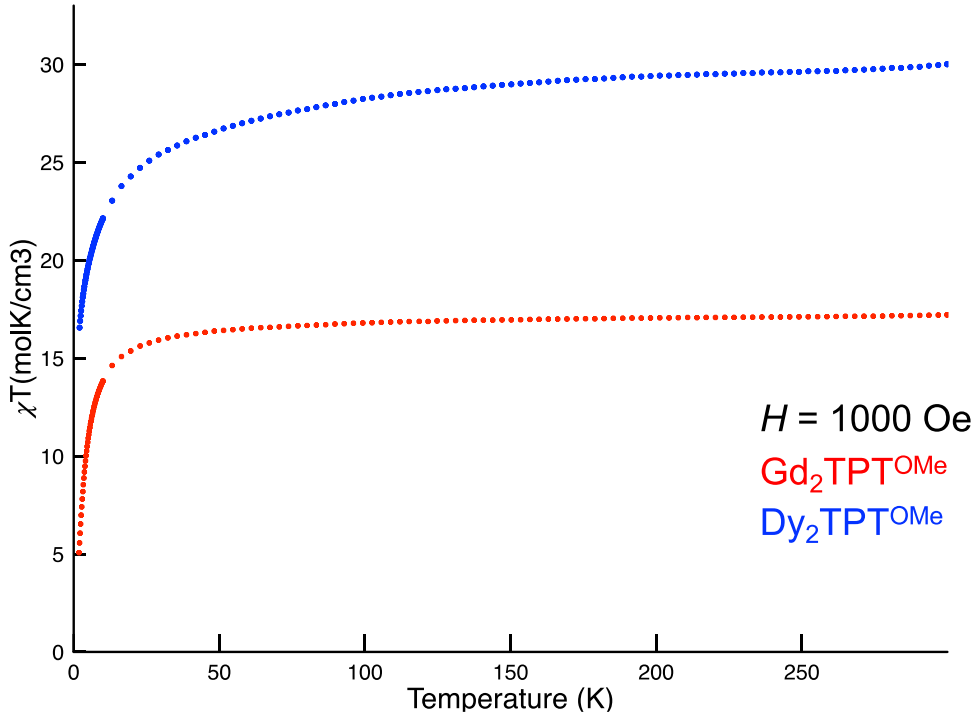

Figure 6.6. SQUID trace of **Gd_2TPT^{OMe}** and **Dy_2TPT^{OMe}**.

CHAPTER 7

EMPLOYING INTRINSIC LEWIS-ACIDITY IN THE GENERATION OF A BIMETALLIC AMERICIUM COMPLEX

7.1 Introduction

The separation of the minor actinides (Am, Cm) from lanthanides at an industrial scale remains a significant challenge for closing the nuclear fuel cycle. Methods to significantly reduce the volume and radiotoxicity of waste for safe storage and handling is currently being investigated.[145,146] Due to their high radiotoxicity, particular attention must be paid to the transuranic actinides, specifically Am and Cm, that contribute >99% of the radiotoxicity even after several hundred years of storage.[147] In partitioning and transmutation strategies, these long-lived radionuclides are recovered and converted into shorter-lived or stables ones through irradiation in dedicated reactors. The development of highly efficient methods to recover these elements from spent nuclear fuel is an ongoing problem and requires further fundamental research to learn about the structure, bonding, reactivity, and coordination behavior of these minor actinides.

Due to their chemical similarity, lanthanides are often difficult to separate from the minor actinides in high-level waste. Under typical reaction conditions Am shares both comparable ionic radii and the 3+ oxidation state with lanthanide ions. However, slight dissimilarities allow us to investigate their chemical and electronic differences that inform the development of ligand designs and separation schemes. N-rich ligands have been of particular interest for their discrimination between lanthanides and actinides. Generally, these N-donor ligands are softer than O-donors on the Pearson scale,[125] and show a preference for binding actinides vs. lanthanides.[148] This "softness" is amplified by the energetic degeneracy of the ligand 2*p* orbitals and metal-based orbitals, that leads to the energy-degeneracy driven covalency with a small, but non-negligible, orbital overlap bonding component.[149] Many of these N-donor ligand designs for lanthanide-actinide separations contain one or more pyridine moieties.

Cryptand ligands have also been designed to form a variety of lanthanide coordination complexes and have received interest as multidentate ligands with unique topological properties and as chelates for bimetallic systems. The synthesis of the neutral N-donor cryptand **TPT** (**TPT**

= Tris(Pyridinediimine)bis[Tren])[137] was previously described by the condensation of 2,6-diformlylpryidine with tris-(2-aminoethyl)amine (Tren). The Lewis-acidity of the lanthanides was employed to generate bimetallic complexes within an imine/hemiacetalate framework to provide the series **Ln_2TPT^{OMe}** [**TPT^{OMe}** = Tris(Pyridineimine)(Tren)tris(methoxyhemiacetalate] (Ln = Ce-Lu). These products are generated from hydrolysis and methanolysis of the cage ligand **TPT** likely facilitated by inductive effects stemming from the Lewis acidic lanthanide cation. A clear demarcation in reactivity is observed between Sm and Eu, where the lighter and larger lanthanides generate a mixture of products, **Ln_2TPT^{OMe}** and **[LnTPT][3(NO_3)]**. Meanwhile, the heavier and smaller lanthanides generate exclusively the bimetallic **Ln_2TPT^{OMe}**. Am^{3+} ($5f^6$) is isoelectronic to Eu^{3+} ($4f^6$) and shares the same ionic radius as Nd^{3+} (1.163 Å, 9-coordinate).[150] It is between these lanthanides that a change in reactivity is observed in the series. In order to expand this study, we sought to compare the reactivity of Am between the different *f*-elements by combining synthetic, crystallographic, multinuclear NMR, and UV/vis/NIR spectroscopy.

7.2 Experimental

7.2.1 General considerations and instrumentation

Caution! ^{243}Am ($t_{1/2}$= 7.38 × 10^3years) has potential health risks due to its α and γ emission, along with the emission of its daughter^{239}Np ($t_{1/2}$= 2.35 days).^{239}Np undergoes β and γ emission.

All manipulations were performed in a radiologic fume hood without exclusion of air and water. Solvents used for manipulations in air including MeOH (Sigma), Et_2O (Sigma), and DMSO-*d6* (Sigma) were used as received. ^{243}Am in the form $AmCl_3$ was received by Los Alamos National Laboratory. **TPT** was prepared according to literature.[136]

UV/vis/NIR spectroscopic data were obtained from single crystals using a CRAIC Technologies UV/vis/NIR microspectrophotometer. Crystals were placed on quartz slides under Krytox oil and data were collected from 300 nm to 1200 nm. ^1H NMR spectra were recorded on a Bruker 400 MHz spectrometer operating at 400.1 MHz, at 298 K unless otherwise stated. ^1H NMR spectra were referenced internally to solvent resonances. NMR samples were dissolved in DMSO-*d6* and placed in an NMR tube with no attempt to exclude air or water. Single crystals selected for data collection were mounted on a MITOGEN mount™ cryoloop and optically

aligned on a Bruker D8 Quest X-ray diffractometer. Crystallographic data were collected under a low-temperature nitrogen gas flow using a Mo-Kα (λ = 0.71069 Å) X-ray micro source and a CMOS detector. The unit cell determination and subsequent data collection was performed using the APEX III software.[40] Raw data frames were processed using SAINT[41] and SADABS.[42] Subsequent calculations were carried out using the OLEX 2 program.[43] Structures were solved by ShelX and refined by full-matrix least-squares on F^2 techniques.

7.2.2 Synthesis

$Am(NO_3)_3$ was prepared in the following manner: 2.5 mg (0.128 mmol) of $AmCl_3$ in 2 M HCl (125 μL) was converted to $Am(OH)_3 \bullet xH_2O$ with excess ammonium hydroxide and centrifuged. The supernatant was removed and $Am(OH)_3 \bullet xH_2O$ was washed with water. This was performed three times. $Am(OH)_3 \bullet xH_2O$ was dissolved in concentrated HNO_3 and dried to a residue as $Am(NO_3)_3$. The residue was then dissolved in 1 mL MeOH, which produced a pale pink solution. 6 mg **TPT** in 1 mL MeOH was added to the Am, producing a cloudy orange solution. Overnight crystals suitable for single crystal X-ray diffraction were isolated as yellow-orange gem-like crystals, washed with Et_2O and dried in air.

7.3 Results and Discussion

7.3.1 Crystallography

Several **TPT** lanthanide cryptates were synthesized by directly reacting the free ligand with the lanthanide nitrate, forming the reported encapsulated metal complexes **[LnTPT][3(NO$_3$)]** (Ln = Nd, Eu – Tb), as red, block-like crystals which are poorly characterized due to poor solubility properties. In Chapter 6 we discussed an observed a clear demarcation in reactivity between Sm and Eu, where the lighter and larger lanthanides generate a mixture of products, **Ln$_2$TPT^{OMe}** and **[LnTPT][3(NO$_3$)]**. Meanwhile, the heavier and smaller lanthanides generate exclusively bimetallic **Ln$_2$TPT^{OMe}** under our reaction conditions.

Am$_2$TPT^{OMe}(MeOH) was prepared in a similar manner to the previously reported **Ln$_2$TPT^{OMe}** complexes. Briefly, in air, addition of 0.5 equivalents of **TPT** in MeOH to a solution of $Am(NO_3)_3 \bullet xH_2O$ in MeOH results in the formation of a cloudy-orange solution. Allowing to sit undisturbed yielded X-ray quality crystals overnight. Single-crystal X-ray diffraction studies

reveal the structure to be isomorphous to the **Ln_2TPT^{OMe}(MeOH)** (Ln = Nd, Sm) analogs and crystallize in the orthorhombic space group, P*222,* **Figure 7.1**. As observed with all the lanthanide analogs, the Tren moiety is cleaved off in the reaction, presumably forming the trinitrate $[H_3Tren][NO_3]_3$ byproduct. Am(1) coordinates inside the **TPT** pocket to the pyridyl and imine-nitrogen atoms, forming a 9-coordinate tricapped trigonal prism. However unlike the Ln analogs, Am(2) forms a 9-coordinate distorted bicapped square antiprism coordinated to the hemiacetalate, only five oxygens from the nitrate groups, and a coordinating MeOH. Additionally, while the lanthanide series (Nd-Lu) crystallized as yellow needles and plates, **Am_2TPT^{OMe}(MeOH)** crystallized as yellow-orange blocks, similar to the habbit of **Ce_2TPT^{OMe}(MeOH)**. Currently the 9-coordinate ionic radii for Am^{3+} coordination complexes remains unknown, but is expected to be close to Nd (1.163 Å).[150] The M–M distance and M–O–M angle of **$AmTPT^{OMe}$** [3.629(1) Å , 97.1(2)° respectively] are significantly larger than that for **Nd_2TPT^{OMe}(MeOH)**, and smaller than **Pr_2TPT^{OMe}(MeOH)**, **Table G.1**.

A second attempt at synthesis using $Am(NO_3)_3$ prepared from diluted HNO_3 (6 M) following the same procedure yielded poor X-ray quality crystals of a second product, **[AmTPT][$Am(NO_3)_6$], Figure 7.2**. This cryptand product is similarly observed in co-crystallization with **$LnTPT^{OMe}$** (Ln = Sm, Nd) as [**LnTPT][$3(NO_3)$]**. These reported [**LnTPT][$3(NO_3)$]** cryptates all feature three outer-sphere NO_3 or halide counterions.[138,139] However the counterion for the **$AmTPT^{3+}$** complex features a 10-coordinate $Am(NO_3)_6^{3-}$, which has previously only been reported up to Pu.[151–154]

7.3.2 Spectroscopy

The ^{1}H NMR spectrum of **$AmTPT^{OMe}$(MeOH)** in DMSO-*d6* shows small quantities (<10%) of unexpected peaks attributed to a minor product that were also observed for **Lu_2TPT^{OMe}**. This suggest the formation of isomeric complexes, coordination of DMSO or H_2O, or decomposition. Solid-state UV/vis/NIR of **Am_2TPT^{OMe}(MeOH)** is absent of a charge transfer band, but shows several 5*f*→5*f* transitions at 421, 518, 815 nm with splitting of the $^7F_0 \rightarrow {}^5L_6$ and $^7F_0 \rightarrow {}^5D_1$ transitions. Solution-phase UV/vis/NIR in DMSO-*d6* depicts an absorption band at approximately 350 nm likely due to excess ligand in solution, followed by the same splitting patterns of the 5*f* transitions, **Figure 7.3**. Solid state UV-vis/NIR absorption spectrum of

[AmTPT][Am(NO$_3$)$_6$] reveals the same 5*f*→5*f* transitions of Am^{3+} at 502 and 806 nm, **Figure 7.4**. No emissive properties were observed with either product.

7.4 Conclusion

The reaction of **TPT** with $Am(NO_3)_3$ produced two products; a bimetallic **Am$_2$TPT^{OMe}(MeOH)**, and monometallic **AmTPT** structure in the **[AmTPT][Am(NO$_3$)$_6$]** salt pair. **Am$_2$TPT^{OMe}(MeOH)** crystallizes as euhedral orange blocks in the P*222* space group, isomorphous to the Sm and Nd analogs. **[AmTPT][Am(NO$_3$)$_6$]** was synthesized in the same manner from a dilute nitric acid solution of $Am(NO_3)_3$. This reaction formed orange anhedral **[AmTPT][Am(NO$_3$)$_6$]** crystals with a unique $[Am(NO_3)_6]^{3-}$ counterion, unlike the lanthanide analogs that feature $[(NO_3)_3]^{3-}$. The reactivity of Am compares well to the Nd and Sm analogs in the lanthanide series, and further experiments with the early-mid actinides may reveal a break in reactivity in the formation of **AnTPT^{OMe}** vs. **AnTPT**.

7.5 Figures

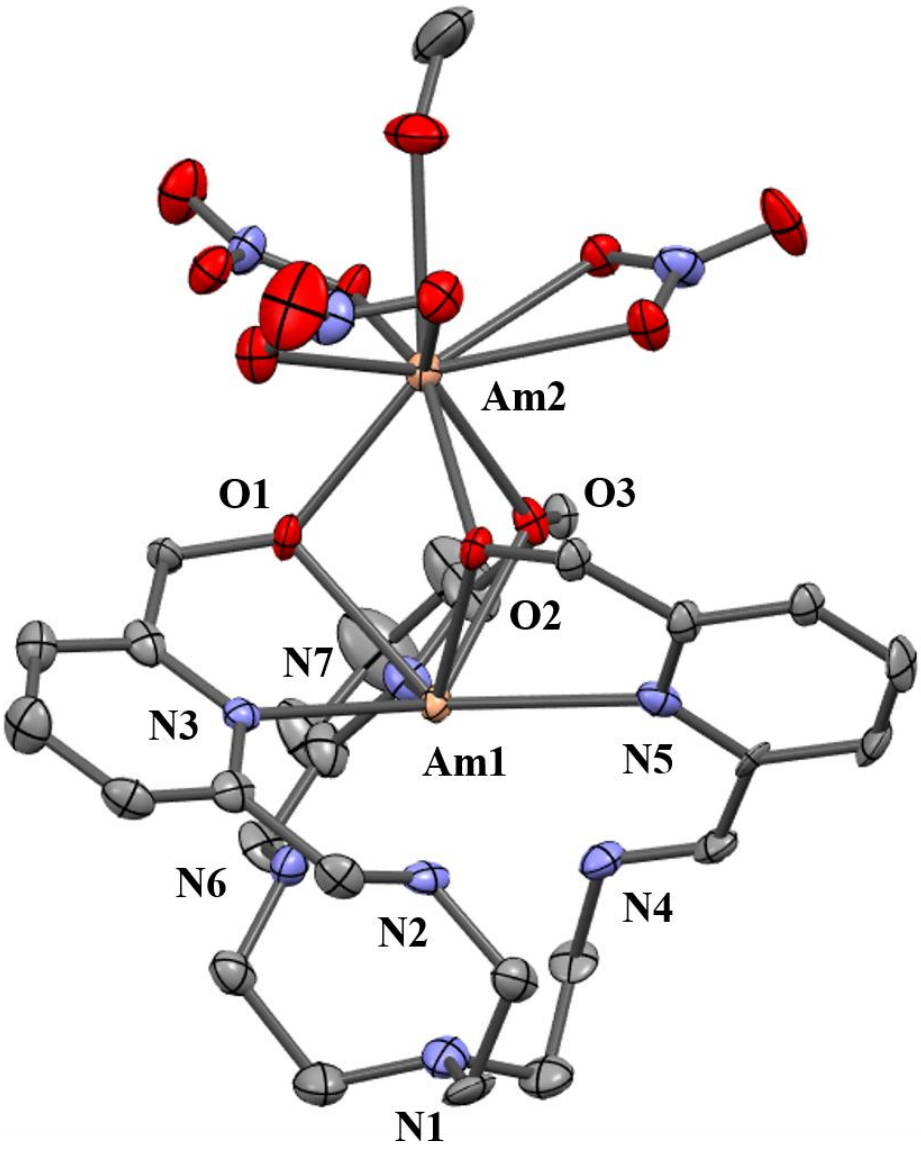

Figure 7.1. Molecular structure of **Am_2TPT^{OMe}(MeOH)** drawn at 50% probability ellipsoids; H atoms, pendant OMe groups, and lattice-solvent are omitted for clarity.

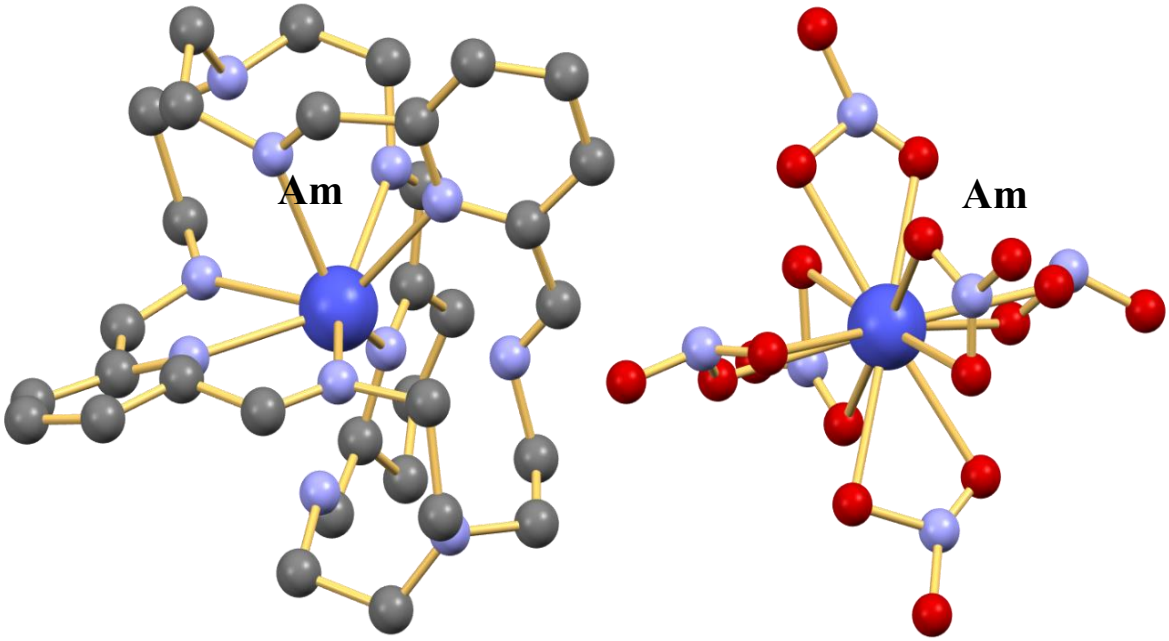

Figure 7.2. Ball and stick diagram of **[AmTPT][Am(NO$_3$)$_6$]**, H atoms omitted for clarity.

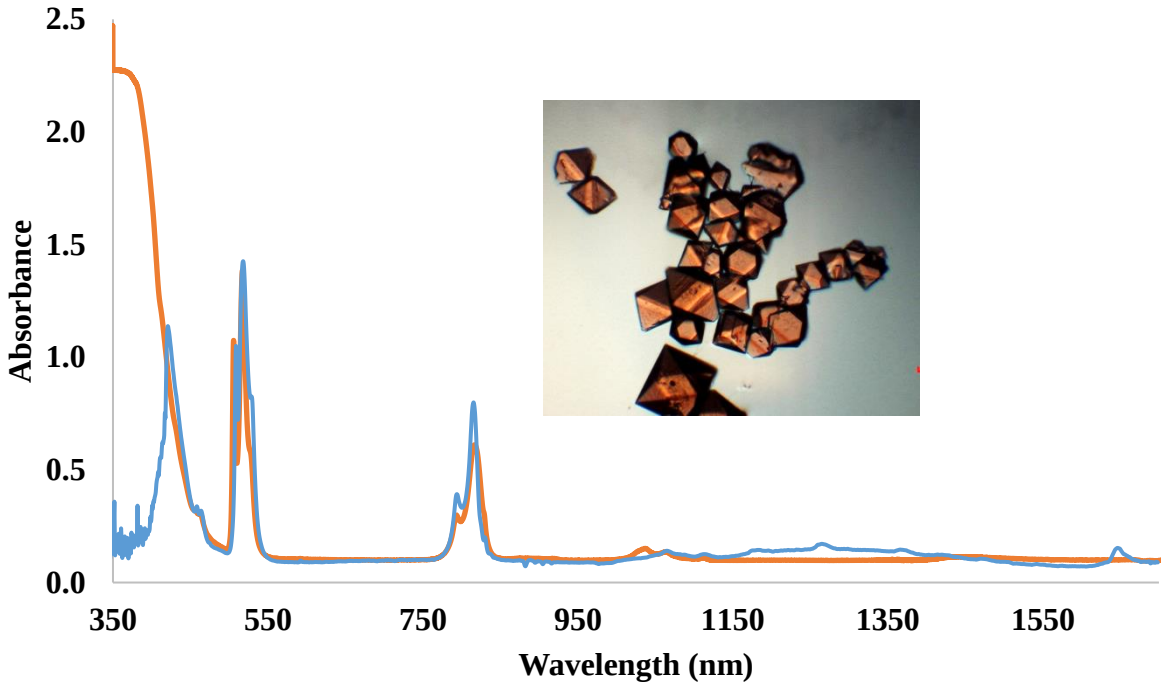

Figure 7.3. Solution-phase (orange), in DMSO-*d6*, and solid-state (blue) UV/vis/NIR and photograph of **Am_2TPT^{OMe}(MeOH)** at room temperature.

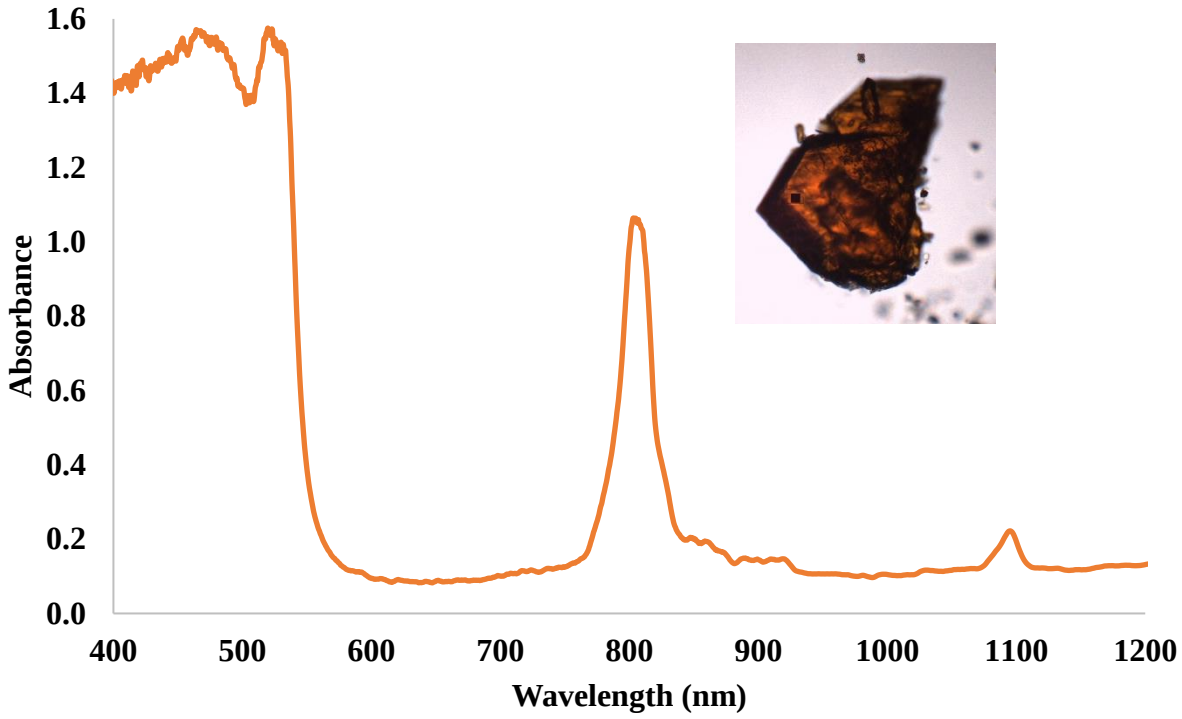

Figure 7.4. Solid-state UV/vis/NIR absorption spectrum and photograph of **[AmTPT][$(NO_3)_6$]** at room temperature.

CHAPTER 8
SYNTHESIS OF TRIVALENT PLUTONIUM AND CERIUM CRYPTATES

8.1 Introduction

The chemistry of Pu and other early to mid-actinides is crucial for the nuclear energy industry, waste disposal, nuclear deterrents, and environmental monitoring. Yet the progress in Pu studies lags grossly behind current knowledge of transition metal, lanthanide, and early actinide (Th and U) chemistry. For example, according to the Cambridge Crystallographic Database, the ratio of Pu:U:Fe structures reported is 1:38:300. This demonstrates the lack of information on the reactivity, structural behavior, and bonding preferences in Pu complexes. With the increasing development of new Pu compounds, we can support the ongoing research for the separation and extraction of Pu from organic solutions.

The majority of coordination chemistry and reactivity studies explored with Pu have been conducted under aqueous conditions. Nonaqueous conditions however allows for possible coordination to a variety of ligands otherwise not accessible and can provide further electronic structure and bonding information. Neutral ligands such as phosphine oxides and cryptands are often employed to tune steric and electronic properties of molecules, aid in crystallization, and to understand trends in the relative binding strengths of neutral donors toward hard 5*f*-metal cations. The synthesis of the neutral donor cryptand **TPT**, (**TPT =** Tris(Pyridinediimine)bis[Tren]), was previously described by the condensation of 2,6-diformylpyridine with tris-(2-aminoethyl)amine (Tren). Several **TPT** lanthanide cryptates have been synthesized in acetonitrile and/or methanol, forming an encapsulated-metal complex, reported as [**LnTPT][3(NO$_3$)]** (Ln = Nd, Eu, Tb) and **[GdTPT][3Cl]**. In recent work, we have shown the method of Lewis-acid catalysis to develop an imine-cleavage methodology to generate bimetallic complexes from **TPT** in the form **MTPT^{OMe}** [**TPT^{OMe}** = Tris(Pyridineimine)(Tren)tris(methoxyhemiacetalate); (M = Ce-Lu, Am)], from their nitrate salts. The cleaved cage ligand retains the imino pyridine coordination site in the pocket of the ligand, and a hemiacetalate functional group for coordination to the terminal lanthanide. However, a divergence of coordination activity of the lanthanides is shown with Nd and Sm, and Am, which co-crystallize with the monometallic cage complex.

Lanthanides are often employed as analogs for actinide chemistry to reduce radiation exposure, cost, and refine synthesis on a small (< 10 mg) scale. In this case, Ce is most often used as an analog for Pu due to its similarities in ionic radii, $M^{3+} \rightarrow M^{4+}$ redox potentials, and coordination geometries, which often lead to isotypic series. Here, we extend our studies to the Ce and Pu **TPT** cage complexes utilizing single-crystal X-ray crystallography, multinuclear NMR, UV/vis/near-IR (NIR) spectroscopy, and electrochemistry.

8.2 Experimental

8.2.1 General considerations and instrumentation

Caution! ^{239}Pu [$t_{1/2}$ = 24,110(30) y] is a serious health threat, due to its radioactive decay, as well as that of its daughters. Hence, all studies with actinides were conducted with appropriate controls for the safe handling and manipulation of radioactive materials, i.e. in a radiation laboratory equipped with a HEPA filtered hood. All free-flowing solids that contained plutonium were handled in negative-pressure gloveboxes or were covered in oil.

Where noted, manipulations were performed with the rigorous exclusion of air and water using glovebox techniques under an argon atmosphere. All air sensitive actinide manipulations were conducted in a negative pressure glovebox dedicated to actinide (Th – Cf) chemistry. All manipulations of actinides not inside a glovebox were conducted in a well ventilated fume hood. Other solvents used for manipulations in air including MeOH (Sigma), Et_2O (Sigma), MeOD-*d4* (Sigma), DMSO (Sigma), and ammonium hydroxide (Sigma) were used as received. $CeBr_3 \bullet xH_2O$ was prepared from CeO_2 (G. Frederick Smith Chemical Co.) and ^{239}Pu in the form $PuCl_3$ was supplied by Los Alamos National Laboratory. **TPT** was prepared according to literature.[136]

Solid-state UV/vis/NIR spectroscopic data were obtained from single crystals using a CRAIC Technologies UV/vis/NIR microspectrophotometer. Crystals were placed on quartz slides under Krytox oil and data were collected from 300 nm to 1700 nm. ^1H and ^{13}C NMR spectra were recorded on a Bruker 400 MHz spectrometer operating at 400.1 and 100.6 MHz, respectively, at 298 K unless otherwise stated. ^1H and $^{13}C\{^1H\}$ NMR spectra were referenced internally to solvent resonances. NMR samples were dissolved in MeOD-*d4* and placed in an NMR tube with no attempt to exclude air or water. Electrochemical data was recorded on a CH

Instruments Model 600E Series potentiostat. A three-electrode configuration comprising a platinum disk working electrode (2 mm diameter), a platinum wire counter electrode, and silver wire pseudo-reference electrode were used in all experiments. Cyclic voltammetric scans were conducted in DMSO with 0.2 M [TBA][PF_6] electrolyte for characterization of the ligand species, **[CeTPT][3Br]** and **[PuTPT][3Br]**. Single crystals selected for data collection were mounted on a MITOGEN mount™ cryoloop and optically aligned on a Bruker D8 Quest X-ray diffractometer. Crystallographic data were collected under a low-temperature nitrogen gas flow using a Mo-Kα (λ = 0.71069 Å) X-ray micro source and a CMOS detector. The unit cell determination and subsequent data collection was performed using the APEX III software. Raw data frames were processed using SAINT and SADABS. Subsequent calculations were carried out using the OLEX 2 program. Structures were solved by ShelXL and refined by full-matrix least-squares on F^2 techniques. Crystallographic information is included in **Table H.1**.

8.2.2 Synthesis

[CeTPT][3Br]. Method A. In the open atmosphere **TPT** (18 mg, 0.031 mmol) in MeOH (0.25 mL) was added to a solution of $CeBr_3$•xH_2O, assuming x = 6 (15 mg, 0.031 mmol) in MeOH (0.25 mL). The solution quickly changed from colorless to orange. Vapor diffusion with ether (5 mL) after 1 d at room temperature yielded dendritic and orange block-like X-ray quality crystals of the same product (16.5 mg, 55% crystalline yield). ^{1}H NMR (MeOD-*d4*): δ 13.90 (s, 6H, *H*-C(Ar)=N), 10.46 (t, 3H, Ar-*H*), 10.22 (d, 6H, Ar-*H*), 3.07 (d, 6H, CH_2), 0.88 (m, 6H, CH_2), -1.03 (d, 6H, CH_2), -2.53 (t, 6H, CH_2); ^{13}C{^{1}H} NMR ($CDCl_3$): δ 169.72 (Ar-*C*=N), 158.04 (Ar-*C*), 146.26 (Ar-*C*), 136.12 (Ar-*C*), 57.93 (*C*H_2), 52.34 (*C*H_2).

Method B. In the open atmosphere **TPT** (5 mg, 0.008 mmol) in THF (0.25 mL) was added to a solution of $CeBr_3$•xH_2O, assuming x = 6 (4 mg, 0.008 mmol) in THF (0.25 mL). The solution quickly changed from colorless to orange. Vapor diffusion with ether (5 mL) after 1 d at room temperature yielded an orange powder cursorily identified as **[CeTPT][$CeBr_6$]**. The powder was dissolved in DMSO (0.5 mL) and vapor diffused with benzene (5 mL). After 1 d at room temperature, **[CeTPT][3Br]** and **$CeBr_3$(DMSO)$_8$** crystallized in high yield as orange square plates and colorless block-like crystals, respectively.

[PuTPT][3Br]. ^{239}Pu (2 mg, 0.008 mol) in the form $PuCl_3$•xH_2O was converted to $PuOH_x$ using NH_4OH and washed twice with ultra-pure water. $PuOH_x$ was redissolved in concentrated

HBr (3 mL) and dried to a soft residue as $PuBr_3 \cdot xH_2O$. **TPT** (4.9 mg, 0.008 mmol) in MeOH (0.25 mL) was added to a solution of $PuBr_3 \cdot xH_2O$ in MeOH (0.25 mL). The solution quickly changed from violet to black. Vapor diffusion with ether (5 mL) after 1 d at room temperature yielded black block-like X-ray quality crystals and black dendritic crystals of the same product. ^{1}H NMR (MeOD-*d4*): δ 14.49 (s, 6H, *H*-C(Ar)=N), 9.27 (t, 4H, Ar-*H*), 8.22 (d, 6H, Ar-*H*), 4.97 (d, 6H, C*H*$_2$), 3.85 (d, 6H, C*H*$_2$), 3.63 (d, 12H, C*H*$_2$).

8.3 Results and Discussion

8.3.1 Crystallography

MBr_3 (M = Pu, Ce) was reacted with one equivalent of **TPT** in methanol and stirred for several minutes forming a cloudy black and yellow/orange solution respectively. The solutions were vapor diffused with Et_2O, producing black (Pu), and orange (Ce) crystals overnight in two different habbits. The chelation of the metal bromides works in high yield, though the water content of the methanol can be problematic. Crystals obtained from MeOH are poor quality due to symmetry issues, and bromide and MeOH partial-occupancy in several sites in the lattice. To circumvent this, an alternative synthetic route was attempted with $CeBr_3$. The chelation of $CeBr_3$ in THF results in the formation of the salt pair **[CeTPT][CeBr$_6$]** as an orange powder. Previously, a similar unique product, **[AmTPT][AmBr$_6$]**, was crystallized by the chelation of $Am(NO_3)_3$ to **TPT** in MeOH. The recrystallization of **[CeTPT][CeBr$_6$]** from DMSO diffused with benzene yields two products both in high yields as **[CeTPT][3Br]** and **CeBr$_3$(DMSO)$_8$**, **Figure 8.2**.

X-ray analysis reveals **[CeTPT][3Br]** to crystallize the P*2*/c space group. The metal is 9-coordinate in the pocket of **TPT** forming a three-face centered trigonal prism. The average Ce–N_{Pyr} and Ce–N_{Tren} bond distances are 2.6328(12) Å, 2.6620(11) Å respectively, with a Ce–N(1) distance of 3.7360(13) Å.

8.3.2 Spectroscopy

^{1}H and ^{13}C NMR in MeOH-*d4* confirm the formation of the **[PuTPT][3Br]** and **[CeTPT][3Br]** complexes by crystallization from MeOH (Method A), **Figures 8.3-5**. Solid-state and solution-phase UV/vis/NIR absorption spectrum of **[PuTPT][3Br]** reveal a large charge

transfer band that continues into the NIR accounting for the intense dark coloring of the crystal, with λ_{max} of 440 nm (solid state), **Figure 8.6**. Due to the intense absorption band, we were unable to obtain ε values from the solution phase spectra, **Figure 8.7**. The sharper, less intense peaks at longer wavelengths are the $5f \rightarrow 5f$ Laporte-forbidden transitions of Pu^{3+}. The solid-state UV/vis/NIR absorption spectrum of **[CeTPT][3Br]** also shows a large broad band with λ_{max} at 396 nm. Neither compounds were found to exhibit emissive properties, **Figure 8.8**.

8.3.3 Electrochemistry

Due to the limited solubility of **TPT** and the complexes, cyclic voltammetry was conducted in DMSO. **TPT** exhibits redox active behavior with several oxidation peaks between approximately –1.2 and –2.2 V, **Figure 8.9**. The $Ce^{3+/4+}$ redox couple is shown to be quasi-reversible with an $E_{1/2}$ of 0.144 V and peak to peak separation of 0.635 V, **Figure 8.10**. **[PuTPT][3Br]** displays similar behavior, with four well resolved ligand-based peaks between approximately –1.2 and –2.2 V. The $Pu^{3+/4+}$ redox couple at $E_{1/2}$ = 0.184 V is quasi-reversible with peak to peak separation of 0.448 V, **Figure 8.11**. A reproducible peak present at $E_{1/2}$ = –2.5 V is speculated to be attributed to decomposition, with a small oxidation peak at –2.4 V.

8.4 Conclusion

The synthesis of the monometallic complexes, [**MTPT][3Br]**, is an example of the importance of starting materials and reactivity of the *f*-block series. **[PuTPT][3Br]** and **[CeTPT][3Br]** have been synthesized similarly to the bimetallic series, utilizing the bromide in place of the nitrate salt. Initial X-ray data along with NMR and UV/vis/NIR spectroscopy confirm the formation of the monometallic complexes. Recrystallization in DMSO produces X-ray quality crystals suitable for structural characterization.

8.5 Figures

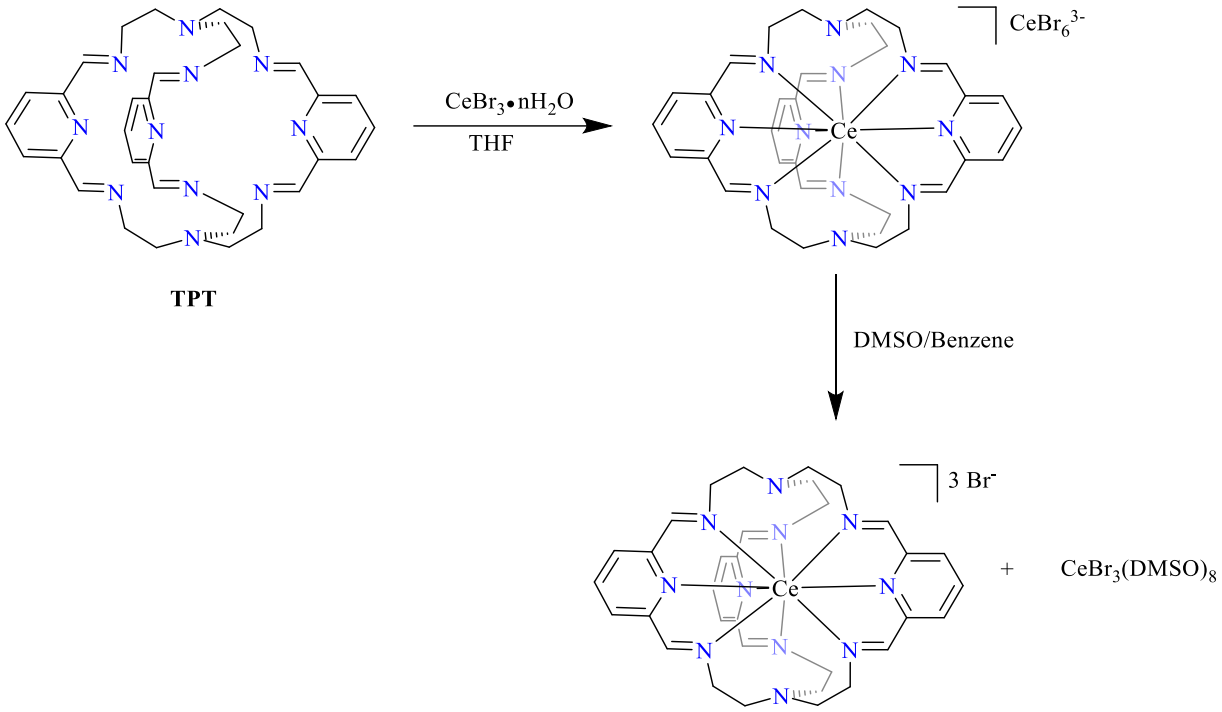

Figure 8.1. Summary of the synthesis of **[CeTPT][3Br]**.

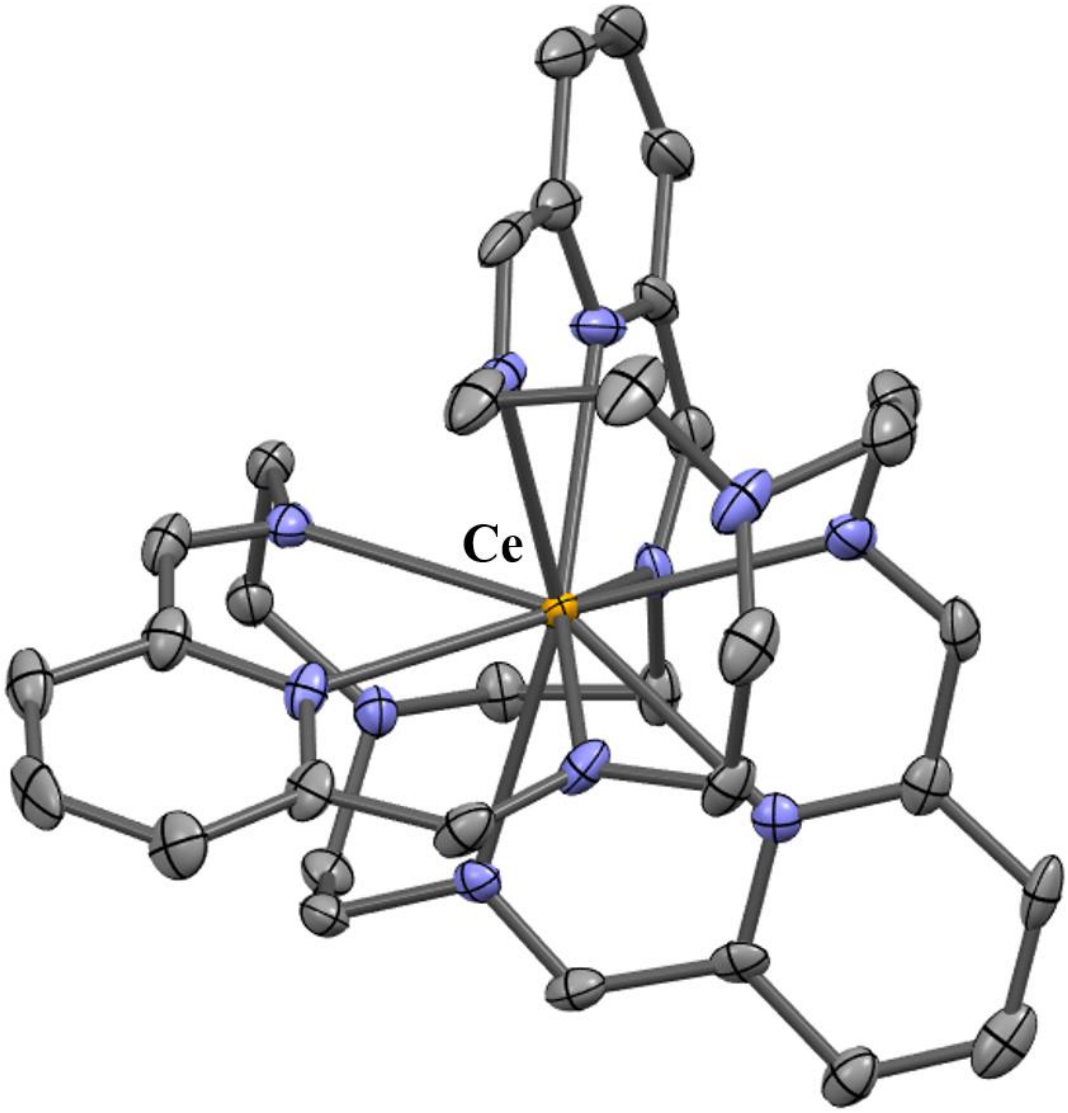

Figure 8.2. Molecular structure of **[CeTPT][3Br]** at the 50% probability level, omitting H and Br-atoms, and lattice solvent for clarity.

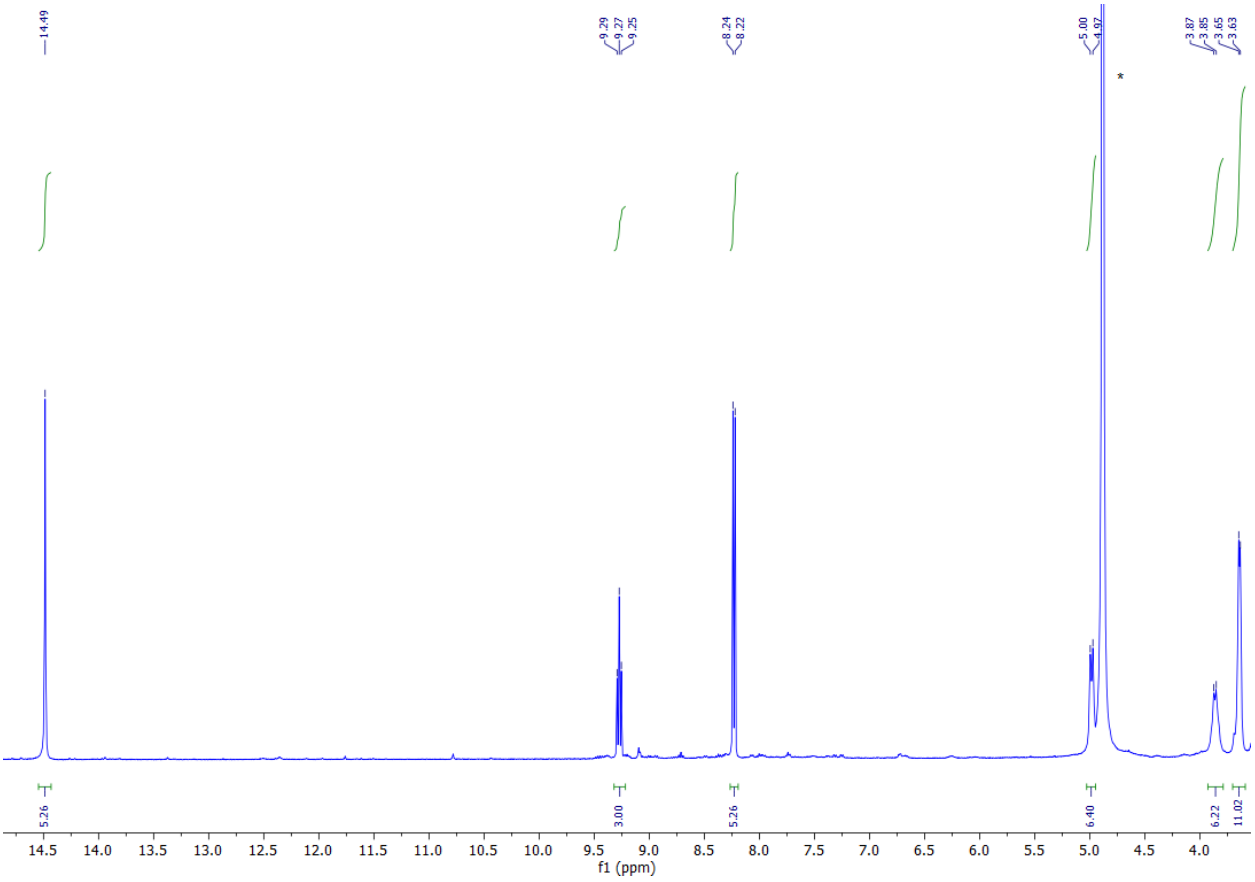

Figure 8.3. ^{1}H NMR of **[PuTPT][3Br]** in MeOH-*d4* at room temperature. * denoting solvent peaks.

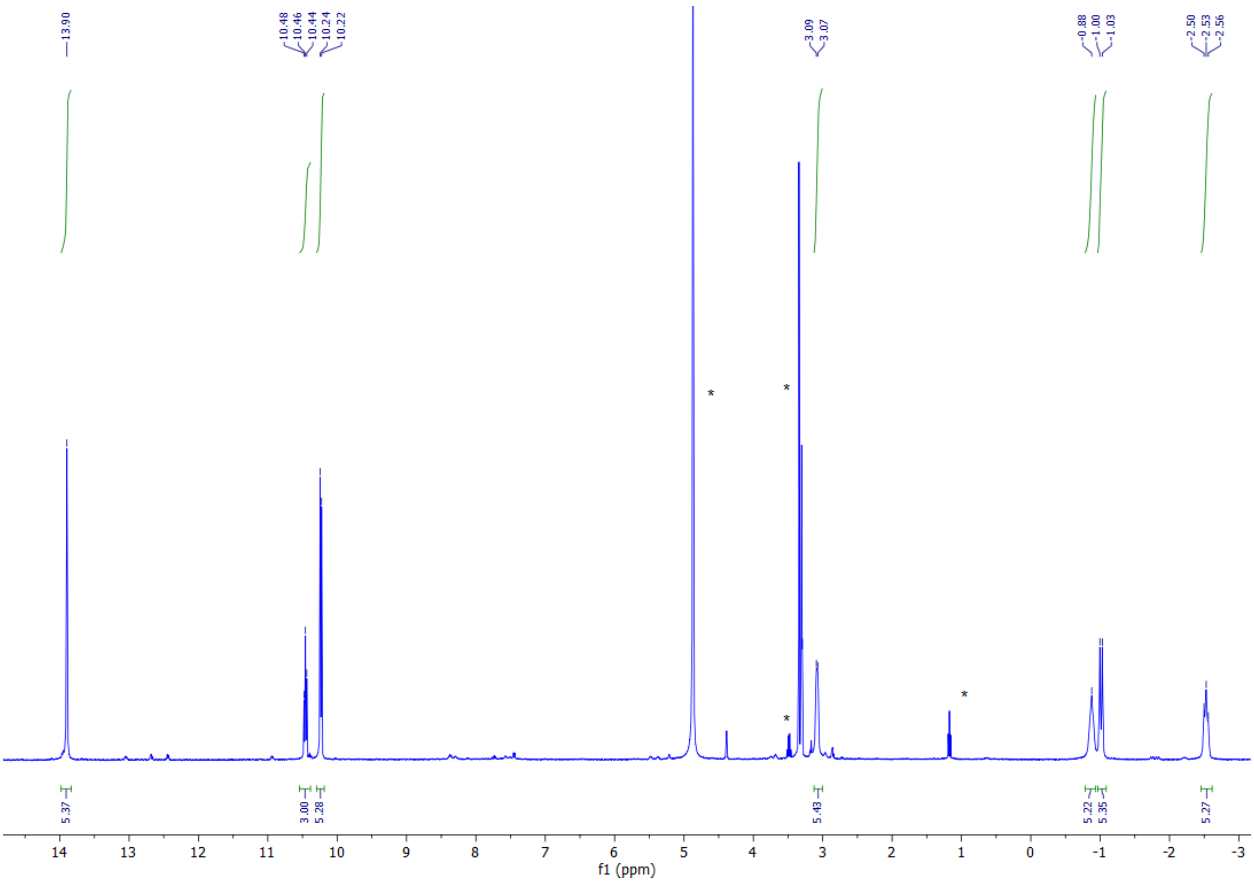

Figure 8.4. ^{1}H NMR spectrum of **[CeTPT][3Br]** in MeOH-*d4* a room tempterature. * denoting solvent peaks.

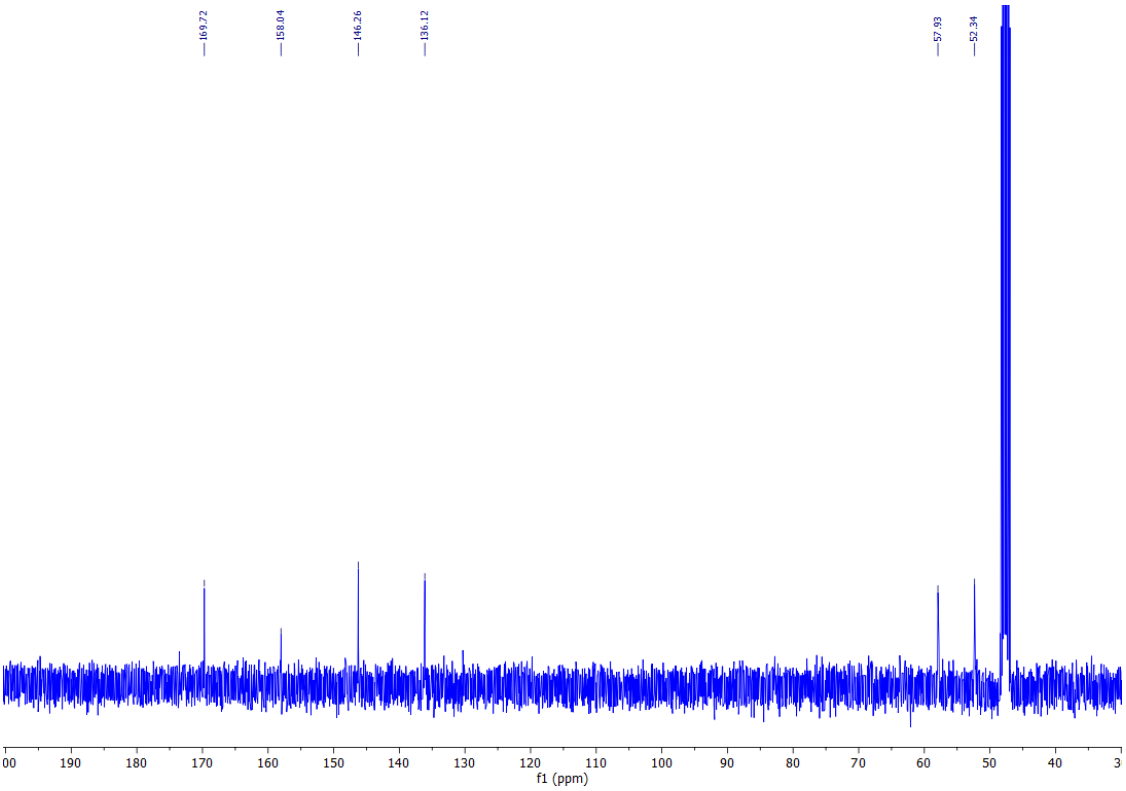

Figure 8.5. ^{13}C NMR spectrum of **[CeTPT][3Br]** in MeOH-*d4* at room temperature.

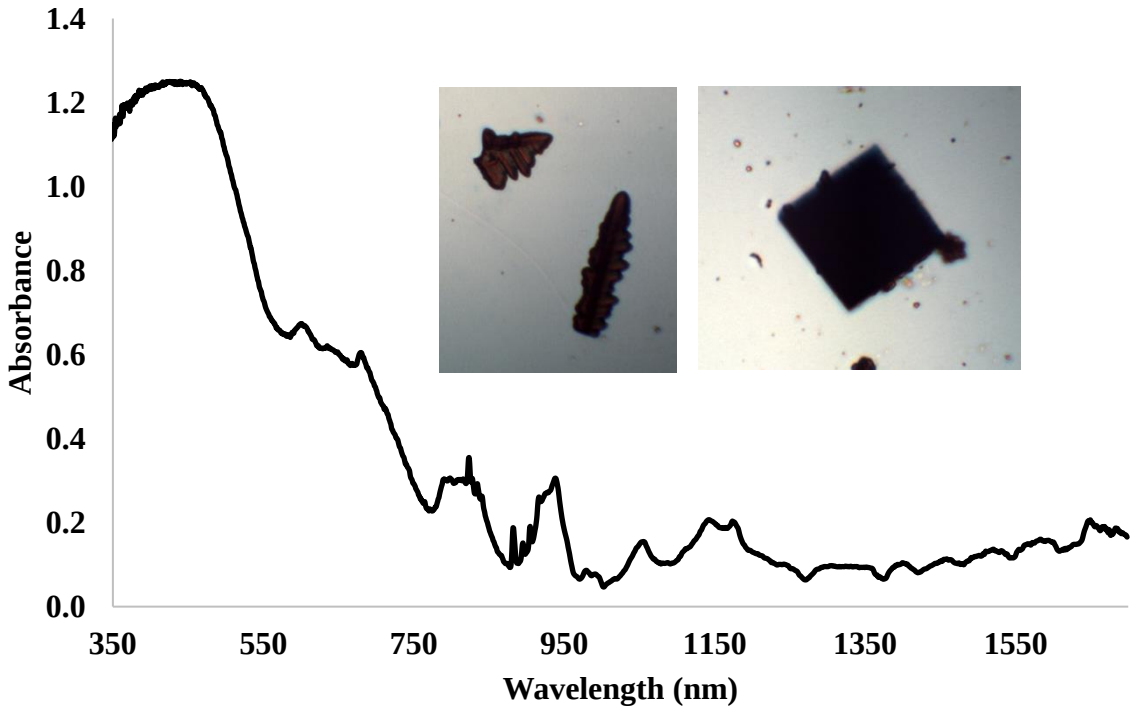

Figure 8.6. Solid-state UV/vis/NIR spectrum and photographs of **[PuTPT][3Br]** at room temperature.

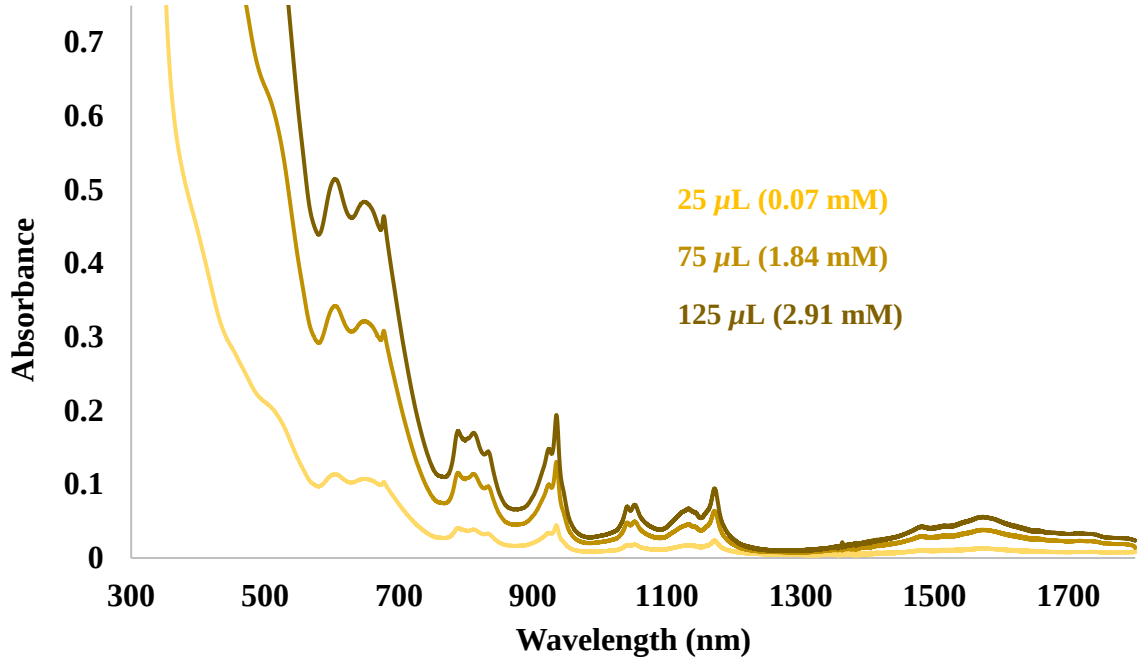

Figure 8.7. Solution-phase UV/vis/NIR of **[PuTPT][3Br]** in 1 g DMSO-*d6* at various concentrations where 125 μL = 3 mg **[CeTPT][3Br]** complex.

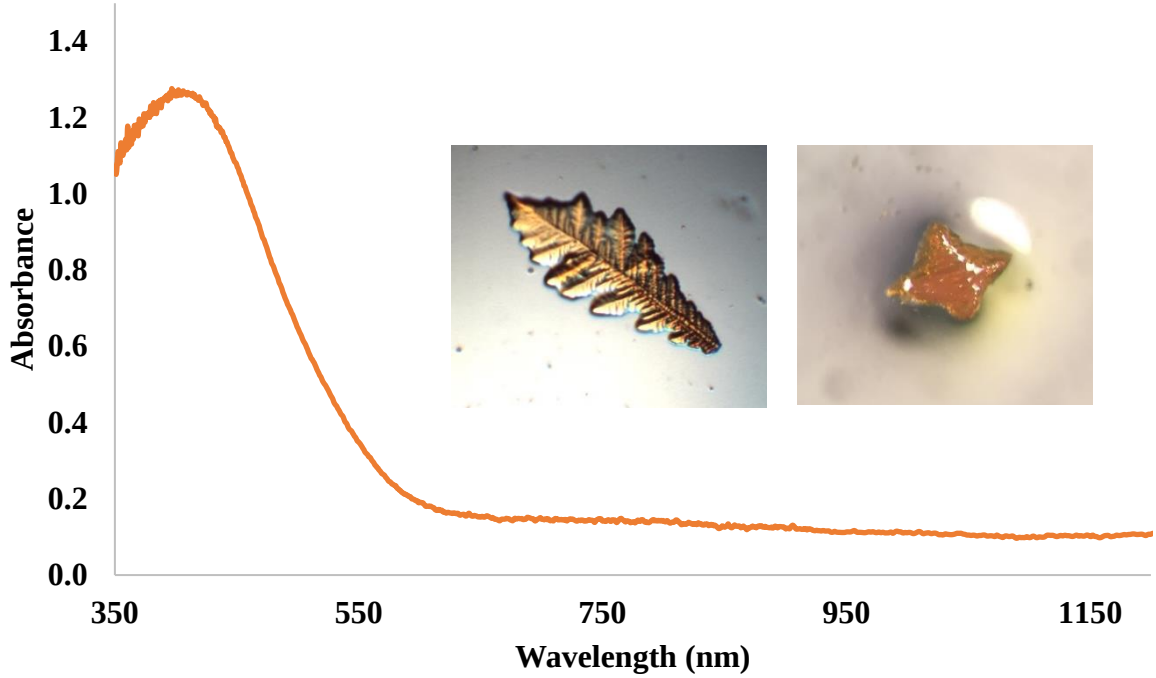

Figure 8.8. Solid-state UV/vis/NIR spectrum and photographs of **[CeTPT][3Br]** at room temperature.

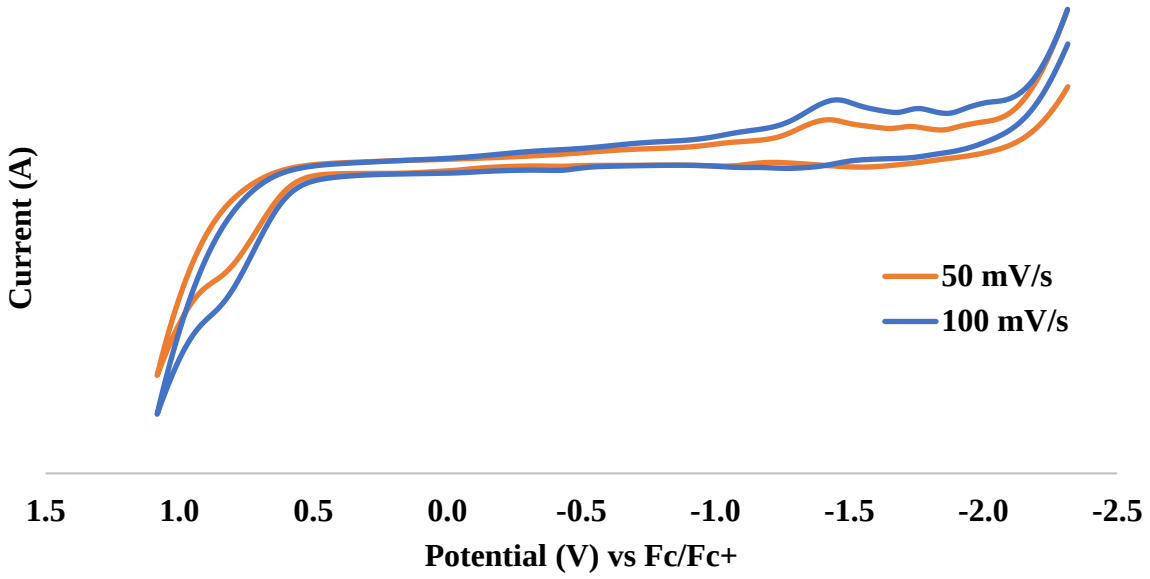

Figure 8.9. Cyclic voltammograms of 5 mM **TPT** in DMSO with 0.2 M [TBA][PF_6] supporting electrolyte.

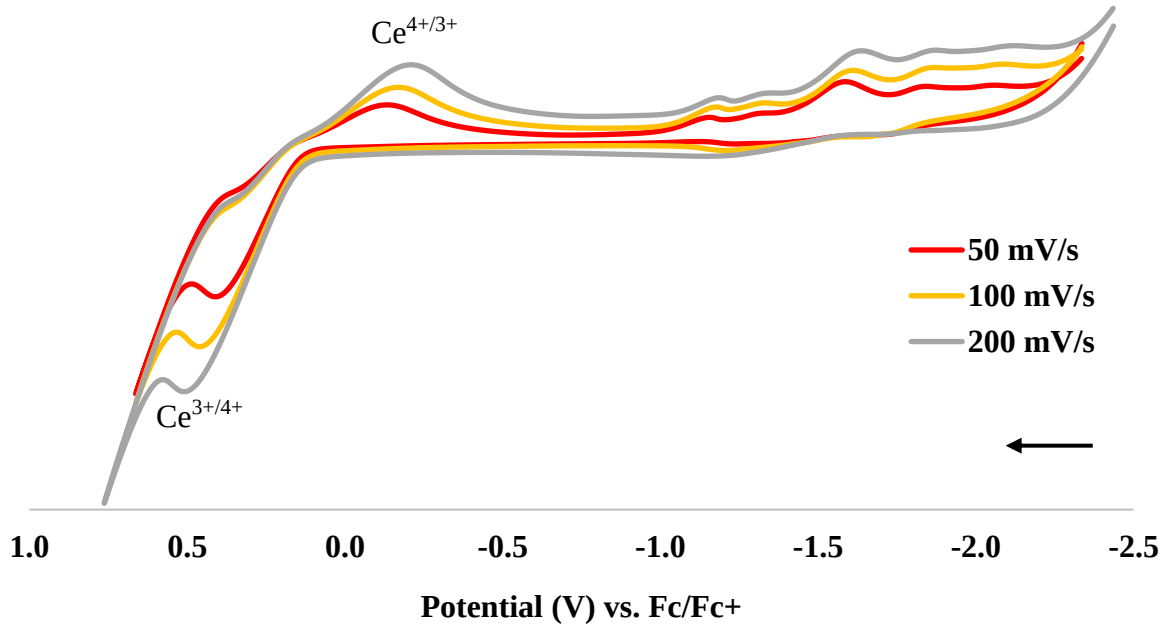

Figure 8.10. Cyclic voltammograms of 5 mM **[CeTPT][3Br]** in DMSO with 0.2 M [TBA][PF_6] supporting electrolyte at various scan rates.

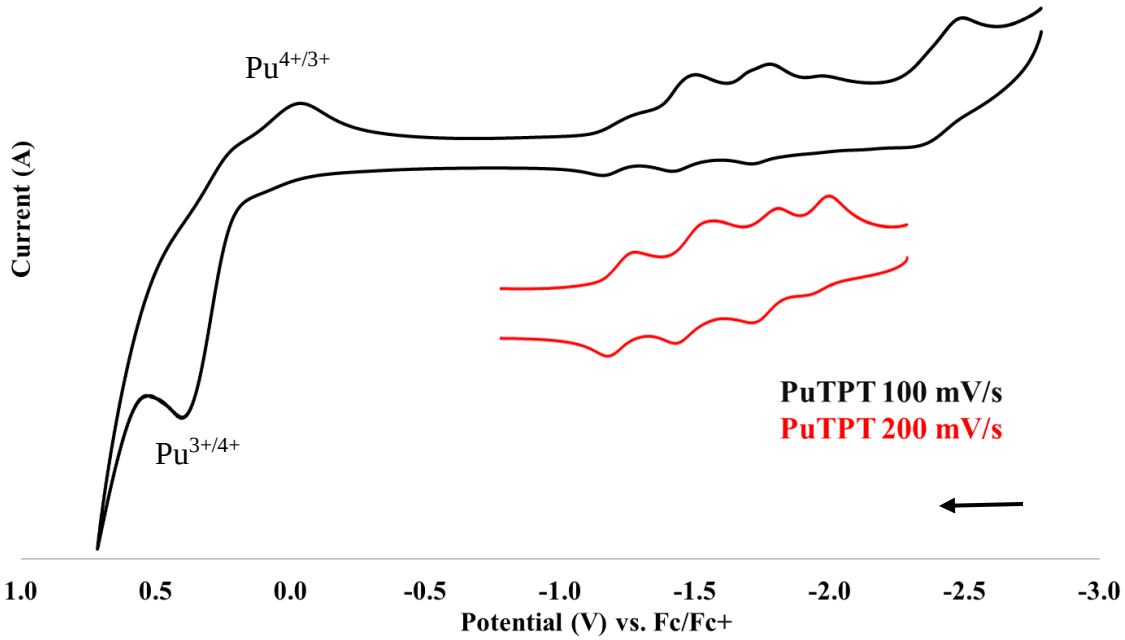

Figure 8.11. Cyclic voltammograms of 5 mM **[PuTPT][3Br]** in DMSO with 0.2 M [TBA][PF_6] supporting electrolyte. 100 mV/s scan in black and 200 mV/s scan highlighting the ligand redox couples in red.

CHAPTER 9
CONCLUSION

The work presented throughout this dissertation provides a new perspective on the periodicity of the lanthanide and early actinide series through non-aqueous coordination chemistry. The field of actinide chemistry lags significantly behind the rest of the periodic table due to their scarcity and radioactive nature. Understanding the complex chemistry of the actinide elements is important for civilian nuclear fuel production, spent nuclear fuel reprocessing, nuclear deterrents, waste disposal, and environmental monitoring. Currently, most of our knowledge on the behavior of these elements is limited to aqueous conditions. Under non-aqueous conditions, a large variety of ligands with various properties become available to study the coordination and bonding behavior of the actinides and lanthanides. Soft donor ligands also provide insight to the differences in the electronic bonding structure between actinides and lanthanides due to their selective behavior. Presented here, the Schiff base ligand, **L**, and neutral N-donor cryptand, **TPT**, are utilized to synthesize and characterize the lanthanide and actinide series through crystallographic, spectroscopic, electrochemical, and theoretical techniques.

The Schiff base ligand allows for characterization and comparison of the lanthanides and actinides in the trivalent, tetravalent, and hexavalent states. The first series described in this chapter describes the homoleptic tetravalent transition metal, lanthanide, and actinide complexes. Each metal is 8-coordinate in distorted square antiprism geometry, with the ligands stacked in sandwich-type structure. Bonding analysis shows the actinides follow a linear trend, while Ce displays less covalent behavior. Electrochemical experiments show that both **CeL_2** is stabilized by the ligand but displays irreversible behavior. In contrast, **PuL_2** is stabilized by the ligand to a greater extent and displays quasi-reversible behavior.

In the hexavalent Schiff base series, the uranyl system crystallized two products in the form **$UO_2L(MeOH)$** and **$UO_2Cl_2(H_2L)$. This demonstrates** the importance of the starting material as well as pH and salinity. Crystallographic analysis finds that **$UO_2L(MeOH)$** adopts the typical 7-coordinate uranyl Schiff base "boat confirmation." Rate constants were calculated from electrochemical experiments, confirming a quasi-reversible UO_2^{2+}/UO_2^{+} couple. In contrast, the 6-coordinate **$UO_2Cl_2(H_2L)$** complex features a neutral ligand with an unusual coordination mode outside of the N_2O_2 binding site. Theoretical analysis shows that

$UO_2Cl_2(H_2L)$ exhibits slightly more covalent character in the equatorial plane than **$UO_2L(MeOH)$** due to the covalent contributions from the U−Cl bonds. This may also explain the co-crystallization of these two complexes despite basic conditions. **$NpO_2L(MeOH)$** is isomorphous to the uranyl analog, however does not form the neutral ligand adduct "**$NpO_2Cl(H_2L)$**." Electrochemical experiments directly compare to the uranyl complex, showing the greater stabilization of the UO_2^{2+} complex compared to the NpO_2^{2+}.

A heterobimetallic series was synthesized, utilizing a transition metal and *f*-element. Of the first row transition metal salts used, the **$(ZnL)_2M(NO_3)_2Br(H_2O)$** (M = Ce, Nd, Am, Sm, Eu, Gd, Dy, Er) was the most successfully characterized product due to the favourable geometry of the 2+ transition metal. The Zn cations are bound to the inner N_2O_2 pocket of the ligand, forming two ZnL units approximately parallel to each other, with M bound to the phenolic oxygens of the ligand. M is further bound by two nitrates, exhibiting a distorted square antiprism geometry. None of these complexes exhibited emissive properties in the solid state.

The Lewis-acidity of the lanthanides was then employed to generate bimetallic complexes within an imine/hemiacetalate framework to provide the series **M_2TPT^{OMe}**. These products are generated from hydrolysis and methanolysis of the cage ligand likely facilitated by inductive effects stemming from the Lewis acidic lanthanide cation. These complexes result from imine cleavage to generate two metal binding sites; one pocketed site within the macrocycle and the other terminal site capping the hemiacetalate substituents. A clear demarcation in reactivity is observed between Sm and Eu, where the lighter and larger lanthanides generate a mixture of products, **Ln_2TPT^{OMe}** and **$[LnTPT][3(NO_3)]$**. Meanwhile, the heavier and smaller lanthanides generate exclusively bimetallic **Ln_2TPT^{OMe}**. The cleavage reactivity to form **Ln_2TPT^{OMe}** was extended beyond methanol to include other primary alcohols.

Utilizing the ligand, the **[MTPT][3Br]** (M = Pu, Ce) cage complexes were synthesized with the bromide salts. Initial X-ray data along with NMR and UV/vis/NIR spectroscopy confirm the formation of the monometallic complexes, however recrystallization in DMSO produces X-ray quality crystals suitable for structural characterization. CV experiments reveal **[PuTPT][3Br]** to exhibit more reversible redox couples compared to **[CeTPT][3Br]**.

Overall, this work captures several series of *f*-element coordination complexes in various oxidation states to better understand the periodicity and relative participation of actinide frontier orbitals in bonding. While current progress in actinide studies lag behind contemporary

knowledge of transition metal and lanthanide chemistry, these systems provide an opportunity to increase our knowledge of the structural preferences, reactivity signatures, and bonding interactions in *f*-element complexes.

APPENDIX A

TABLES FROM CHAPTER 1

Table A.1. Comparison of the number of structures in the Cambridge Crystallographic Data Center compared to the abundance of elements in the Earth's crust relative to Si.

Noble Metal	Abundance (ppm) Relative to Si	Number of Structures (CCDC)	*f*-element	Abundance (ppm) Relative to Si	Number of Structures (CCDC)
Ru	1×10^{-3}	30,422	Pu	NA	171
Rh	1×10^{-3}	14,090	U	2.7	6,587
Ir	1×10^{-3}	11,550	Th	9.6	1,012
Os	1.5×10^{-3}	6,420	Ce	66.5	2,460
Pt	5×10^{-3}	21,190	Total An	NA	8,041

Table A.2. Known lanthanide and actinide oxidation states, ( ) indicating instability. An = actinide.

La	Ce	Pr	Nd	Pm	Sm	Eu	Gd	Tb	Dy	Ho	Er	Tm	Yb	Lu
2	(2)	(2)	(2)	(2)	2	2	(2)	(2)	(2)	(2)	(2)	(2)	2	(2)
3	3	3	3	3	3	3	3	3	3	3	3	3	3	3
	4	(4)	(4)					(4)						

Ac	Th	Pa	U	Np	Pu	Am	Cm	Bk	Cf	Es	Fm	Md	No	Lr
	(2)	(2)	(2)	(2)	(2)	(2)		(2)	(2)	(2)	2	2	2	3
3	(3)	(3)	3	3	3	3	3	3	3	3	3	3	3	
	4	4	4	4	4	4	(4)	4	(4)					
		5	5	5	5	5								
			6	6	6	6								
				(7)	(7)	(7)								

APPENDIX B

TABLES FROM CHAPTER 2

Table B.1 Crystallographic information for **ML_2** (M = Ce, Pu, U, Zr, Hf, Th)

Compound	**CeL_2•2(CH_2Cl_2)**	**PuL_2•2(CH_2Cl_2)**	**UL_2•2(CH_2Cl_2)**
Empirical Formula	$C_{58}H_{68}Cl_4N_8O_4Ce$	$C_{58}H_{68}Cl_4N_8O_4Pu$	$C_{58}H_{68}Cl_4N_8O_4U$
Color	Black	Red	Red
Habit	Block	Irregular	Columnar
Temperature (K)	299(2)	298(2)	150(2)
Crystal System	Monoclinic	Monoclinic	Monoclinic
Space Group	*C2/c*	*C2/c*	*C2/c*
***a* (Å)**	15.120(6)	15.0632(9)	14.855(2)
***b* (Å)**	25.007(9)	24.9196(15)	24.820(3)
***c* (Å)**	15.405(6)	15.3540(9)	15.374(3)
α (deg)	90	90	90
β (deg)	95.137(9)	95.012(2)	95.234(2)
γ (deg)	90	90	90
Volume (Å^3)	5801(4)	5741.4(6)	5645(1)
Z	4	4	4
ρ_{calcd} (Mg/m^3)	1.400	1.533	1.554
μ (mm^{-1})	1.021	1.387	3.119
R1^a ($I > 2.0\sigma$(I))	0.0412	0.0491	0.0185
wR2 (all data)	0.0868	0.0906	0.0434

Table B.1 -continued

Compound	**ZrL_2•$(THF)_{0.25}$**	**HfL_2•$(THF)_{0.25}$**	**ThL_2•$2(CH_2Cl_2)$**
Empirical Formula	$C_{228}H_{264}N_{32}O_{17}Zr_4$	$C_{228}H_{264}N_{32}O_{17}Hf_4$	$C_{58}H_{68}Cl_4N_8O_4Th$
Color	Yellow	Yellow	Yellow
Habit	Columnar	Columnar	Columnar
Temperature (K)	120(2)	120(2)	120(2)
Crystal System	Monoclinic	Monoclinic	Monoclinic
Space Group	*$P2_1/c$*	*$P2_1/c$*	*C2/c*
***a* (Å)**	14.846(2)	14.8530(19)	14.880(3)
***b* (Å)**	19.683(3)	19.686(3)	24.966(5)
***c* (Å)**	35.574(5)	35.692(5)	15.406(5)
α (deg)	90	90	90
β (deg)	91.188(5)	91.044(4)	95.145
γ (deg)	90	90	90
Volume ($Å^3$)	10393(3)	10434(2)	5700(2)
Z	2	2	4
ρ_{calcd} (Mg/m^3)	1.307	1.413	1.532
μ (mm^{-1})	0.266	2.054	2.857
R1[a] (*I* > 2.0σ(I))	0.0544	0.0361	0.0193
wR2 (all data)	0.1324	0.0803	0.0455

[a]Definitions: $R1 = \Sigma||F_o| - |F_c||/\Sigma|F_o|$, $wR2 = [\Sigma w(F_o^2 - F_c^2)^2/\Sigma w(F_o^2)^2]^{1/2}$.

Goof = $S = [\Sigma[w(F_o^2-F_c^2)^2] / (n-p)]^{1/2}$ where n is the number of reflections and p is the total number of parameters refined.

Table B.2. Metrical comparisons of **ThL_2** with other 8-coordinate Th-Schiff base complexes.

Title complex	Avg. Th−O (Å)	Avg. Th−N (Å)	O−Th−O (˚)	N−Th−N (˚)
ThL_2	2.306(1)	2.639(1)	87.40(4)	60.43(4)
$Th(L^1)_2$	2.3(4)	2.65(2)	93.69	60.01
$Th(L^4)_2$	2.29(3)	2.63(1)	83.9(3)	61.4(2)
$Th(L^5)_2$	2.270(1)	2.658(2)		
$Th(L^3)Cl_2(py)_2$	2.21(1)	2.61(1)	154.1(6)	64.3(6)

Only distances pertaining to the Schiff base ligand(s) are given. L = *N*,*N*′-bis[(4, 4'-diethylamino)salicylidene]-1,2-phenylenediamine, R = NEt_2; L^1 = Salophen = *N,N*′-disalicylidene-o-phenylenediaminate, R = H; L^4 = 1,1′-{(1E,1′E)-[1,2-phenylenebis-(azanylylidene)}bis(methanylylidene)}bis(naphthalen-2-ol), R = H; L^5 = bis-[*N*,*N*′-bis-(3-allyl salicylidene)-o-phenylenediamine], R = $CH_2CH{=}CH_2$; L^3 = (±)-trans-3,3′-diethoxy-2,2′-[cyclohexane-1,2-diylbis(nitrilomethanylylidene)]diphenol, R = OCH_2CH_3.

Table B.3. Metrical comparisons of **UL_2** with other 8-coordinate U-Schiff base complexes.

Title complex	Avg. U−O (Å)	Avg. U−N_L (Å)	O−U−O (˚)	N−U−N (˚)
UL_2	2.250(1)	2.588(2)	86.23(5)	61.09(5)
$U(L^1)_2$	2.3(1)	2.62(2)	86.50	61.11
$U(L^2)_2$	2.23(2)	2.60(1)	154.6(2)	62.6(2)
$U(L^3)Cl_2(Py)_2$	2.190(4)	2.59(2)	152.2(2)	65.7(2)

Only distances pertaining to the Schiff base ligand(s) are given. L = *N*,*N*′-bis[(4, 4'-diethylamino)salicylidene]-1,2-phenylenediamine, R = NEt_2; L^1 = Unsubstituted salophen = *N,N*′-disalicylidene-o-phenylenediaminate, R = H; L^2 = *N,N*′-bis(3-methoxysalicylidene)-o-phenylenediaminate, R = OCH_3; L^3 = (±)-trans-3,3′-diethoxy-2,2′-[cyclohexane-1,2-diylbis(nitrilomethanylylidene)]diphenol, R = OCH_2CH_3.

Table B.4. Metrical comparisons of **HfL_2** and **ZrL_2** with other 8-coordinate Zr-salophen complexes.

Title Complex	Avg. M−O (Å)	Avg. M−N (Å)	O−M−O (˚)	N−M−N (˚)
HfL_2	2.108(2)	2.358(3)	74.29(8)	66.54(9)
ZrL_2	2.113(2)	2.375(2)	74.73(7)	66.21(8)
$Zr(L^6)_2$	2.109(5)	2.40(2)	74.25(7)	66.21

Table B.4. -continued

$Zr(L^7)_2$	2.085(5)	2.42(1)	96.5(2)	67.2(4)

Only distances pertaining to the Schiff base ligand(s) are given. L = *N*,*N*′-bis[(4, 4'-diethylamino)salicylidene]-1,2-phenylenediamine, R = NEt_2; L^6 = (5-methoxysalicylidene)-4,5-dimethyl-1,2-phenylenediamine, R = OCH_3; L^7 = Bis(4-amino-*N*,*N*′-disalicylidene-l,2-phenylenediaminato), R = H.

Table B.5. Metrical comparisons of average selected bond distances (Å) and angles (˚) for **ML_2** (M = Zr, Hf, Ce, Th, U, Pu) complexes

Complex	8-Coordinate ionic radius	M−O_{avg} (Å)	M−N_{avg} (Å)	O−M−O (°)	N−M−N (°)
HfL_2	0.83	2.11(1)	2.36(1)	74.1(6)*	66.5(5)*
ZrL_2	0.84	2.11(1)	2.38(1)	74.7(6)*	66.2(5)*
PuL_2	0.96	2.225(1)	2.55(2)	84.9(1)	61.6(1)
CeL_2	0.97	2.24(2)	2.59(1)	85.82(6)	61.09(6)
UL_2	1.0	2.250(8)	2.58(1)	86.23(5)	61.09(5)
ThL_2	1.05	2.306(1)	2.369(1)	87.40(4)	60.43(4)

*Average bond angles

Table B.6. Transitions assignment for main bands in absorbance spectra from **Figure 2.5** in the main text.

Band	Wavelength (nm)	Assignment
1a	498	$\pi \rightarrow f\pi$ (LMCT)[a]
		$\pi \rightarrow f$ (LMCT)
		$f\pi \rightarrow \pi$ (MLCT)[b]
1b	570	$\pi \rightarrow f\pi$ (LMCT)[a]

Table B.6. -continued

		$\pi \rightarrow f$ (LMCT)
2a	798	$f \rightarrow f$
		$f \rightarrow f\pi$
2b	800	$f \rightarrow f\pi$
		$f\pi \rightarrow f\pi$
3a	1138	$f \rightarrow f$
		$f \rightarrow f\pi$
3b	1090	$f \rightarrow f$
		$f \rightarrow f\pi$

[a] Not formally a ligand-to-metal charge transfer transition due to strong mixing between orbitals

[b] Not formally a metal-to-ligand charge transfer transition due to strong mixing between orbitals

Table B.7. Transitions assignment for main bands in absorbance spectra from Figure 2.8.

Band	Wavelength (nm)	Assignment
a	390	$\pi \rightarrow \pi^*$
		$\pi \rightarrow d\pi$ (LMCT)[a]
b	370	$\pi \rightarrow \pi^*$
		$\pi \rightarrow d\pi$ (LMCT)[a]
c	460	$\pi \rightarrow f$ (LMCT)
		$\pi \rightarrow f\pi$ (LMCT)[a]
d	405	$\pi \rightarrow \pi^*$
		$\pi \rightarrow d\pi$ (LMCT)[a]
		$\pi \rightarrow f\pi$ (LMCT)[a]

[a] Not formally a LMCT transition due to strong mixing between orbitals

Table B.8. Bonding metrics derived from QTAIM theory. M−O and M−N data correspond to the stronger bonds for each oxygen and nitrogen bond.

	ρ(r)	|V(r)|/G(r)	H(r)	H(r)/ρ(r)
Hf−O(avg)	0.0905	1.1413	-0.0162	-0.1793
Ce−O(2)	0.0856	1.1856	-0.0163	-0.1905
Th−O(1)	0.0805	1.1853	-0.0152	-0.1881
U−O(2)	0.0907	1.1860	-0.0180	-0.1990
Pu−O(2)	0.0914	1.1724	-0.0181	-0.1980
Hf−N(avg)	0.0625	1.1807	-0.0104	-0.1662
Ce−N(1)	0.0487	1.1026	-0.0038	-0.0782
Th−N(2)	0.0488	1.1560	-0.0056	-0.1142
U−N(1)	0.0529	1.1476	-0.0060	-0.1126
Pu−N(2)	0.0531	1.1254	-0.0056	-0.1053

APPENDIX C

TABLES FROM CHAPTER 3

Table C.1 Crystallographic information for **$UO_2L(MeOH)$** and **$UO_2Cl_2(H_2L)$**

Compound	**$UO_2L(MeOH)$**	**$UO_2Cl_2(H_2L)$**
Empirical Formula	$C_{29}H_{36}N_4O_5U$	$C_{28}H_{34}Cl_2N_4O_4U$
Formula Weight	758.65	799.52
Color	Red	Orange
Habit	Plate	Plate
Temperature (K)	150(1)	150(1)
Crystal System	Monoclinic	Triclinic
Space Group	$P2_1/c$	$P\bar{1}$
***a* (Å)**	14.5672(14)	9.4250(11)
***b* (Å)**	10.0842(10)	11.8107(14)
***c* (Å)**	19.3197(18)	15.4884(18)
α (deg)	90	110.159(4)
β (deg)	99.197(3)	95.049(4)
γ (deg)	90	99.191(3)
Volume (Å^3)	2801.6(5)	1578.6(3)
Z	4	2
ρ_{calcd} (Mg/m^3)	1.799	1.682
μ (mm^{-1})	5.839	5.348
GOF F^2	1.058	1.070
R1[a] ($I > 2.0\sigma$(I))	0.0236	0.0271
wR2 (all data)	0.0477	0.0505

[a]Definitions: $R1 = \Sigma||F_o| - |F_c||/\Sigma|F_o|$, $wR2 = [\Sigma w(F_o^2 - F_c^2)^2/\Sigma w(F_o^2)^2]^{1/2}$.

Goof = $S = [\Sigma[w(F_o^2-F_c^2)^2] / (n-p)]^{1/2}$ where n is the number of reflections and p is the total number of parameters refined.

Table C.2. Metrical comparisons of 7-coordinate **$UO_2(L^x)(MeOH)$** complexes[a]

	$UO_2L(MeOH)$	$UO_2L^1(MeOH)$	$UO_2L^2(MeOH)$	$UO_2L^3(MeOH)$
Avg. U−O_L (Å)	2.285(2)	2.29(3)	2.234(3)	2.288(4)
Avg. U−N_L (Å)	2.543(2)	2.56(2)	2.555(4)	2.548(5)
Avg. O≡U≡O (Å)	1.783(2)	1.77(1)	1.796(4)	1.789(4)
O_{yl}–U–O_{yl} (˚)	178.92(7)	178.6(6)	176.9(2)	176.6(2)
O_L−U−O_L (˚)	157.01(6)	155.73	157.1(1)	153.0(2)
N−U−N (˚)	63.15(6)	66.2(4)	62.9(1)	63.7(2)

[a]Only distances pertaining to the Schiff base ligand and uranyl moiety are given. L = *N,N′*-bis[(4, 4'-diethylamino)salicylidene]-1,2-phenylenediamine; L^1 = unsubstituted salen = *N,N′*-Bis(salicylidene)ethylenediamine; L^2 = *N,N′*-bis(3,5-di-t-butylsalicylidene-4,5-dimethyl-1,2-henylenediamine; L^3 = *N,N′*-di(5-bromosalicylidene)-*o*-phenylenediaminate

Table C.3. Decomposition of the multiconfigurational ground states using the SO-PT2(6,10) wave functions. Ligand orbitals p_σ and p_π refer to the 2*p* oxygen orbitals that mix with the 5*f* orbitals are depicted in red.

State	UO_2^{2+}		**$UO_2Cl_2(H_2L)$**		**$UO_2(MeOH)L$**	
Σ_g	79%	$p_\pi^4 p_\sigma^2 f_\delta^0 f_\varphi^0 f_\pi^0 f_\sigma^0$	76%	$p_\pi^4 p_\sigma^2 f_\delta^0 f_\varphi^0 f_\pi^0 f_\sigma^0$	73%	$p_\pi^4 p_\sigma^2 f_\delta^0 f_\varphi^0 f_\pi^0 f_\sigma^0$
	13%	$p_\pi^3 p_\sigma^2 f_\delta^0 f_\varphi^0 f_\pi^1 f_\sigma^0$	14%	$p_\pi^3 p_\sigma^2 f_\delta^0 f_\varphi^0 f_\pi^1 f_\sigma^0$	17%	$p_\pi^3 p_\sigma^2 f_\delta^0 f_\varphi^0 f_\pi^1 f_\sigma^0$
	3%	$p_\pi^4 p_\sigma^1 f_\delta^0 f_\varphi^0 f_\pi^0 f_\sigma^1$	4%	$p_\pi^4 p_\sigma^1 f_\delta^0 f_\varphi^0 f_\pi^0 f_\sigma^1$	5%	$p_\pi^4 p_\sigma^1 f_\delta^0 f_\varphi^0 f_\pi^0 f_\sigma^1$

Table C.4. NBOs involving the UO_2^{2+} ion, their compositions in terms of natural hybrid orbitals, assignment, and occupation numbers derived from PBE0/TZVP wavefunctions

NBO	Bond type	**UO_2^{2+}**		**$UO_2Cl_2(H_2L)$**		**$UO_2L(MeOH)$**	
		NHOs	Occ	NHOs	Occ	NHOs	Occ
BD(1)	π	76% $O_{yl}(p)$ + 24% U(*fd*)	1.99	79% $O_{yl}(p)$ + 21% U(*fd*)	1.99	79% $O_{yl}(p)$ + 21% U(*fd*)	1.99
BD(2)	π	76% $O_{yl}(p)$ + 24% U(*fd*)	1.99	79% $O_{yl}(p)$ + 21% U(*fd*)	1.99	80% $O_{yl}(p)$ + 20% U(*fd*)	1.99
BD(3)	σ	64% $O_{yl}(sp^3)$ + 36% U(*fd*)	1.90	73% $O_{yl}(sp^3)$ + 27% U(*fd*)	1.92	73% $O_{yl}(sp^3)$ + 27% U(*fd*)	1.92
BD(4)	π	76% $O_{yl}(p)$ + 24% U(*fd*)	1.99	79% $O_{yl}(p)$ + 21% U(*fd*)	1.99	80% $O_{yl}(p)$ + 20% U(*fd*)	1.99
BD(5)	π	76% $O_{yl}(p)$ + 24% U(*fd*)	1.99	79% $O_{yl}(p)$ + 21% U(*fd*)	1.99	79% $O_{yl}(p)$ + 21% U(*fd*)	1.98
BD(6)	σ	64% $O_{yl}(sp^6)$ + 36% U(*fd*)	1.90	73% $O_{yl}(sp^3)$ + 27% U(*fd*)	1.91	75% $O_{yl}(sp^3)$ + 25% U(*fd*)	1.92
LV(1)	NB	U(87% 7*s* + 13% 6*d*)	0.04	U(100% 6*d*)	0.37	U(58% 5*f* + 42% 6*d*)	0.38
LV(2)	NB	U(100% 5*f*)	0.00	U(48% 5*f* + 35% 7*s* + 17% 6*d*)	0.31	U(84% 6*d* + 16% 5*f*)	0.31
LV(3)	NB	U(100% 5*f*)	0.00	U(100% 5*f*)	0.22	U(76% 7*s* + 14% 6*d* + 10% 5*f*	0.20

Table C.4 -continued

LV(4)	NB	U(100% 5*f*)	0.00	U(66% 6*d* + 34% 7*s*)	0.20	U(42% 6*d* + 39% 5*f* + 19% 7*s*)	0.20
LV(5)	NB	U(100% 5*f*)	0.00	U(51% 5*f* + 30% 7*s* + 19% 6*d*)	0.17	U(78% 5*f* + 18% 6*d* + 4% 7*s*)	0.15
LV(6)			0.00	U(100% 5*f*)	0.13	U(84% 5*f* + 16% 6*d*)	0.07
LV(7)			0.00	U(75% 5*f* + 20% 6*d* + 5% 7*p*)	0.01	U(100% 5*f*)	0.03
BD*(1)	π*	76% U(*fd*)+ 24% O_{yl}(*p*)	0.02	79% O_{yl}(*p*) + 21% U(*fd*)	0.06	79% U(*fd*) + 21% O_{yl}(*p*)	0.03
BD*(2)	π*	76% U(*fd*)+ 24% O_{yl}(*p*)	0.02	79% O_{yl}(*p*) + 21% U(*fd*)	0.06	80% U(*fd*) + 20% O_{yl}(*p*)	0.06
BD*(3)	σ*	64% U(*fd*)+ 36% O_{yl}(sp^3)	0.13	73% O_{yl}(sp^3) + 27% U(*fd*)	0.17	73% U(*fd*) + 27% O_{yl}(sp^3)	0.17
BD*(4)	π*	76% U(*fd*)+ 24% O_{yl}(*p*)	0.02	79% O_{yl}(*p*) + 21% U(*fd*)	0.05	80% U(*fd*) + 20% O_{yl}(*p*)	0.04
BD*(5)	π*	76% U(*fd*)+ 24% O_{yl}(*p*)	0.02	79% O_{yl}(*p*) + 21% U(*fd*)	0.06	79% U(*fd*) + 21% O_{yl}(*p*)	0.05
BD*(6)	σ*	64% U(*fd*)+ 36% O_{yl}(sp^3)	0.13	73% O_{yl}(sp^3) + 27% U(*fd*)	0.19	75% U(*fd*) + 25% O_{yl}(sp^3)	0.16

Table C.5. QTAIM metrics derived from SO-PT2(6,10) wave functions. The corresponding units (in parenthesis) are ρ (e/Bohr^3), G (kJ/mol Bohr^3), V (kJ/mol Bohr^3), H (kJ/mol Bohr^3), H/ρ (kJ/mol per electron)

		ρ(r)	G(r)	V(r)	|V(r)|/G(r)	H(r)	H(r)/ρ(r)
UO_2^{2+}	$U{\equiv}O_{yl}$	0.349	1135.9	-2064.7	1.818	-928.7	-2663.4
$UO_2Cl_2(H_2L)$	$U{\equiv}O_{yl}$	0.310	958.4	-1733.7	1.809	-775.3	-2498.6
	$U{\equiv}O_{yl}$	0.312	961.2	-1718.9	1.788	-757.6	-2426.8
	$U\text{-}O_L$	0.079	227.5	-258.2	1.135	-30.7	-388.8
	$U\text{-}O_L$	0.081	231.1	-264.7	1.145	-33.5	-415.6
	U-Cl	0.062	121.4	-151.3	1.246	-29.9	-485.4
	U-Cl	0.063	124.3	-155.0	1.247	-30.7	-490.9
$UO_2L(MeOH)$	$U{\equiv}O_{yl}$	0.301	915.7	-1622.9	1.772	-707.2	-2350.3
	$U{\equiv}O_{yl}$	0.302	911.0	-1621.9	1.780	-710.8	-2356.1
	$U\text{-}O_L$	0.094	263.6	-316.9	1.202	-53.3	-565.8
	$U\text{-}O_L$	0.079	207.7	-242.8	1.169	-35.1	-446.6
	$U\text{-}O_{MeOH}$	0.053	143.5	-152.1	1.060	-8.6	-161.9
	$U\text{-}N_L$	0.059	122.7	-143.3	1.167	-20.5	-347.0
	$U\text{-}N_L$	0.055	113.1	-130.5	1.154	-17.4	-315.0

Table C.6. Covalency degree (kJ/mol per electron) values in axial and equatorial contributions.

Covalency Degree	Axial	Equatorial	Total
UO_2^{2+}	-5326.8	-	-5326.8
$UO_2Cl_2(H_2L)$	-4925.4	-1780.7	-6706.1
$UO_2L(MeOH)$	-4706.4	-1836.2	-6542.6

Table C.7. IQA energy decomposition analysis. The total energy of interaction between atoms A and B (E_{AB}) is decomposed into their Coulomb/electrostatic (E_C) and exchange (E_X) parts. The analysis is based on a HF calculation. Energies are expressed in kJ/mol.

	A–B	E_C	E_X	E_{AB}	% E_X
UO_2^{2+}	U≡O_{yl}	-1810.4	-1431.3	-3241.7	44.2
$UO_2Cl_2(H_2L)$	U≡O_{yl}	-3249.7	-1097.2	-4346.9	25.2
	U≡O_{yl}	-3182.9	-1112.3	-4295.2	25.9
	U-Cl	-1514.2	-223.9	-1738.1	12.9
	U-Cl	-1519.4	-222.0	-1741.5	12.8
	U-O_L	-2884.4	-213.2	-3097.6	6.9
	U-O_L	-2877.2	-207.0	-3084.1	6.7
$UO_2L(MeOH)$	U≡O_{yl}	-3250.3	-1072.8	-4323.0	24.8
	U≡O_{yl}	-3194.4	-1086.5	-4280.9	25.4

Table C.7. -continued

$U\text{-}O_L$	-2917.7	-211.1	-3128.8	6.7
$U\text{-}O_L$	-3033.4	-255.3	-3288.7	7.8
$U\text{-}O_{MeOH}$	-2548.0	-126.9	-2674.9	4.7
$U\text{-}N_L$	-2945.8	-144.8	-3090.6	4.7
$U\text{-}N_L$	-3033.9	-154.4	-3188.4	4.8

APPENDIX D

TABLES FROM CHAPTER 4

Table D.1. Crystallographic information for **NpL_2** and **$NpO_2L(MeOH)$**

Compound	**NpL_2·2DCM**	**$NpO_2L(MeOH)$**
Empirical Formula	$C_{58}H_{68}N_8O_4Cl_4Np$	$C_{29}H_{36}N_4O_5Np$
Color	Orange	Black
Habit	Columnar	Irregular
Temperature (K)	298(2)	100
Crystal System	Monoclinic	Monoclinic
Space Group	*C*2/*c*	$P2_1/c$
***a* (Å)**	14.9971(12)	14.4694(6)
***b* (Å)**	24.825(2)	10.0621(4)
***c* (Å)**	15.306(2)	19.2240(8)
α (deg)	90	90
β (deg)	95.112(2)	99.0190(10)
γ (deg)	90	90
Volume (Å^3)	5675.8(10)	2764.3(2)
Z	4	4
ρ_{calcd} (Mg/m^3)	1.545	1.820
μ (mm^{-1})	2.073	3.805
R1[a] ($I > 2.0\sigma$(I))	0.0334	0.0256
wR2 (all data)	0.0700	0.0608

[a]Definitions: $R1 = \Sigma||F_o| - |F_c||/\Sigma|F_o|$, $wR2 = [\Sigma w(F_o^2 - F_c^2)^2/\Sigma w(F_o^2)^2]^{1/2}$.

Goof = $S = [\Sigma[w(F_o^2-F_c^2)^2] / (n-p)]^{1/2}$ where n is the number of reflections and p is the total number of parameters refined.

Table D.2. Metrical comparisons of average selected bond distances (Å) and angles (˚) for **NpL_2** and **ML_2** (**M = Pu, Ce, U, Th**) complexes

Complex	8-Coord Ionic Radius[150]	M−O_{avg} (Å)	M−N_{avg} (Å)	O−M−O (°)	N−M−N (°)
PuL_2[97]	0.96	2.225(3)	2.555(1)	84.9(1)	61.6(1)
CeL_2[97]	0.97	2.240(2)	2.590(2)	85.82(6)	61.09(6)
NpL_2	0.98	2.231(2)	2.562(2)	85.37(7)	61.38(7)
UL_2[98]	1.00	2.250(1)	2.588(2)	86.23(5)	61.09(5)
ThL_2[98]	1.05	2.306(1)	2.639(1)	87.40(4)	60.43(4)

Table D.3. Metrical comparisons of **$NpO_2L(MeOH)$** with other NpO_2 Schiff base complexes.

	$NpO_2L(MeOH)$	$Np^{6+}O_2(salen)(MeOH)$[36]	$\{[Np^{5+}O_2(salen)]_4L'_2\}L''_2$[37]
Avg. Np−O_L (Å)	2.266(2)	2.25(6)	2.37(1)
Avg. Np−N (Å)	2.530(3)	2.53(3)	2.59(3)
O_{yl}=Np=O_{yl} (Å)	1.762(2)	1.757	1.86(3)
O_{yl}−Np−O_{yl} (°)	179.2(1)	179.2	175(1)
O_L−Np−O_L (˚)	156.64(9)	154.25	153(1)

Only distances pertaining to the Schiff base ligand(s) are given. Salen = *N,N′*-disalicylidene-o-phenylenediaminate; L′ = μ_8-K; L″ = K(18C6)py.

Table D.4. Kinetic data for **$NpO_2L(MeOH)$.**

Scan Rate (V/s)	Reversibility ΔE_p (mV)	Nicholson Parameter (Ψ)
0.025	91	0.80
0.05	103	0.55
0.1	117	0.39
0.2	136	0.26
0.3	148	0.21
0.4	158	0.18

APPENDIX E

TABLES FROM CHAPTER 5

Table E.1. Metrical comparisons of **1-M** (M = Ce, Nd, Am, Sm, Eu, Gd, Dy, Er).

M	M^{3+} ionic radii (Å)	M–O (Å)	Zn···Zn (Å)	Zn···M (Å)	Zn···M···Zn (°)
Ce	1.143	2.4115(4)	4.591(1)	3.47975(6)	82.542(11)
Nd	1.09	2.3560(6)	4.545(1)	3.4133(7)	83.489(15)
Am	1.09	2.3839(3)	4.580(1)	3.4515(4)	83.135(8)
Sm	1.079	2.3471(3)	4.546(1)	3.4121(4)	83.537(8)
Eu	1.066	2.3310(4)	4.531(1)	3.3947(6)	83.3513(4)
Gd	1.053	2.4161(3)	4.506(1)	3.3539(4)	84.408(8)
Dy	1.027	2.3001(5)	4.523(1)	3.3744(6)	84.166(12)
Er	1.004	2.2773(8)	4.521(1)	3.3525(10)	84.79(2)

APPENDIX F

TABLES FROM CHAPTER 6

Table F.1 Crystallographic information for **LnTPT^{X}**

Compound	**Ce_2TPT^{OMe} (MeOH) •2MeOH**	**Pr_2TPT^{OMe} (MeOH) •2MeOH**	**Nd_2TPT^{OMe} (MeOH) •2MeOH**
Empirical Formula	$C_{33}H_{48}N_{10}O_{18}Ce_2$	$C_{33}H_{48}N_{10}O_{18}Pr_2$	$C_{33}H_{48}N_{10}O_{18}Nd_2$
Temperature (K)	100	100	100
Crystal System	Monoclinic	Monoclinic	Orthorhombic
Space Group	$P2_1/n$	$P2_1/n$	$P2_12_12_1$
***a* (Å)**	11.332(2)	11.264(2)	13.15(1)
***b* (Å)**	12.702(2)	12.683(2)	15.14(26)
***c* (Å)**	30.630(4)	30.668(5)	21.85(2)
α (°)	90	90	90
β (°)	91.243(2)	91.194(2)	90
γ (°)	90	90	90
Volume (Å^3)	4408(1)	4380(1)	4351(8)
Z	4	4	4
ρ_{calcd} (Mg/m^3)	1.7375	1.7522	1.7727
μ (mm^{-1})	2.123	2.282	2.444
R1^a ($I > 2.0\sigma$(I))	0.0262	0.0350	0.0271
wR2 (all data)	0.0525	0.0709	0.0519

Table F.1. -continued

Compound	**Sm_2TPT^{OMe} (MeOH) •MeOH**	**Eu_2TPT^{OMe} •2MeOH**	**Gd_2TPT^{OMe} •2MeOH**	**Tb_2TPT^{OMe} •2MeOH**
Empirical Formula	$C_{32}H_{44}N_{10}O_{17}Sm_2$	$C_{32}H_{44}N_{10}O_{17}Eu_2$	$C_{32}H_{44}N_{10}O_{17}Gd_2$	$C_{32}H_{44}N_{10}O_{17}Tb_2$
Temperature (K)	100	100	100	100
Crystal System	Orthorhombic	Orthorhombic	Orthorhombic	Orthorhombic
Space Group	$P2_12_12_1$	$P2_12_12_1$	$P2_12_12_1$	$P2_12_12_1$
***a* (Å)**	13.165(2)	13.101(3)	12.965(6)	12.889(3)
***b* (Å)**	17.806(3)	17.964(5)	18.029(8)	18.016(4)
***c* (Å)**	18.247(3)	18.121(5)	18.124(8)	18.072(4)
α (°)	90	90	90	90
β (°)	90	90	90	90
γ (°)	90	90	90	90
Volume (Å^3)	4277(1)	4264(2)	4236(3)	4196(1)
Z	4	4	4	4
ρ_{calcd} (Mg/m^3)	1.776	1.6829	1.7107	1.7635
μ (mm^{-1})	2.800	2.987	3.177	3.424
R1^a ($I > 2.0\sigma$(I))	0.0354	0.0341	0.0290	0.0295
wR2 (all data)	0.0856	0.0784	0.0637	0.0779

Table F.1. -continued

Compound	**Dy_2TPT^{OMe} •2MeOH**	**Ho_2TPT^{OMe} •2MeOH**	**Er_2TPT^{OMe} •MeOH**	**Tm_2TPT^{OMe} •2MeOH**
Empirical Formula	$C_{32}H_{44}N_{10}O_{17}Dy_2$	$C_{32}H_{44}N_{10}O_{17}Ho_2$	$C_{31}H_{42}N_{10}O_{16}Er_2$	$C_{32}H_{44}N_{10}O_{17}Tm_2$
Temperature (K)	100	100	100	100
Crystal System	Orthorhombic	Orthorhombic	Orthorhombic	Orthorhombic
Space Group	$P2_12_12_1$	$P2_12_12_1$	$P2_12_12_1$	$P2_12_12_1$
***a* (Å)**	12.925(4)	12.932(8)	12.752(9)	12.821(5)
***b* (Å)**	17.985(5)	18.10(1)	17.88(1)	17.929(7)
***c* (Å)**	18.125(5)	18.14(1)	17.96(1)	18.024(7)
α (°)	90	90	90	90
β (°)	90	90	90	90
γ (°)	90	90	90	90
Volume (Å^3)	4213(2)	4245(5)	4096(5)	4143(3)
Z	4	4	4	4
ρ_{calcd} (Mg/m^3)	1.7367	1.8315	1.880	1.8895
μ (mm^{-1})	3.593	3.783	4.153	4.339
R1^a ($I >$ 2.0σ(I))	0.0301	0.0273	0.0494	0.0265
wR2 (all data)	0.0614	0.0607	0.0805	0.0603

Table F.1. -continued

Compound	**Yb_2TPT^{OMe} •2MeOH**	**Lu_2TPT^{OMe} •2MeOH**	**Lu_2TPT^{OMeEt} •MeOEt**	**Lu_2TPT^{OBz} •BzOH**
Empirical Formula	$C_{32}H_{44}N_{10}O_{17}Yb_2$	$C_{32}H_{44}N_{10}O_{17}Lu_2$	$C_{39}H_{56}N_{10}O_{20}Lu_2$	$C_{55}H_{56}N_{10}O_{16}Lu_2$
Temperature (K)	100	100	100	100
Crystal System	Orthorhombic	Orthorhombic	Monoclinic	Monoclinic
Space Group	$P2_12_12_1$	$P2_12_12_1$	$P2_1/n$	$P2_1/n$
***a* (Å)**	12.769(4)	12.766(2)	10.836(2)	11.074(2)
***b* (Å)**	17.909(6)	17.851(2)	22.155(3)	24.442(3)
***c* (Å)**	18.014(6)	17.993(2)	20.002(3)	19.911(3)
α (°)	90	90	90	90
β (°)	90	90	95.691(3)	90.557(3)
γ (°)	90	90	90	90
Volume (Å^3)	4119(2)	4100.3(8)	4778(1)	5389(1)
Z	4	4	4	4
ρ_{calcd} (Mg/m^3)	1.9136	1.929	1.858	1.8031
μ (mm^{-1})	4.597	4.827	4.188	3.725
R1^a ($I > 2.0\sigma$(I))	0.0382	0.0266	0.0316	0.0311
wR2 (all data)	0.0915	0.0628	0.0689	0.0701

Table F.2. Metrical comparisons of averaged **Ln_2TPT^{OMe}(MeOH)** (Ln = Ce–Sm) and **Ln_2TPT^{OMe}** (Ln = Eu–Lu) complexes.[a]

Ln1	Ln–N_{Tren} (Å) [a]	Ln–N_{Pyr} (Å) [a]	Ln1–Ln2 (Å)	Ln1–O–Ln2 (°)	Twist angle imine-pyridine plane	Twist angle pyridine-acetalate plane	Twist angle imine-acetalate plane
Ce	2.738(2)	2.650(2)	3.689(1)	97.89(6)	46.89	49.78	23.77
Pr	2.721(3)	2.621(3)	3.656(1)	97.59(8)	47.83	49.96	22.38
Nd	2.677(4)	2.581(4)	3.587(2)	96.66(9)	49.34	49.28	21.47
Sm	2.657(4)	2.560(4)	3.548(1)	96.64(2)	49.99	50.19	19.78
Eu	2.632(5)	2.547(5)	3.506(1)	96.04(1)	50.32	50.79	18.88
Gd	2.616(4)	2.540(4)	3.487(1)	95.80(1)	50.89	50.81	18.25
Tb	2.606(5)	2.524(5)	3.457(1)	95.75(5)	50.99	51.50	16.89
Dy	2.602(5)	2.504(5)	3.447(1)	95.61(1)	51.22	51.68	16.98
Ho	2.599(4)	2.461(4)	3.437(1)	95.30(1)	51.74	51.97	16.22
Er	2.579(8)	2.465(8)	3.394(2)	95.23(2)	52.16	52.33	15.48
Tm	2.567(4)	2.476(4)	3.383(1)	95.26(1)	52.17	52.62	15.25
Yb	2.564(7)	2.419(7)	3.363(1)	94.90(2)	52.49	53.08	14.35
Lu	2.554(6)	2.458(6)	3.347(1)	94.70(2)	52.94	53.35	13.77

[a] N_{Tren} = N2, N4, N6; N_{Pyr} = N3, N5, N7.

Table F.3. Metrical comparisons of averaged **Lu_2TPT^X** (X = OMe, MeOEt, OBz) complexes.

	TPT^{OMe}	TPT^{MeOEt}	TPT^{OBz}
Ln–N_{Tren} (Å)	2.554(6)	2.552(4)	2.533(3)
Ln–N_{Pyr} (Å)	2.458(6)	2.467(4)	2.467(3)
Ln1–Ln2 (Å)	3.347(1)	3.340(1)	3.327(1)
Ln1–O–Ln2 (˚)	94.7(2)	94.2(1)	94.0(1)
N1–Ln1 (Å)	3.889(7)	3.870(4)	3.887(4)
C–N1–C (˚)	117.8(7)	117.6(4)	118.3(4)

APPENDIX G

TABLES FROM CHAPTER 7

Table G.1. Crystallographic information for **AmTPT^{OMe}**.

Compound	**Am_2TPT^{OMe} (MeOH)•2MeOH**
Empirical Formula	$C_{33}H_{48}N_{10}O_{18}Am_2$
Temperature (K)	100.0
Crystal System	orthorhombic
Space Group	$P2_12_12_1$
***a* (Å)**	13.331(10)
***b* (Å)**	15.114(7)
***c* (Å)**	21.826(9)
α (°)	90
β (°)	90
γ (°)	90
Volume (Å^3)	4398(4)
Z	4
ρ_{calcd} (Mg/m^3)	2.051
μ (mm^{-1})	3.546
R1^a ($I > 2.0\sigma$(I))	0.0329
wR2 (all data)	0.0640

Table G.2. Metrical comparisons of averaged **Am_2TPT^{OMe}**.

M1	Ln–N_{Tren} (Å) [a]	Ln–N_{Pyr} (Å) [a]	Ln1–Ln2 (Å)	Ln1–O–Ln2 (˚)
Ce	2.738(2)	2.650(2)	3.689(1)	97.89(6)
Pr	2.721(3)	2.621(3)	3.656(1)	97.59(8)
Am	2.681(9)	2.589(9)	3.629(1)	97.1(2)
Nd	2.677(4)	2.581(4)	3.587(2)	96.66(9)

[a] N_{Tren} = N2, N4, N6; N_{Pyr} = N3, N5, N7.

APPENDIX H

TABLES FROM CHAPTER 8

Table H.1. Crystallographic information for **[CeTPT][3Br]•DMSO**.

Compound	**[CeTPT][3Br]•DMSO**
Empirical Formula	$C_{35}H_{45}Br_3CeN_{11}OS$
Temperature (K)	1047.73
Crystal System	100.15
Space Group	monoclinic
***a* (Å)**	$P2_1/c$
***b* (Å)**	13.770(6)
***c* (Å)**	14.168(7)
α (°)	20.285(9)
β (°)	90
γ (°)	93.937(5)
Volume (Å^3)	90
Z	3948(3)
ρ_{calcd} (Mg/m^3)	4
μ (mm^{-1})	1.763
R1^a ($I > 2.0\sigma$(I))	0.0659
wR2 (all data)	0.1595

[a]Definitions: R1 = $\Sigma||F_o| - |F_c||/\Sigma|F_o|$, wR2 = $[\Sigma w(F_o^2 - F_c^2)^2/\Sigma w(F_o^2)^2]^{1/2}$.Goof = S = $[\Sigma[w(F_o^2-F_c^2)^2] / (n-p)]^{1/2}$ where n is the number of reflections and p is the total number of parameters refined.

REFERENCES

(1) *The Chemistry of the Actinide and Transactinide Elements*, 4th ed.; Morss, L. R., Edelstein, N., Fuger, J., J.J., K., Eds.; Springer, 2007; Vol. 44. https://doi.org/10.5860/choice.44-4454.

(2) *Spent Fuel Reprocessing Options*; Vienna, 2008.

(3) Aspinall, H. C. *Chemistry of the F-Block Elements*; CRC Press, 2001.

(4) *IAEA Annual Report 2017*; Vienna, 2017.

(5) *Disposal of High-Level Nuclear Waste*; 2018.

(6) Cross, J. N.; Macor, J. A.; Bertke, J. A.; Ferrier, M. G.; Girolami, G. S.; Kozimor, S. A.; Maassen, J. R.; Scott, B. L.; Shuh, D. K.; Stein, B. W.; et al. Comparing the 2,2′-Biphenylenedithiophosphinate Binding of Americium with Neodymium and Europium. *Angew. Chem. Int. Ed.* **2016**, *55* (41), 12755–12759. https://doi.org/10.1002/anie.201606367.

(7) Cary, S. K.; Su, J.; Galley, S. S.; Albrecht-Schmitt, T. E.; Batista, E. R.; Ferrier, M. G.; Kozimor, S. A.; Mocko, V.; Scott, B. L.; Van Alstine, C. E.; et al. A Series of Dithiocarbamates for Americium, Curium, and Californium. *Dalt. Trans.* **2018**, *47* (41), 14452–14461. https://doi.org/10.1039/C8DT02658K.

(8) J. Gaunt, A.; D. Reilly, S.; E. Enriquez, A.; L. Scott, B.; A. Ibers, J.; Sekar, P.; I. M. Ingram, K.; Kaltsoyannis, N.; P. Neu, M. Experimental and Theoretical Comparison of Actinide and Lanthanide Bonding in $M[N(EPR_2)_2]_3$ Complexes (M = U, Pu, La, Ce; E = S, Se, Te; R = Ph, IPr, H). *Inorg. Chem.* **2007**, *47* (1), 29–41. https://doi.org/10.1021/ic701618a.

(9) D. Schnaars, D.; J. Gaunt, A.; W. Hayton, T.; B. Jones, M.; Kirker, I.; Kaltsoyannis, N.; May, I.; D. Reilly, S.; L. Scott, B.; Wu, G. Bonding Trends Traversing the Tetravalent Actinide Series: Synthesis, Structural, and Computational Analysis of $An^{IV}(Aracnac)_4$ Complexes (An = Th, U, Np, Pu; Aracnac = ArNC(Ph)CHC(Ph)O; Ar = 3,5-$TBu_2C_6H_3$). *Inorg. Chem.* **2012**, *51* (15), 8557–8566. https://doi.org/10.1021/ic301109f.

(10) Jones, M. B.; Gaunt, A. J.; Gordon, J. C.; Kaltsoyannis, N.; Neu, M. P.; Scott, B. L. Uncovering F-Element Bonding Differences and Electronic Structure in a Series of 1 : 3 and 1 : 4 Complexes with a Diselenophosphinate Ligand. *Chem. Sci.* **2013**, *4* (3), 1189–1203. https://doi.org/10.1039/C2SC21806B.

(11) W. Löble, M.; M. Keith, J.; B. Altman, A.; Chantal E. Stieber, S.; R. Batista, E.; S. Boland, K.; D. Conradson, S.; L. Clark, D.; Lezama Pacheco, J.; A. Kozimor, S.; et al. Covalency in Lanthanides. An X-Ray Absorption Spectroscopy and Density Functional Theory Study of $LnCl_6^{x-}$ (x = 3, 2). *J. Am. Chem. Soc.* **2015**, *137* (7), 2506–2523. https://doi.org/10.1021/ja510067v.

(12) Clark, D. L.; Hobart, D. E.; Neu, M. P. Actinide Carbonate Complexes and Their Importance in Actinide Environmental Chemistry. *Chem. Rev.* **1995**, *95* (1), 25–48. https://doi.org/10.1021/cr00033a002.

(13) Jantunen, K. C.; Scott, B. L.; Kiplinger, J. L. A Comparative Study of the Reactivity of Zr(IV), Hf(IV) and Th(IV) Metallocene Complexes: Thorium Is Not a Group IV Metal after All. *J. Alloy. Compd.* **2007**, *444–445* (SPEC. ISS.), 363–368. https://doi.org/10.1016/j.jallcom.2007.03.138.

(14) A. Kozimor, S.; Yang, P.; R. Batista, E.; S. Boland, K.; J. Burns, C.; L. Clark, D.; D. Conradson, S.; L. Martin, R.; P. Wilkerson, M.; E. Wolfsberg, L. Trends in Covalency for D- and f-Element Metallocene Dichlorides Identified Using Chlorine K-Edge X-Ray Absorption Spectroscopy and Time-Dependent Density Functional Theory. *J. Am. Chem. Soc.* **2009**, *131* (34), 12125–12136. https://doi.org/10.1021/ja9015759.

(15) Neidig, M. L.; Clark, D. L.; Martin, R. L. Covalency in F-Element Complexes. *Coord. Chem. Rev.* **2013**, *257* (2), 394–406. https://doi.org/10.1016/j.ccr.2012.04.029.

(16) Jones, M. B.; Gaunt, A. J. Recent Developments in Synthesis and Structural Chemistry of Nonaqueous Actinide Complexes. *Chem. Rev.* **2013**, *113* (2), 1137–1198. https://doi.org/10.1021/cr300198m.

(17) G. Minasian, S.; S. Boland, K.; K. Feller, R.; J. Gaunt, A.; A. Kozimor, S.; May, I.; D. Reilly, S.; L. Scott, B.; K. Shuh, D. Synthesis and Structure of $(Ph_4P)_2MCl_6$ (M = Ti, Zr, Hf, Th, U, Np, Pu). *Inorg. Chem.* **2012**, *51* (10), 5728–5736. https://doi.org/10.1021/ic300179d.

(18) Silver, M. A.; Albrecht-Schmitt, T. E. Evaluation of F-Element Borate Chemistry. *Coord. Chem. Rev.* **2016**, *323* (15), 36–51. https://doi.org/10.1016/j.ccr.2016.02.015.

(19) Cozzi, P. G. Metal–Salen Schiff Base Complexes in Catalysis: Practical Aspects. *Chem. Soc. Rev.* **2004**, *33* (7), 410–421. https://doi.org/10.1039/B307853C.

(20) Dame, A. N.; Bharara, M. S.; Barnes, C. L.; Walensky, J. R. Synthesis of Thorium(IV) and Uranium(IV) Salicylaldiminate Pseudo-Halide Complexes. *Eur. J. Inorg. Chem.* **2015**, *2015* (18), 2996–3005. https://doi.org/10.1002/ejic.201500378.

(21) Wu, W.; Sun, J.; Ji, S.; Wu, W.; Zhao, J.; Guo, H. Tuning the Emissive Triplet Excited States of Platinum(II) Schiff Base Complexes with Pyrene, and Application for Luminescent Oxygen Sensing and Triplet–Triplet-Annihilation Based Upconversions. *Dalt. Trans.* **2011**, *40* (43), 11550–11561. https://doi.org/10.1039/C1DT11001B.

(22) Tian, Z.; Cui, S.; Liu, G.; Wang, R.; Pu, S. A New Fluorescent Sensor for Zn^{2+} Based on Diarylethene with a 4-Diethylamino-Salicylaldehyde Schiff Base Unit. *J. Phys. Org. Chem.* **2016**, *29* (8), 421–429. https://doi.org/10.1002/poc.3552.

(23) Sahraei, A.; Kargar, H.; Hakimi, M.; Tahir, M. N. Distorted Square-Antiprism Geometry of New Zirconium (IV) Schiff Base Complexes: Synthesis, Spectral Characterization,

Crystal Structure and Investigation of Biological Properties. *J. Mol. Struct.* **2017**, *1149* (5), 576–584. https://doi.org/10.1016/j.molstruc.2017.08.022.

(24) Gao, T.; Yan, P. F.; Li, G. M.; Hou, G. F.; Gao, J. S. Ion Size Dominated 1D and 2D Salen Lanthanide Coordination Complexes and Their Luminescence. *Polyhedron* **2007**, *26* (18), 5382–5388. https://doi.org/10.1016/j.poly.2007.08.011.

(25) Yan, P.; Sun, W.; Li, G.; Nie, C.; Gao, T.; Yue, Z. Synthesis, Characterization and Fluorescence of Lanthanide Schiff-Base Complexes. *J. Coord. Chem.* **2007**, *60* (18), 1973–1982. https://doi.org/10.1080/00958970701217602.

(26) Gao, B.; Zhang, Q.; Yan, P.; Hou, G.; Li, G. Crystal Engineering of Salen Type Cerium Complexes Tuned by Various Cerium Counterions. *Cryst. Eng.* **2013**, *15* (20), 4167–4175. https://doi.org/10.1039/C3CE40207J.

(27) Pospieszna-Markiewicz, I.; Radecka-Paryzek, W.; Kubicki, M.; Korabik, M.; Hnatejko, Z. Different Supramolecular Architectures in Self-Assembled Praseodymium(III) and Europium(III) Complexes with Rare Coordination Pattern of Salicylaldimine Ligand. *Polyhedron* **2015**, *97* (5), 167–174. https://doi.org/10.1016/j.poly.2015.05.022.

(28) Hardy, E. E.; Wyss, K. M.; Gorden, J. D.; Ariyarathna, I. R.; Miliordos, E.; Gorden, A. E. V. Th(IV) and Ce(IV) Napthylsalophen Sandwich Complexes: Characterization of Unusual Thorium Fluorescence in Solution and Solid-State. *Chem. Commun.* **2017**, *53* (88), 11984–11987. https://doi.org/10.1039/C7CC06868A.

(29) Salmon, L.; Thuéry, P.; Ephritikhine, M. Synthesis and Crystal Structure of Uranium(IV) Complexes with Compartmental Schiff Bases: From Mononuclear Species to Tri- and Tetranuclear Clusters. *Dalt. Trans.* **2004**, No. 10, 1635–1643. https://doi.org/10.1039/B403459G.

(30) Camp, C.; Mougel, V.; Horeglad, P.; Pécaut, J.; Mazzanti, M. Multielectron Redox Reactions Involving C−C Coupling and Cleavage in Uranium Schiff Base Complexes. *J. Am. Chem. Soc.* **2010**, *132* (49), 17374–17377. https://doi.org/10.1021/ja1089364.

(31) He, F.-F.; Wang, H.-Q.; Wang, X.-F.; Wang, Y.-Y. Crystal Structure of Bis-[N,N'-Bis-(3-Allyl Salicylidene)-o-Phenylene Diamine]Thorium (IV), $C_{52}H_{44}N_4O_4Th$. *Z. Krist. - New Cryst. Struct.* **2014**, *277* (4), 521–524.

(32) Stobbe, B. C.; Powell, D. R.; Thomson, R. K. Schiff Base Thorium(IV) and Uranium(IV) Chloro Complexes: Synthesis, Substitution and Oxidation Chemistry. *Dalt. Trans.* **2017**, *46* (15), 4888–4892. https://doi.org/10.1039/C7DT00580F.

(33) Camp, C.; Toniolo, D.; Andrez, J.; Pécaut, J.; Mazzanti, M. A Versatile Route to Homo- and Hetero-Bimetallic 5f–5f and 3d–5f Complexes Supported by a Redox Active Ligand Framework. *Dalt. Trans.* **2017**, *46* (34), 11145–11148. https://doi.org/10.1039/C7DT01993A.

(34) Wolter, F. J.; Diehl, H. C. J. Plutonium Compounds and Proccess for Their Preparation.

2819280, 1958.

(35) Magnusson, L. B. Separation Process for Transuranic Element and Compounds Thereof. 2,830,066, 1958.

(36) Chuguryan, D. G.; Dzyubenko, V. I.; Grigor'ev, M. I.; Yanovskii, A. I.; Struchkov, Y. T. Crystal and Molecular Structure of Uranium (VI) and Neptunium (VI) Complexes with N,N'-Bis(Salicylidene)Ethylenediamine. *Sov. Radiochem.* **1988**, *20* (24), 39–44.

(37) Copping, R.; Mougel, V.; Den Auwer, C.; Berthon, C.; Moisy, P.; Mazzanti, M. A Tetrameric Neptunyl(V) Cluster Supported by a Schiff Base Ligand. *Dalt. Trans.* **2012**, *41* (36), 10900–10902. https://doi.org/10.1039/C2DT31072D.

(38) L. Kiplinger, J.; E. Morris, D.; L. Scott, B.; J. Burns, C. Convenient Synthesis, Structure, and Reactivity of $(C_5Me_5)U(CH_2C_6H_5)_3$: A Simple Strategy for the Preparation of Monopentamethylcyclopentadienyl Uranium(IV) Complexes. *Organometallics* **2002**, *21* (26), 5978–5982. https://doi.org/10.1021/om0206610.

(39) Chen, C.; Chen, H.; Yan, P.; Hou, G.; Li, G. Structure and Electrochemistry of Salen Type Cerium (IV) Complexes Tuned by Multiform Counterions. *Inorg. Chim. Acta* **2013**, *405* (24), 182–187. https://doi.org/10.1016/j.ica.2013.05.014.

(40) APEX3. Bruker AXS, Inc.: Madison, WI 2017.

(41) SAINT. Bruker AXS, Inc: Madison, WI 2012.

(42) Sheldrick, G. M. SADABS. Bruker AXS, Inc: Madison, WI 2012.

(43) OLEX2. Olex Sys Ltd.: Durham, U.K.

(44) Neese, F. The ORCA Program System. *WIREs Comput. Mol. Sci.* **2012**, *2* (1), 73–78. https://doi.org/10.1002/wcms.81.

(45) Sukumar, N.; Breneman, C. M. QTAIM in Drug Discovery and Protein Modeling. In *The Quantum Theory of Atoms in Molecules*; John Wiley & Sons, Ltd, 2007; pp 471–498. https://doi.org/10.1002/9783527610709.ch18.

(46) Lu, T.; Chen, F. Multiwfn: A Multifunctional Wavefunction Analyzer. *J . Comput. Chem.* **2012**, *33* (5), 580–592. https://doi.org/10.1002/jcc.22885.

(47) Diwu, J.; Wang, S.; J. Good, J.; H. DiStefano, V.; E. Albrecht-Schmitt, T. Deviation Between the Chemistry of Ce(IV) and Pu(IV) and Routes to Ordered and Disordered Heterobimetallic 4f/5f and 5f/5f Phosphonates. *Inorg. Chem.* **2011**, *50* (11), 4842–4850. https://doi.org/10.1021/ic200006m.

(48) Szłyk, E.; Wojtczak, A.; Dobrzańska, L.; Barwiołek, M. X-Ray Crystal Structure and Nuclear Overhauser Effect Studies of Cerium(IV) Complexes with Schiff Bases Obtained from N,N′-(1R,2R)(-)-1,2-Cyclohexanediamine and Benzaldehyde Derivatives.

Polyhedron **2008**, *27* (2), 765–776. https://doi.org/10.1016/j.poly.2007.11.004.

(49) Camp, C.; Guidal, V.; Biswas, B.; Pécaut, J.; Dubois, L.; Mazzanti, M. Multielectron Redox Chemistry of Lanthanide Schiff-Base Complexes. *Chem. Sci.* **2012**, *3* (8), 2433–2448. https://doi.org/10.1039/C2SC20476B.

(50) Hill, C. 11 - Development of Highly Selective Compounds for Solvent Extraction Processes: Partitioning and Transmutation of Long-Lived Radionuclides from Spent Nuclear Fuels. In *Advanced Separation Techniques for Nuclear Fuel Reprocessing and Radioactive Waste Treatment*; Nash, K. L., Lumetta, G. J., Eds.; Woodhead Publishing Series in Energy; Woodhead Publishing, 2011; pp 311–362. https://doi.org/https://doi.org/10.1533/9780857092274.3.311.

(51) Illingsworth, M. L.; Rheingold, A. L. Synthesis and Molecular Structure of the Eight-Coordinate Complex Bis(4-Amino-N,N′ - Disalicylidene-l,2-Phenylenediaminato)Zirconium(IV), a New Reagent for Preparing Coordination Polymers. *Inorg. Chem.* **1987**, *26* (26), 4312–4318. https://doi.org/10.1021/ic00273a008.

(52) Kumar Saha, T.; Ramkumar, V.; Chakraborty, D. Salen Complexes of Zirconium and Hafnium: Synthesis, Structural Characterization, Controlled Hydrolysis, and Solvent-Free Ring-Opening Polymerization of Cyclic Esters and Lactides. *Inorg. Chem.* **2011**, *50* (7), 2720–2722. https://doi.org/10.1021/ic1025262.

(53) Matsumoto, K.; Watanabe, A.; Uchida, T.; Ogi, K.; Katsuki, T. Construction of a New Asymmetric Reaction Site: Asymmetric 1,4-Addition of Thiol Using Pentagonal Bipyramidal Hf(Salen) Complex as Catalyst. *Tetrahedron Lett.* **2004**, *45* (11), 2385–2388. https://doi.org/10.1016/j.tetlet.2004.01.095.

(54) Bard, J. A.; Faulkner, L. R. *Electrochemical Methods: Fundamentals and Applications*, 2nd ed.; John Wiley & Sons, Inc., 2001.

(55) J. Cohen, A.; Mori-Sánchez, P.; Yang, W. Challenges for Density Functional Theory. *Chem. Rev.* **2011**, *112* (1), 289–320. https://doi.org/10.1021/cr200107z.

(56) Cremer, D.; Kraka, E. Chemical Bonds without Bonding Electron Density — Does the Difference Electron-Density Analysis Suffice for a Description of the Chemical Bond? *Angew. Chemie Int. Ed. English* **1984**, *23* (8), 627–628. https://doi.org/10.1002/anie.198406271.

(57) Espinosa, E.; Alkorta, I.; Elguero, J.; Molins, E. From Weak to Strong Interactions: A Comprehensive Analysis of the Topological and Energetic Properties of the Electron Density Distribution Involving X–H···F–Y Systems. *J. Chem. Phys.* **2002**, *117* (12), 5529–5542. https://doi.org/10.1063/1.1501133.

(58) Kerridge, A. F-Orbital Covalency in the Actinocenes (An = Th–Cm): Multiconfigurational Studies and Topological Analysis. *RSC Adv.* **2014**, *4* (24), 12078–12086. https://doi.org/10.1039/C3RA47088A.

(59) Beekmeyer, R.; Kerridge, A. Assessing Covalency in Cerium and Uranium Hexachlorides: A Correlated Wavefunction and Density Functional Theory Study. *Inorganics* **2015**, *3* (4), 482–499.

(60) Gregson, M.; Lu, E.; Tuna, F.; McInnes, E. J. L.; Hennig, C.; Scheinost, A. C.; McMaster, J.; Lewis, W.; Blake, A. J.; Kerridge, A.; et al. Emergence of Comparable Covalency in Isostructural Cerium(IV)– and Uranium(IV)–Carbon Multiple Bonds. *Chem. Sci.* **2016**, *7* (5), 3286–3297. https://doi.org/10.1039/C6SC00278A.

(61) Sodaye, H.; Nisan, S.; Poletiko, C.; Prabhakar, S.; Tewari, P. K. Extraction of Uranium from the Concentrated Brine Rejected by Integrated Nuclear Desalination Plants. *Desalination* **2009**, *235* (1–3), 9–32. https://doi.org/10.1016/j.desal.2008.02.005.

(62) Ok Kang, S.; Vukovic, S.; Custelcean, R.; P. Hay, B. Cyclic Imide Dioximes: Formation and Hydrolytic Stability. *Ind. Eng. Chem. Res.* **2012**, *51* (19), 6619–6624. https://doi.org/10.1021/ie300492z.

(63) Das, S.; Oyola, Y.; T. Mayes, R.; J. Janke, C.; Kuo, L.-J.; Gill, G.; R. Wood, J.; Dai, S. Extracting Uranium from Seawater: Promising AI Series Adsorbents. *Ind. Eng. Chem. Res.* **2015**, *55* (15), 4103–4109. https://doi.org/10.1021/acs.iecr.5b03135.

(64) Abney, C. W.; Mayes, R. T.; Saito, T.; Dai, S. Materials for the Recovery of Uranium from Seawater. *Chem. Rev.* American Chemical Society December 13, 2017, pp 13935–14013. https://doi.org/10.1021/acs.chemrev.7b00355.

(65) Parker, B. F.; Zhang, Z.; Rao, L.; Arnold, J. An Overview and Recent Progress in the Chemistry of Uranium Extraction from Seawater. *Dalt. Trans.* **2018**, *47* (3), 639–644. https://doi.org/10.1039/C7DT04058J.

(66) S. Bharara, M.; Strawbridge, K.; Z. Vilsek, J.; H. Bray, T.; E. V. Gorden, A. Novel Dinuclear Uranyl Complexes with Asymmetric Schiff Base Ligands: Synthesis, Structural Characterization, Reactivity, and Extraction Studies. *Inorg. Chem.* **2007**, *46* (20), 8309–8315. https://doi.org/10.1021/ic7010315.

(67) Szigethy, G.; Raymond, K. N. The Influence of Linker Geometry in Bis(3-Hydroxy-N-Methyl-Pyridin-2-One) Ligands on Solution Phase Uranyl Affinity. *Chem. Eur. J.* **2011**, *17* (6), 1818–1827. https://doi.org/10.1002/chem.201002372.

(68) Tsushima, S. On the "Yl" Bond Weakening in Uranyl(VI) Coordination Complexes. *Dalt. Trans.* **2011**, *40* (25), 6732–6737. https://doi.org/10.1039/C1DT10481K.

(69) L. Arnold, P.; Pécharman, A.-F.; M. Lord, R.; M. Jones, G.; Hollis, E.; S. Nichol, G.; Maron, L.; Fang, J.; Davin, T.; B. Love, J. Control of Oxo-Group Functionalization and Reduction of the Uranyl Ion. *Inorg. Chem.* **2015**, *54* (7), 3702–3710. https://doi.org/10.1021/acs.inorgchem.5b00420.

(70) Hayton, T. W. Understanding the Origins of Oyl–U–Oyl Bending in the Uranyl (UO_2^{2+}) Ion. *Dalt. Trans.* **2018**, *47* (4), 1003–1009. https://doi.org/10.1039/C7DT04123C.

(71) Bell, N.; L.; Shaw, B.; L. Arnold, P.; B. Love, J. Uranyl to Uranium(IV) Conversion through Manipulation of Axial and Equatorial Ligands. *J. Am. Chem. Soc.* **2018**, *140* (9), 3378–3384. https://doi.org/10.1021/jacs.7b13474.

(72) Azam, M.; Al-Resayes, S. I.; Velmurugan, G.; Venuvanalingam, P.; Wagler, J.; Kroke, E. Novel Uranyl(VI) Complexes Incorporating Propylene-Bridged Salen-Type N_2O_2-Ligands: A Structural and Computational Approach. *Dalt. Trans.* **2015**, *44* (2), 568–577. https://doi.org/10.1039/C4DT02112F.

(73) Zhao, X.; Zhang, D.; Yu, R.; Chen, S.; Zhao, D. Tetrahydrosalen Uranyl(VI) Complexes: Crystal Structures and Solution Binding Study. *Eur. J. Inorg. Chem.* **2018**, *2018* (10), 1185–1191. https://doi.org/10.1002/ejic.201701401.

(74) Nguyen Trung, C.; M. Begun, G.; A. Palmer, D. Aqueous Uranium Complexes. 2. Raman Spectroscopic Study of the Complex Formation of the Dioxouranium(VI) Ion with a Variety of Inorganic and Organic Ligands. *Inorg. Chem.* **2002**, *31* (25), 5280–5287. https://doi.org/10.1021/ic00051a021.

(75) Fortier, S.; Hayton, T. W. Oxo Ligand Functionalization in the Uranyl Ion (UO_2^{2+}). *Coord. Chem. Rev.* **2010**, *254* (3–4), 197–214. https://doi.org/10.1016/j.ccr.2009.06.003.

(76) Lv, L.; Chen, B.; Liu, J.; Chen, J.; Xu, C.; Yang, Y. A Structural and Thermodynamic Study of the Complexes of U(VI) with Azinecarboxylates. *Dalt. Trans.* **2019**, *48* (2), 566–577. https://doi.org/10.1039/C8DT04099K.

(77) Cotton, A. F.; Wilkinson, G. Advanced Inorganic Chemistry; John Wiley & Sons, Inc.: New York, 1980; pp 1005–1049.

(78) Hayes, C. E.; Leznoff, D. B. Actinide Coordination and Organometallic Complexes with Multidentate Polyamido Ligands. *Coord. Chem. Rev.* **2014**, *266–267* (1), 155–170. https://doi.org/10.1016/j.ccr.2013.11.020.

(79) Takao, K.; Ikeda, Y. Structural Characterization and Reactivity of UO_2(Salophen)L and [UO_2(Salophen)]$_2$: Dimerization of UO_2(Salophen) Fragments in Noncoordinating Solvents (Salophen = N,N′-Disalicylidene-o-Phenylenediaminate, L = N,N-Dimethylformamide, Dimethyl Sulfoxide). *Inorg. Chem.* **2007**, *46* (5), 1550–1562. https://doi.org/10.1021/ic0611950.

(80) Kannappan, R.; Tanase, S.; Tooke, D. M.; Spek, A. L.; Mutikainen, I.; Turpeinen, U.; Reedijk, J. Separation of Actinides and Lanthanides: Crystal and Molecular Structures of N,N′-Bis(3,5-Di-t-Butylsalicylidene)-4,5-Dimethyl-1,2-Phenylenediamine and Its Uranium Complex. *Polyhedron* **2004**, *23* (14), 2285–2291. https://doi.org/10.1016/j.poly.2004.07.004.

(81) Hardwick, H. C.; Royal, D. S.; Helliwell, M.; Pope, S. J. A.; Ashton, L.; Goodacre, R.; Sharrad, C. A. Structural, Spectroscopic and Redox Properties of Uranyl Complexes with a Maleonitrile Containing Ligand. *Dalt. Trans.* **2011**, *40* (22), 5939–5952. https://doi.org/10.1039/C0DT01580F.

(82) Bandoli, G.; Clemente, D. A.; Croatto, U.; Vidali, M.; Vigato, P. A. Preparation and Crystal and Molecular Structure of [NN′-o-Phenylene-Bis(Salicylideneiminato)UO_2(EtOH)]. *J. Chem. Soc. D* **1971**, No. 21, 1330–1331. https://doi.org/10.1039/C29710001330.

(83) Bandoli, G.; Clemente, D. A.; Croatto, U.; Vidali, M.; Vigato, P. A. Crystal and Molecular Structure of [NN′-Ethylenebis(Salicylideneiminato)](Methanol)Dioxouranium. *J. Chem. Soc. Dalt. Trans.* **1973**, No. 21, 2331–2335. https://doi.org/10.1039/DT9730002331.

(84) Evans, D. J.; Junk, P. C.; Smith, M. K. The Effect of Coordinated Solvent Ligands on the Solid-State Structures of Compounds Involving Uranyl Nitrate and Schiff Bases. *Polyhedron* **2002**, *21* (23), 2421–2431. https://doi.org/10.1016/S0277-5387(02)01182-8.

(85) S. Nicholson, R. Theory and Application of Cyclic Voltammetry for Measurement of Electrode Reaction Kinetics. *Anal. Chem.* **2002**, *37* (11), 1351–1355. https://doi.org/10.1021/ac60230a016.

(86) Heinze, J. Cyclic Voltammetry—"Electrochemical Spectroscopy". New Analytical Methods (25). *Angew. Chem. Int. Ed.* **1984**, *23* (11), 831–847. https://doi.org/10.1002/anie.198408313.

(87) S. Nicholson, R.; Shain, I. Theory of Stationary Electrode Polarography. Single Scan and Cyclic Methods Applied to Reversible, Irreversible, and Kinetic Systems. *Anal. Chem.* **2002**, *36* (4), 706–723. https://doi.org/10.1021/ac60210a007.

(88) Mizuoka, K.; Kim, S.-Y.; Hasegawa, M.; Hoshi, T.; Uchiyama, G.; Ikeda, Y. Electrochemical and Spectroelectrochemical Studies on UO_2(Saloph)L (Saloph = N,N'-Disalicylidene-o-Phenylenediaminate, L = Dimethyl Sulfoxide or N,N-Dimethylformamide). *Inorg. Chem.* **2003**, *42* (4), 1031–1038. https://doi.org/10.1021/ic0260926.

(89) Takao, K.; Kato, M.; Takao, S.; Nagasawa, A.; Scheinost, A. C.; Bernhard, G.; Hennig, C.; Ikeda, Y. Structural and Electrochemical Studies on Uranyl(VI) Complex with Pentadentate Schiff Base Ligand: A Guide to Stable Uranyl(V). *Conf. Ser. Mater. Sci. Eng.* **2010**, *9*, 12030. https://doi.org/10.1088/1757-899x/9/1/012030.

(90) Albright, D.; Kramer, K. *Neptunium 237 and Americium: World Inventories and Proliferation Concerns*; 2005.

(91) Veliscek-Carolan, J. Separation of Actinides from Spent Nuclear Fuel: A Review. *J. Haz. Mat.* **2016**, *318*, 266–281. https://doi.org/10.1016/j.jhazmat.2016.07.027.

(92) Thompson, R. C. Neptunium: The Neglected Actinide: A Review of the Biological and Environmental Literature. *Radiat. Res.* **1982**, *90* (1), 1. https://doi.org/10.2307/3575792.

(93) Sessler, J. L.; Melfi, P. J.; Pantos, G. D. Uranium Complexes of Multidentate N-Donor Ligands. *Coord. Chem. Rev.* **2006**, *250* (7–8), 816–843. https://doi.org/10.1016/j.ccr.2005.10.007.

(94) Bart, S. C.; Meyer, K. Highlights in Uranium Coordination Chemistry. In *Struct. Bond.*; Springer, Berlin, Heidelberg, 2008; Vol. 127, pp 119–176. https://doi.org/10.1007/430_2007_081.

(95) J. Hudson, M.; M. Harwood, L.; M. Laventine, D.; W. Lewis, F. Use of Soft Heterocyclic N-Donor Ligands To Separate Actinides and Lanthanides. *Inorg. Chem.* **2012**, *52* (7), 3414–3428. https://doi.org/10.1021/ic3008848.

(96) Cotton, S. *Lanthanide and Actinide Chemistry*; John Wiley & Sons, Inc.: West Sussex, England, 2006. https://doi.org/10.1002/0470010088.

(97) Klamm, B. E.; Windorff, C. J.; Marsh, M. L.; Meeker, D. S.; Albrecht-Schmitt, T. E. Schiff-Base Coordination Complexes with Plutonium(IV) and Cerium(IV). *Chem. Commun.* **2018**, *54* (62), 8634–8636. https://doi.org/10.1039/C8CC03571G.

(98) Klamm, B.; E.; J. Windorff, C.; Celis-Barros, C.; L. Marsh, M.; S. Meeker, D.; E. Albrecht-Schmitt, T. Experimental and Theoretical Comparison of Transition-Metal and Actinide Tetravalent Schiff Base Coordination Complexes. *Inorg. Chem.* **2018**, *57* (24), 15389–15398. https://doi.org/10.1021/acs.inorgchem.8b02700.

(99) Yu, T.; Zhang, K.; Zhao, Y.; Yang, C.; Zhang, H.; Fan, D.; Dong, W. A New Trinuclear Zinc(II) Complex Possessing Five- and Six-Coordinated Central Ions and Its Photoluminescent Property. *Inorg. Chem. Commun.* **2007**, *10* (4), 401–403. https://doi.org/10.1016/j.inoche.2006.12.010.

(100) Li, Q.; Yan, P.; Chen, P.; Hou, G.; Li, G. Salen Type Sandwich Triple-Decker Tri- and Di-Nuclear Lanthanide Complexes. *J. Inorg. Organomet. Polym.* **2012**, *22* (5), 1174–1181. https://doi.org/10.1007/s10904-012-9714-8.

(101) Kubono, K.; Hirayama, N.; Kokusen, H.; Yokoi, K. X-Ray Crystallographic Approach to the Design of Phenolic Schiff Base Reagents for the Mutual Separation of Lanthanoids. *Anal. Sci.* **2001**, *17* (1), 193–197. https://doi.org/10.2116/analsci.17.193.

(102) Gottfriedsen, J.; Spoida, M.; Blaurock, S. Synthesis and Structure of the Cerium Schiff-Base Complexes [Ce(Salen′)$_2$] and [(THF)$_2$KCe(Salen′)$_2$]. *Z. Anorg. Allg. Chem.* **2008**, *634* (3), 514–518. https://doi.org/10.1002/zaac.200700451.

(103) Rice, N.; T.; A. Popov, I.; R. Russo, D.; Bacsa, J.; R. Batista, E.; Yang, P.; Telser, J.; S. La Pierre, H. Design, Isolation, and Spectroscopic Analysis of a Tetravalent Terbium Complex. *J. Am. Chem. Soc.* **2019**, *141* (33), 13222–13233. https://doi.org/10.1021/jacs.9b06622.

(104) Mazzanti, M.; Palumbo, C.; Willauer, A.; Scopelliti, R.; Douair, I.; Zivkovic, I.; Maron, L. Stabilization of the +IV Oxidation State in Siloxide Supported Terbium Compounds. *Angew. Chem. Int. Ed. n/a* (n/a). https://doi.org/10.1002/anie.201914733.

(105) Bustillos, C.; Hawkins, C.; Copping, R.; Reilly, S.; Scott, B.; May, I.; Nilsson, M. Complexation of High-Valency Mid-Actinides by a Lipophilic Schiff Base Ligand:

Synthesis, Structural Characterization, and Progress toward Selective Extraction. *Inorg. Chem.* **2019**, *58*. https://doi.org/10.1021/acs.inorgchem.8b02849.

(106) Mota, V. Z.; de Carvalho, G. S. G.; Corbi, P. P.; Bergamini, F. R. G.; Formiga, A. L. B.; Diniz, R.; Freitas, M. C. R.; da Silva, A. D.; Cuin, A. Crystal Structure and Theoretical Studies of the Keto-Enol Isomerism of N,N′-Bis(Salicylidene)-o-Phenylenediamine (Salophen). *Spectrochim. Acta, Part A.* **2012**, *99*, 110–115. https://doi.org/10.1016/j.saa.2012.09.002.

(107) Yu, T.; Zhang, K.; Zhao, Y.; Yang, C.; Zhang, H.; Qian, L.; Fan, D.; Dong, W.; Chen, L.; Qiu, Y. Synthesis, Crystal Structure and Photoluminescent Properties of an Aromatic Bridged Schiff Base Ligand and Its Zinc Complex. *Inorg. Chim. Acta* **2008**, *361* (1), 233–240. https://doi.org/10.1016/j.ica.2007.07.012.

(108) Hagan, P. G.; Cleveland, J. M. The Absorption Spectra of Neptunium Ions in Perchloric Acid Solution. *J. Inorg. Nuc. Chem.* **1966**, *28* (12), 2905–2909. https://doi.org/10.1016/0022-1902(66)80016-7.

(109) Terzis, A.; Mentzafos, D.; Tajmir-Riahi, H. A. Eight-Coordination. Synthesis and Structure of the Schiff-Base Chelate Bis(N,N′-Disalicylidene-1,2-Phenylenediamino)Cerium(IV). *Inorg. Chim. Acta* **1984**, *84* (2), 187–193. https://doi.org/10.1016/S0020-1693(00)82406-8.

(110) E. Klamm, B.; J. Windorff, C.; Celis-Barros, C.; L. Marsh, M.; E. Albrecht-Schmitt, T. Synthesis, Spectroscopy, and Theoretical Details of Uranyl Schiff-Base Coordination Complexes. *Inorg. Chem.* **2019**, *0* (0). https://doi.org/10.1021/acs.inorgchem.9b00477.

(111) Cornet, S. M.; Redmond, M. P.; Collison, D.; Sharrad, C. A.; Helliwell, M.; Warren, J. The Unusual Stability of $[NpO_2Cl_4]_2$-: Synthesis and Characterisation of $[NpO_2(DPPMO_2)_2Cl]_2[NpO_2Cl_4]$ and $[Ph_3PNH_2]_2[NpO_2Cl_4]$. *C. R. Acad. Sci., Ser. IIc Chim.* **2010**, *13* (6–7), 832–838. https://doi.org/10.1016/j.crci.2010.04.013.

(112) Elgrishi, N.; J. Rountree, K.; D. McCarthy, B.; S. Rountree, E.; T. Eisenhart, T.; L. Dempsey, J. A Practical Beginner's Guide to Cyclic Voltammetry. *J. Chem. Educ.* **2017**, *95* (2), 197–206. https://doi.org/10.1021/acs.jchemed.7b00361.

(113) J. Bard, A. Elements of Molecular and Biomolecular Electrochemistry: An Electrochemical Approach to Electron Transfer Chemistry By Jean-Michel Savéant (Université de Paris 7, Denis Diderot). J. Wiley & Sons, Inc.: Hoboken, NJ. 2006. ISBN 0-471-4. *J. Am. Chem. Soc.* **2006**, *129* (1), 242–242. https://doi.org/10.1021/ja069754p.

(114) Randviir, E. P. A Cross Examination of Electron Transfer Rate Constants for Carbon Screen-Printed Electrodes Using Electrochemical Impedance Spectroscopy and Cyclic Voltammetry. *Electrochim. Acta.* **2018**, *286*, 179–186. https://doi.org/10.1016/J.ELECTACTA.2018.08.021.

(115) Lavagnini, I.; Antiochia, R.; Magno, F. An Extended Method for the Practical Evaluation of the Standard Rate Constant from Cyclic Voltammetric Data. *Electroanalysis* **2004**, *16*

(6), 505–506. https://doi.org/10.1002/elan.200302851.

(116) Khan, T.; Vaidya, S.; S. Mhatre, D.; Datta, A. The Prospect of Salophen in Fluorescence Lifetime Sensing of Al^{3+}. *J. Phys. Chem. B* **2016**, *120* (39), 10319–10326. https://doi.org/10.1021/acs.jpcb.6b05854.

(117) Khan, T.; Datta, A. Impact of Molecular Arrangement and Torsional Motion on the Fluorescence of Salophen and Its Metal Complexes. *J. Phys. Chem. C* **2017**, *121* (4), 2410–2417. https://doi.org/10.1021/acs.jpcc.6b11903.

(118) Bunzli, J. Lanthanide Luminescence for Biomedical Analyses and Imaging. *Chem. Rev.* **2010**, *5*, 2729–2755. https://doi.org/10.1021/cr900362e.

(119) Heffern, M.; Matosziuk, L.; Meade, T. Lanthanide Probes for Bioresponsive Imaging. *Chem. Rev.2* **2014**, *114* (8), 4496–4539. https://doi.org/10.1021/cr400477t.

(120) Blanusa, M.; Varnai, V.; Piasek, M.; Kostial, K. Chelators as Antidotes of Metal Toxicity: Therapeutic and Experimental Aspects. *Curr. Med. Chem.* **2005**, *12* (23), 2771–2794. https://doi.org/10.2174/092986705774462987.

(121) Xue, X.; Wang, F.; Liu, X. Emerging Functional Nanomaterials for Therapeutics. *J. Mater. Chem.* **2011**, *21*, 13107–13127. https://doi.org/10.1039/c1jm11401h.

(122) Kronholm, B.; Anderson, C. G.; Taylor, P. R. A Primer on Hydrometallurgical Rare Earth Separations. *JOM* **2013**, *65* (10), 1321–1326. https://doi.org/10.1007/s11837-013-0718-9.

(123) Paulenova, A. 2 - Physical and Chemical Properties of Actinides in Nuclear Fuel Reprocessing. In *Advanced Separation Techniques for Nuclear Fuel Reprocessing and Radioactive Waste Treatment*; Nash, K. L., Lumetta, G. J., Eds.; Woodhead Publishing Series in Energy; Woodhead Publishing, 2011; pp 23–57. https://doi.org/https://doi.org/10.1533/9780857092274.1.23.

(124) Tranter, T. J. 13 - Solid-Phase Extraction Technology for Actinide and Lanthanide Separations in Nuclear Fuel Reprocessing. In *Advanced Separation Techniques for Nuclear Fuel Reprocessing and Radioactive Waste Treatment*; Nash, K. L., Lumetta, G. J., Eds.; Woodhead Publishing Series in Energy; Woodhead Publishing, 2011; pp 377–413. https://doi.org/https://doi.org/10.1533/9780857092274.3.377.

(125) Pearson, R. Hard and Soft Acids and Bases. *J. Am. Chem. Soc.* **1963**, *85* (22), 3533–3539. https://doi.org/10.1021/ja00905a001.

(126) Aravena, D.; Atanasov, M.; Neese, F. Periodic Trends in Lanthanide Compounds through the Eyes of Multireference Ab Initio Theory. *Inorg. Chem.* **2016**, *55* (9), 4457–4469. https://doi.org/10.1021/acs.inorgchem.6b00244.

(127) Cotton, S. A.; Raithby, P. R. Systematics and Surprises in Lanthanide Coordination Chemistry. *Coord. Chem. Rev.* **2017**, *340*, 220–231. https://doi.org/10.1016/J.CCR.2017.01.011.

(128) Boland, K. S.; Hobart, D. E.; Kozimor, S. A.; MacInnes, M. M.; Scott, B. L. The Coordination Chemistry of Trivalent Lanthanides (Ce, Nd, Sm, Eu, Gd, Dy, Yb) with Diphenyldithiophosphinate Anions. *Polyhedron* **2014**, *67*, 540–548. https://doi.org/10.1016/J.POLY.2013.09.019.

(129) Hamilton, A. D. Crown Ethers and Cryptands. *Compr. Heterocycl. Chem.* **1984**, 731–761. https://doi.org/10.1016/B978-008096519-2.00127-2.

(130) Suresh Kumar, D.; Alexander, V. Synthesis of Lanthanide(III) Complexes of Chloro- and Bromo Substituted 18-Membered Tetraaza Macrocycles. *Polyhedron* **1999**, *18* (11), 1561–1568. https://doi.org/10.1016/S0277-5387(99)00016-9.

(131) Radecka-Paryzek, W.; Patroniak-Krzyminiewska, V.; Litkowska, H. The Template Synthesis and Characterization of the Yttrium and Lanthanide Complexes of New 19-Membered Pentadentate Azaoxa Macrocycle. *Polyhedron* **1998**, *17* (9), 1477–1480. https://doi.org/10.1016/S0277-5387(97)00409-9.

(132) Radecka-Paryzek, W.; Patroniak, V.; Lisowski, J. Metal Complexes of Polyaza and Polyoxaaza Schiff Base Macrocycles. *Coord. Chem. Rev.* **2005**, *249* (21–22), 2156–2175. https://doi.org/10.1016/J.CCR.2005.02.021.

(133) Manseki, K.; Sakiyama, H.; Sakamoto, M.; Nishida, Y.; Aono, H.; Sadaoka, Y.; Ohba, M.; Okawa, H. A New Type Copper(II)-Gadolinium(III) Complex of Phenol-Based Side-Off Type Dinucleating Ligand Containing Fully Saturated Amino Nitrogens as Coordinating Atoms. *Synth. React. Inorg. Met-Org. Chem.* **2001**, *31* (8), 1443–1451. https://doi.org/10.1081/SIM-100107209.

(134) Brianese, N.; Casellato, U.; Tamburini, S.; Tomasin, P.; Vigato, P. A. Functionalized Acyclic Schiff Bases and Related Complexes with D- and f-Metal Ions. *Inorg. Chim. Acta* **1998**, *272* (1–2), 235–251. https://doi.org/10.1016/S0020-1693(97)05909-4.

(135) Echenique-Errandonea, E.; Zabala-Lekuona, A.; Cepeda, J.; Rodríguez-Diéguez, A.; Seco, J. M.; Oyarzabal, I.; Colacio, E. Effect of the Change of the Ancillary Carboxylate Bridging Ligand on the SMM and Luminescence Properties of a Series of Carboxylate-Diphenoxido Triply Bridged Dinuclear ZnLn and Tetranuclear Zn_2Ln_2 Complexes (Ln = Dy, Er). *Dalt. Trans.* **2019**, *48* (1), 190–201. https://doi.org/10.1039/C8DT03800G.

(136) Tadanobu, S.; Ken, S.; Tar, T. Conformational Change of a Macrobicyclic Complex. Structure of Free Ligand and Interactions with DMSO. *Chem. Lett.* **1993**, *22* (5), 859–862. https://doi.org/10.1246/cl.1993.859.

(137) Hu, X.; Qiu, L.; Sun, W.; Ng, S. [1,4,12,15,18,26,31,39,42,43,44-Undeca-aza-penta-cyclo[13.13.13.16,10.120,24.133,37]Tetra-tetra-conta-4,6,8,10(44),11,18,20,22,24(43),25,31,33,35,37(42),38-Penta-deca-ene-K_9N_4,N_{11},N_{18},N_{26},N_{31},N_{39},N_{42},N_{43},N_{44}]Gadolinium(III) Trichloride Trihydrate. *Acta Crystallogr. Sect. E Struct. Rep. Online* **2006**, *62* (12), m3351–m3353. https://doi.org/10.1107/S1600536806047477.

(138) Hu, X.; Lu, Y.; Luo, Q. Characerization and Crystal Structure of Lanthanide Cryptates of a Ligand Derived from 2,6-Diformyl Pyridine. *Polyhedron* **2004**, *23* (1), 49–53. https://doi.org/10.1016/j.poly.2003.09.024.

(139) Hu, X.; Li, Y.; Luo, Q. Synthesis and Crystal Structure of a New Neodymium Cryptate of a Ligand Derived from 2,6-Diformylpyridine. *J. Coord. Chem.* **2003**, *56* (15). https://doi.org/10.1080/00958970310001650349.

(140) Xuelei, H.; Li, Q.; Zhong, C.; Qimao, H.; Zhiquan, P. Synthesis of Alkaline Earth and Lanthanide Cryptates with Pyridine-Based Group. *J. Rare Earth* **2007**, *25* (6), 674–678. https://doi.org/10.1016/S1002-0721(08)60005-8.

(141) Martin, N.; G. Bünzli, J.-C.; McKee, V.; Piguet, C.; Hopfgartner, G. Self-Assembled Dinuclear Lanthanide Helicates: Substantial Luminescence Enhancement upon Replacing Terminal Benzimidazole Groups by Carboxamide Binding Units. *Inorg. Chem.* **1998**, *37* (3), 577–589. https://doi.org/10.1021/ic971401r.

(142) Bünzli, J.-C. G.; André, N.; Elhabiri, M.; Muller, G.; Piguet, C. Trivalent Lanthanide Ions: Versatile Coordination Centers with Unique Spectroscopic and Magnetic Properties. *J. Alloy. Compd.* **2000**, *303–304*, 66–74. https://doi.org/10.1016/S0925-8388(00)00609-5.

(143) Orchard, A. F. *Magnetochemistry*; Oxford University Press, 2003.

(144) Carlin, R. L. Rare Earths or Lanthanides. In *Magnetochemistry*; Springer Berline Heidelberg, 1986; pp 237–261.

(145) V. Gelis, A.; J. Lumetta, G. Actinide Lanthanide Separation Process—ALSEP. *Ind. Eng. Chem. Res.* **2014**, *53* (4), 1624–1631. https://doi.org/10.1021/ie403569e.

(146) Wilden, A.; Modolo, G.; Sypula, M.; Geist, A.; Magnusson, D. The Recovery of An(III) in an Innovative-Sanex Process Using a Todga-Based Solvent and Selective Stripping with a Hydrophilic BTP. *Procedia Chem.* **2012**, *7*, 418–424. https://doi.org/10.1016/j.proche.2012.10.065.

(147) Gorietti, D.; Giardina, I.; Arginelli, D.; Battisti, P. Determination of Plutonium, Americium and Curium Isotopes in Radioactive Metal Wastes Deriving from Nuclear Decommissioning. *J. Radioanl. Nucl. Chem.* **2017**, *314* (3), 1785–1792. https://doi.org/10.1007/s10967-017-5553-y.

(148) Andreev, G. B.; Budantseva, N. A.; Fedoseev, A. M. Coordination Interaction of Transuranium Elements with N-Donor Ligands. In *Structural Chemistry of Inorganic Actinide Compounds*; Elsevier, 2007; pp 363–407. https://doi.org/10.1016/B978-044452111-8/50011-9.

(149) Prodan, I. D.; Scuseria, G. E.; Martin, R. L. Covalency in the Actinide Dioxides: Systematic Study of the Electronic Properties Using Screened Hybrid Density Functional Theory. *Phys. Rev. B* **2007**, *76* (3), 033101. https://doi.org/10.1103/PhysRevB.76.033101.

(150) Shannon, R. D. Revised Effective Ionic Radii and Systematic Studies of Interatomic Distances in Halides and Chalcogenides. *Acta Crystallogr., Sect A Found. Crystallogr.* **1976**, *32* (5), 751–767. https://doi.org/10.1107/S0567739476001551.

(151) Reilly, S. D.; Scott, B. L.; Gaunt, A. J. $[N(n\text{-}Bu)_4]_2[Pu(NO_3)_6]$ and $[N(n\text{-}Bu)_4]_2[PuCl_6]$: Starting Materials To Facilitate Nonaqueous Plutonium(IV) Chemistry. *Inorg. Chem.* **2012**, *51* (17), 9165–9167. https://doi.org/10.1021/ic301518g.

(152) Surbella, R. G.; Ducati, L. C.; Autschbach, J.; Pellegrini, K. L.; McNamara, B. K.; Schwantes, J. M.; Cahill, C. L. Plutonium Chlorido Nitrato Complexes: Ligand Competition and Computational Metrics for Assembly and Bonding. *Chem. Commun.* **2018**, *54* (85), 12014–12017. https://doi.org/10.1039/C8CC05578E.

(153) Reilly, S. D.; Su, J.; Keith, J. M.; Yang, P.; Batista, E. R.; Gaunt, A. J.; Harwood, L. M.; Hudson, M. J.; Lewis, F. W.; Scott, B. L.; et al. Plutonium Coordination and Redox Chemistry with the $CyMe_4$ -BTPhen Polydentate N-Donor Extractant Ligand. *Chem. Commun.* **2018**, *54* (89), 12582–12585. https://doi.org/10.1039/C8CC06015K.

(154) Matonic, J. H.; Neu, M. P.; Enriquez, A. E.; Paine, R. T.; Scott, B. L. Synthesis and Crystal Structure of a Ten-Coordinate Plutonium(IV) Ion Complexed by 2-[(Diphenylphosphino)Methyl]Pyridine N,P-Dioxide: $[Pu(NO_3)_3\{2\text{-}[(C_6H_5)_2P(O)CH_2]C_5H_4NO\}_2][Pu(NO_3)_6]_{0.5}$. *J. Chem. Soc., Dalt. Trans.* **2002**, No. 11, 2328–2332. https://doi.org/10.1039/b106624m.

(155) Wong, W.-K.; Yang, X.; Jones, R. A.; Rivers, J. H.; Lynch, V.; Lo, W.-K.; Xiao, D.; Oye, M. M.; Holmes, A. L. Multinuclear Luminescent Schiff-Base Zn−Nd Sandwich Complexes. *Inorg. Chem.* **2006**, *45* (11), 4340–4345. https://doi.org/10.1021/ic051866e.

BIOGRAPHICAL SKETCH

Bonnie E. Klamm

EDUCATION

Ph.D. | Florida State University, Tallahassee, FL | August 2017 – Present
Inorganic Chemistry
·Cumulative GPA 4.00

B.A. | University of New Mexico, Albuquerque NM | August 2015 – July 2017
Major: Earth and Planetary Science | Minor: Chemistry
·Summa Cum Laude
·Cumulative GPA 4.16

Washington State University, Pullman WA | June 2015 – July 2015
Nuclear Forensics Undergraduate Summer School, provided by U.S. Department of Homeland Security
·Graduate Courses: Radiochemistry & Radiotracers, Radiochemistry Laboratory
·Cumulative GPA: 4.00

Western Washington University, Bellingham WA | September 2013 – December 2014
Study: Biochemistry
·Cumulative GPA: 3.32

Skagit Valley Community College, Oak Harbor WA | September 2012 – June 2013
Running Start, Dual Credit
·Cumulative GPA: 3.95

FELLOWSHIPS, GRANTS, AND SCHOLARSHIPS RECIEVED

Graduate School:

·Innovations in Nuclear Technology R&D Awards | 2019

·Florida State University Summer Departmental Travel Award | 2019

·Nuclear Energy University Program Fellowship | 2019 - 2020

·G. T. Seaborg Institute Research Fellowship | 2019

·Florida State University Graduate Grant | 2018

·Florida State University Graduate Grant | 2017

Undergraduate:

· Student Intern | Sandia National Laboratories | 2016 - 2017

·Amigo Transfer Scholarship | University of New Mexico | 2015 - 2017

·Nuclear Forensics Undergraduate Summer School | U.S. Department of Homeland Security/Washington State University | 2015

·Student Undergraduate Laboratory Internship | Los Alamos National Laboratory | 2015

·Academic Scholarship | St. Paul Methodist Church | 2014

·Presidents List | Western Washington University | 2014

·Presidents Scholarship | Western Washington University | 2013

·Presidents Award | Presidents Education Awards Program | 2013

RESEARCH EXPERIENCE

Los Alamos National Laboratories | Nuclear Energy University Program | Visiting Student Intern
Research Advisor: Ben Stein and Aaron Tondreau
January 2020 – Present

Molten Salt Spectroscopy Characterization

In-situ UV/vis measurements on various molten salt complexes, coupled with the synthesis of actinide-chloride compounds relevant to molten salt systems to learn the application of these advanced spectroscopic techniques as applied to molten salts under realistic conditions.

Florida State University | Graduate School
Research Advisor: Professor Thomas Albrecht-Schmitt
August 2017 – Present

Synthesis and Characterization of Schiff Base Coordination Complexes with Actinides

Synthesis and characterization of Schiff base coordination complexes with lanthanides and actinides. Focus extensively on advanced X-ray crystallography, cyclic voltammetry, NMR, and UV/vis/NIR in order to probe the electronic structure of *f*-block compounds.

Los Alamos National Laboratories | Seaborg Fellowship | Graduate Research Assistant

Research Advisor: Aaron Tondreau
May 2019 – August 2019, continued

Controlling Lewis Acid Catalysis with Lanthanides to form Bimetallic Complexes

Synthesis and characterization of homo- and hetero-bimetallic coordination complexes with lanthanides. Characterization via X-ray crystallography, UV/vis/NIR, and IR spectroscopy, as well as NMR and SQUID.

Sandia National Laboratories | Student Intern | Advanced Materials Laboratory
Research Advisor: Ryan Falcone Hess
February 2016 – July 2017

Development of a Downhole Electrochemical Sensor for Ionic Species Measurement

Develop ion selective and reference electrodes as well as pH monitor capable of measuring geothermal conditions.

Synthesis and Characterization of UO_2/Zircaloy Interface

Replicate the UO_2/Zircaloy interface of a nuclear fuel rod to simulate damage accumulated over time, and address the resulting strain of the material.

Recycling Rare Earth Elements Using Ion Exchange Chemistry

Quantitatively characterize the separation of lanthanides using selective resins at various conditions and ICP-MS.

Los Alamos National Laboratory | SULI Internship | Neutron Science Center
Research Advisor: Brenda Dingus
January 2015 – May 2015

Simulating Lorenzt Invariance with High Altitude Water Cherenkov (HAWC)

Constrain quantum gravity (E_{QG}) between 10^{18} – 10^{21} GeV by modeling energy dependent photons using Monte Carlo simulations in ROOT. Use HAWC sensitivity to gamma ray bursts to simulate Lorentz invariance violations (LIV) using 15 source models by varying distance and flux.

WORK AND TEACHING EXPERIENCE

Florida State University | General Chemistry I, II Lab Assistant
Employer: Stephanie Dillon
August 2017 – May 2018

Western Washington University | Organic Chemistry Lab Assistant | Chemistry
Employer: Hla Win-Piazza

June 2014 – December 2014

Western Washington University | Organic Chemistry Lab Prepper | Chemistry
Employer: Hla Win-Piazza
June 2014 – August 2014

PUBLICATIONS

11. **Klamm, B.E.**; Windorff, C. J.; Celis-Barros, C.; Beltran-Levia, M. J,; Sperling, J. M.; Albrecht-Schmitt, T. E. A. "Exploring the Oxidation States of Neptunium Schiff Base Coordination Complexes" In preparation

10. **Klamm, B. E.**; Windorff, C. J.; Albrecht-Schmitt, T. E. A.; Scott, B. L.; Tondreau, A. M. "Synthesis of Trivalent Plutonium and Cerium Cryptates" In preparation.

9. Sperling, J. M.; Warzecha, E. J.; Windorff, C. J.; **Klamm, B. E**.; Gaiser, A. N.; Whitefoot, M. A.; White, F. D. ; Poe, T. N.; Albrecht-Schmitt, T. E. "Pressure-Induced Spectroscopic Changes in a Californium 1D Material are Twice as Large as Found in the Holmium Analog" *Inorg. Chem*. **2020** Submitted.

8. **Klamm, B. E.**; Albrecht-Schmitt, T. E.; Billow, B. S.; White, F. D.; Kozimor, S. A.; Scott, B. L.; Tondreau, A. M. "Using Intrinsic Lewis-Acidity in the Generation of Bimetallic Lanthanide Complexes" *Inorg. Chem*. **2020** Submitted.

7. Windorff, C. J.; Chemey, A.; Sperling, J. M.; **Klamm, B. E.**; Albrecht-Schmitt, T. E. "Examination of Molten Salt Reactor Relevant Elements Using Hydrothermal Synthesis" *Inorg. Chem*. **2020** In review.

6. Sperling, J. M.; Warzecha, E. J.; Celis-Barros, C.; Sergentu, D. C; Wang, W.; **Klamm, B. E.**; Windorff, C. J.; Gaiser, A. N.; White, F. D.; Beery, D. A.; Chemey, A. T.; Whitefoot, M. A.; Long, B. N.; Hanson, K.; Kogerler, P.; Speldrich, M.; Zurek, E.; Autschbach, J.; Albrecht-Schm "Compression of Certain Curium Coordination Complexes Enhances Covalency" *Nature*. **2019** In review.

5. Sperling, J. M.; Gaiser, A. N.; Windorff, C. J.; **Klamm, B. E.**; Whitefoot, M.; Chemey, A.; Long, B.; Campbell, J.; Albrecht-Schmitt, T. E. "Structural and Spectroscopic Investigation of Two Plutonium Mellitates" *Inorg. Chem.* **2020**, 59, 5, 3085-3090

DOI: 10.1021/acs/inorg.chem.9b03432

4. **Klamm, B. E.**; Windorff, C. J.; Cristian Celis-Barros; Marsh, M. L.; Albrecht-Schmitt, T. E. "Synthesis, Spectroscopy, and Theoretical Details of Uranyl Schiff Base Coordination Complexes" Klamm, B. E.; Windorff, C. J.; Cristian Celis-Barros; Marsh, M. L.; Albrecht-Schmitt, T. E. *Inorg. Chem.* **2020**, 59(1), 23-31

DOI: 10.1021/acs.inorgchem.9b00477

3. **Klamm, B. E.**; Windorff, C. J.; Cristian Celis-Barros; Marsh, M. L.; Meeker, D. S.; Albrecht-Schmitt, T. E. "Experimental and Theoretical Comparison of Transition-Metal and Actinide Tetravalent Schiff Base Coordination Complexes" *Inorg. Chem.* **2018**, 57 (24), pp 15389-15398

DOI: 10.1021/acs.inorgchem.8b02700

2. **Klamm, B. E.**; Windorff, C. J.; Marsh, M. L.; Meeker, D. S.; Albrecht-Schmitt, T. E. "Schiff-base Coordination Complexes with Plutonium(IV) and Cerium(IV)" *Chem. Commun.* **2018**, 54 (62), pp 8634-8636.

DOI: 10.1039/C8CC03571G

1. Corbin, C. W.; Grzegorz Cieslewski, G.; Hess, R. F.; **Klamm, B. E**.; Goldfarb, L.; Boyle, T. J.; Yelton, W. G. Development of a Downhole Tool for Measuring Enthalpy in Geothermal Reservoirs" Proceedings: Workshop on Geothermal Reservoir Engineering. **2017**, 42.

PRESENTATIONS

Graduate:

f-element Schiff Base Coordination Complexes | CAST Meeting | Philadelphia | 2019

Schiff Base Coordination Complexes with Tetravalent Cations | Transactinide Conference | Wilhelmshaven Germany | 2019

Controlling Lewis Acid Catalysis with Lanthanides to form Bimetallic Complexes | Student Symposium | Los Alamos National Laboratory | 2019

Schiff Base Coordination Complexes with the *f*-elements | ACS National Meting | Florida State University | 2019

Schiff Base Coordination Complexes with Pu(IV) and Ce(IV) | Plutonium Futures Conference | Florida State University | 2018

Undergraduate:

Development of a Downhole Technique for Measuring Enthalpy in Geothermal Reservoirs | Sandia National Laboratory | NM Senators, Tom Udall, Martin Heinrich | 2016

Synthesis of UO_2-Zircaloy thin films to address pellet-cladding debonding | ACS National Meeting | Sandia National Laboratory | 2016

Simulating Lorentz Invariance Violation with HAWC | Los Alamos National Laboratory | 2015